Ferrimagnetic Rare-Earth-Transition-Metal Heterostructures: Implications for Future Data Storage, Sensors, and Unconventional Computing

Dissertation

zur Erlangung des akademischen Grades

Dr. rer. nat.

eingereicht an der
Mathematisch-Naturwissenschaftlich-Technischen Fakultät
der Universität Augsburg

von

Michael Heigl

Augsburg, April 2022

Universität
Augsburg
University

Erstgutachter:	Prof. Dr. Manfred Albrecht
Zweitgutachter:	Prof. Dr. Dieter Suess
Drittgutachter:	Prof. Dr. Hans Josef Hug

Tag der mündlichen Prüfung: 24.06.2022

Bibliographic Record

Heigl, Michael:
Ferrimagnetic Rare-Earth-Transition-Metal Heterostructures: Implications for Future Data Storage, Sensors, and Unconventional Computing

Dissertation
University of Augsburg, Faculty of Mathematics, Natural Sciences, and Materials Engineering (2022)

Abstract

In this work, different ferrimagnetic rare-earth-transition-metal heterostructures are investigated. The findings provide implications for future data storage, sensor, and unconventional computing devices.

In the first part, ferri- and ferromagnetic films are exchange-coupled and studied as potential composite media for magnetic recording technologies. For this, the underlying individual layers are examined, too. Within this study, the influence of Pd and Pt insertion layers in ferromagnetic Co/Ni multilayers is investigated. In these systems, the maximum effective magnetic anisotropy is more than doubled by the introduced insertion layers, while the initial saturation magnetization and Curie temperature are reduced. Further, amorphous Tb-FeCo alloys and multilayers are studied as the second building block of the desired composite medium. In particular, the structural and magnetic properties are analyzed upon post-annealing. At temperatures above 400 K, irreversible effects on the structural properties are found, which also influence the magnetic properties. It is shown that these changes in properties cannot be prevented by tuning the composition or by a multilayer structure of the film. However, key insights on the structural and magnetic properties upon annealing are provided for future high-temperature devices. Afterward, the exchange-coupled ferrimagnetic/ferromagnetic bilayer is studied. Measurements on the dependency on temperature, the ferrimagnetic composition, and the thickness of the ferromagnet are carried out. Two distinct magnetic reversal mechanisms are revealed. The reversal characteristics depend critically on the thickness of the ferromagnetic layer. The underlying microscopic origin is revealed by high-resolution magnetic force microscopy. Above a certain thickness of the ferromagnet, the switching process is driven by in-plane domain wall propagation. In contrast, thinner ferromagnetic layers exhibit a nucleation-dominated reversal due to grain-to-grain variations in magnetic anisotropy. Although the realization of an exchange-coupled composite medium for magnetic recording can not be achieved, insights for the future realization of sub-micron high energy density permanent magnets and spintronic devices are gained.

In the second part of this work, topologically protected spin structures, including skyrmions and antiskyrmions, are investigated in Fe/Gd-based multilayers. Particularly in coexisting phases, different topologically protected magnetic quasi-particles may show fascinating physics and potential for spintronic devices. While skyrmions are observed in a wide range of materials, until now, antiskyrmions have been exclusive to materials with D_{2d} or S_4 symmetry. In this work, first and second-order antiskyrmions are stabilized for the first time by magnetic dipole-dipole interaction. Using Lorentz transmission electron microscopy imaging, coexisting first- and second-order antiskyrmions, Bloch skyrmions, and type-2 bubbles are observed, and the range of material properties and magnetic fields where the different spin objects form and dissipate is determined. The discovered phase pocket of metastable antiskyrmions for low saturation magnetization and uniaxial magnetic anisotropy values is confirmed by micromagnetic simulations and represents a recipe, which has to be satisfied for the stabilization of antiskyrmions by dipole-dipole interaction in other material systems. Furthermore, the nucleation process of the spin objects and the influence of an in-plane magnetic field are studied. Additionally, post-deposition techniques are employed to locally change the anisotropy of the samples and influence the nucleation and stability range of the spin objects. The gained knowledge significantly simplifies future investigations of antiskyrmions. Moreover, the coexisting phases of different topologically protected spin objects and their controlled nucleation provide great potential for further studies on magnetic quasi-particle interactions, spin dynamics, as well as for possible future applications in spintronics, namely the racetrack memory, skyrmionic interconnections, skyrmion-based unconventional computing, and sensor devices.

Contents

Chapter 1

Introduction - The Future of Data Storage

In the year 2020, 64 zettabytes of data were created or replicated [1]. This corresponds to $64 \cdot 10^{21}$ bytes or 64 billion terabytes (TB). Due to the COVID-19 pandemic, the year 2020 exhibited a an exceptionally high growth rate in data. Nevertheless, even without the unprecedented effects of this pandemic, the long-term trend of global data creation shows an annual growth rate of over 20% [1, 2]. The reasons for this are manifold. Not only the world population but with it also the number of unique mobile users, the adoption rate of internet services such as social media, and the number of data-creating devices are growing. Nowadays, more and more everyday objects have the ability to connect to the internet and thus collect data for their targeted control and analysis, which coined the term *Internet of Things*. While 0.08 internet-connected devices per person were active in the year 2003, in 2020, every human owns on average three connected devices [3]. Furthermore, the field of *Machine Learning* has rapidly increased its application spectrum over the last years. This term describes special computer algorithms that are designed to base their decision-making on previously seen training data [4]. This means that the practicality of these algorithms depends mainly on the availability and quality of the training data. Therefore, different actors, including major tech companies, started to collect as much utilizable data as possible to train their machine learning models. The following shift to a centralization of data is also often mentioned in connection with the buzzword *Big Data*. It is associated with the change that a growing ratio of data is no longer managed by individual persons and devices but by large technology companies and data centers [1]. As a result, users increasingly only access their data via the internet, which in turn has coined the term *Cloud* storage.

On another note, an artificial factor that spiked the demand for data storage recently is *Cryptocurrency*. While most of these decentralized digital assets are designed to be created/mined by solving complex computational math problems, new, less compute, and energy-intensive currencies are of great interest. One of these currencies is *Chiacoin*, which uses available data storage space as the limiting factor. Dependent on how much data space is available, the value that can be mined per time is set. In early 2021, the rise in popularity of these cryptocurrencies led to a temporary increase in the price of storage media of more than 60% [5].

Another shift that becomes more and more obvious is that the classic *Von-Neumann Computer Architecture* starts to fail the demands of modern computing challenges. The architecture used by most computers today is fundamentally bottlenecked by the so-called *Memory Wall* and is not suited, for example, for the high concurrency of artificial neural networks [6]. Due to the physical separation of the processing and memory unit, the bandwidth between these two constrains the possible performance and energy efficiency [7]. New unconventional computer architectures are needed, as well as memory solutions directly implemented in the processing units. One example of a possible computer architecture suited for the high concurrency of artificial neural networks is the brain-inspired *Neuromorphic Architecture*. It includes not only many parallel connected processing units but also directly connects memory elements, which can be manipulated individually and parallel to each other [8].

All the described trends above lead to an ever-increasing demand for more available data storage at the lowest possible price, as well as a need for new forms of memory devices. Over the last decades, the relation between price and data storage can be best described by the self-fulfilling prophecy of *Moore's Law*. He first predicted the exponential growth of the number of transistors in an integrated circuit and the exponentially decrease in cost [9]. The law was later refined by specifying that the number would double on a two-year basis with no increase in cost [10]. While the original law was only stated for transistors, it was soon also applied to data storage solutions. Here, a similar doubling of bit density at a constant price was expected and observed [11]. It is important to note that cost per bit data is not the only metric to keep in mind for data storage solutions. Other vital aspects are read and write speed, energy efficiency, volatility, longevity, and concurrency.

In the past decade, three non-volatile (NV) storage solutions in particular dominated the market, each with its own benefits: *Linear Tape-Open* (LTO) tape cartridges, *Hard Disk Drives* (HDD), and *NAND Flash* based storage devices including *Solid-State Drives* (SSD). While LTO tape is not popular for consumer devices, it is still in high demand for business solutions. The main advantage over its competitors is its low bit error rate, longevity, which can last over 30 years, scalability, and low cost over time, but the high upfront costs and necessity of a special driver keeps it in its niche existence [12]. In modern consumer devices, SSDs mostly replaced HDDs due to their faster read and write speeds [13]. In contrast, HDDs are still the primarily used storage solution for large-scale cloud storage because of the lower cost per data bit [12]. While all three have fulfilled the expectations of Moore's law partially for more than 40 years, they could no longer achieve this goal in their recent past and are in desperate need of new technologies [14].

There are also other specialized forms of computer memory, like random-access memory (RAM). In these semiconductor-based devices, the NV is sacrificed for fast read and write operations. They are usually used in syntheses with NV memories to store working data and machine code and to bridge the gap between the memory and computing unit [15].

In this work, the outlined challenges of modern and future data storage solutions are tackled by investigating ferrimagnetic systems as potential building blocks. Chapter 2 and 3 lay the necessary fundamentals of the occurring magnetic phenomena and the used experimental techniques.

In chapter 4 ferrimagnetic and ferromagnetic films are exchange-coupled and studied as potential composite media for magnetic recording technologies. Section 4.1 describes the recent development of HDDs and introduces the concept of *Heat-Assisted Magnetic Recording* (HAMR). Here, the recording medium is heated during the data writing process to enable materials with larger bit densities. The investigated bilayers are presented as a potential candidate for this new technology (Sec. 4.1.3). The potential application of *Magneto-Resistive Random Access Memories* (MRAM) is also established, which could replace modern RAM solutions with comparable speeds and the additional benefit of non-volatility. First, the individual layers are systematically analyzed in regard to their magnetic and structural properties, starting with the ferromagnetic Co/Ni-based multilayers (MLs) (Sec. 4.2) and followed by amorphous ferrimagnetic Tb-FeCo alloys and MLs (Sec. 4.3). Afterward, the two systems are investigated as a bilayer system coupled by direct exchange interaction (Sec. 4.4). The summarized results and implications for future data storage technologies are elaborated in Sec. 4.5.

Chapter 5 focuses on the nucleation, stability, and behavior of different dipolar-stabilized spin textures in Fe/Gd-based MLs. Different kinds of topologically protected magnetic whirls called *Skyrmions* and *Antiskyrmions*, are created and analyzed. The observed coexisting spin objects have implications for the proposed *Racetrack Memory*, which potentially can compete with the current NV SSD and HDD data storage solutions. Here, the information is stored in moving skyrmions present on a magnetic film (Sec. 5.1.1). The coexisting spin objects also show huge potential as the smallest information carriers for unconventional computing solutions. One possibility is the use of skyrmions in memory elements in future neuromorphic computers, where they act as artificial synapses, which is further described in Sec. 5.1.2. Additionally to data storage and unconventional computer solutions, skyrmions also exhibit promising properties for new sensor types elaborated in Sec. 5.1.3. Skyrmion-hosting Fe/Gd MLs are investigated in Sec. 5.2, before the layer stack is expanded by the insertion of Ir and other metals to host even more sophisticated spin objects, like antiskyrmions (Sec. 5.3). Different imaging techniques for spin objects are compared in Sec. 5.4. The influence of a magnetic in-plane field (Sec. 5.5) and post-deposition anisotropy engineering by ion irradiation (Sec. 5.6) is also shown. Finally, a summary is given for dipolar-stabilized spin objects, and the next necessary research steps are outlined. Further, the results are put into perspective in the context of applications in data storage, unconventional computing, and sensor solutions in Sec. 5.7.

In the last chapter, the presented results of this work are evaluated in terms of their impact on future research.

Chapter 2

Fundamentals

The most important theoretical fundamentals as well as the most prominent magnetic phenomena present in this work are described in this chapter. First, the different magnetic interactions and energy terms are outlined. Afterward, prominent resulting phenomena are described: *Ferrimagnetism* (Sec. 2.2), *Interfacial Exchange Coupling* including the *Exchange Bias* (EB) effect (Sec. 2.3), and different kinds of spin textures (Sec. 2.4). The latter section includes different domain and domain wall (DW) types as well as the characterization of nanometer-large topologically protected magnetic whirls called *Skyrmions*.

2.1 Magnetic Energies

Systems strive to minimize their total energy. To apply this fundamental rule of physics to magnetism, four major magnetic energy terms are briefly introduced in the following sections: *Exchange Energy* (Sec. 2.1.1), *Zeeman Energy* (Sec. 2.1.2), *Dipolar Energy* (Sec. 2.1.3), and *Anisotropy Energy* (Sec. 2.1.4). Global and local minima of the sum of theses energies represent the observable stable and meta-stable states in the presented results in chapter 4 and 5. A more detailed description of the theoretical background can be found in Ref. [16–20].

2.1.1 Exchange Energy

The arguably most important magnetic energy term has its origin in the short-range exchange interaction between magnetic moments. The quantum mechanical phenomena responsible for this interaction can be distinguished between the direct and indirect exchange interaction. Please note that the literature sometimes uses a finer classification of the different interactions due to diffuse boundaries of the different possible exchange types [21].

Direct Exchange Interaction

The direct exchange interaction stems from the overlapping wave functions of the electrons of the same atom or nearest neighbor atoms. The consequent influence on their spin orientation in respect to each other enables long-range magnetic ordering, namely ferromagnetism, antiferromagnetism, and ferrimagnetism. The exchange energy

$$E_{\mathrm{ex}} = -2 \sum_{i<j} J_{ij} \boldsymbol{S}_i \boldsymbol{S}_j \tag{2.1}$$

depends on the quantum mechanical exchange integral J_{ij} and the direction of the interacting spins $\boldsymbol{S}_i$ and $\boldsymbol{S}_j$. Therefore, a predominately positive or negative J_{ij} favors potentially a parallel (ferromagnet) or antiparallel (antiferromagnet, ferrimagnet) alignment of the spins, respectively. Equation 2.1 can be also expressed as the integral over the sample volume

$$E_{\mathrm{ex}} = A \int_V (\nabla \boldsymbol{M})^2 \, \mathrm{d}V \tag{2.2}$$

with $\boldsymbol{M}$ being the local magnetization and A being the material-specific *Exchange Stiffness Constant*. The here described interactions are, as stated, very short-ranged and only significant for neighboring atoms. Longer-ranged interactions usually occur via intermediary atoms, which is described in the following.

Indirect Exchange Interaction

The two most prominent examples of indirect magnetic exchange interactions are the *Ruderman-Kittel-Kasuya-Yosida* (RKKY) interaction and the *Dzyaloshinskii–Moriya Interaction* (DMI).

The RKKY interaction describes the exchange coupling of nuclear [22] and inner electron [23] spins through the spins of conduction electrons [24, 25]. It has been observed that two magnetic layers couple ferromagnetically or antiferromagnetically, dependent on the thickness of a non-magnetic metal layer between them [26, 27]. This behavior plays a significant role in the *Giant Magnetoresistance* (GMR) effect, whose discovery was awarded the Nobel Prize 2007 [28]. The effect describes a significant change in electrical resistance dependent on the alignment of two ferromagnetic layers connected by a non-magnetic layer [29, 30].

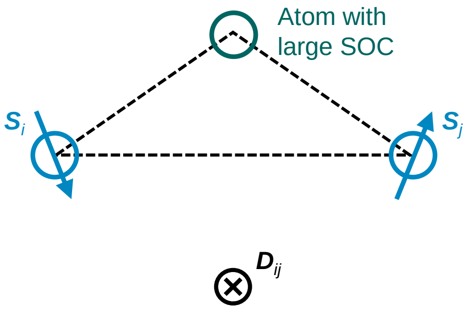

Figure 2.1: Schematic explanation of interfacial DMI. Two spins S_i and S_j are canted to each other due to the superposition of the ferromagnetic direct exchange and the super-exchange interaction with a neighboring atom with large spin-orbit coupling (SOC).

DMI or antisymmetric exchange interaction is an additional contribution that can lead to spin canting of otherwise (anti)parallel aligned spins [31]. The energy contribution can be written as

$$E_{\mathrm{DMI}} = \boldsymbol{D}_{ij} \cdot (\boldsymbol{S}_i \times \boldsymbol{S}_j) \tag{2.3}$$

with $\boldsymbol{D}_{ij}$ being the DMI vector. Dependent on the origin, the inversion symmetry of the two interacting neighboring magnetic spins $\boldsymbol{S}_i$ and $\boldsymbol{S}_j$ is tilted in different directions leading to different DMI vectors. One possibility is the so-called bulk DMI induced by atomic structures without inversion symmetry. This effect induced the first observed skyrmions in manganese silicide (MnSi) in 2009 [32]. These topologically protected spin objects have been the subject of intense research since then and are described in more detail in Sec. 2.4.2. Dependent on the crystal symmetry, two distinct types of skyrmions are possible, namely, Bloch [32–36] and Néel [37, 38] skyrmions.

The other possible mechanism is the interface DMI, illustrated in Fig. 2.1. Here, two atomic spins $\boldsymbol{S}_i$ and $\boldsymbol{S}_j$ are canted to each other, due to the superposition of the ferromagnetic direct exchange and the super-exchange interaction with a neighboring atom with large spin-orbit coupling (SOC) at the interface of the magnetic layer [39]. This mechanism is used in multilayers (MLs) consisting of ferromagnetic layers and non-magnetic heavy metal layers with large SOC to stabilize Néel skyrmions [40, 41]. To achieve constructive DMI, it is crucial to use two different non-magnetic layers enclosing the ferromagnetic layers. Otherwise, the DMI of the top and bottom interface cancel each other out. It is important to note that the sign of the DMI value depends on not only the non-magnetic but also the magnetic material. A detailed description of the microscopic origin of interface DMI is given by Jadaun et al. in Ref. [42]. Two prominent combinations of materials with large SOC and opposed DMI values with Fe or Co are Ir-Pt [41, 43] and Pt-Ta [44, 45].

Special symmetries of magnetic crystals and their resulting DMI allow the stabilization of even more complex spin objects. One example is the observation of antiskyrmions, due to the D_{2d} symmetry in acentric tetragonal Heusler compounds [46–49].

2.1.2 Zeeman Energy

Magnetic moments tend to align with along magnetic fields. The total energy of magnetic moments unaligned with an external magnetic field H_{ext} is given by the *Zeeman Energy* E_{zee} calculated by

$$E_{\mathrm{zee}} = -\frac{\mu_0}{2} \int\limits_V \boldsymbol{M}\boldsymbol{H}_{\mathrm{ext}} \,\mathrm{d}V \ . \tag{2.4}$$

For simplicity, external magnetic fields are often only referred to as H in this work.

2.1.3 Dipolar Energy

In a ferromagnet (FM), the magnetic centers, acting as magnetic dipoles, not only interact through overlapping wave functions but also perceive each other's magnetic fields. The sum of all these dipolar fields is called demagnetization field $\boldsymbol{H}_{\mathrm{d}}$, and its name reflects the tendency to reduce the total magnetization. $\boldsymbol{H}_{\mathrm{d}}$ components outside of the magnetic material itself are called stray fields. The energy of the demagnetization field is given by

$$E_{\mathrm{d}} = -\frac{\mu_0}{2} \int\limits_V \boldsymbol{M}\boldsymbol{H}_{\mathrm{d}} \,\mathrm{d}V \ , \tag{2.5}$$

where μ_0 is the magnetic permeability of vacuum and V the volume of the magnet. To minimize the *Dipolar Energy* E_{d}, a system favors a breakup into many smaller regions of different orientated $\boldsymbol{M}$ to provide the best possible flux closure of $\boldsymbol{H}_{\mathrm{d}}$. These regions are called *Magnetic Domains*. Magnetic domains are contained by domain walls (DWs), which increase the exchange energy due to the non-parallel alignment of its magnetic moments. If the needed exchange energy of the DWs is smaller than the decrease in dipolar energy, a splitting into magnetic domains of a certain size represents an energetically more favorable state. A more detailed description of the magnetic parameters influencing the domain size, as well as a description of different domain and DW types, is given in Sec. 2.4.1.

If the shape of the magnetic material is not a sphere, the magnetic moments tend to align along the axis of the material's largest expansiveness. This effect is often described as the *Magnetic Shape Anisotropy* K_{shape}. In this work, magnetic films with thicknesses multiple magnitudes smaller (nanometers) than their extension in the plane (millimeters) are investigated. In this case, the extension of the film can be assumed as infinite. Therefore, $\boldsymbol{H}_{\mathrm{d}}$ inside the magnet has the same amplitude as the total magnetization of the film. The *Saturation Magnetization* M_{s} represents the maximum magnetization per volume and together with Eq. 2.5 describes the energy density

$$K_{\mathrm{shape}} = -\frac{\mu_0}{2} M_{\mathrm{s}}^2 \tag{2.6}$$

favoring an orientation of the magnetization in the in-plane (ip) direction over the out-of-plane (oop) direction. Hence, the magnetic shape anisotropy K_{shape} describes the work per volume required to switch the magnetization of a thin magnetic film from the ip to the oop direction purely because of its dipolar energy.

2.1.4 Anisotropy Energy

In addition to the described magnetic shape anisotropy, there are other possibilities why magnetic films prefer certain directions for their magnetization. They are usually quantified by energy densities called magnetic anisotropies. The most important ones are listed in this section. A magnet can exhibit multiple magnetic anisotropies with their sum determining the energetically preferred direction of the magnetization. This direction is called the magnetic *Easy-Axis* and the energetically most unfavorable direction is called the *Hard-Axis*. The energy difference between these states is usually quantified by the *Effective Magnetic Anisotropy* K_{eff}. It represents the energy per volume needed to change the magnetization from its easy-axis to its hard-axis. In this work, mainly amorphous and polycrystalline magnetic films are discussed. Hence, there is usually no macroscopic magnetic anisotropy in the plane of the films. Consequently, it has to be only distinguished between anisotropies favoring an oop or ip orientation of the magnetic moments.

If the magnetization M is measured as a function of an applied field H in both the easy- and hard-axis direction, the resulting *M-H* hysteresis loops can be used to calculate the effective anisotropy K_{eff}. Figure 2.2 a shows an exemplary easy- and hard-axis pair. The *Coercive Field* or *Coercivity* H_{c} and the *Anisotropy Field* H_{a} represent the magnetic field needed to rotate half the saturation magnetization M_{s} and the field needed to saturate the total magnetization in the direction of the hard-axis, respectively. The magnetic *Remanence* or *Remanent Magnetization* M_{r} denotes the magnetization value left after saturation at zero magnetic field. In Fig. 2.2 a $M_{\mathrm{r}} = M_{\mathrm{s}}$, due to a collective

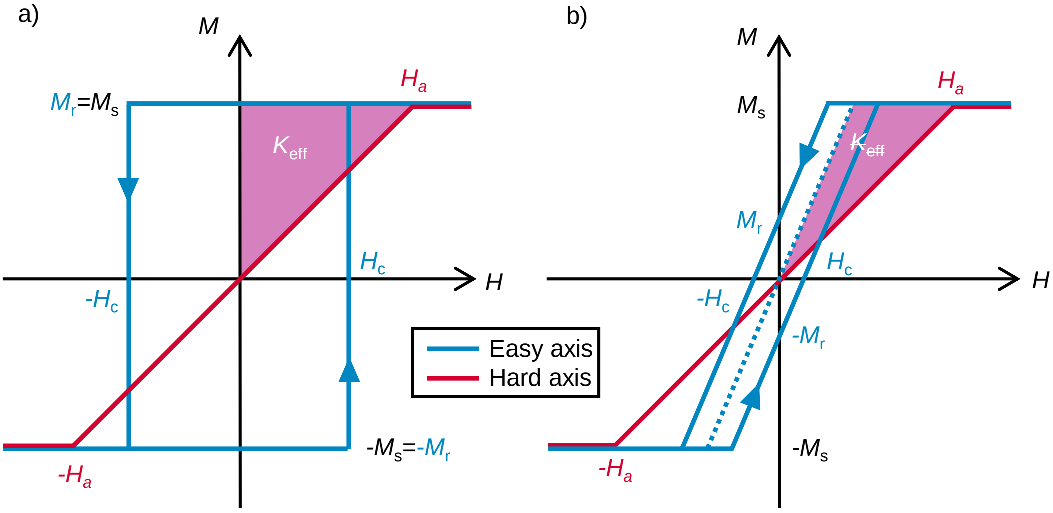

Figure 2.2: Graphical determination of the effective magnetic anisotropy. Magnetization M as a function of an applied field H in the direction of the easy (blue) and hard-axis (red). The effective magnetic anisotropy K_{eff} is given by the enclosed area marked in purple (a). The effective anisotropy of samples whose switching process is driven by domain processes cannot be calculated in this way (b). The coercivity H_{c}, the anisotropy field H_{a}, the saturation magnetization M_{s}, and the remanent magnetization M_{r} are marked in both images.

switching process at H_{c}. If the switching is a continuous process, M_{r} differs from M_{s} (Fig. 2.2 b). The value of K_{eff} is given by one side of the enclosed area between the averaged magnetization values of the two hysteresis loops:

$$K_{\text{eff}} = \mu_0 \int_0^\infty M_{\text{soft}}\, \mathrm{d}H_{\text{soft}} - \mu_0 \int_0^\infty M_{\text{hard}}\, \mathrm{d}H_{\text{hard}} \, . \tag{2.7}$$

If, like in Fig. 2.2 a, the easy- and hard-axis loops resemble a rectangular and linear shape, respectively, the approximation

$$K_{\text{eff}} = \pm \frac{\mu_0}{2} H_{\text{a}} \cdot M_{\text{s}} \tag{2.8}$$

can be used to calculate K_{eff}. In this work, it is specified that positive K_{eff} values translate to an easy-axis in the oop direction and negative K_{eff} values to an easy-axis in the ip direction. It is important to note that hysteresis loops can only be used to calculate K_{eff}, if the exchange and dipolar energies of multidomain states during the switching process are ignored. Figure 2.2 b illustrates exemplary loops where the energy contributions of multidomain states have to be included. Here, the magnetization switches continuously with an increasing field H, in contrast to the collective switching in Fig. 2.2 a. Consequently, K_{eff} cannot be calculated accurately with the presented approach.

While the shape anisotropy prefers a magnetic orientation ip of thin magnetic films, anisotropies that push the easy-axis in the oop direction are summarized in the *Uniaxial Magnetic Anisotropy* K_{u} or the *Perpendicular Magnetic Anisotropy* (PMA). Therefore, the effective anisotropy can also be expressed by

$$K_{\mathrm{eff}} = K_{\mathrm{u}} + K_{\mathrm{shape}} = K_{\mathrm{u}} - \frac{\mu_0}{2} M_{\mathrm{s}}^2 \ . \tag{2.9}$$

Further, the energy cost of rotating the magnetization from its preferred easy-axis by an angle κ is given by the *Anisotropy Energy* E_{ani} and can be calculated by

$$E_{\mathrm{ani}} = \int_V |K_{\mathrm{eff}}| \sin^2 \kappa \, \mathrm{d}V \ . \tag{2.10}$$

In the following, the most important origins and categories of anisotropies are listed and described.

Magnetocrystalline Anisotropy

The crystal structure of a magnetic film largely influences its electron orbits and, due to SOC, its spins, too. Consequently, the magnetic anisotropy is affected by the orientation of the crystal axes. Due to the amorphous or polycrystalline nature of the magnetic films discussed in this work, crystalline anisotropies do not exist or cancel each other out. Therefore, it will not be discussed further. A more detailed description of *Magnetocrystalline Anisotropies* can be found in Ref. [16, 50].

Magnetoelastic Anisotropy

Because of SOC and the influence of the material structure on the magnetic anisotropies, also strain-caused anisotropy contributions have to be considered and are often dealt with separately. These effects are cumulated under the name *Magnetoelastic Anisotropy* K_{strain} and can be quantified with the material-dependent saturation magnetostriction constant λ_{s} and the mechanical strain σ' as

$$K_{\mathrm{strain}} = -\frac{3}{2} \lambda_{\mathrm{s}} \sigma' \ . \tag{2.11}$$

Here, tensile strain is represented by positive and compressive strain by negative values. The saturation magnetostriction constant can be both negative and positive, dependent on the material, structure, and temperature [51]. Other than physical deformation, strain can stem from crystal defects, lattice mismatch [52], and be inherent to amorphous magnetic thin films [53]. In these cases, it can be strongly influenced by the chosen deposition conditions and can be the dominating anisotropy contribution [54].

Interfacial and Volume Anisotropy

It is quite common not to classify magnetic anisotropies by their physical cause but their scaling properties. Thus, anisotropy contributions can be separated into the *Interfacial Anisotropy* K_s and the *Volume Anisotropy* K_V. The effective anisotropy of a magnetic thin film with two interfaces can now be expressed depending on the thickness t as

$$K_{\text{eff}} = K_{\text{shape}} + K_V + \frac{2K_s}{t} \ . \tag{2.12}$$

Interfacial anisotropies are not exclusively based on magnetoelastic effects. For example, the hybridization of the cobalt (Co) 3d and palladium (Pd) or platin (Pt) 5d orbitals are responsible for the strong PMA seen at Co/Pd(/Pt) interfaces [55, 56]. To further benefit from the effects of interfaces, usually, MLs are used. Here, a certain layer stack is repeated N times to multiply the effects of the interfaces. This procedure is also exploited in Sec. 4.2 to achieve Co/Ni-based MLs with strong PMA.

2.2 Ferrimagnetism

Both, ferrimagnets (FIs) and antiferromagnets (AFs) exhibit a negative quantum mechanical exchange integral J_{ij} in Eq. 2.1. In contrast to an AF, the magnetizations of the different sublattices in a FI do not cancel each other out, and thus the magnetization of a FI typically does not equal zero [19, 20]. The most prominent group of FIs is a combination of ferromagnetic 3d transition metals (TMs) and heavy rare earths (REs). The ferromagnetic TMs consist of Co, iron (Fe), and nickel (Ni) and represent the only elements that are ferromagnetic at room temperature (RT). The heavy REs that this work focuses on are gadolinium (Gd) and terbium (Tb). Both need to be cooled below RT to exhibit ferromagnetic properties. Their magnetic moment stems from the localized 4f electrons.

2.2.1 Sublattice Coupling in a Ferrimagnet

If the named TMs and REs interact in the form of an alloy or at an interface, an interatomic hybridization occurs between the 3d electrons of the TM and the 5d orbital of the RE [57]. This hybridization process and its consequences for the density of states dependent on the energy are illustrated in Fig. 2.3. The basic ionic state is shown in Fig. 2.3 a.

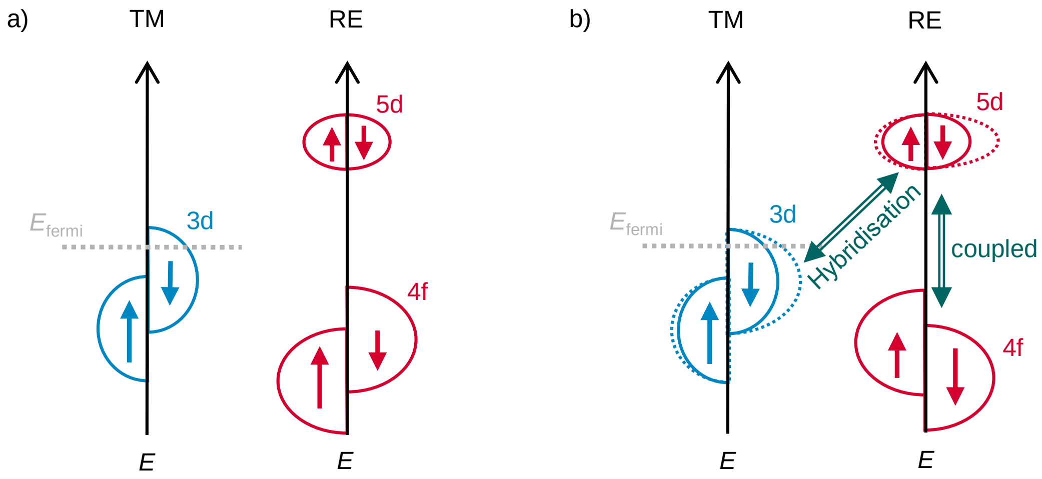

Figure 2.3: Illustration of the 3d-transition-metal-heavy-rare-earth coupling, due to the 3d-5d hybridization. Basic ionic (a) and hybridized (b) density of states of the TM and RE dependent on the energy. Adapted from Ref. [57].

The 3d electrons of the TM exhibit an energy splitting of the available states depending on their spin due to the Stoner criterion [58]. The fully occupied majority band is closer to the nucleus and thus energetically more favorable than the minority band, which is partially above the Fermi energy E_{fermi}. For the RE, only the 4f and not the 5d band show a spin-dependent energy splitting. In Fig. 2.3 b the two different element types hybridize. Due to the smaller energy difference between the TM's 3d minority band and the RE's 5d bands, they hybridize more strongly with each other, and the spin moments of the 5d band get polarized. Thus, the spin moments of the RE's 5d band are predominantly parallel to those of the TM's 3d minority band. The resulting total moment of the TM is represented by the 3d majority band. This means that the spin moments of the RE's 5d band are antiparallel aligned to the total spin moment of the TM's 3d band. Via the intraatomic coupling in the RE metal, the 5d and 4f total spin moments are always aligned parallel to each other. For a heavy RE, the valence shell is more than half-filled and, according to Hund's third rule, this means that the 4f orbital moment is aligned parallel to its spin moments. The result is that the total spin moment of the 3d metal is antiparallel to the total moment (spin + orbital moment) of the RE element.

2.2.2 Temperature Dependence of the Ferrimagnetic Sublattices

Due to the involvement of different elements in FIs, the exchange interactions of Sec. 2.1.1 have to be extended to multiple different partners with different exchange integrals. The coupling between RE atoms is weaker than the coupling between TM atoms [59, 60]. Additionally, different local magnetic anisotropy contributions affect the sublattices. Therefore, the ferrimagnetic nature of these materials can be specified as a *Sperimagnet* [61]. Here, the stronger coupled TM moments exhibit a collinear alignment, while the weaker coupled RE moments show a fan-shaped distribution. X-ray magnetic circular dichroism (XMCD) and Mößbauer-Spectroscopy measurements have been used to measure the opening angle of the different sublattices [62–64].

Another consequence of the differing properties of the sublattices is the individual magnetization dependence on the temperature. The resulting total magnetization is then made up by the sum of the sublattice contributions. An example of the individual magnetization of the TM M_{TM} and the RE M_{RE} together with the resulting total magnetization M_{total} dependent on the temperature T is given in Fig. 2.4. Depending on which sublattice shows the larger effective magnetization, the sample is called RE or TM dominant. Generally, both magnetization contributions decrease with temperature due to increasing spin fluctuations and eventually reach zero at the *Curie Temperature* T_{c}. Nevertheless, the magnetization of REs exhibits a stronger dependency on T than the magnetization of the TMs, because of their weaker exchange coupling. Thus, a RE dominant sample, as displayed in Fig. 2.4, has a decreasing M_{total} with the temperature T. At a certain temperature, the magnetization of the RE and the TM sublattice are equal, and the resulting M_{total} is zero. This temperature is called the *Compensation Temperature* T_{comp}. In this state, a FI can be directly compared to an AF and is interesting for a variety of applications. If the temperature is increased further, M_{total} increases, and the sample is TM dominant till T_{c} is reached, and the effective magnetization vanishes.

It is important to note that only certain compositions of FIs exhibit a compensation temperature. If the ratio is too much in favor of the TM material, the sample is TM dominant over the whole temperature range. If the ratio is more in favor of the RE material, T_{comp} can be at larger temperatures than T_{c} and therefore does not exist. Another interesting aspect of T_{comp} is the divergent behavior of the coercive field close to it. Different values for T_{comp} dependent on the composition are given for GdFe, TbFe,

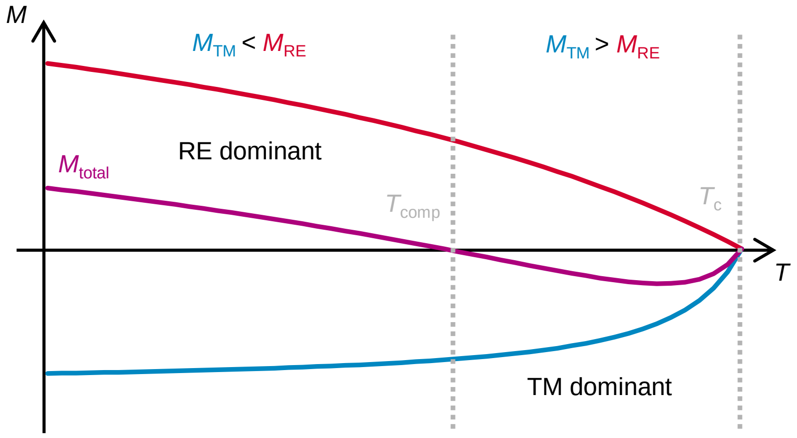

Figure 2.4: Schematic illustration of the individual and total magnetization of the two sublattices dependent on the temperature. The magnetization of the transition metal M_{TM} and the rare earth M_{RE} make up the total magnetization M_{total} of the ferrimagnet. M_{RE} is the dominant contribution for temperatures T below the compensation temperature T_{comp}, while M_{TM} dominates at temperatures higher than T_{comp} and lower than the Curie temperature T_{c}.

TbCo, and TbFeCo in Ref. [65], [66], [67], and [68], respectively. Please note that T_{comp} does not only depend on the composition but also on the thickness [69], the seed layer [70], and the sputter conditions [71].

2.2.3 Uniaxial Magnetic Anisotropy in Ferrimagnetic Systems

In the year 1973, GdFe and GdCo alloys were the first observed amorphous FIs with an oop easy-axis [72]. TbFe, TbCo, and TbFeCo are just some of the amorphous FIs that followed and showed strong PMAs in certain compositions, too [61]. The reason for this is the so-called *Short Range Order* (SRO). It was shown that although amorphous materials do not exhibit a structural long-range order, specific materials show a certain distribution function for the distance between their different elements [61, 73–76]. As stated in Sec. 2.1.3, due to dipolar magnetic interaction, the magnetization of ferromagnetic thin films prefers an ip orientation. Oppositely, a ferrimagnetic system with a SRO can exhibit a PMA purely because of dipolar interaction [77]. However, it was also pointed out that this contribution alone cannot explain the K_{u} values observed in TbFe ferrimagnets. The other origin is the so-called single ion magnetic anisotropy [78]. Here, the interaction between the 4f electrons of the RE and the surrounding ions leads to an oop orientation of the magnetic moments. This also explains the major differences between GdFe- and TbFe-based alloys. While TbFe, TbCo, and TbFeCo are known for being hard magnets with large coercivities [61], GdFe is a soft magnet without any significant coercive fields [72]. This can be attributed to the differences in the 4f electron charge distributions. While TbFe-based systems exhibit an oblate ellipsoid [79], which gives rise to an additional PMA contribution, GdFe-based systems show no significant 4f deformation [80]. This property is quantified for different REs by the *Stevens Factor* [81].

2.3 Interfacial Exchange Coupling

If two magnetic materials are in direct contact with each other, direct interfacial exchange coupling occurs, and the magnetic properties of both systems can change drastically. The most prominent example is the so-called exchange bias effect. Here, a magnetically coupled system consisting of a ferromagnetic and an antiferromagnetic layer exhibits a shift of the M-H hysteresis loop along the field axis H. This unidirectional shift occurs after the AF is cooled below its Néel temperature T_n. Here, a preferred direction exists for the FM due to the coupling to the now ordered AF. A schematic illustration of the AF/FM bilayer and its corresponding M-H hysteresis loop above and below T_n is shown in Fig. 2.5 a and b, respectively. The achieved shift of the switching process of the ferromagnetic layer is quantified by the exchange bias field H_eb, which is defined by

$$H_\mathrm{eb} = \frac{H_\mathrm{c,2} + H_\mathrm{c,1}}{2} \,. \tag{2.13}$$

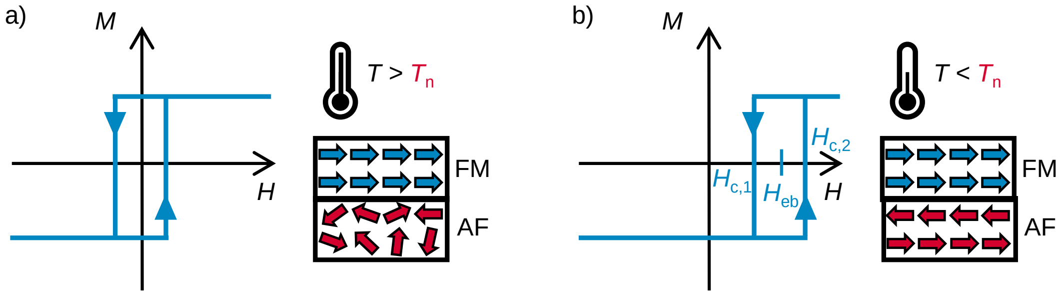

Figure 2.5: Schematic illustration of the exchange bias effect. An exchange-coupled ferromagnet (FM)/antiferromagnet (AF) bilayer above the Néel temperature T_n of the AF (a). The AF is not magnetically ordered, and the magnetization reversal of the FM remains unaffected, which is also apparent by its displayed symmetric M-H hysteresis loop. If the bilayer is cooled below T_n, the interfacial exchange coupling leads to a favorable remanent state of the FM (b). The resulting loop shift can be quantified by the exchange bias field H_eb, which lies between the two coercive fields $H_\mathrm{c,1}$ and $H_\mathrm{c,2}$.

At H_{eb}, the Zeeman energy of the ferromagnetic layer equals the exchange coupling energy. The coercivity of the ferromagnetic layer is calculated by the two switching fields $H_{\mathrm{c},1}$ and $H_{\mathrm{c},2}$ with

$$H_{\mathrm{c}} = \frac{H_{\mathrm{c},2} - H_{\mathrm{c},1}}{2} \; . \tag{2.14}$$

Since 1956, the exchange bias effect has been studied intensely in many different systems and is used for example in GMR sensors [82–84].

If two ferrimagnetic RE-TM or ferromagnetic TM layers are coupled by direct interfacial exchange, the exchange interaction usually manifests itself in the preferred parallel alignment of the magnetic moments of the TMs. The bilayer can exhibit a simultaneous single switching process or separated individual switching processes dependent on the properties of the individual layers (e.g. effective magnetic anisotropy K_{eff}, exchange stiffness A, thickness t, ...) [85–87]. If the bilayer exhibits a single switching process and the two individual layers have a large PMA, the nucleation field H_{n} of the bilayer can be estimated by

$$H_{\mathrm{n}} = \frac{2(t_1 K_{\mathrm{eff},1} + t_2 K_{\mathrm{eff},2})}{t_1 M_{\mathrm{s},1} + t_2 M_{\mathrm{s},2}} \tag{2.15}$$

with the thicknesses t_1 and t_2, the effective anisotropies $K_{\mathrm{eff},1}$ and $K_{\mathrm{eff},2}$, and the saturation magnetizations $M_{\mathrm{s},1}$ and $M_{\mathrm{s},2}$ of the two individual layers 1 and 2 [86]. Two-stage switching can only occur, if the thickness of the magnetically softer layer is roughly ten times larger than the domain wall width δ_{dw} of the magnetically harder layer [85–87]. Above this thickness, the magnetically softer layer can switch individually without the magnetically harder layer. To investigate the switching process of the magnetically softer layer, a so-called minor M-H hysteresis loop can be measured. Here, the applied magnetic field is cycled with its maximum strength being smaller than the switching field of the magnetically harder layer. The resulting hysteresis loop can exhibit a shift similar to the exchange bias effect in AF/FM systems. The achieved shift of the switching process of the magnetically softer layer can be quantified by the exchange bias field H_{eb} according to Eq. 2.13. Particularly in FI/FM [88, 89] and FI/FI [90, 91] bilayers, large exchange bias fields were achieved. The advantage of these systems in comparison to AF/FM systems is that the magnetic properties of all involved layers can be modified. Further, the shift of the switching process of the softer layer occurs in both directions depending on the magnetic field history and does not need to be set by temperature changes.

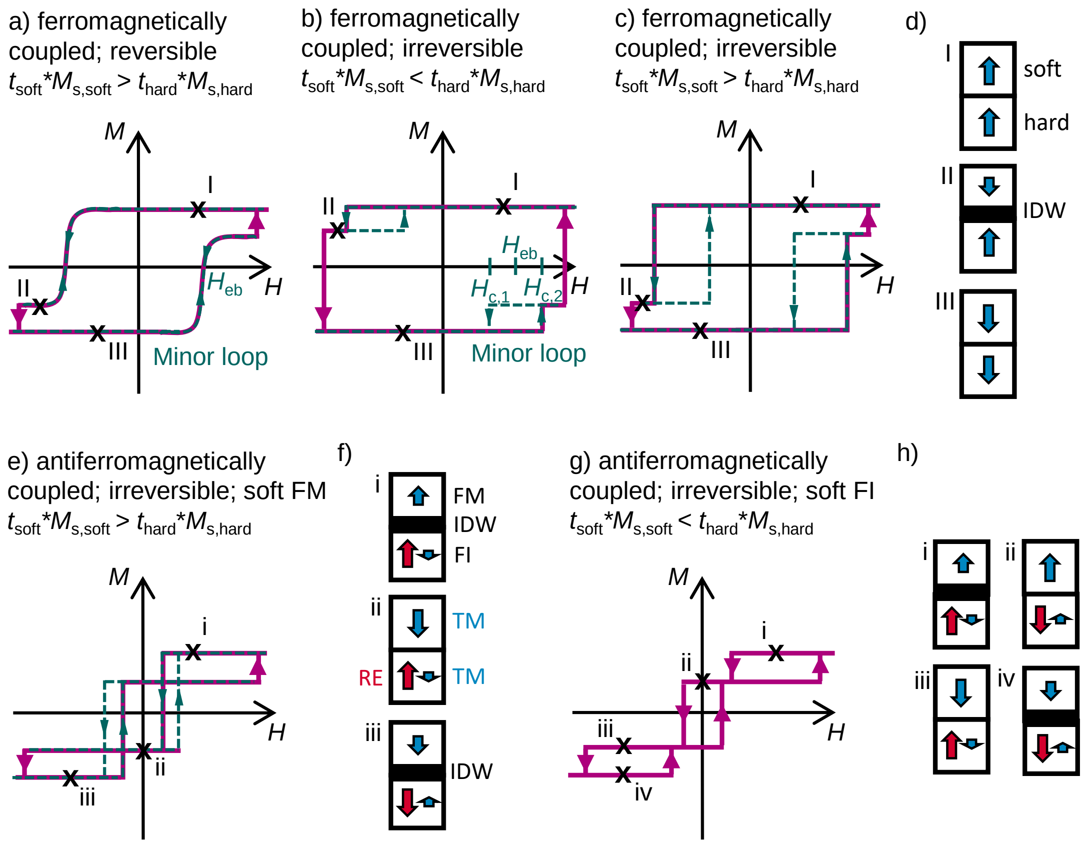

Figure 2.6: Exemplary *M-H* hysteresis loops and magnetic configuration of interfacial exchange-coupled bilayers. *M-H* hysteresis loops of a soft and hard ferromagnet coupled ferromagnetically exhibiting reversible (a) and irreversible (b,c) switching and the corresponding magnetic configurations (d). Which reversal type occurs depends on the thicknesses of the soft t_{soft} and hard layer t_{hard}, as well as their saturation magnetizations $M_{\mathrm{s,soft}}$ and $M_{\mathrm{s,hard}}$. The exchange bias field H_{eb} and the two coercive fields $H_{\mathrm{c,1}}$ and $H_{\mathrm{c,2}}$ can be extracted from the minor loop analogous to Fig. 2.5. Exemplary loops and magnetic configurations of antiferromagnetically coupled ferro-/ferrimagnetic bilayers with two-step switching (e,f) and three-step switching (g,h).

If the bilayer shows a two-stage switching process and the magnetically softer layer is below a particular thickness, the bilayer exhibits the so-called *Exchange Spring* behavior [85, 87, 92, 93]. Here, the magnetic moments of the softer layer continuously rotate in the direction of the applied field H, while the moments localized at the interface remain unaffected due to strong interface exchange coupling. The interface domain wall (IDW), which is formed in this case, exhibits a helical twist of the magnetic moments and the rotation angles increase with the distance from the interface. If one removes the external field, the initial state of parallel orientation of the TM moments is reversibly reached. The reversible alignment of the magnetic moments corresponds to the elastic movement of a spring, from which the name for this process originated. Figure 2.6 a shows an exemplary *M-H* hysteresis loop with fully reversible switching of the softer layer. The schematic magnetic configuration at different magnetic fields is shown in Fig. 2.6 d. Generally, the magnetic moments of two ferromagnetically exchange-coupled layers prefer a parallel alignment (Fig. 2.6 d I). If a strong enough external magnetic field is applied antiparallel to the current magnetization direction, the Zeeman energy surpasses the exchange energy, the magnetic coupling is broken, and the softer layer reorientates. The result is an IDW, which costs energy according to Eq.2.1 (Fig. 2.6 d II) [94–97]. If the field is further increased, the magnetically harder layer switches, too. Thus, the whole bilayer is switched (Fig. 2.6 d III) in comparison to its original state (Fig. 2.6 d I). If the thickness of the softer layer is increased [93, 98] or the coupling strength between the layers weakened [99], an irreversible switching process can be observed. Two exemplary loops with a relatively larger and smaller saturation magnetization of the softer layer $M_{\mathrm{s,soft}}$ are shown in Fig. 2.6 b and c, respectively. The switching process illustrated in Fig. 2.6 d also applies here.

If a RE-TM ferrimagnetic layer is involved, the preferred alignment of the overall moments of the individual layers depends on the composition of the FI. The exchange interaction manifests itself in the preferred parallel alignment of the TM moments. Thus, a RE dominant FI couples antiparallel to an adjacent FM. Figure 2.6 e-h show two exemplary *M-H* hysteresis loops of antiferromagnetically coupled bilayers (e,g) and their schematic magnetic configuration (f,h). The two layers prefer an antiparallel alignment at zero field (Fig. 2.6 f,h ii). If a strong enough external magnetic field *H* is applied, the antiparallel layer reorientates with the field, and an IDW is formed in the case of Fig. 2.6 f i and iii. Additional to the two-step switching (Fig. 2.6 e,f), a three-step switching process can occur (Fig. 2.6 g,h). Here, the whole bilayer switches at low fields (Fig. 2.6 h ii,iii) before the coupling of the two layers is broken and an IDW is formed (Fig. 2.6 h i,iv).

In this work, the interfacial exchange coupling between ferrimagnetic TbFeCo layers and ferromagnetic Co/Ni-based multilayers is investigated. The preferred parallel alignment of the TM moments in the FI (FeCo) and FM (Co/Ni) leads to an antiferromagnetically coupled system for the Tb dominant ferrimagnetic layers. In Sec. 4.4.3 and in *Heigl, M. et al. ACS Appl. Nano. Mater. 3, 9218 (2020)* [100] the microscopic origin of reversible and irreversible switching is closer investigated for a ferrimagnetic TbFeCo layer coupled antiferromagnetically to a ferromagnetic Co/Ni-based multilayer.

2.4 Magnetic Domain Theory and Spin Objects

Magnetic domains and other magnetic textures form due to the minimization process of the total free energy of the magnetic system. Thus, the energy terms discussed in Sec. 2.1

$$E_{\mathrm{tot}} = E_{\mathrm{ex}} + E_{\mathrm{zee}} + E_{\mathrm{d}} + E_{\mathrm{ani}} \tag{2.16}$$

have to exhibit either a local or a global energy minimum. While the exchange E_{ex} and the dipolar energy E_{d} play an important role in every magnetic system, the anisotropy E_{ani} and Zeeman energy E_{zee} have not to be present necessarily. In Sec. 2.1.3, it was already discussed how magnetic domains reduce the dipolar energy at the expense of the exchange energy. In this section, the concept is expanded, and further types of magnetic textures and their causes are presented. A more detailed description of different magnetic domain phenomena can be found, among others, in Ref. [101].

2.4.1 Domain Types and Sizes

Magnetic domains are areas of parallel aligned magnetic moments. Domains with different orientations are separated by magnetic domain walls (DWs), which exhibit a gradual reorientation of the individual moments across a finite distance δ_{dw}. There are two different types of magnetic DWs, which are both displayed in Fig. 2.7. *Bloch Walls* are named after Felix Bloch and their magnetic moments rotate about the normal of the DW, which can also be called the axis of rotation (Fig. 2.7 a). They exhibit no divergence in the plane of the magnetization and thus do not contribute to stray fields out of the plane. This property makes them energetically favorable for most magnetic films, especially if the thickness of the material is larger than the DW width δ_{dw} [102]. *Néel Walls* are named after the Nobel Prize winner Louis Néel. Here, the magnetic moments rotate about a line that is orthogonal to the axis of rotation (Fig. 2.7 b). Néel walls are usually only stable in magnetic films with thicknesses thinner than their wall width [102].

The formation of magnetic domains decreases the expanse of stray fields and the dipolar energy E_{d} of a magnetic film (Sec. 2.1.3). At the same time, the resulting DWs cost exchange energy E_{ex}, because of the misalignment of neighboring magnetic moments inside of them (Sec. 2.1.1). Additionally, the magnetic moments of the DW have an angle to the magnetic easy-axis, which also increases the anisotropy energy E_{ani} (Sec. 2.1.4).

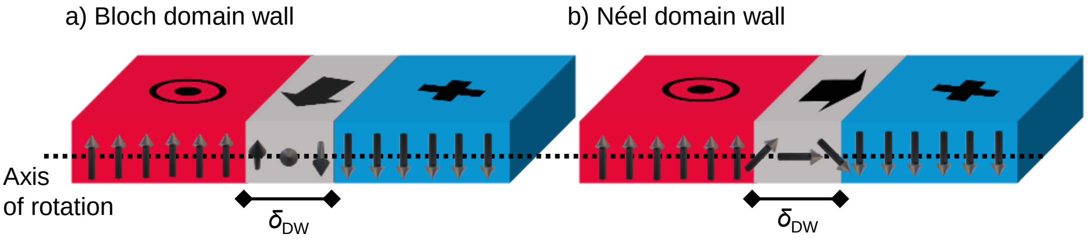

Figure 2.7: Schematic illustration of the magnetic moment configuration across a Bloch and a Néel domain wall. A Bloch wall with the magnetic moments rotating about the axis of rotation (a). A Néel domain wall with the magnetic moments rotating about a line that is orthogonal to the normal of the axis of rotation (b). δ_{dw} is the domain wall width. Please note that the ip components could also be aligned antiparallel to the displayed configuration.

The thickness of the DW δ_{dw} depends on the ratio between the exchange and anisotropy constants. If the dipolar energy of the DW is not taken into account, which can be easily assumed for Bloch walls due to their previous discussed lack of an ip divergence, the DW width δ_{dw} can be estimated by

$$\delta_{\mathrm{dw}} = \pi \left(\frac{A}{K_{\mathrm{u}}} \right)^{1/2} \tag{2.17}$$

with the exchange stiffness constant A and the uniaxial anisotropy K_{u}. Further, the energy cost of a DW per area γ_{dw} can be calculated by

$$\gamma_{\mathrm{dw}} = 4 \cdot (A K_{\mathrm{u}})^{1/2} \,. \tag{2.18}$$

This indicates that large K_{u} and small A values lead to narrow DWs [103]. Typical values for DW widths range from 5 nm for $Nd_2Fe_{14}B$ [104] to 2000 nm for $Ni_{80}Fe_{20}$ [105]. In order to calculate the energetically most favorable size of magnetic domains in a film with certain parameters, the energy cost of DWs e_{dw} per area of the film can be calculated by

$$e_{\mathrm{dw}} = \gamma_{\mathrm{dw}} \cdot \frac{t}{D} \,. \tag{2.19}$$

with t and D being the film thickness and the domain length/size, respectively. The calculation of the dipolar energy per area e_{d} is more complicated and strongly dependent on the film thickness, but it can be found for all thicknesses by the equation [106]

$$e_{\mathrm{d}} = \frac{4\mu_0 M_{\mathrm{s}}^2 D}{\pi^3} \sum_{n=1}^{\infty} \frac{1}{2n} \left(1 - \exp\left(-\frac{2n\pi t}{D}\right)\right) \,. \tag{2.20}$$

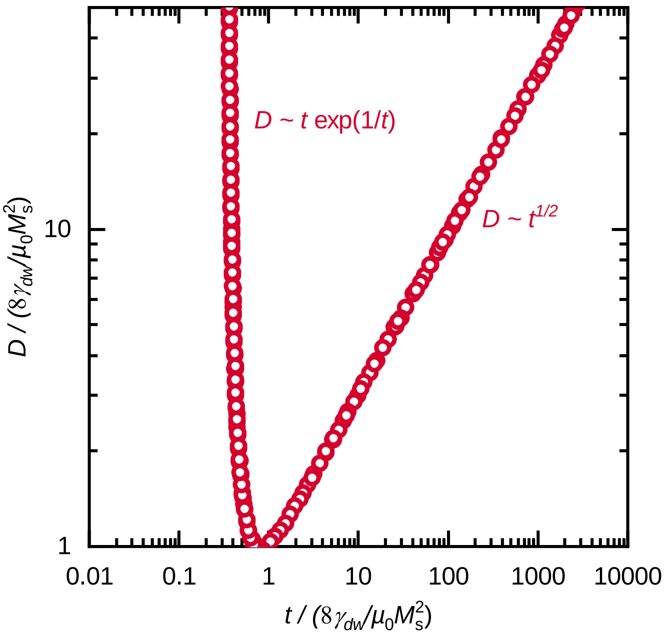

Figure 2.8: Domain size as a function of the film thickness. The numerically calculated curve displays the optimal domain size D dependent on the film thickness t, which is given by the minimization of the total free energy.

The sum of the energies of Eq. 2.19 and 2.20 has to be minimized to obtain the optimal domain size D. The solution for this can only be found numerically [107]. The result is plotted in logarithmic scale in Fig. 2.8. The axis is normalized by $8\,\gamma_{\mathrm{dw}}/\mu_0 M^2$, which is equal to the minimum domain size.

As a result, the law of Kittel [103] $D \sim t^{1/2}$ is confirmed for $t >> D$. Here, the stray fields created by the surface charges do not interact with the other surface. Therefore, the dipolar energy equals two times the energy of a single surface. For $t << D$, the surface charges of both sides interact and D increases with $D \sim t \cdot \exp \frac{1}{t}$.

An analytical solution can be found under the assumption $t << D$. Hence, the Taylor expansion of t/D up to the second order can be used to give

$$e_{\mathrm{d}} = \frac{1}{2}\mu_0 M_{\mathrm{s}}^2 t(1 - 0.67\frac{t}{D} + \frac{2t}{\pi D}\ln\frac{t}{D}) \tag{2.21}$$

as an expression for the dipolar energy [108]. In this case, the sum of Eq. 2.19 and 2.21 is minimized resulting in

$$D(t) = 0.95t \cdot \exp\frac{4\pi\sqrt{AK_{\mathrm{u}}}}{t\mu_0 M_{\mathrm{s}}^2}\,. \tag{2.22}$$

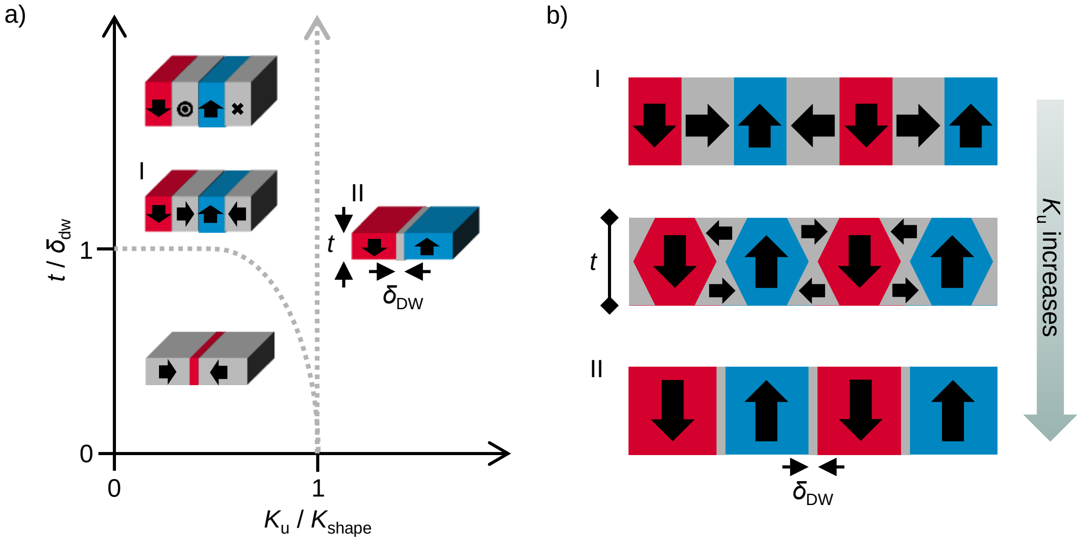

Figure 2.9: Different domain types depending on the magnetic properties. Magnetic stripe, out-of-plane, and in-plane domains depending on the ratio between uniaxial and shape anisotropy on the x-axis and depending on the ratio between the thickness of the film and the DW on the y-axis (a). The transformation of stripe domains to out-of-plane domains with an increasing K_u value (b). Adapted from Ref. [50].

As discussed in Sec. 2.1.4, the easy-axis of the magnetization usually lies in the plane of a thin film, as long as no strong uniaxial anisotropy contribution exists. This changes, if the thickness of the magnetic film is increased and smaller and smaller domains become the preferred state. In order to decrease the dipolar energy of the system even further, equal amounts of ip and oop domains form. These kinds of magnetic domains are called *Stripe Domains*. The predicted thickness values t, which are needed for this to happen, were calculated to be [103]

$$t \geq e_{\mathrm{dw}} \cdot \frac{1}{2}\mu_0 \left(\frac{M_{\mathrm{s}}}{K_{\mathrm{u}}}\right)^2 . \tag{2.23}$$

Theoretical estimates simplify this equation and determine the critical thickness for the onset of stripe domains to [109, 110]

$$t = 1.4 \cdot \sqrt{A}\frac{\mu_0 M_{\mathrm{s}}^2}{K_{\mathrm{u}}^{3/2}} , \tag{2.24}$$

with the exchange stiffness constant A. Figure 2.9 a illustrates the different possible domain types depending on the ratio between uniaxial K_{u} and shape anisotropy K_{shape}

on the x-axis and depending on the ratio between the thickness t of the film and the DW δ_{dw} on the y-axis. Domains with magnetizations in the oop direction are always preferred if $K_{\mathrm{u}} > K_{\mathrm{shape}}$. If $K_{\mathrm{u}} < K_{\mathrm{shape}}$, ip or stripe domains are the energetically most favorable state, depending on the thickness of the film. The transformation of stripe domains to oop domains with an increasing K_{u} value is displayed in Fig. 2.9 b.

Domain Wall Chirality

In addition to the size and the rotation type of magnetic DWs, a key aspect is their so-called *Chirality*. In magnetism, this property describes a preferred sense of rotation of the magnetic moments inside a DW. In this context, two different rotation directions of the same Bloch or Néel type are often described as right-handed and left-handed. In most magnetic materials the domain morphology is governed by the interplay of the previous described energy terms: direct exchange (Sec. 2.1.1), Zeeman (Sec. 2.1.2), dipolar (Sec. 2.1.3), and uniaxial anisotropy energy (Sec. 2.1.4). All of them exhibit no chiral interactions and are usually energetically degenerated for left- or right-handed DW textures. Thus, this property can be manipulated by different techniques, like the control of the magnetic domain textures by electric signals [111, 112], using different magnetic field sequences [113], and laser excitation [114]. One way to lift this degeneracy is the presence of an indirect exchange such as DMI and its asymmetric nature [31]. Therefore, systems with strong DMI are homochiral [115]. Another example is a frustrated magnet with multiple next-nearest neighbor interactions, which prefer different alignments to each other [116].

Under certain circumstances, magnetic domains can shrink down to self-contained circular objects. The previously discussed properties of the original domain then have a significant influence on the resulting spin objects. These objects can be described as magnetic quasi-particles, and their manifoldness is presented in the next section.

2.4.2 Spin Objects - Topology and Characterization

Over the last years, topological non-trivial magnetic quasi-particles have attracted a lot of attention. The trend was further underpinned by the Nobel Prize in Physics in 2016 for the use of topological concepts in theoretical condensed matter physics [117]. These concepts are also applied in the description of the noncollinear spin textures presented in this section.

The most prominent topologically protected magnetic spin objects are magnetic *Skyrmions*, which were experimentally first observed in 2009 [32]. These nanometer-large cylindrical-like magnetic domains are the subject of intensive research due to their enormous stability and small size. The term skyrmion was introduced due to the relation to Skyrme's work in nuclear physics, where he investigated topological non-trivial field solutions to describe elementary particles [118]. In the magnetic community, a clear definition of what constitutes a skyrmion is still missing [119]. It can be agreed that a skyrmion is defined as being a topologically protected spin object in which the center magnetization is aligned antiparallel to the magnetization of its boundary and which can be mapped once to a sphere. An additional requirement mentioned in some publications is the responsible twisting mechanism. Here, Dzyaloshinskii–Moriya-skyrmions stabilized by DMI and skyrmionic bubbles or type-1 bubbles stabilized by dipolar interaction are distinguished, although they can share the same topological properties [120].

In the following, a variety of different spin objects are discussed and characterized by their topological properties. The description is reduced to two dimensions due to the primarily homogeneous nature of the presented spin objects along the film normal. Examples of three-dimensional spin objects follow at the end of the section. The first notable property of topologically non-trivial magnetic objects is that the magnetization density $\boldsymbol{m}(\boldsymbol{r})$ cannot be continuously transformed to a ferromagnetic state. This topological property is quantified by the *Topological Charge*

$$N_{\mathrm{Sk}} = \int \mathrm{d}^2 r \frac{1}{4\pi} \boldsymbol{m}(\boldsymbol{r}) \cdot \left[\frac{\partial \boldsymbol{m}(\boldsymbol{r})}{\partial x} \times \frac{\partial \boldsymbol{m}(\boldsymbol{r})}{\partial y} \right] . \tag{2.25}$$

While it is mathematically impossible to change the topological charge of a structure with continuous transformations, real physical systems exhibit discrete moments and defects. Thus, real topologically non-conservative transformations have only a finite non-zero energy barrier to overcome. For spherical spin objects, an expression in spherical coordinates with the polar angle ϕ and the azimuthal angle θ is natural. The position vector is then given by $\boldsymbol{r} = r(\cos\phi, \sin\phi)$. The radial symmetry of the oop magnetization density $\theta = \theta(r)$ can be exploited and the topologically charge N_{Sk} simplified to [121]

$$\begin{aligned} N_{\mathrm{Sk}} &= \frac{1}{4\pi}\int_0^\infty \mathrm{d}r \int_0^{2\pi} \mathrm{d}\phi \frac{\partial\boldsymbol{\phi}(\phi)}{\partial\phi}\frac{\partial\theta(r)}{\partial r}\sin\theta(r) \\ &= -\frac{1}{2}\cos\theta(r)|_{r=0}^{\infty} \cdot \frac{1}{2\pi}\boldsymbol{\phi}(\phi)|_{\phi=0}^{2\pi} \end{aligned} \tag{2.26}$$

with $\boldsymbol{\phi}$ being the ip magnetization density. The first part of the equation describes the oop orientation of the magnetization. As already stated, one of the requirements of a skyrmion is that the oop magnetization in the center is aligned antiparallel to the surrounding magnetization. Thus, the first part of Eq. 2.26 for skyrmion-like objects depends purely on the oop magnetization orientation of the host. Accordingly, this part can be quantified by the so-called *Polarity*

$$p = -\frac{1}{2}\cos\theta(r)|_{r=0}^{\infty} = \pm 1 \;. \tag{2.27}$$

The second part of the Eq. 2.26 describes the so-called *Vorticity* v and determines how often the polar angle wraps around in multiples of 2π [122]:

$$v = \frac{1}{2\pi}\boldsymbol{\phi}(\phi)|_{\phi=0}^{2\pi} = 0,\ \pm 1,\ \pm 2,\ \dots\,. \tag{2.28}$$

With Eq. 2.27 and 2.28, Eq. 2.26 allows only integer topological charges resulting from the product of the polarity p and the vorticity v:

$$N_{\mathrm{Sk}} = p \cdot v = 0,\ \pm 1,\ \pm 2,\ \dots\,. \tag{2.29}$$

One other quantity, which is used to differentiate skyrmions, is the *Helicity* γ. It describes the offset of the linear relation between the polar angles of the position vector ϕ and the magnetization density

$$\boldsymbol{\phi} = m\phi + \gamma \;. \tag{2.30}$$

The magnetization profile of a skyrmion can be generally described by the three introduced quantities as

$$\boldsymbol{m}_{\text{sk}}(\boldsymbol{r}) = \begin{pmatrix} (\frac{x}{r}\cos\gamma - v\frac{y}{r}\sin\gamma)\sin(\frac{\pi}{r_0}r) \\ (\frac{x}{r}\sin\gamma + v\frac{y}{r}\cos\gamma)\sin(\frac{\pi}{r_0}r) \\ p\cos(\frac{\pi}{r_0}r)) \end{pmatrix} \tag{2.31}$$

with r_0 being the radius of the skyrmion. To compare different spin objects, the polarity p is usually seen as a constant and only changes for a different global oop orientation. The three remaining quantities topological charge, vorticity, and helicity can be written as $(N_{\text{sk}}, v, \gamma)$.

In Fig. 2.10 an exemplary overview of spin objects is given. All displayed spin objects have a positive polarity $p = +1$ and thus $N_{\text{sk}} = v$. The panels in Fig. 2.10 a-d illustrate four different skyrmion types that can be fully described by the Eq. 2.31. They all share the same vorticity and topological charge with $N_{\text{sk}} = v = +1$ and are only differed by their helicity γ. In Fig. 2.10 a, the ip component of the magnetization is always aligned parallel to the radial vector. Thus, the helicity is zero. Fig. 2.10 b exhibits ip components oriented antiparallel to their $\boldsymbol{r}$ and with it a helicity of π. These two spin objects are called Néel skyrmions and only differ in the out (a) or in (b) orientation of their ip components. They are typically observed in systems with interface DMI [123–125]. If the ip components of the magnetization are oriented perpendicular to the radial vector, the spin object is called Bloch skyrmion (Fig. 2.10 c, d). These skyrmions with a helicity of $\pm\pi/2$ were the first magnetic skyrmions ever to be observed [32]. Their ip components can be either aligned in a counterclockwise (ccw) (c) or clockwise (cw) (d) direction. They are usually stabilized by bulk DMI [33–36, 126, 127]. Alternatively, they also present a metastable state in systems without DMI due to the competition between long-range dipolar interaction, direct exchange, and magnetic anisotropy. In this case, magnetic domains shrink continuously or collapse with an applied oop magnetic field until they reach the skyrmionic state. Due to the topological protection, the system stays in this state over a certain field range before it saturates. In order to achieve this state, it was shown that very similar properties for stripe domains (Eq. 2.23) are necessary [128]. Systems hosting dipolar-stabilized Bloch skyrmions are the focus in chapter 5 and typically exhibit coexisting skyrmions with both helicities in equal quantities. Although they share the same topological properties, the magnetic community sometimes refers to these objects as skyrmionic bubbles or type-1 bubbles instead of skyrmions [120]. They

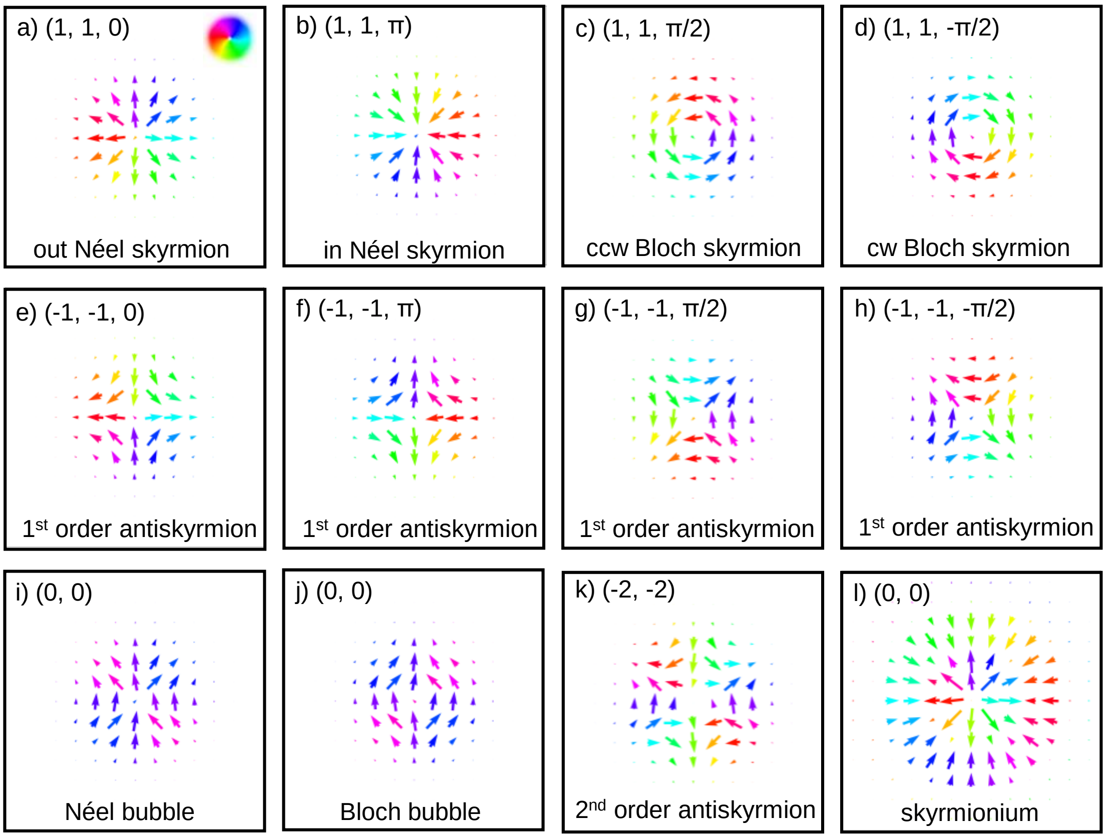

Figure 2.10: Overview of different spin objects. The three topological quantities, topological charge, vorticity, and helicity, are written as (N_{sk}, v, γ). The arrows and their color depict the directions of the ip components, with their sizes displaying the strengths. a-d) display Néel and Bloch skyrmions fully described by their topological quantities. e-h) show antiskyrmions with arbitrary helicities representing their initial skyrmionic state. i) and j) illustrate topologically trivial bubbles. More exotic spin objects are presented in k) and l) with a second-order antiskyrmion and a skyrmionium or target skyrmion, respectively.

can also be distinguished by size. While DMI-stabilized skyrmions are usually between 10 and 100 nm, dipolar-stabilized skyrmions are larger than 100 nm [129].

Another novel magnetic quasi-particle that gained a lot of interest over the last few years is displayed in Fig. 2.10 e-h. Here, *First-Order Antiskyrmions* in different orientations are shown. They cannot be described with Eq. 2.31, due to the non-linear relation between the polar angles of the position vector and the magnetization density. Thus, the helicity is only arbitrary and represents the initial skyrmionic state before the antiskyrmion was created via a reflection with respect to a plane perpendicular to the plane of the skyrmion [130–132]. Antiskyrmions exhibit a negative vorticity and topological charge, have a two-fold symmetry, and consist of alternating Néel- and Bloch-type DWs that confine the inner oop magnetic moments from the surrounding antiparallel moments. While there have been many predictions of antiskyrmions stabilized by magnetic dipolar interaction [133, 134], interface DMI [135, 136], and non-centrosymmetric D_{2d} or S_4 symmetry [133, 137, 138], until now only the latter could experimentally be realized in Heusler compounds with D_{2d} symmetry [46–49] and in schreibersite with S_4 symmetry [139]. Very recently, the coexistence of antiskyrmions and skyrmions was observed as well in D_{2d} Heusler compounds [140, 141]. In these crystalline bulk systems, the spin objects exist only in a geometrically deformed state and in specific planes of the crystal. In dipolar dominated systems, only local artificial antiskyrmions could be created and observed outside of this work [142]. In Sec. 5.3, a recipe is describe to stabilize antiskyrmions purely by dipolar interaction.

Figure 2.10 i and j illustrate topologically trivial spin objects consisting primarily of Néel (i) and Bloch (j) DWs. They do not possess a helicity and have a topological charge and vorticity of zero. They are called magnetic *bubbles* or *type-2 bubbles* to be distinguished from skyrmionic type-1 bubbles. They are well-known spin objects already observed in the 70s [143], which are stabilized by dipolar interaction and occur in materials with effective anisotropies close to zero [128, 144–150]. In order to simplify the distinction in this work, skyrmionic type-1 bubbles are called *Skyrmions* and topological trivial type-2 bubbles *Bubbles*.

Figure 2.10 k shows an example of a higher-order skyrmion with $|v| > 1$. This *Second-Order Antiskyrmion* with an additional iteration of a Néel- and a Bloch-type wall has the vorticity $v = -2$, no definable helicity, and shows a three-fold symmetry. While they have been theoretically predicted [151], they have thus far only been observed experimentally in the framework of the presented studies in Sec. 5.3.

The last exemplary spin object is a so-called *Skyrmionium* or *Target Skyrmion* (Fig. 2.10 l). It can be viewed as a coalition of two Néel skyrmions with opposite topological charges. Thus, the topological charges of the inner and outer ip magnetization densities cancel each other out, resulting in a total topological charge and vorticity of zero. This characteristic makes them a promising candidate for current-driven devices, due to their lack of a *Skyrmion Hall Effect* (SkHE) [152, 153], which is further discussed in Sec. 2.4.3. Very recently, intrinsic skyrmioniums have been reported for the first time in 2D materials [154]. Otherwise, they are primarily stabilized in nanodiscs [155]. They can also be used as a stepping stone to create 3D spin objects like *Hopfions* [156].

Other 2D topological non-trivial spin objects to be named here, that are not included in Fig. 2.10, are: *Intermediate Skyrmions* with a helicity of $\gamma = \pi/4$ [157, 158], *Higher-Order*

Skyrmions [159], *Bimerons* [160, 161] consisting of two *Merons* [162], and *Biskyrmions* consisting of two overlapping skyrmions [163]. Besides hopfions, another 3D spin objects worth mentioning is the *Chiral Bobber* [164, 165]. Here the skyrmion tube, a continuation of the 2D skyrmion in the normal of the film plane, only exists at the surface of a sample and ends inside the film in a so-called *Bloch Point*. Bloch points are singularities in the local magnetization in which the topological charge and magnetization cannot change continuously [166].

An extensive overview of all the mentioned spin objects is given in Ref. [167].

2.4.3 Current-Induced Spin Object Dynamics

The dynamics of the described self-contained magnetic objects are crucial for possible applications, which are further discussed in Sec. 5.1. It has been demonstrated that spin objects can be moved by an applied current and that their topological properties are reflected in their current-induced dynamics. The movement is the result of the *Spin Transfer Torque* (STT) induced by a spin-polarized current passing through the spin-object-hosting layer [168]. An additional transverse movement of skyrmions, when driven by a current, was predicted and called the *Skyrmion Hall Effect* (SkHE) [169]. The extent to which a skyrmion is deflected by the SkHE is measured by the *Skyrmion Hall Angle*. The first experimental demonstration of the current-induced motion of skyrmions was done by Woo et al. in 2016 [124]. The direct experimental observation of the SkHE followed in 2017 [170]. It was shown that the skyrmion Hall angle significantly depends on the helicity of the spin object, and thus, the trajectories of Bloch and Néel skyrmions differentiate [171]. A special case is the movement properties of antiskyrmions. Due to their missing rotation symmetry, their skyrmion Hall angle depends on the orientation of the antiskyrmion to the current flow [172]. It was even shown that a SkHE can be avoided for antiskyrmions under certain orientations.

In the last few years, many different approaches were tested to reduce the spin Hall angle to zero to increase the speed of current-driven skyrmions and improve the energy efficiency of possible skyrmion dynamic devices [173]. The most promising candidates in this area were ferrimagnetic [174] and antiferromagnetic [175] systems due to their antiparallel orientated sublattices, which also counteract each other's induced SkHE. Other options are the use of more exotic spin objects, including the previously mentioned skyrmioniums [152, 153] and antiskyrmions [172]. It is also possible to suppress or cancel the SkHE by an additional induced spin current [176] or by the antiferromagnetic exchange coupling of two skyrmion-hosting ferromagnetic layers, forming a so-called *Synthetic Antiferromagnet* (SAF) [177].

Chapter 3

Experimental Techniques

In the following, the most relevant experimental techniques for this thesis are described briefly. First, the preparation of the samples is presented (Sec. 3.1). Afterward, Sec. 3.2 and 3.3 outline the used structural and magnetic characterization techniques, respectively.

3.1 Sample Preparation

The investigated magnetic films in this work are deposited by magnetron sputtering, which is described in the next section (Sec. 3.1.1). Additionally, some films are modified by the ex-situ technique of ion irradiation to locally change the magnetic properties (Sec. 3.1.2).

3.1.1 Film Deposition Using Magnetron Sputtering

In this work, all samples are fabricated by magnetron sputtering. Sputtering is a method of thin-film deposition by bombarding the to-deposit target with ions from a plasma [178]. The collisions of high kinetic plasma ions and the surface of the target lead to the evaporation of the target material. The liberated target particles propagate away from their source and coat everything in their path. This allows depositions of layer thicknesses in the range of less than a nanometer to hundreds of micrometers. In order to confine most of the charged plasma particles close to the surface of the target and improve efficiency, magnetrons are deployed [179, 180]. They utilize strong overlying magnetic fields that force the electrons on a cycloidal path. Schematic illustrations of a magnetron sputter gun and a magnetron sputter chamber are displayed in Fig. 3.1 a and b, respectively.

Typically, sputter processes are carried out in an ultra-high vacuum (UHV) chamber to ensure a sufficient mean free path for the target particles and the plasma ions and

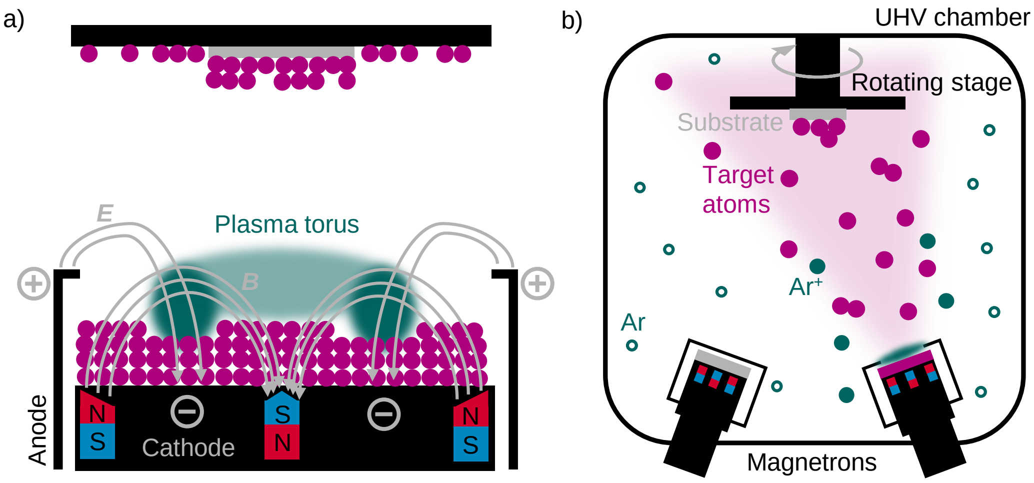

Figure 3.1: Schematic drawings of a magnetron sputtering system. Close-up of an active magnetron (a). Electric and magnetic field lines are shown confining the plasma torus. Ultra-high vacuum (UHV) chamber filled with Ar as working gas (b). One magnetron gun with an ignited plasma and an open shutter is displayed (right), as well as an inactive magnetron with a closed shutter (left).

electrons, as well as to avoid contamination of the sputtered layers. After a sufficiently low base pressure, usually $< 10^{-8}$ mbar, is achieved, a highly pure working gas is injected. Non-reactive noble gases are preferably used, in the case of this work argon (Ar). To establish a plasma, an electric field $\boldsymbol{E}$ from a direct current (DC) source is applied between the target holder (cathode) and the cylinder (anode) around it (Fig. 3.1 a). Generally, some of the working gas atoms are always ionized. Thus, the free electrons accelerate to the cylinder/anode and the ions to the target/cathode. On their way, collisions lead to further ionization. The overlying magnetic field $\boldsymbol{B}$ contains the free electrons and leads to the formation of a plasma torus directly above the target. The ions, which are less affected by the magnetic field and still accelerated by the electric field, collide with the target and transfer energy to the target. The shape of the plasma torus leads to an increased probability of impacts directly beneath it, which creates the typical circular erosion profile at the target surface. The stream of particles is controlled by individual shutters above the magnetron. The excited charge-less target clusters, molecules, and atoms leave the sputter gun and coat the inside of the chamber and the designated substrate. The distribution of the target particle stream shows a club-like shape. Therefore, a homogeneous thin film is achieved by rotating the stage and by centering the designated substrate slightly off the focus of the particle club (Fig. 3.1 b). On the path of the target particles, they can collide with Ar atoms, get deflected, and lose kinetic energy. The probability of this depends on the Ar pressure as well as the distance between the target and the substrate. The kinetic energy of the target atoms has a large impact on the film morphology. The rate of deposition is controlled by the applied power for the plasma, the position of the particle club, and with it, the size of the homogeneous deposition area, the Ar pressure, and the distance and angle between target and substrate. A quartz crystal balance can be used to measure the deposition rates.

In this work, all samples are deposited in a custom-built *Bestec* system (project number 450) stationed at the University of Augsburg. Ar with a typical pressure of a few µbar is used as working gas. The distance between the target and the substrate is 56 mm. The tilt angle of the magnetron is 17.5° for all depositions. The substrate stage rotates with 60 rpm. All used targets must be pre-sputtered to prevent possible contamination of the deposited films. This is especially important for highly reactive RE targets, which oxidize quickly on the surface. Otherwise, the oxygen in the target is incorporated into the layers, and the properties of the deposited film are influenced. The targets used for deposition have a minimum purity of 99.9%. Please note that for ferromagnetic targets, the magnets of the magnetrons need to be modified to guarantee a plasma torus above the target.

The deposition rates are preliminarily measured by a quartz balance at the exact position of the substrates. Therefore, no corrections with tooling factors are necessary. To sputter binary and trinary alloys containing the elements X and Y with the compositions x and y in at.%, the right ratios between the different sputter rates R need to be obtained. The ratio of the rates for the binary alloy X_xY_{100-x} are calculated by

$$\frac{R(X)}{R(Y)} = \frac{m'(X)}{m'(Y)} \cdot \frac{\rho(Y)}{\rho(X)} \,. \tag{3.1}$$

The density ρ of the materials is given. The mass ratio $m'(X)/m'(Y)$ is equivalent to $(x/(100-x)) \cdot (u(X)/u(Y))$ with u being the atomic mass. Therefore, Eq. 3.1 can be expressed as

$$\frac{R(X)}{R(Y)} = \frac{x}{100-x} \cdot \frac{u(X)}{u(Y)} \cdot \frac{\rho(Y)}{\rho(X)} \,. \tag{3.2}$$

For a binary alloy, one of the two rates is fixed, and the other one is calculated for a certain composition x according to Eq. 3.2. For a trinary alloy, also one rate is fixed, and the second and third rates are calculated first collectively and afterward individually by the binary equations Eq. 3.2. The sputtering time is calculated by the division of the desired thickness by the sum of all co-sputter rates. Please note that these calculations ignore potential changes in composition due to resputter effects. These effects have especially to be considered for high-energy depositions and co-sputter processes whose target materials have a large difference in atomic mass [181]. Here, additional post-deposition composition measurements are necessary, which are presented in Sec. 3.2.

An overview of all fabricated samples, which have been used for the presented data, as well as their deposition parameters, is given in Sec. A.4.

3.1.2 Nanosphere Lithography and Ion Irradiation

Ion irradiation is a method to change the properties of a film after its deposition. The high-energy ions induce intermixing and amorphization by traveling through the film [182]. In Sec. 5.6, He^+ ions are accelerated by an *Eaton NV-3204* system with energies of 200 keV in UHV [183]. A heated filament is used as the ion source. The ions are pre-accelerated by an electric field of 20 kV and filtered by traveling through a magnetic field. Depending on their charge and mass, the ions exhibit different trajectories due to the Lorentz force. Afterward, the ions are accelerated to their final velocity by the accelerator tube. The resulting ion beam is focused by triplet-quadrupole electrostatic lenses. The focused beam is then scanned over the sample. The dose with which the film is irradiated can be measured by the beam current divided by the scanned area. A more detailed description of this technique can be found in Ref. [184].

Nanosphere Deposition

In order to achieve a hexagonal pattern of irradiated and non-irradiated areas, self-assembled nanosphere lithography is used in Sec. 5.6.1. The method is illustrated in Fig. 3.2. A magnetic film (red) on top of a substrate (green) is the starting point (Fig. 3.2 a).

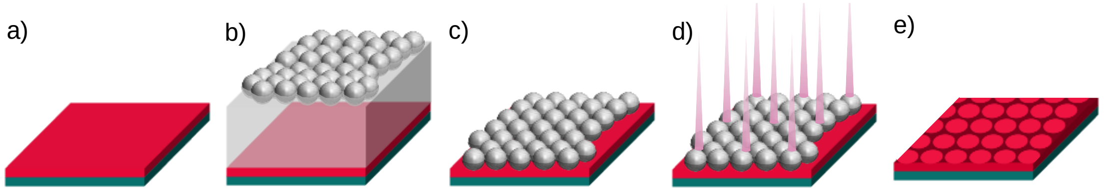

Figure 3.2: Patterned ion radiation via self-assembled nanosphere lithography. Magnetic film on a substrate (a). Mono-disperse aqueous polystyrene nanosphere suspension with average diameters of 782 nm, 425 nm, or 196 nm are deposited on the film (b). After drying, a highly ordered hexagonal close-packed monolayer of the spheres is created by self-assembly (c). The sample is irradiated by He^+ ions (d). A magnetically hexagonal modulated film is the result (e).

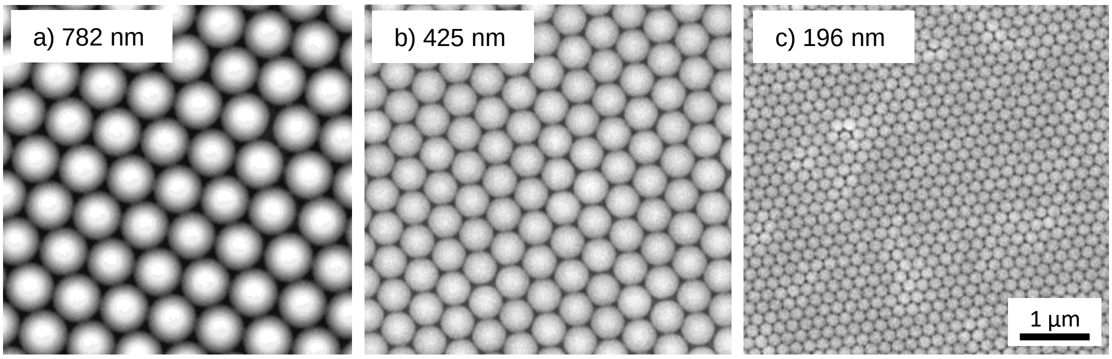

Figure 3.3: Scanning electron microscopy images of nanospheres with different periodicity. SEM images of nanospheres with a diameter of 782 nm (a), 424 nm (b), and 196 nm (c) confirming the hexagonal long-range order.

A mono-disperse aqueous non-functionalized polystyrene nanosphere suspension is deposited on the magnetic film (Fig. 3.2 b). The used nanospheres have diameters of 782, 425, or 196 nm. During the drying process, the nanospheres self-assemble in a highly ordered hexagonal close-packed monolayer (Fig. 3.2 c). The ordered nanospheres with different diameters are imaged by scanning electron microscopy (SEM) and displayed in Fig. 3.3.

In Fig. 3.2 d, the film with a monolayer of nanospheres on top is irradiated by He^+ ions, resulting in a change in the properties of the film in the uncovered areas. The spheres are removed by a supersonic assisted lift-off process.

Focused Ion Beam

Alternatively, a *Focused Ion Beam* (FIB) setup is used in Sec. 5.6.2. Here, Ga^+ ions are accelerated to an energy of 1-50 keV and focused by electrostatic lenses. This way, irradiation with 5 nm spatial resolution can be achieved [185]. Custom patterns of changed material properties can be written, which are not limited to the hexagonal lattice symmetry presented in Fig. 3.3.

At the same time, the system can be used for imaging and targeted sputtering [186].

3.2 Structural Characterization Techniques

In this work, the magnetic properties of the presented systems are in the foreground. However, to describe them precisely, knowledge about the structural properties is required, too. Therefore, different structural characterization techniques are utilized and presented in this section.

3.2.1 Composition Measurements by Rutherford Backscattering

Rutherford Backscattering (RBS) utilizes the electrostatic interaction of the Coulomb potentials of high kinetic ions with the atomic nuclei of a bulk material to determine the chemical composition and thickness of the irradiated layer. If the elastically scattered ions have enough energy to leave the material, their energy loss and large scatter angle yield the necessary information [187]. Figure 3.4 a illustrates the schematic of a RBS setup. A Van-de-Graaf tandem-ion-accelerator provides high-kinetic ions [188].

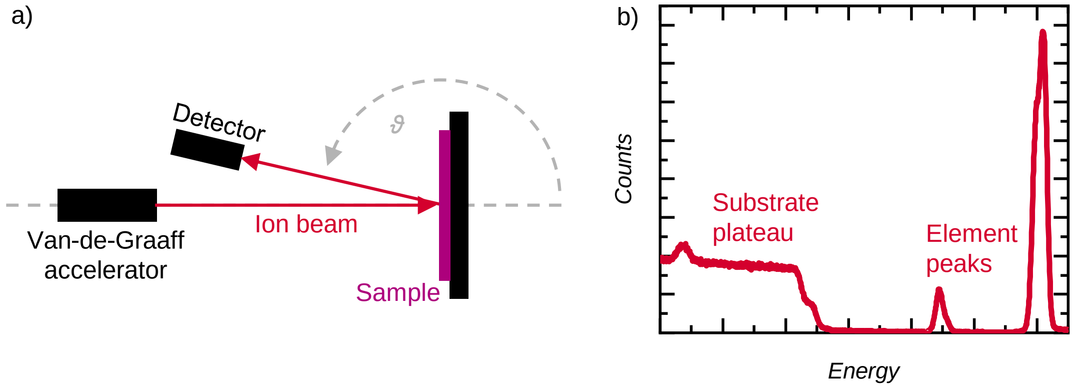

Figure 3.4: Schematic illustration of a Rutherford backscattering setup and an exemplary Rutherford backscattering spectrum. Beam geometry of a Rutherford backscattering setup with a Van-de-Graaf accelerator providing high-kinetic ions (a). The detector analyses the scattered ions at an angle ϑ. Exemplary Rutherford backscattering spectrum of $Tb_{28}(Fe_{85}Co_{15})_{72}$ (20 nm) (b). The analysis of this spectrum and its corresponding simulated spectra, confirming the composition, are shown in Sec. 4.3.1.

The ion backscattering can be approximated by a classical elastic scattering process. Therefore, the kinetic energy of the backscattered ion E_{ion} can be calculated by

$$E_{\text{ion}} = E_{0,\text{ion}} \left(\frac{m'_{\text{ion}} \cdot \cos\vartheta + \sqrt{(m'_{\text{nucleus}})^2 - (m'_{\text{ion}})^2 \sin^2\vartheta}}{m'_{\text{ion}} + m'_{\text{nucleus}}} \right)^2 , \tag{3.3}$$

with the incident ion energy $E_{0,\text{ion}}$, the ion mass m'_{ion}, the mass of the scattering nuclei m'_{nucleus}, and the scattering angle ϑ.

The detector is typically mounted at a fixed angle ϑ. The resulting spectrum is given by the number of arriving ions against their energy. An exemplary RBS spectrum of

$Tb_{28}(Fe_{85}Co_{15})_{72}$ (20 nm) is shown in Fig. 3.4 b. The analysis of this spectrum and its corresponding simulated spectra, confirming the composition, are shown and discussed in Fig. 4.11 and Sec. 4.3.1, respectively. The plateau at low energies is caused by the substrate. The peaks provide information about the thin film on top of the substrate. For layer stacks or alloys, multiple superimposed peaks are observed. By the use of a RBS simulation software like *SIMNRA*, the composition of a sample can be calculated with an accuracy within 1 at.% [189].

Although RBS is considered a non-destructive method of analysis, the input energy of the method can lead to local changes in the system.

In this work, He^+ and He^{2+} ions with an energy of 1.7 and 4.0 MeV and a scattering angle of $\vartheta = 170^\circ$ are used to confirm the composition of the TbFeCo alloys in Sec. 4.3.2 after the deposition. The ions are accelerated by a Van-de-Graaf tandem-ion-accelerator system from *High Voltage Engineering Europa B.V.*.

3.2.2 Determining Crystal Structures by X-Ray Diffraction

In order to determine the existence, kind, and orientation of crystal structures *X-Ray Diffraction* (XRD) is used in this work. X-rays provided by a copper (Cu) $K_{\alpha 1}$ source scatter at atoms. If the atoms are part of a crystal structure, constructive interference can occur. The Laue equation

$$e^{i[(\boldsymbol{k'}-\boldsymbol{k})\cdot\boldsymbol{R}]} = 1 \tag{3.4}$$

with the incident wave vector $\boldsymbol{k}$, the scatter wave vector $\boldsymbol{k'}$, and the reciprocal lattice vector $\boldsymbol{R}$ gives the condition for constructive interference in reciprocal space [190]. In real space, it can be reduced to Bragg's law

$$N\lambda = 2a_{hkl}\sin\theta = \Delta s \ , \tag{3.5}$$

with the integer number N, the wavelength of the incident X-rays λ, the distance of the lattice planes a_{hkl}, the glancing angle θ, and the path difference Δs [191]. Figure 3.5 a and b illustrate the Laue equation and Bragg's law, respectively. Constructive interference occurs if the path difference Δs of the X-rays, which are scattered at different lattice planes, is an integer multiple N of their wavelength λ.

In this work, XRD is measured in the $\Theta - 2\Theta$ configuration by a *XRD 3003 PTS* system from *Seifert* with a parallel X-ray beam. The X-rays are provided by a Cu $K_{\alpha 1}$

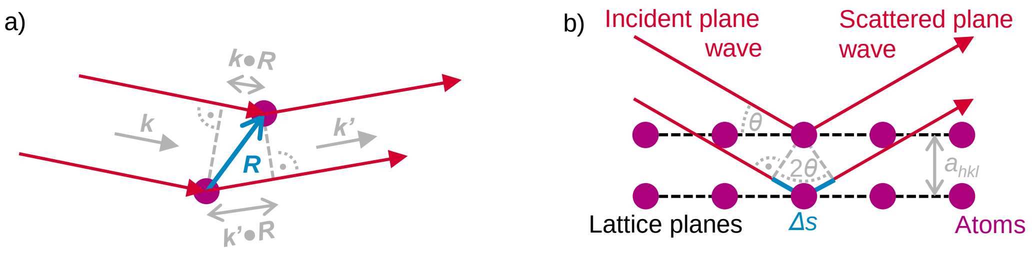

Figure 3.5: Schematic illustration of the Laue condition and Bragg's law. Laue condition in reciprocal space with the incident wave vector $\boldsymbol{k}$, the scatter wave vector $\boldsymbol{k'}$, and the reciprocal lattice vector $\boldsymbol{R}$ (a). Bragg's law in real space with the distance of the lattice planes a_{hkl}, the glancing angle θ, and the path difference Δs (b).

source with a wavelength of 0.15418 nm. The angle of incidence θ of the X-rays is set via the tilt angle of the sample to the detector since the sample can be rotated around its own axis. The detector can also be moved in its position on a circular path with the sample in the center [192]. The resulting diffractogram shows the intensity of the diffracted X-ray radiation as a function of the angle of incidence. If a diffraction reflex (intensity peak) occurs under a certain angle, the distance of the lattice plane can be calculated and matched to a certain crystal structure.

3.2.3 Creation of Height Profiles by Laser Scanning Microscopy

A *Laser Scanning Microscope* (LSM) is a type of confocal microscope. Laser light is focused on the surface of the sample, and the reflected beam is captured. If the surface moves out of the focal point during scanning, less reflected laser light is detected. The necessary movement of the surface to be back in focus is recorded. While the scanning area of this technique is quite large with 50 mm × 50 mm, the height and spatial resolution are limited by the diffraction of light and therefore larger than 100 nm [193].

In this work, the surfaces of membranes are measured with a *Keyence VK-X1000 LSM* at 20× and 50× magnification and evaluated using the corresponding *VK Analyzer* software (Sec. 5.5.3).

3.2.4 Surface Imaging by Scanning Electron Microscopy

Scanning Electron Microscopy (SEM) uses a focused electron beam to scan the sample surface and detect the secondary electrons emitted by the excited atoms. While conventional light microscopy is limited by the wavelength of the incident light, electron microscopes use the wave-particle duality of electrons and the resulting De Broglie wavelength to achieve much higher resolutions [194]. The wavelengths of electrons λ_e can be calculated relativistically by

$$\lambda_\mathrm{e} = \frac{h}{\sqrt{2m'_\mathrm{e}E_\mathrm{kin}(1+\frac{2E_\mathrm{kin}}{m'_\mathrm{e}c^2})}} \,, \tag{3.6}$$

where h is Planck's constant, m'_e the electron rest mass, E_kin the kinetic energy, and c the speed of light. Please note that a relativistic calculation is not necessary for low energy electrons. However, the later introduced electron imaging techniques require it (Sec. 3.2.7). Typical electron energies of a SEM range from 0.2 to 40 keV, which result in wavelengths of 123 to 8 pm according to Eq. 3.6, respectively. However, the resolution is mainly limited by the interaction volumes of the electron beam, which depend on the imaged material, sample geometry, electron spot size, and beam current. Typical resolutions are between 1 and 20 nm [195].

3.2.5 Measuring the Surface Roughness by Atomic Force Microscopy

In order to measure the height profile and roughness of a sample, *Atomic Force Microscopy* (AFM) is also an option. It offers a superior resolution in comparison to LSM at the cost of smaller scan areas. Recording the interacting atomic forces of the sample surface with a probe tip provides information about the surface morphology. For measuring the height profile, the attractive short-range Van der Waals and capillary forces counteract the repulsive force due to the Pauli principle and the Coulomb interaction. The resulting forces depending on the distance between the tip and the surface can be described by the Lennard-Jones potential [196]. Figure 3.6 displays a simplified schematic measuring setup consisting of a cantilever, which has a small tip at the end of the lower side. The tip has a typical curvature radius of 5 to 10 nm, allowing atomic resolution [197]. While the tip scans the surface, the deflection of a laser beam, which is reflected from the top surface of the cantilever, is recorded with a quadrant photodiode detector. During the scan procedure, the sample is moved by piezo actuators. Three different measurement modes exist: contact, tapping, and non-contact.

The investigations of the samples presented in this work are carried out exclusively in the tapping mode. This mode prevents the tip from sticking to the surface, which is quite common in ambient conditions [198]. During the measurement, the cantilever oscillates at approximately its resonant frequency. The excitation of the natural frequency of the cantilever is performed by piezo elements. A change in frequency provides information about the interacting material surface while the amplitude is kept constant. To keep the

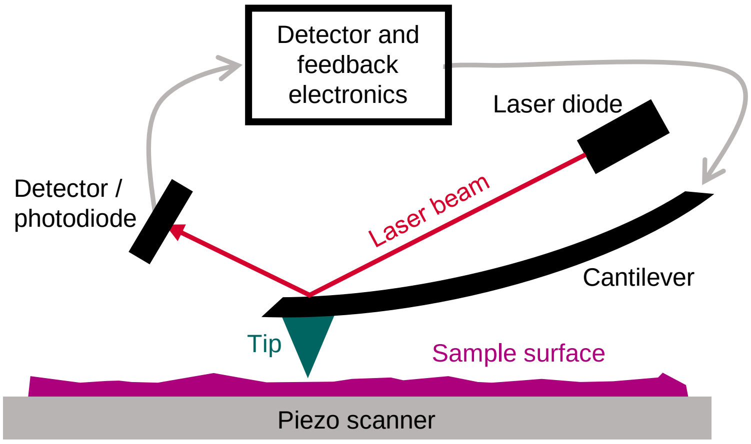

Figure 3.6: Schematic illustration of an atomic force microscope. The sample surface is scanned with a small tip. The deflection of the laser beam reflected from the top surface of the cantilever is recorded with a photodiode detector and analyzed to gain a height profile of the sample.

amplitude of the tip constant, feedback electronics continuously correct the height during the scanning. The resolution of this technique is mainly limited by the tip. Subatomic resolutions down to 0.2 nm have been demonstrated [199]. While AFM measurements are performed at heights of a few nanometers, where the Van der Waals and capillary forces are dominant, information about the magnetic stray fields of a sample surface can be gathered at higher heights and with magnetic tips. This is further elaborated in Sec. 3.3.2.

3.2.6 Resistivity Measurements via the Van der Pauw Method

The *Van Der Pauw Method* describes the technique to measure the average resistance of a sample with an arbitrary shape via the placement of four electrodes around the perimeter of the sample [200]. It requires a homogeneous and approximately two-dimensional sample without holes and the area of contact has to be at least an order of magnitude smaller than the area of the sample.

Scattering events of the conduction electrons and various types of defects control the electrical resistivity in metals. The *Drude-Sommerfeld Theory* estimates the resulting resistivity ς by

$$\varsigma = \frac{m_\mathrm{e}^*}{ne^2\tau} \tag{3.7}$$

with the effective electron mass m_e^*, the electron charge e, the density of electrons n, and the average free time between scattering events τ [201]. Scattering events occur especially at grain boundaries, dislocations, impurity atoms, vacancies, and inhomogenities in general.

In Sec. 4.3, the sheet resistance $\sigma = \varsigma/\text{thickness}$ is measured as a function of the annealing temperature in nitrogen atmosphere. Here, increasing temperatures do not only change the resistance due to more phonon electron scattering events but also due to irreversible changes in the structure of the material. Therefore, resistivity measurements can be used to reveal structural changes, which occur at certain temperatures in a given material. Generally, an amorphous material like TbFeCo increases its resistivity at certain elevated temperatures due to its loss of chemical short-range-order. At further increased temperatures, crystallization processes can lead to an additional increase in inhomogeneity. However, a fully crystallized film typically exhibits a smaller σ than amorphous ones [202–206]. Another possible effect due to annealing is the dewetting of the film. Caused by structural changes, the interplay between the substrate and the film changes and surface tensions can give rise to island formation. Hence, the continuity of the film is broken, and a rise in resistivity is measured [207].

3.2.7 Film Structure Investigations by Cross-Section Transmission Electron Microscopy

To gather further information about the structural properties of a sample, nanometer-thin films can be directly imaged by *Transmission Electron Microscopy* (TEM). Here, electrons are transmitted through a thin sample and scattered or absorbed by it. The typical electron energies range from 100 to 300 keV, which result in wavelengths of 3.3 to 1.5 pm according to Eq. 3.6. The smallest visible distance d between two objects, which can be distinguished, is given by the so-called Abbe diffraction limit [208]:

$$d = \frac{\lambda}{n' \sin\alpha} = \frac{\lambda}{NA} \; . \tag{3.8}$$

Here, n' is the refractive index of the medium between the objects and the objective and α the opening angle of the objective. In optics, NA is the numerical aperture, which quantifies the light gathering ability of a microscope. For a wavelength of 1.5 pm, a maximum resolution of 50 pm is possible according to Eq. 3.8 and a reasonable NA value of 0.03 [209]. In order to transmit sufficiently enough electrons through the sample, the thickness of the sample has to be less than 200 nm.

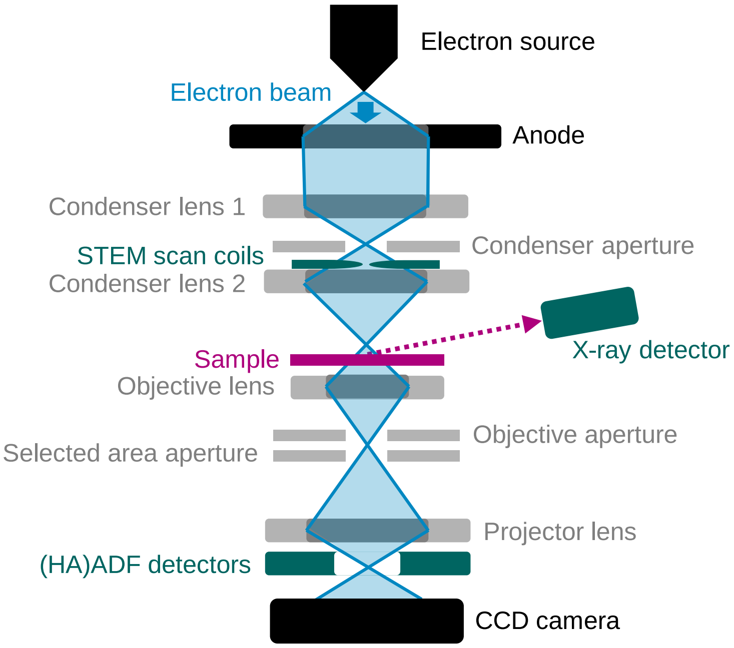

Figure 3.7: Schematic illustration of a transmission electron microscope. The blue electron beam travels through the grey optical components and the purple sample. The resulting signal is recorded by a CCD camera. Green parts are optional and used for certain operating modes. The whole setup is under a high vacuum.

The working principle of a TEM is schematically illustrated in Fig. 3.7. The electron source (gun) is made up of a cold field emitter. The emitted electrons are then accelerated through the high voltage anode and focused by an arrangement of electromagnetic condenser lenses and the condenser aperture on the sample. The scatter contrast of the electrons is then transmitted through the objective lens and magnified by it and the projection lens. The diffraction pattern or real space image is finally projected on a fluorescent screen attached to a charge-coupled device (CCD) camera.

Depending on the desired information, TEMs can be operated in different ways. The optional parts necessary for certain modes are displayed in green in Fig. 3.7. In the following, the TEM techniques used for the structural characterization are listed. Descriptions of the available modes to image magnetic morphologies are given in Sec. 3.3.3. An overview of all established TEM methods is, for example, given in Ref. [210].

High Resolution Transmission Electron Microscopy

In the most commonly used (high resolution) transmission electron microscopy mode, diffraction patterns of the scattered electrons are used. A magnification of ×500k and more is possible. Depending on the incident angle of the electron beam, the microscope can be operated in the Bright-Field (BF) and Dark-Field (DF) submodes. In the BF, areas where electrons transmit unscattered appear brighter. Accordingly, these areas appear darker in DF.

Scanning Transmission Electron Microscopy

In the *Scanning Transmission Electron Microscopy* (STEM) mode, the electron beam is focused on a fine spot (0.05-0.20 nm [211]). The beam is then rastered over the sample by the STEM scan coils. BF and DF can be utilized here by changing the position of the objective aperture. The BF mode places the objective aperture in the center of the back focal plane and therefore filters out scattered electrons.

In the *Annular Dark-Field* (ADF) mode, only electrons scattered under a certain angle are captured and appear bright in the resulting image. To emphasize the impact of the atomic number of the scattering atoms, only electrons scattered at very large angles can be captured [212]. This specific version of the ADF method is called *High Angle Annular Dark-Field* (HAADF) mode. Both the ADF as well as the HAADF mode require special (HA)ADF detectors.

One of the main advantages of STEM is the possibility to simultaneously measure in BF and DF, while capturing the chemical composition with *Energy-Dispersive X-Ray Spectroscopy* (EDS/EDX), which is described next. The gained images and information can then be directly correlated. The drawbacks of STEM are the longer scan times and the high intensity of a focused electron beam, which can locally damage the sample.

Energy-Dispersive X-Ray Spectroscopy

In order to chemically characterize a sample, the EDS capabilities of a TEM can be used. The focused electron beam in STEM mode locally stimulates the emission of characteristic X-rays, which can be analyzed by an energy-dispersive x-ray spectrometer. The characteristics of the gained spectrum can then be accurately associated to certain elements and its unique discrete energy level transitions by Moseley’s law [213].

In this work, both a *FEI Titan* and a *JEOL NEOARM-200F* system are used, which are located at the *Central European Institute of Technology* (CEITEC) in Brno, Czech Republic, and at the University of Augsburg, respectively. Cross-sectional TEM samples are prepared by mechanical dimpling followed by ion polishing. HAADF-STEM imaging and EDS are performed at an accelerating voltage of 200 kV to obtain the element composition, confirm the structural properties, and to analyze interface intermixing. Additionally, high-resolution TEM images are taken to judge the crystallinity of individual layers. The used techniques for imaging the magnetic structures are described in Sec. 3.3.3.

3.3 Investigations of the Magnetic Properties

The experimental methods required for the characterization of the magnetic properties are presented in this section. First, a method to investigate the integral magnetic parameters is described, followed by two techniques to image different components of the magnetic spin structure.

3.3.1 Integral Magnetic Measurements Using a Superconducting Quantum Interference Device

For the precise measurement of the magnetic moment of a sample, the *Vibrating Sample Magnetometer* (VSM) with an included *Superconducting Quantum Interference Device* (SQUID) is used. If the volume of the sample is known, the underlying magnetization can be calculated from the measurement.

The typical design of a DC-SQUID-VSM is illustrated in Fig. 3.8 and described in the following, while a more detailed discussion of the mechanisms and setup can be found in Ref. [214] and [215], respectively.

First, the sample is mounted on a sample holder. Depending on the geometry of the magnetic film on the holder, the oop or ip magnetic components are measured. During the measurement, the sample holder vibrates sinusoidally inside four symmetric detection coils perpendicular to the areas of the coils. The inner two coils have an opposite winding direction to the outer two coils. This second-order gradiometer setup suppresses the first-order magnetic field gradients, for example, from the applied magnetic field, and is only susceptible to the second-order ones ($\mathrm{d}^2B_z/\mathrm{d}z^2$) [216]. Depending on the amplitude of the vibration, the sample induces more or less current in the detection coils. The current δI and with it the external magnetic flux Φ_ext is

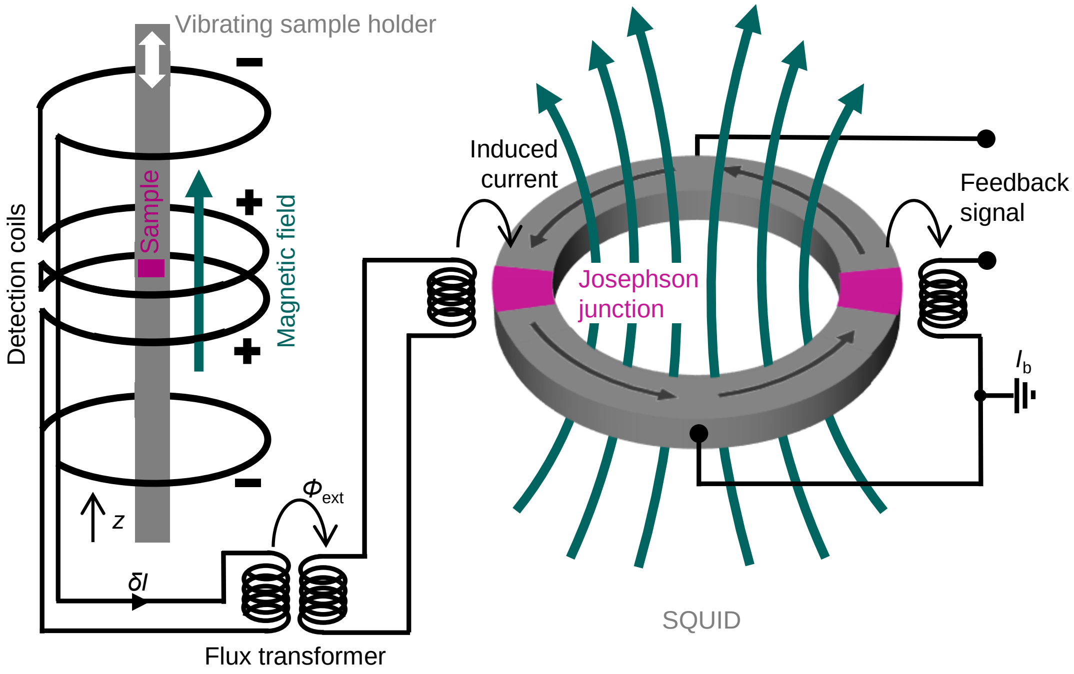

Figure 3.8: Schematic illustration of a DC superconducting quantum interference device - vibrating sample magnetometer. The sample holder and sample vibrate inside the detection coils, while an optional magnetic field is applied. The induced current δI and with it the external magnetic flux Φ_{ext} is forwarded by the flux transformer to the superconducting quantum interference device (SQUID). The SQUID ring has two Josephson junctions and an applied bias current I_{b}. The resulting feedback signal provides information about the moment of the measured sample. The illustration is based on Ref. [215].

forwarded by the flux transformer via induction coupling to the SQUID sensor. This superconducting ring has two non-superconducting *Josephson Junctions* [217]. The whole ring is superconducting as long as the flowing current is below the critical current I_{c}. In this state, the conduction particles consisting of two electrons (*Cooper Pair* [218]) are able to tunnel through the junctions without a voltage drop. The magnetic flux of the SQUID ring is quantized by $\Phi_0 = h/2e$, with h and e being the Planck constant and the electron charge, respectively [219]. Additionally to the induced current δI, a bias current I_{b} is applied, which is slightly larger than twice I_{c}, due to the two used Josephson junctions. Therefore, the ring is in a non-superconducting transition state. Hence, a small amount of the induced current δI in the opposite direction translates to a phase transition and a large change in the voltage δU. Using the feedback signal, I_{b} can be changed accordingly to δI and thus, a constant transition state between superconducting and non-superconducting is established. This technique enables the determination of the external magnetic flux Φ_{ext} and, therefore, the magnetic moment of the sample as an integer multiple of Φ_0.

In this work, the *Magnetic Property Measurement System 3* (MPMS3) from *Quantum Design* is used [215]. Measurements can be conducted at sample temperatures between 1.8 and 1000 K while magnetic fields up to ±7 T are applied. To measure samples in varying geometries and at these elevated temperatures, different sample holders are available. While the sample is glued on a flat glass holder for ip measurements, the sample is pinched in a plastic straw for oop measurements. To reach sample temperatures above 400 K, a self-heating sample holder and thermally conductive cement is required.

It should be noted that this technique has limits and several potential obstacles to overcome to guarantee precise results. A small summary of the most important ones for this work is given in the following. A more detailed overview of them can be found in Ref. [220].

1) The system fully automatically fits the measured induction under the assumption that the sample is a perfectly positioned ideal magnetic dipole between the detection coils. Thus, larger sample sizes and incorrect positioning on the sample holder lead to errors. These errors can be minimized by certain correction factors for different sample geometries and sizes [216, 221, 222]. For example, the correction factor of a typical $5 \times 5 \times 0.5\,\text{mm}^3$ sample in ip measurement geometry is 0.9833 [221].

2) The area and thickness of the magnetic film must be precisely known to calculate the magnetization. While the area can be measured by an optical microscope, the precise determination of the thickness is more complex and RBS or TEM (Sec. 3.2) is usually necessary. The results of these techniques introduce errors on their own.

3) The magnetometer measures every deviation from the homogeneous sample holder. Hence, in addition to the magnetic film, the signal of the substrate, inhomogeneities of the sample holder, glue, and contaminations are measured. In order to remove most of these para- or diamagnetic contributions, the linear background of a *M-H* measurement is removed. However, this can be challenging if the magnetic saturation is not reached within the available ±7 T.

4) The magnet of the device exhibits a residual offset field due to pinned fluxes in the superconducting magnet. After the magnet creates a strong positive field, it exhibits negative magnetic fields up to -3 mT, while being nominal at zero. To achieve an effective magnet field closer to zero, the so-called *Magnet Reset* or an oscillating reduction of the field can be used. Within a magnet reset process, the magnet is heated up above its critical temperature and cooled back down to remove the pinned fluxes. However, afterward a shift of 0.2 mT is still observable. Another option to correct the offset field is the use of a calibration measurement. A calibration sample consisting of an ideal para- or diamagnet is measured by the to-calibrate *M-H* sequence. The resulting *M-H* curve should be linear with zero magnetization at zero field. Deviations from this behavior can be attributed to the offset of the magnetic field and used to correct the following measurements.

5) Another artifact is the so-called magnetic soft-phase. Here, the *M-H* curves exhibit an additional FM contribution with a small coercivity. In the framework of this work, this artifact was investigated in close collaboration with H. Hug's group at the *Swiss Federal Laboratories for Materials Science and Technology* (EMPA). The results are published in *Mandru, A.-O., Yilidrim, O., Marioni, M.A., Rohrmann, H., Heigl, M., et al. J. Vac. Sci. 38, 023409 (2020)* [223]. In most cases, the coated sides of the measured samples could be identified as the source of the soft phase. Thus, the appearance of the artifact can be prevented by cutting the edge of the sample or using masks during the deposition. However, magnetic contamination from the cutting and handling tools can also introduce these kinds of artifacts. To clearly differentiate between soft-phase artifacts and actually soft magnetic contributions from the magnetic film, other techniques to measure the magnetization can be used. *Magneto-Optic Kerr Effect* (MOKE) [224] and *X-Ray Magnetic Circular Dichroism* (XMCD) measurements [225] are two examples.

3.3.2 Mapping of the Stray Fields by Magnetic Force Microscopy

Magnetic Force Microscopy (MFM) uses the AFM setup illustrated in Sec. 3.2.5 with only a small addition: a magnetic tip, which has its magnetic easy-axis perpendicular to the sample surface. Therefore, the tip is now also sensitive to the oop components of the magnetic stray fields. To image only the magnetic information without a strong superposition of the topography, the sample is typically first scanned in tapping mode at a low height. Afterward, the actual MFM scan is carried out several tenths of nanometers

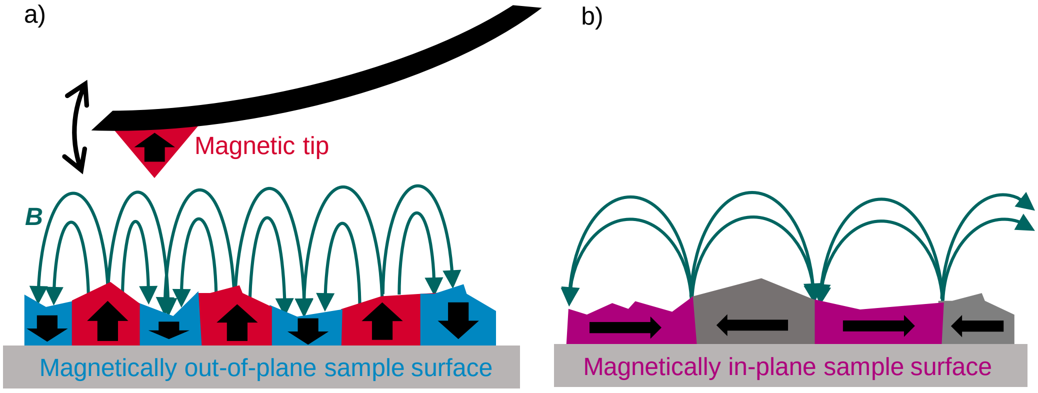

Figure 3.9: Schematic illustration of the magnetic stray fields measured by a magnetic force microscope. Stray fields ***B*** of a magnetically out-of-plane (a) and in-plane (b) sample surface are measured by a magnetic tip. A contrast between the differently aligned domains can be observed for a), while a contrast between the domain walls and the domains can be observed for b) under the assumption that the domain walls are of the Néel type.

above the beforehand measured surface. This way, the magnetic contrast is enhanced relative to the other forces, which exhibit a stronger dependence on the distance.

The magnetic contrast is given by the gradient of the oop components of the stray fields at a certain height above the sample surface. Hence, magnetic oop domains with different orientations exhibit a contrast between each other with this technique (Fig. 3.9 a). For a magnetic ip sample surface, only ip divergences, like Néel domain walls, are depictable (Fig. 3.9 b). It is important that the tip is chosen accordingly to the specimen. Samples with weak stray fields require tips with large moments to achieve a reasonable signal. On the other hand, samples with strong stray fields should be measured with tips resilient to strong fields and, therefore, with large coercivities. Otherwise, the magnetization of the tip switches in the measured stray fields. Furthermore, for magnetically soft samples, tips with large magnetizations should not be used. Otherwise, the domain morphology is significantly affected by the tip [226].

Additionally to the MFM measurements at ambient conditions by a *Bruker Dimension FastScan* microscope, low-temperature ultrahigh vacuum MFM measurements at fields up to 7 T are carried out with another MFM system in Sec. 4.4.3. Details on this system in particular and the necessary data processing can be found in Ref. [227, 228]. Here, quantifiable results are extracted from the MFM measurements due to the detailed knowledge about the properties of the used tip. Another high-resolution MFM system operating in vacuum is used in Sec. 5.4 to differentiate the different spin objects by their stray fields.

While the mainly used Bruker system does not have the built-in option to apply magnetic fields, it is possible to use different permanent magnets and spacers to achieve certain oop magnetic fields during the measurement. Please note that with this method, it is not possible to change the applied magnetic field in a continuous way. Also, the magnetic field can only be increased until the magnetization of the tip and/or the resonance of the cantilever are significantly affected.

3.3.3 Imaging of the Magnetic Domain Morphology by Lorentz Transmission Electron Microscopy

The TEM described in Sec. 3.2.7 is not limited to the structural characterization of samples. Information about magnetic fields in the specimen can also be imaged based on the deflection of the electron beam. Here, the cause of deflection is the Lorentz force $\boldsymbol{F}_\mathrm{l}$. It acts on the transmitting electron charge $-e$, which moves with the velocity $\boldsymbol{v}$ inside an electric $\boldsymbol{E}$ and magnetic field $\boldsymbol{B}$:

$$\boldsymbol{F}_\mathrm{l} = -e[\boldsymbol{E} + (\boldsymbol{v} \times \boldsymbol{B})] \; . \tag{3.9}$$

In the following, it is assumed that the electric field $\boldsymbol{E}$ is zero inside the specimen. If an electron moves through a specimen with a constant ip component of the magnetic induction B_ip and the thickness t, the angle of deflection β_l for a certain electron wavelength λ_e is given by [229]

$$\beta_\mathrm{l} = \frac{e\lambda_\mathrm{e}B_\mathrm{ip}t}{h} \tag{3.10}$$

with h being the Planck's constant. This means, sufficient ip magnetization and thicknesses are necessary to achieve measurable deflection in this mode. Typical thicknesses and magnetizations lead to Lorentz deflection angles multiple orders of magnitude smaller than Bragg diffraction, which is imaged by classic TEM. Therefore, multiple different techniques were developed to image magnetic contrasts, which are listed and explained later in this section. TEM modes using this mechanism are summarized under the term *Lorentz Transmission Electron Microscopy* (LTEM). An overview of modern TEM techniques to image magnetic nanostructures, on which this section is partially based, is given in Ref. [230].

The Eq. 3.9 and 3.10 consider only classical mechanics. To describe the contrast and image building of TEM in more detail, quantum mechanics, and with it, the wave properties of the electron beam, have to be considered. Here, the relation between the phase shift of the electrons and the magnetization is described by the Aharanov-Bohm effect [231]. A detailed description of this can also be found in Ref. [230].

One challenge of LTEM magnetic imaging is the strong magnetic fields created by the different used electron lenses. To achieve a perfectly field-free space for the specimen, ideally, with the option to apply a controlled magnetic field, modifications to the previous TEM designs have been made and an additional objective lens had to be introduced [229, 232].

In the following, different imaging modes of LTEM are described.

Fresnel Mode

The Fresnel LTEM mode is the most commonly used. Here, a parallel electron beam is used in a defocused lens setup. The deflection of the electrons by the ip components of the magnetization leads to areas with more or fewer electrons hitting the detector and, therefore, a contrast. Due to the small deflection angles caused by magnetic fields (Eq. 3.10), magnetic contrast is only visible in a strong over- or underfocus of multiple micrometers in this mode. A change between dark and bright can be achieved by

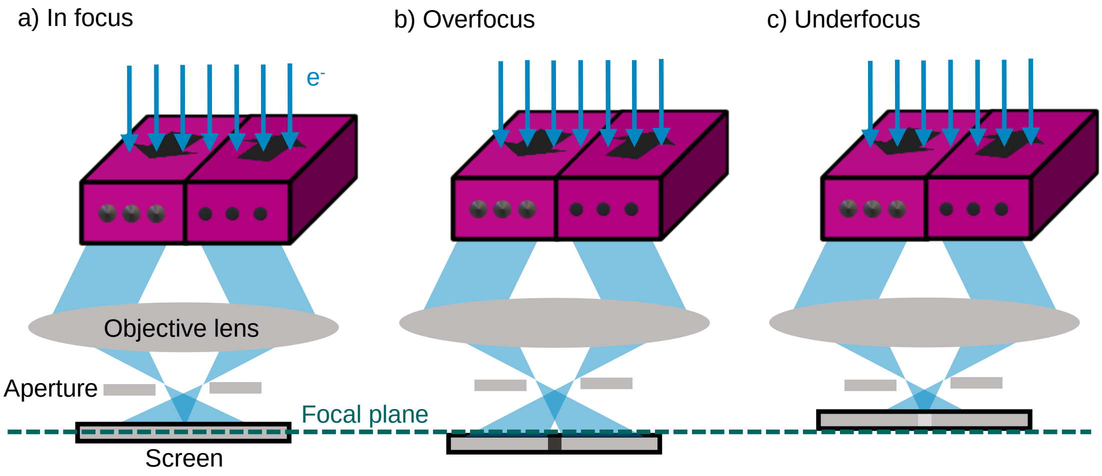

Figure 3.10: Schematic illustration of the electron beam path in focus, overfocus, and underfocus. A parallel electron beam deflects at a magnetic sample with ip domains resulting in no contrast, a black line, and a white line in focus (a), overfocus (b), and underfocus (c), respectively.

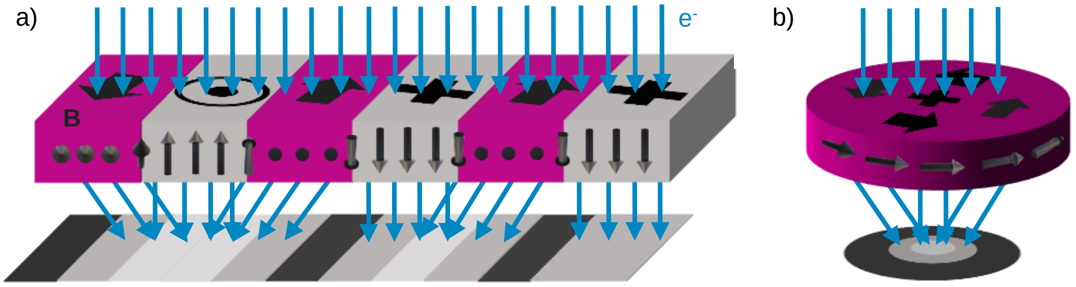

Figure 3.11: Schematic illustration of the electron beam deflecting in magnetic materials and the resulting LTEM contrast. A parallel electron beam deflects at a sample with different magnetic stripe domains resulting in bright and dark stripes with different periodicities (a). A counterclockwise Bloch skyrmion focuses the electron beam resulting in a bright spot (b).

a change from over- to underfocus. The principle is illustrated by two ip magnetic domains in Fig. 3.10.

An improvement of the magnetic contrast by increasing the defocus Δf is always accompanied by a deterioration of the local resolution. The proportionality of the resolution limit d to a certain defocus Δf and the electron wavelength λ_e is given according to [233, 234] by

$$d \propto \Delta f \lambda_e \,. \tag{3.11}$$

The resolution limit for a typical defocus value of 2 mm and a 1.5 pm wavelength is around 30 nm [234].

Figure 3.11 displays a magnetic film with stripe domains with different chiralities (a) and a Bloch skyrmion (b), as well as the resulting contrast measured in the Fresnel LTEM mode. It is evident that the thickness of the resulting dark and bright stripes contains information about the underlying chirality of the stripes. The larger brighter stripe on the left side of Fig. 3.11 a is caused by the two antiparallel ip domains surrounding the oop domain. The thinner stripes on the right side are the result of ip domains pointing in the same direction (stripes without a chirality). It is important to note that the shown domain walls/ip stripes are of the Bloch-type. Continuous Néel-type domain walls exhibit no contrast in Fresnel LTEM due to their deflection resulting in an even electron contribution. Also, no contrast occurs from pure oop magnetization due to their parallelism to the incident electron beam. To still image Néel-type and oop magnetic objects, it is possible to tilt the sample holder of the TEM and consequently artificially create a magnetization component perpendicular to the electron beam [158, 235].

Figure 3.11 b illustrates the deflection resulting from a counterclockwise (ccw) Bloch skyrmion. Here, the electron beam is focused, which is analogous to a focus lens. Hence, a bright round spot with a dark surrounding emerges. Analogously, a clockwise (cw) Bloch skyrmion creates a dark spot with a bright surrounding.

Creation of Magnetic Induction Maps by the Transport of Intensity Equation

If a Fresnel LTEM image series at different focus lengths is recorded, it is possible to calculate magnetic induction maps by the *Transport of Intensity Equation* (TIE) from them. This equation was originally developed for light microscopes and describes the intensity change depending on the defocus [236]. Under the assumption that all phase changes occur due to magnetic fields and with a linear approximation of over- and underfocused images, a solution for the underlying magnetic induction can be found. To improve the results, multiple images at different over- and underfocus levels are helpful, as well as an image in focus to filter contrast caused by structural properties. A precise description of the underlying equations and necessary solving algorithms can be found, for example, in Ref. [237]. Recently, it was also demonstrated that a single Fresnel LTEM image is enough to map the magnetic phase of uniform thin film samples using a simplified TIE approach [238].

Foucault Mode

An alternative LTEM imaging mode is the Foucault mode. Here, the objective lens is kept in focus, and a single crystalline specimen is necessary. The resulting diffraction pattern is partly covered by displacing the object aperture in the focal plane. Electrons that are deflected by the magnetization are either deflected through the aperture or not, resulting in a dark or bright contrast between ip domains with antiparallel orientations. This means that multiple calibration measurements are needed to find the precise aperture placement for every sample and ip component orientation. One advantage of this mode is that no tilting of the sample is needed to observe Néel-type domain walls. While this technique is extremely challenging, due to the necessary precise placement of the aperture, resolutions of 5-6 nm have been demonstrated, which are superior to the Fresnel mode [239]. However, due to the amorphous and polycrystalline nature of the studied samples in this work, this technique can not be utilized.

Differential Phase Contrast

The *Differential Phase Contrast* (DPC) mode leads to the best possible resolutions of LTEM imaging. Here, the TEM is operated similarly to the STEM mode using a focused electron beam. The beam is scanned over the sample by the STEM scan coils. The deflection of the beam caused by the Lorentz force then provides information about the ip magnetic components. The technique was introduced in 1978 [240] and constantly improved over the years. It can not only be used to image magnetic domains but also to image nanoscopic electric fields [241]. Typically, the deflection of the focused ion beam is captured by a quadrant detector. Here, the difference in electron signal of each segment and, with it, the shift from the central position describes the information about the magnetic and electric induction. Alternatively, a fast-readout CCD camera or pixelated detector can be used. DPC allows the depiction of all ip components independent of their Bloch- or Néel-type. The best possible resolution reported for DPC LTEM is 0.9 nm [242]. This excellent resolution can only be achieved at the cost of long measuring times and large amounts of created data, especially in comparison to Fresnel and Foucault imaging.

In this work, the magnetic domain morphology is mostly imaged by Lorentz TEM using a *FEI Titan* and a *JEOL NEOARM-200F* system with a defocus of around -2 mm in Fresnel mode. The measurement temperature is controlled from RT down to 100 K by the *Gatan Double Tilt Liquid Nitrogen Cooling Holder* and by the *JEOL Single Tilt Liquid Nitrogen Cooling Holder* for the low-temperature measurements at the FEI and JEOL system, respectively. Additionally, the first magnetic induction maps are created by LTEM images with multiple defoci and exemplary DPC images are shown in Sec. 5.4. The DPC information is captured by a fast-readout CCD camera at the JEOL system.

To investigate the influence of ip magnetic fields in Sec. 5.5, the *Gatan High Tilt Holder* is used at the JEOL system. The maximum tilt angle β of this holder is 45°. The ip field component is created by tilting the sample holder while a magnetic field is applied. The oop H_{oop} and ip field components H_{ip} can be calculated from the applied field H_{appl} by

$$H_{\text{oop}} = \cos(\beta) H_{\text{appl}} \tag{3.12}$$

and

$$H_{\text{ip}} = \sin(\beta) H_{\text{appl}} \, . \tag{3.13}$$

To measure increasing ip fields at constant oop fields, the measurement script has the option to increase the applied field accordingly after every step of 2.5° or less in the tilt angle. It is important to note that the tilt measurements are done at the eucentric height to prevent changes in the imaged area, focus, and magnification by tilting.

In order to match the different contrast patterns to their underlying spin structures, the theoretical contrast is simulated by a *Python* script. The script was originally programmed by J. Hintermayr [243] and continuously modified for this work. Parallel incoming electrons are modeled as vectors to impinge on the spin structure on a discrete 2D grid at an angle of 90°. Analytical functions of the ip component of the 2D spin objects are used to model the internal magnetic field as vectors. In the magnetic field of the structure, electrons are deflected by the Lorentz force into a direction perpendicular to their own velocity and the local magnetization direction of the spin structure. In the code, the cross-product of the magnetic field vectors and the incoming electron vectors are multiplied by a scaling factor to adjust for weaker or stronger deflection. After iterating over all electrons/vectors in the image and calculating their impact points on the virtual detector, the collected data is converted to a continuous probability density using the *kdeplot* function from the *seaborn* Python library, implementing a kernel density estimation. The result is a continuous grayscale image, where bright areas indicate areas toward which many electrons/vectors are deflected, whereas dark regions indicate regions with a below-average electron/vector incident count. The program additionally plots a representation of the spin structure as a discrete grid of arrows, whose length and direction indicate the local orientation and magnitude of the spin structure. The arrows' colors are mapped to their direction on a *Hue Saturation Value* (HSV) spectrum using the arctan2 function from the Python library *numpy*.

3.3.4 Additional Techniques

In the context of this thesis, additional techniques have been used, which do not have their own subsection in this chapter and whose results are not explicitly shown. These include measurements utilizing the *Magneto-Optic Kerr Effect* (MOKE) [224], *X-Ray Magnetic Circular Dichroism* (XMCD) [225], different Hall effects [244] including the *Spin Hall Effect* (SHE) [245], *Anomalous Hall Effect* (AHE) [246], *Topological Hall Effect* (THE) [247], *First-Order-Reversal-Curve* (FORC) [248], *Ferromagnetic Resonance* (FMR) [249], and *Brillouin Light Scattering* (BLS) [250, 251].

Magneto-Optic Kerr Effect

The MOKE, on the one hand, is measured by a 635 nm laser diode in an oop geometry while an ±1.2 T field can be applied (polar MOKE), and on the other hand, by a Kerr microscope with polarized white light, which images magnetic domains while fields up to 0.6 T are applied. Although the resulting *M-H* hysteresis loops of the polar MOKE only display the moment of the 3d TM components, no additional information is gained for the presented systems in comparison to the SQUID-VSM described in Sec. 3.3.1. Therefore, this technique is mostly used as a confirmation tool and not closer elaborated on in this work. Kerr microscopy is optically limited by a resolution of around 200 nm. While, in theory, it is possible to image the presented spin objects of chapter 5 [252], it is technically extremely challenging and not possible to differentiate between the different types of spin objects. Therefore, it was only used to perform some preliminary tests of the switching processes of the larger domains of the systems presented in chapter 4.

X-Ray Magnetic Circular Dichroism

XMCD measurements were carried out at the synchrotron radiation source BESSY II. The element-specific loops confirmed the switching processes described in Sec. 4.4. Due to the previously published work on XMCD studies on similar systems [253], these results are not shown and only served as a confirmation for the presented switching mechanisms.

Hall Effects

Hall resistivity measurements are carried out to extract the superposition of the ordinary, anomalous, and topological Hall effect (THE). Attempts were made to extract the THE resistivity by subtracting the linear ordinary Hall contribution and the anomalous Hall contribution with SQUID-VSM *M-H* curves from the Hall measurement curves. An existing THE resistivity allows an identification of topologically protected spin objects in the given field range [254]. Most likely, due to the low density of skyrmions in the measured sample, it was not possible to measure the THE.

First-Order-Reversal-Curve

The first-order-reversal-curve (FORC) is used to identify irreversible changes in the magnetization upon field reversal. These insights can be used to predict and characterize stabilization windows of different magnetic textures like skyrmions [43]. FORC measurements consist of a series of *M-H* hysteresis loops and thus can be created by SQUID-VSM, polar MOKE, or Hall measurements. Due to the large number of necessary hysteresis loops, fast techniques are preferred for FORC measurements. At the point of writing, the FORC results are not conclusive and, therefore, will not be further elaborated on in here.

Ferromagnetic Resonance

In this work, FMR measurements are used to extract the uniaxial magnetic anisotropy constant K_u [249]. This is particularly important if the dipolar energies in a system can not be ignored, and, therefore, the calculation of K_u via the enclosed area of the hysteresis loops is no option. Thus, FMR has to be used in Sec. 5.3. The FMR measurements were carried out by A. Semisalova from the University of Duisburg-Essen with a Bruker spectrometer and a X-band resonator at a microwave frequency $f = 9.45\,\mathrm{GHz}$. FMR spectra are recorded at different temperatures for different orientations of the static magnetic field with respect to the sample plane (polar angular dependence). The g-factor is extracted from frequency-dependent FMR measurements at RT with a co-planar wave-guide and microwave generator. The angular-dependent resonance field is analyzed within the Smit-Beljers approach, which yields the value of the effective magnetization [255]. The K_u value is extracted using the known value of the saturation magnetization.

Brillouin Light Scattering

In Sec. 5.3, the interface Dzyaloshinskii-Moriya interaction (DMI) is extracted from non-reciprocal spin-wave dispersion using BLS measurements. The BLS measurements were performed by C. Ping from the *École Polytechnique Fédérale de Lausanne* (EPFL) in Switzerland. The wave-vector-resolved BLS in backscattering geometry is conducted at RT using a monochromatic continuous-wave solid-state laser with a wavelength of 473 nm [256]. Backscattered light is collected and processed with a six-pass Fabry–Perot interferometer TFP-2 (JRS Scientific Instruments). In this configuration, magnetostatic surface spin waves (MSSWs) are excited in the sample [251]. By varying the incident angle, the wave vectors are tuned. MSSWs propagating along opposite directions lead to resonance peaks of Stokes and anti-Stokes signals in the BLS spectra. The two peaks are asymmetric in both peak intensity and frequency. The intensity difference is attributed to the non-reciprocity of MSSWs. The frequency difference originates from the asymmetry of the dispersion relations resulting from the interface DMI. The frequency difference is used to determine the interface DMI constant D according to Ref. [250].

Chapter 4

Exchange-Coupled Ferri-/Ferromagnetic Bilayers

In this chapter, amorphous ferrimagnetic TbFeCo films and ferromagnetic Co/Ni-based multilayers (MLs) are investigated individually and exchange-coupled. The work is motivated by the potential use as a storage medium for heat-assisted magnetic recording (HAMR) devices and was part of the DACH project 277153257: *Solving the Recording Quadrilemma by Curie Temperature Modulated Structures*. The project has been carried out in close collaboration with D. Suess' group from the University of Vienna in Austria and H. J. Hug's group from the Swiss Federal Laboratories for Materials Science and Technology (EMPA) in Dübendorf, Switzerland.

After a short explanation of different potential applications and the underlying magnetic mechanisms used in HAMR, the challenges and requirements for a competitive ferrimagnet(FI)/ferromagnet(FM) bilayer storage system are outlined. Co/Ni MLs are identified as one of the prime candidates for ferromagnetic thin films with a strong perpendicular magnetic anisotropy (PMA) and a large remanent magnetization. In contrast to Co/Pd and Co/Pt, the potential of Co/Ni MLs has been limited by its sensibility to seed layers and post-deposition treatments to achieve large PMA for high repetition numbers. In Sec. 4.2, these systems are combined by adding Pt or Pd insertion layers to Co/Ni MLs to partially solve this problem. The influence of the insertion layers on the magnetic properties, e.g., magnetic anisotropy, saturation magnetization, coercivity, magnetic domain size, and Curie temperature, is systematically investigated. These highly tunable trilayer-based systems are discussed and compared with Co/Ni reference samples without insertion layers. The experimental data of this section was partially acquired as part of the Master and Bachelor theses of R. Wendler and S. Haugg, respectively, and the results are summarized in *Heigl, M., Wendler, R., Haugg, S. &*

Albrecht, M. J. Appl. Phys. 127, 233902 (2020) [257]. Section 4.3 lays out a study on individual amorphous ferrimagnetic TbFeCo films. The focus is in particular on Tb dominant compositions with Fe:Co ratios between 15:85 and 40:60 and a compensation temperature. Due to the presented low thermal stability of TbFeCo alloys, Tb/FeCo MLs are studied and compared as a potential solution in the Sec. 4.3.3. This comparison has been partially carried out by C. Mangkornkarn as part of his Master thesis. The enhanced annealing stability of the ML structure is also described and published in a more compact form in *Heigl, M., Mangkornkarn C., Ullrich, A., Krupinski, M. & Albrecht, M. ACS Advances 11, 085112 (2021)* [206]. The TEM cross-section and the XRR measurements in this section were carried out together with A. Ullrich and M. Krupiński, respectively.

Further, selected films of Sec. 4.2 and 4.3 are antiferromagnetically exchange-coupled in a bilayer system in Sec. 4.4. The magnetic reversal process of these heterostructure systems is investigated, in particular, minor loop measurements, probing solely on the reversal characteristics of the softer ferromagnetic layer. Different thicknesses of the FM reveal two distinct reversal mechanisms. Macroscopic measurements suggest that a rather unusual in-plane (ip) domain wall is involved. In Sec. 4.4.3, the microscopic origin of the magnetization reversal is presented, showing that the reversal is triggered by ip domain walls propagating through the ferromagnetic layer. In contrast, thin ferromagnetic layers show a hysteresis-free reversal, which is nucleation-dominated due to grain-to-grain variations. The high-resolution magnetic force microscopy (MFM) measurements in this section were carried out by A.-O. Mandru and X. Zhao. Furthermore, the experimental results are supported by the theoretical work of C. Vogler. This work is also published in *Heigl, M., Vogler, C. et al. ACS Appl. Nano Mater. 3, 9218 (2020)* [100]. On the basis of this work, the publication *Vogler, C., Heigl, M. et al. Phys. Rev. B 102, 014429 (2020)* [258] shows a purely analytical derivation for the condition of full reversibility switching of the FM layer. Last, the results of all three sections are analyzed concerning their potential for possible applications and are compared to other competitive systems in Sec. 4.5.

4.1 Perspective for Future Data Storage Applications

While the key motivation of this chapter is the evaluation of FI/FM bilayers for HAMR, the presented films and results also have potential implications for a wide range of other applications.

Due to the strong PMA of the individual layers and the coupled heterostructures, they are all potential candidates for different kinds of magnetic memory devices. Additionally to the established perpendicular magnetic recording (PMR) in modern magnetic hard disk drives (HDD) and its successors HAMR and *Microwave-Assisted Magnetic Recording* (MAMR) described in Sec. 4.1.1, new concepts of magnetic memory devices emerged over the last decade, namely magneto-resistive random access memories (MRAM), racetrack memories, and the prospect of writing data by *All-Optical Switching* (AOS). In contrast to the field-driven writing in classic HDD, AOS uses individual or multiple laser pulses to write data [259]. Two distinct types of AOS mechanisms exist: a single pulse helicity-independent switching, discovered in 2007 in GdFeCo films [260] and a two regime helicity-dependent switching observable in a range of different FM and FI films. The latter type was also demonstrated in the FM systems Co/Ni, Co/Pt, and Co/Pd MLs [261], which are comparable to the discussed films in Sec. 4.2. Analogously to the films in Sec. 4.3, helicity-dependent AOS have been demonstrated for TbFe [262], TbCo [263, 264], and TbFeCo [60, 265].

While HAMR tackles the increasing demand for long-term data storage, MRAM is a non-volatile memory (NVM) designed for high-speed data writing and reading. It presents a potential replacement for *Static Random-Access Memory* (SRAM) and *Dynamic Random-Access Memory* (DRAM) with competitive memory capacities, endurance cycles, writing speeds, and the additional benefit of non-volatility [266–268]. An MRAM memory cell consists of a *Magnetic Tunnel Junction* (MTJ) with a free layer (FL), a tunnel barrier, and a fixed layer. The direction of the magnetization of the FL relative to the direction of the fixed layer represents the stored information. Initially, magnetic fields were used to switch the FL, which is not easily scalable. This first generation of MRAM writing is called *Toggle Mode Switching*. Modern MRAMs use the spin-transfer torque (STT) of a spin-polarized current to switch the FL. The stored information is read out via the *Tunnel Magneto-Resistance Effect* (TMR). When the magnetization directions of the two layers are antiparallel, a higher resistance is measured than in the parallel state. Current research investigates MRAMs utilizing the spin-orbit torque (SOT), which shows significantly improved performance [269]. The first commercial toggle MRAM products were launched in 2006, and STT-MRAM products followed in 2017 [270]. The discussed FI/FM bilayers are particularly of interest for MRAM devices due to their decreased coupling frustration in comparison to classical AF-based exchange-coupled systems [90, 271].

The ferrimagnetic TbFeCo layers and the ferromagnetic Co/Ni MLs provide a large tunability of the magnetic anisotropy, which makes them potential hosts of dipolar-stabilized skyrmions in low PMA regimes [272, 273] analogous to the Fe/Gd MLs, which are discussed in chapter 5. The broken symmetry at the Pt or Pd interfaces in the presented Co/Ni-based MLs also enables DMI stabilized skyrmions [274]. The use of skyrmions in the racetrack memory concept is further described in Sec. 5.1.1.

Other than applications in memory devices, the described films have displayed potential as spintronic terahertz emitters [275, 276] and sensor devices in a skyrmion hosting state, which is elaborated in Sec. 5.1.2. The possible applications of each individual layer or heterostructure are also given in the corresponding sections. In the following subsections, the limiting factors of further progress in the HDDs storage capabilities are outlined. Further, HAMR as a solution and the key motivation is presented. Finally, the concept of FI/FM bilayers as Curie temperature modulated structures for HAMR is elaborated at the end of this motivation section.

4.1.1 The Recording Trilemma

Storing data in the form of magnetic orientation in magnetic HDDs is the most predominant way since the 1960s [277]. A series of technologies allowed HDDs to remain in this position, pushing the boundaries of capacity with little effect on cost. The most notably are *Perpendicular Magnetic Recording* (PMR), moving the storage plane from an in-plane (ip) to an out-of-plane (oop) orientation [278, 279], and *Shingled Magnetic Recording* (SMR), overlapping the magnetic tracks [280, 281]. Consequently, the data-bit density increased year by year up to $1\,\mathrm{TB/in^2}$ ($1600\,\mathrm{TB/m^2}$) in 2016 [14, 282]. However, this increase has been slowing down since then. Ultimately, this continuous increase following Moore's Law [9, 10] is limited by fundamental physics. The key restricting factors are formulated in the *Magnetic Recording Trilemma* [283, 284]:

1) A magnetic data-bit is made up of multiple interacting magnetic grains and their number N_{grains} is proportional to the achievable *Signal-to-Noise Ratio* (SNR) during read-out by $\sqrt{N_{\mathrm{grains}}}$ [285]. Consequently, the grain size has to be reduced to increase the data-bit density without sacrificing SNR.

2) The two stable antiparallel magnetic orientations in the grains represent two energy minima. They are separated by the energy barrier

$$\Delta E_0 = K_{\mathrm{eff}} V \tag{4.1}$$

with V and K_{eff} being the volume and the effective magnetic anisotropy of the grains, respectively. At a given temperature T, the finite probability of the magnetization to flip is proportional to $\exp(\Delta E_0/k_\mathrm{B}T)$ with k_B being the Boltzmann constant. The *Néel-Arrhenius Equation*

$$\tau_\mathrm{N} = \tau_0 \exp(\frac{K_\mathrm{eff}V}{k_\mathrm{B}T}) \tag{4.2}$$

provides the Néel relaxation time τ_N that represents the mean time between two flips [286]. τ_0 is the *Attempt Period*, that is characteristic for the material and has a typical value of the order of 10^{-9} seconds [287]. The typical stability criterion for recording systems is

$$\frac{K_\mathrm{eff}V}{k_\mathrm{B}T} > 60\,, \tag{4.3}$$

which corresponds to a recording media stability of around 10 years [285]. In order to reduce the grain volume without sacrificing the long term stability of the data, K_eff needs to be increased according to Eq. 4.2.

3) Based on the Stoner-Wohlfarth model (Sec. 2.1.4), K_eff can be calculated by

$$K_\mathrm{eff} = \frac{\mu_0}{2} M_\mathrm{s} \cdot H_\mathrm{a}\,, \tag{2.8 revisited}$$

with μ_0, M_s, and H_a being the vacuum permeability, the saturation magnetization, and the anisotropy field, respectively. Due to the natural limit of M_s at around 1600 kA/m [288], H_a has to be increased to further soar large K_eff values. The coercive field H_c, and with it the minimum necessary fields to switch the magnetic bit, scales with H_a. Typical write poles of HDDs exhibit maximum effective magnetic field outputs of 1.5 T [289] and limit the further increase in H_c and therefore in K_eff of the storage medium.

In order to solve this trilemma, multiple concepts have been proposed [290]. The most prominent ones are *Bit Patterned Media* (BPM), which uses a different medium structure with large individual grains [291, 292], *Exchange-Coupled Composite* (ECC) media, which couples magnetically soft and hard materials to satisfy both writability and thermal stability [293–296], and changing the material properties during the writing process. The latest example features MAMR, that utilizes localized AC fields at adequate frequencies to reduce the medium coercivity [297, 298] and HAMR, which is discussed in more detail in the following.

4.1.2 Heat-Assisted Magnetic Recording

HAMR utilizes laser radiation to heat the recording area momentarily near the Curie temperature T_c and thus reduces the coercivity locally below the magnetic field provided by the recording head. Therefore, materials with larger K_{eff} values become switchable, which consequently enables smaller grain sizes and larger data densities. To achieve this, the limitation of the minimum diameter of a laser beam spot had to be bypassed. It is given by the diffraction limit, corresponding to half their wavelength. Hence, with modern bit sizes being smaller than 20 nm, a *Near-Field Transducer* (NFT) must be used. The NFT excites collective oscillations of electrons that are called surface plasmons. They are coupled to the light and propagate between the interface of the magnetic film and the dielectric [299].

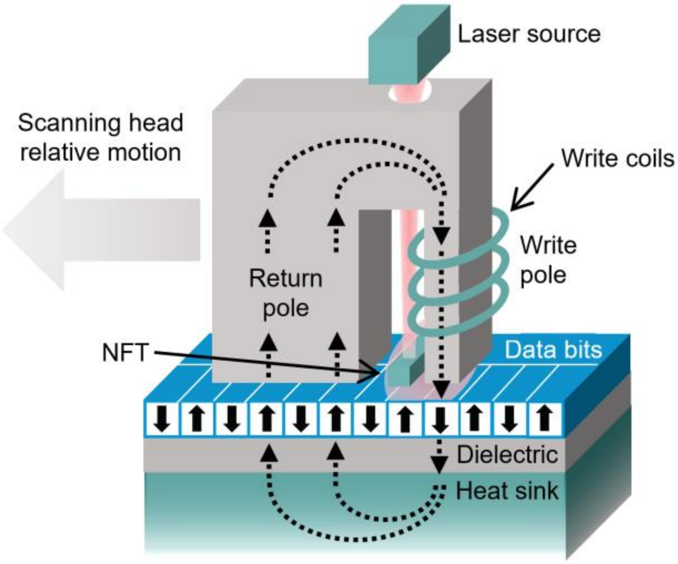

Figure 4.1: Schematic of the heat-assisted magnetic recording process. Writing of magnetic data bits by a HAMR head, due to the local heating of the storage medium by a laser source and a plasmonic near-field transducer (NFT) and the simultaneously applied magnetic field.

In Fig. 4.1 an illustration of the HAMR process is shown. The displayed recording head consists of a write and a return pole, as well as a laser source and an NFT as a heating device. Coils generate the magnetic field, which is focused by the narrow write pole. The broad return pole closes the magnetic field lines while reducing the magnetic field for the areas that should not be switched. Modern magnetic recording heads hover 5 to 10 nm above the surface of the disk, which typically rotates with 7200 rpm [300]. To guarantee reasonable fast writing times and no heat accumulations, excellent heat sinks are necessary for rapid cooling. Unfortunately, additionally to the advantages HAMR offers, it also extends the recording trilemma to a *Magnetic Recording Quadrilemma* [301]:

4) Negligible at room temperature (RT), thermo-dynamical processes during the HAMR induce recording errors [302]. These write errors limit the data bit density due to a larger number of necessary grains for the same SNR.

However, the first generation HAMR HDD products were shipped to selected customers by Seagate [303] in the year 2021. In 2022, the first high-volume products are planned to release with demonstrated bit densities of 2.5 TB/in^2 [303–305]. The estimated density limit of HAMR HDDs is 4 to 5 TB/in^2 according to academic and industrial research [306–309]. This limit can be further extended to 50-100 TB/in^2 by the combination with BPM and ECC [310, 311]. Today, the predominately used storage medium for HAMR research and future devices is chemically L1$_0$ ordered FePt [312–315]. This granular thin film offers high magnetocrystalline anisotropy arising from the alternating monolayers of Fe and Pt atoms [316].

In this chapter, FI/FM bilayers are investigated in regard to their ECC HAMR feasibility. Namely, an amorphous ferrimagnetic TbFeCo thin film, acting as a storage layer, coupled to a soft Co/Ni-based ML, acting as a write and read-out layer, is investigated. The main advantages of this system and a detailed description of operation principles are given in the following section.

4.1.3 Ferri-/Ferromagnetic Bilayer as Exchange-Coupled Composite Medium for Heat-Assisted Magnetic Recording

In this chapter, amorphous ferrimagnetic TbFeCo thin films are investigated as a potential storage layer in a FI/FM ECC media for HAMR. They are known to exhibit strong PMA [202, 317] and are prepared by sputter deposition at RT. This is a key advantage over the competing medium L1$_0$-FePt, which requires high-temperature epitaxial growth or annealing and thus a more complex fabrication procedure. TbFeCo also exhibits a smaller T_c between 400 and 600 K dependent on the Co content [202] compared to FePt with about 750 K [318]. This would significantly increase the lifetime of the NFT and decrease the thermally written errors in a potential HAMR device. Additionally, it has been shown that large Gilbert damping reduces the writing errors [310]. In this regard TbFeCo with a damping of 0.5 [68, 319] notably beats the low damping of FePt, which is between 0.02 and 0.1 [320, 321]. Co/Ni-based MLs are

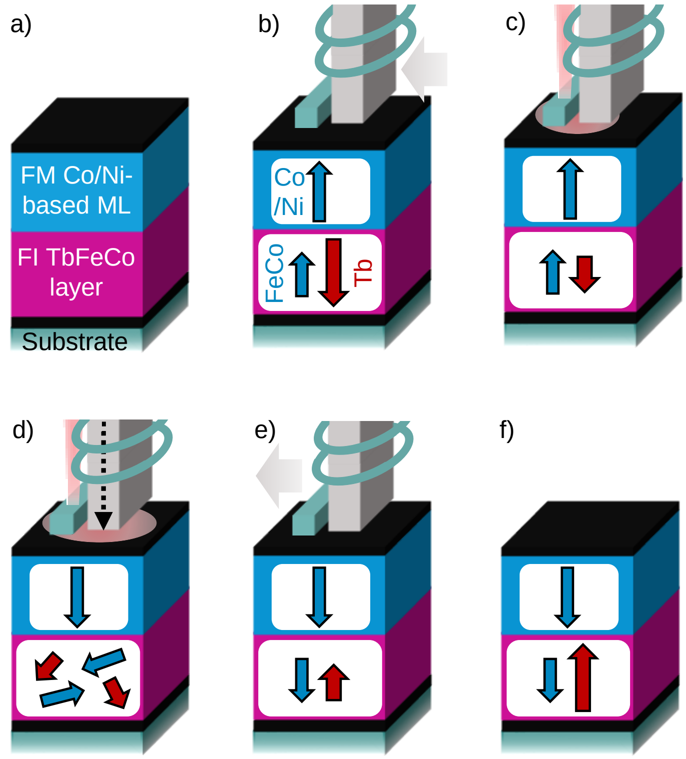

Figure 4.2: Illustration of the switching process concept of a ferri-/ferromagnetic (FI/FM) bilayer for heat-assisted magnetic recording (HAMR). The structure of the bilayer (a). The magnetic state of the bilayer and the arriving HAMR write-head (b). The total moments of the FI and FM are coupled antiparallel. The head is starting to heat up the sample, and the effective Tb moment is decreasing (c). FM and FI are now parallel-coupled. The FI is heated up to its Curie temperature (d). The head is applying a magnetic field to switch the FM. The head is switched off and moves on (e). The FI cools down and aligns with the FM. The bilayer is back to its ambient temperature and now switched relative to b) (f).

analyzed as potential writing and read-out layer. They provide PMA and have been shown to exhibit large M_s and high T_c [56, 322–329]. Their large M_s is necessary to compensate for the relatively low M_s of the FI layer and improve the readability of the stored data.

The system takes advantage of the ferrimagnetic nature of the TbFeCo film as well as the exchange-coupled effect of its heterostructure. To demonstrate this, Fig. 4.2 illustrates the different steps of the switching process concept. Figure 4.2 a displays the overall structure of the magnetic medium. The black layers represent the necessary seed and cover layer to improve the properties of the film and prevent oxidation. The ferrimagnetic layer is around 20 nm thick with the option of further thickening to increase the thermal stability according to Eq. 4.2. The ferromagnetic ML is aimed to have a thickness of 5-10 nm. Together with an expected M_s of 500 to 1000 kA/m, it should have a large enough stray field for the read-out process by state-of-the-art giant magneto-resistive (GMR) or TMR sensors [330, 331]. The arriving write pole and NFT are displayed in Fig. 4.2 b. The system is still at its default temperature, which is roughly RT. The magnetic moments of the ferromagnetic layer and of the antiparallel Tb and FeCo sublattices are marked as arrows. At low temperatures, the effective moment of the Tb sublattice is larger than the Co and Fe moments (see Sec. 2.2). Because of this, the TbFeCo film is overall magnetically Tb dominant. The FeCo in the FI couples parallel to the FM ML. Consequently, the effective moment of the Tb dominant TbFeCo film couples antiparallel to the ML at RT. The advantage of this coupling regime is the decreased total magnetization of the bilayer, which reduces the magnetic stray field interaction of neighboring domains. Thus, the dipolar energy and demagnetization effects are reduced, and the thermal stability in the system is increased. In Fig. 4.2 c, the NFT is driven by the laser and heats up the magnetic film. As shown in Sec. 2.2, the effective Tb moment decreases with temperatures significantly stronger than its TM counterparts. If the composition of the FI is chosen in the right ratio, the temperature of the medium passes the FI's T_{comp}. The FI is now magnetically FeCo dominant and couples parallel to the FM. In Fig. 4.2 d the bilayer is heated up further, close or above the FI's T_c. The ferromagnetic layer should show a higher T_c and its intrinsic properties are preferably unaffected by the increased temperature. Due to the reduced coercivity of the FI at these elevated temperatures, the FM is no longer fixated by the FI and can be switched by the magnetic field of the writing pole. After the switching process, the field and the laser are switched off, and the recording head moves to its next write order (Fig. 4.2 e). The medium is now cooling back down. The TM moments of the FI align parallel to the moments of the ML. The overall parallel alignment of the FI and FM in this state of elevated temperature reduces thermal writing errors [310]. In Fig. 4.2 f the system is back to its initial temperature, but in an opposite alignment in comparison to Fig. 4.2 b. Hence, Fig. 4.2 b and f represent the local "0" and "1" states of this proposed system.

The research goal of this chapter is the fabrication of a bilayer that achieves the described switching process. Therefore, the individual layers that make up the bilayer are deposited and investigated first. Co/Ni-based MLs are investigated in Sec. 4.2 as the soft ferromagnetic write and read-out layer. They should meet the requirements of exhibiting PMA, a large M_s, and a large T_c. TbFeCo alloys and MLs are studied in Sec. 4.3 as the hard ferrimagnetic storage layer. They are tuned to be Tb dominant at RT and to exhibit a T_{comp} between RT and their T_{c}. Finally, the most promising individual films are fabricated on top of each other to investigate the exchange-coupled behavior in Sec. 4.4.

4.2 Ferromagnetic Co/Ni-Based Multilayers with Pd and Pt Insertion Layers

Magnetic thin film systems with PMA have been and are still intensively investigated. PMA is displayed in several Co-based multilayered structures [56, 322–329] and has been shown to be useful for a variety of applications, including perpendicular AOS [332, 333], STT-MRAM [334–338], domain-wall-motion-based devices [339, 340], BPM [341–344], magnetoionics [345], magnetic skyrmions [346, 347], and biomedical applications [348–350]. In this regard, Co/Ni MLs are of particular interest because of their additional high spin polarization [351, 352] and low intrinsic Gilbert damping [324, 334, 353–356]. PMA in these MLs is mainly contributed to interface magnetic anisotropy [325–327, 357] and magnetoelastic anisotropy [358–360] (Sec. 2.1.4). Theoretical calculations predict a maximum PMA for Co/Ni MLs in the fcc(111) structure at a Co thickness of one monolayer and a Ni thickness of two monolayers [326, 361] ($\approx$ Co(0.2 nm)/Ni(0.4 nm)), which has been experimentally confirmed by multiple groups [322, 323, 362–366]. Previous studies have shown that PMA of Co/Ni MLs is strongly affected by the deposition process [367, 368], choice of seed layers [369], and post-treatment processing, e.g. annealing [370, 371], or ion radiation [359, 372]. This limits the feasibility for many applications where the seed layer is not freely selectable, or post-deposition treatments are not an option. One of these potential applications is the use as ECC media for HAMR (Sec. 4.1.3). Here, the ML has to be deposited directly on top of an amorphous FI layer, and post-deposition treatments that could also influence the properties of the FI are no option. On the other hand, Co/Pt and Co/Pd MLs also exhibit large PMA and are less sensitive to seed layers or sputter-deposition conditions [56, 364, 373–376].

In this section, these systems are combined in order to enhance PMA by adding Pt or Pd insertion layers to Co/Ni MLs. These trilayer-based films provide a highly tunable system for a wide range of applications. A previous study of Ni/Co/Pt and Co/Ni/Pt MLs has already demonstrated enhanced PMA and annealing stability compared to Co/Ni MLs [377]. It has also been shown that the stacking order of the trilayer, as well as the Pt thickness, is important. Here, the focus is on Pd insertion layers and their impact on the magnetic properties as a function of ML repetition number and Co layer thicknesses are investigated to provide a comparison to Co/Ni and Co/Ni/Pt MLs.

The results of this section are published and summarized in *Heigl, M. et al. J. Appl. Phys. 127, 233902 (2020)* [257].

4.2.1 Experimental Details on the Deposition and Investigation of Co/Ni-Based Multilayers

A series of $[\mathrm{Co}(t_{\mathrm{Co}})/\mathrm{Ni}(0.4)/\mathrm{X}(0.6)]_N$ MLs ($\mathrm{X} \in \{\mathrm{Pd}, \mathrm{Pt}, \text{no insertion layer}\}$, thicknesses are given in nm) with various repetition numbers N and different individual Co layer thicknesses t_{Co} are investigated. The films are deposited at RT by DC magnetron sputtering (base pressure $< 10^{-8}$ mbar) from elemental targets. The Ar pressure was kept constant at 5×10^{-3} mbar during the deposition process. The individual layer thicknesses are determined using a calibrated deposition rate. The films are prepared on silicon (Si) (001) substrates with a 100-nm-thick thermally oxidized silicon oxide (SiO_x) layer. 5 nm of Pt are used as seed and capping layer for the Co/Ni and Co/Ni/Pt MLs. Accordingly, 5 nm of Pd are used as seed and capping layer for the Co/Ni/Pd MLs. A list of all deposited samples, whose results are shown in this work, together with their deposition parameters and sample numbers is given in Sec. A.4. The Ni layer thickness is fixed to 0.4 nm. The Co layer thickness is varied between 0.1 and 0.5 nm. Chen et al. [377] showed that K_{eff} increases with Pt thickness between 0 and 1 nm for Co/Ni/Pt MLs. This is confirmed in the shown studies, especially for higher repetition numbers (Sec. 4.2.4). Due to the diminishing increase in K_{eff} with Pt layers thicker than 0.6 nm and the decreasing saturation magnetization M_{s}, as well as the largest thermal stability of multilayers with 0.6 nm of Pt [377], a fixed Pd and Pt layer thickness of 0.6 nm is chosen for most of the following studies. The bi- and trilayers are repeated to form MLs with repetition numbers N between 1 and 15. A schematic of the layer stack is depicted in Fig. 4.3 a along with an exemplary transmission electron microscopy (TEM) cross-section image of a $[\mathrm{Co}(0.2)/\mathrm{Ni}(0.4)/\mathrm{Pt}(0.6)]_{20}$ film sample (Fig. 4.3 b) confirming the overall layer structure. Note that it is not possible to differentiate between Co and Ni layers because of their similar atomic number (Z contrast). Thus, only the contrast between two equally thick layers of Co/Ni and Pt is visible.

The integral magnetic properties of the samples are investigated by SQUID-VSM. *M*-*H* hysteresis loops are measured in oop and ip geometry at RT. It has been shown that edge effects can lead to artifacts in the measured *M*-*H* hysteresis loops (Sec. 3.3.1) [223].

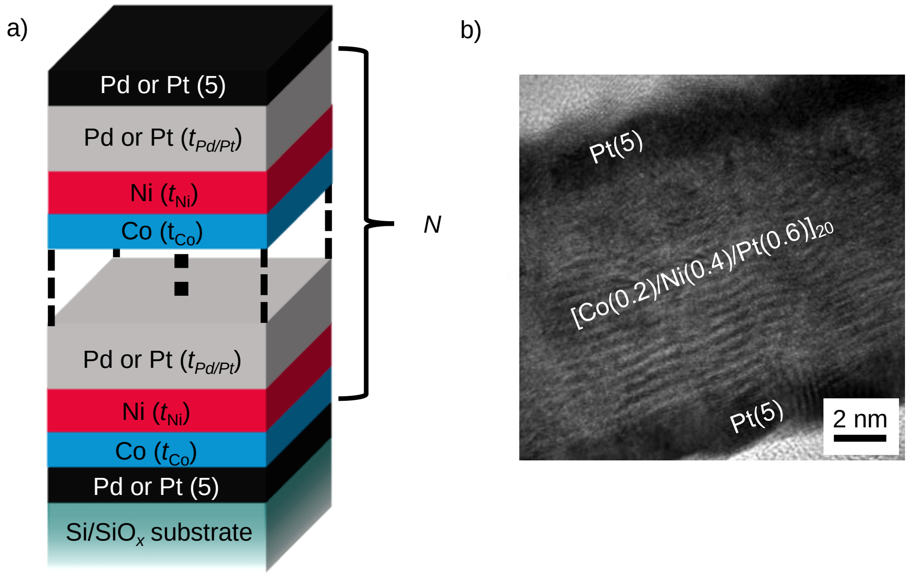

Figure 4.3: Schematic layer stack of the Co/Ni/Pd(/Pt) multilayers and a cross-section TEM image. Schematic image illustrating the layer stacking of Co/Ni/Pd(Pt) MLs (a). Exemplary cross-section TEM image of a Pt(5 nm)/[Co(0.2 nm)/Ni(0.4 nm)/Pt(0.6 nm)]$_{20}$/Pt(5 nm) film sample (b). The figure is also published in Ref. [257].

Thus, their occurrence is prevented by cutting all edges of the measured samples. K_{eff} is determined from the integrated area difference between the oop and ip M-H hysteresis loops. Please note that for calculating M_s, the total film volume (including the insertion layers) is taken into account. In order to obtain T_c, the oop or ip remanent magnetization is measured in the temperature range between 300 and 800 K with a magnetic guiding field of 10 mT. MFM is used to receive information about the magnetic domain structure after sample demagnetization at RT. In order to access the equilibrium domain size, the samples are demagnetized by decaying alternating magnetic fields.

4.2.2 Co Layer Thickness Dependence

First, the individual Co layer thickness t_{Co} is varied between 0.1 and 0.5 nm for three sample series, [Co(t_{Co})/Ni]$_3$, [Co(t_{Co})/Ni/Pd]$_9$, and [Co(t_{Co})/Ni/Pt]$_4$. The Ni and Pd/Pt thicknesses are set to 0.4 and 0.6 nm, respectively. The repetition numbers are chosen to ensure an oop easy-axis at thinner Co thicknesses. In Fig. 4.4, exemplary oop and ip M-H hysteresis loops for four different Co layer thicknesses are displayed. Based on the M-H data, the magnetic properties of the three sample series as a function of Co

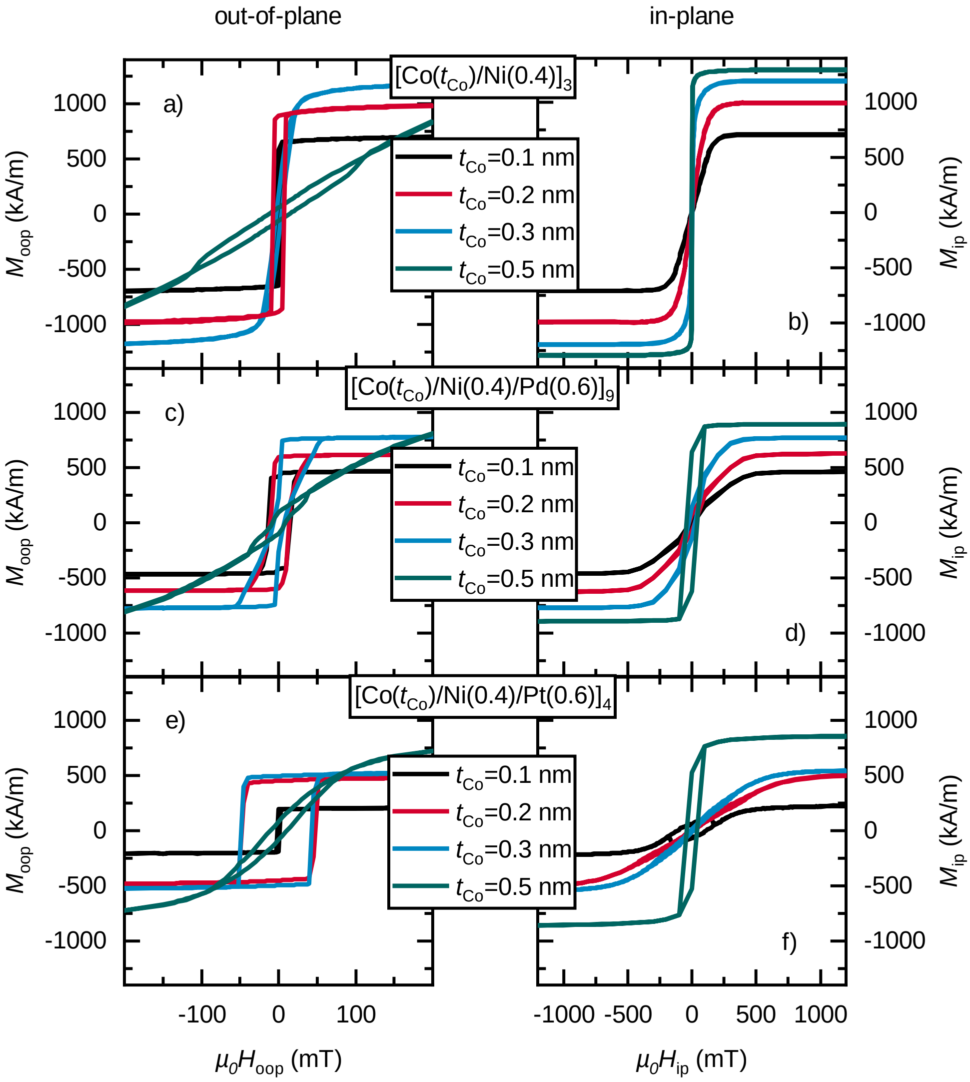

Figure 4.4: Co layer thickness dependent *M-H* hysteresis loops. *M-H* hysteresis loops obtained in oop and ip geometry of [Co(t_{Co})/Ni(0.4)]$_3$ (a, b), [Co(t_{Co})/Ni(0.4)/Pd(0.6)]$_9$ (c, d), and [Co(t_{Co})/Ni(0.4)/Pt(0.6)]$_4$ (e, f) with varying Co layer thickness. The figure is also published in Ref. [257].

layer thickness are extracted and summarized in Fig. 4.5.

The saturation magnetization M_s of all systems displayed in Fig. 4.5 a increases with Co layer thickness. The error bars mainly account for uncorrected geometry effects of the samples during SQUID measurements (around ±10%). The behavior

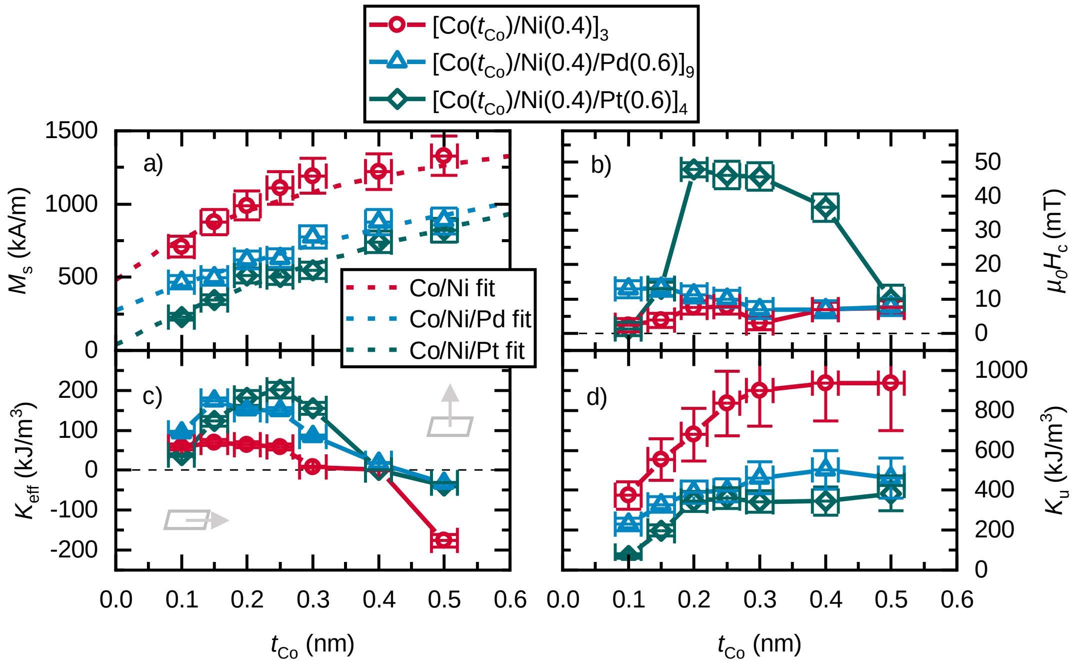

Figure 4.5: Co layer thickness dependent magnetic properties. Saturation magnetization M_s (a), coercive field H_c (b), effective magnetic anisotropy K_{eff} (c), and uniaxial magnetic anisotropy K_u (d) as function of Co layer thickness t_{Co}. The figure is also published in Ref. [257].

of [Co(t_{Co})/Ni(0.4)]$_3$ can be modeled by a linear combination of two individual magnetization contributions:

$$M_s = \frac{t_{Co} M_{s,Co} + 0.4 M_{s,Ni}}{t_{Co} + 0.4}. \tag{4.4}$$

The magnetizations of the Co layer $M_{s,Co}$ and Ni layer $M_{s,Ni}$ are chosen as fit parameters. The measured data and fit can be seen in Fig. 4.5 a. $M_{s,Co}$ has the fit value 1892 kA/m. It exceeds the bulk value of 1440 kA/m [50], which can be partially explained by the increasing polarization of the Pt seed layer with Co layer thickness. Also, superparamagnetic effects play a role for low t_{Co} and lead to a larger slope of the measured values. This effect is neglected by the fit, which leads to an overestimation of $M_{s,Co}$. Weller et al. showed that there is no additional magnetic moment enhancement for Co/Ni interfaces [378]. The fit value of $M_{s,Ni} = 480$ kA/m agrees well with the bulk value of 488 kA/m [50]. The magnetization of the MLs with insertion layers X can be fitted in a similar way:

$$M_\mathrm{s} = \frac{t_\mathrm{Co} M_\mathrm{s,Co+X} + (0.4 + 0.6) M_\mathrm{s,Ni+X}}{t_\mathrm{Co} + 0.4 + 0.6} \,. \tag{4.5}$$

For this fit, the induced polarization of the insertion layer is included both in the t_Co-dependent ($M_\mathrm{s,Co+X}$), as well as the t_Co-independent term ($M_\mathrm{s,Ni+X}$). The fit parameter $M_\mathrm{s,Co+X}$ for Co(t_Co)/Ni(0.4)/Pd(0.6) converges at 2231 kA/m. This increase in magnetization compared to bulk Co can mainly be explained by the polarization of Pd, which is dependent on t_Co in the analyzed thickness range [358]. The t_Co-independent fit parameter $M_\mathrm{s,Ni+X}$ for Co/Ni/Pd equals 272 kA/m. Besides the magnetization of the Ni layer, the Pd layer polarized by Co [358] and Ni [379] contributes. The measured values of [Co(t_Co)/Ni(0.4)/Pt(0.6)]$_4$ lead to the fit parameters $M_\mathrm{s,Co+X} = 2413\,\mathrm{kA/m}$ and $M_\mathrm{s,Ni+X} = 40\,\mathrm{kA/m}$. The high value of $M_\mathrm{s,Co+X}$ is again due to the polarization of Pt by Co. The interface between Ni and Pt is known to form a non-magnetic NiPt alloy [380], which leads to an effectively lower magnetization for the Ni and Pt layers. If the magnetizations of the two insertion layers are compared, it is important to note that the repetition number of [Co(t_Co)/Ni(0.4)/Pt(0.6)]$_4$ is lower than that of [Co(t_Co)/Ni(0.4)/Pd(0.6)]$_9$. Despite that, Pd generally shows a slightly larger induced magnetization, which is less dependent on the Co layer thickness. The same observation was made in Ref. [378], where Co/Pd and Co/Pt MLs were compared. It was reported that Co/Pd MLs exhibit a magnetization value 15% larger than that of Co/Pt MLs, due to enhanced orbital moment of Co and larger polarization of Pd.

Figure 4.5 b shows the coercive field H_c of the oop hysteresis loops for the three sample series. The increase up to t_Co =0.2 nm can be explained by the roughness of the sample and non-continuous growth of the Co layer. H_c roughly scales with K_eff (Fig. 4.5 c). All sample series have their maximum at around 0.2 nm, with the highest value obtained for the [Co/Ni/Pt]$_4$ ML. The large H_c of Co/Ni/Pt in comparison to Co/Ni(/Pd) can be explained by the formation of a non-magnetic NiPt alloy [380] at the Ni/Pt interface in Co/Ni/Pt MLs. This leads to a Pt/Co dominated reversal process which exhibits H_c values closer to Co/Pt MLs. In Co/Ni/Pd MLs this does not occur. Further, Ni/Pd MLs are known for a small PMA [381].

The effective magnetic anisotropy K_eff consists of the uniaxial magnetic anisotropy K_u and the magnetic shape anisotropy $K_\mathrm{shape} = \frac{\mu_0}{2} M_\mathrm{s}^2$ (Sec. 2.1.4):

$$K_\mathrm{eff} = K_\mathrm{u} - \frac{\mu_0}{2} M_\mathrm{s}^2 \,. \tag{2.9 revisited}$$

The measured K_{eff} values are displayed in Fig. 4.5 c. Positive values of K_{eff} imply an oop easy-axis, negative values an ip easy-axis. If the shape anisotropy is larger than the uniaxial one, a transition from an oop to an ip easy-axis occurs. The $[\mathrm{Co}(t_{\mathrm{Co}})/\mathrm{Ni}(0.4)]_3$ series shows a maximum K_{eff} of $70 \pm 7\,\mathrm{kJ/m^3}$ for $0.15\,\mathrm{nm} \leq t_{\mathrm{Co}} < 0.20\,\mathrm{nm}$. For thicker Co layers, K_{eff} decreases and the easy-axis direction changes from oop to ip for $0.30\,\mathrm{nm} < t_{\mathrm{Co}} < 0.40\,\mathrm{nm}$. These results confirm previous studies on thickness dependencies in Co/Ni MLs, revealing an optimal thickness ratio between Co and Ni of about one to two in order to get high PMA values [322, 323, 362–365]. The sample series with insertion layers behave qualitatively similarly. All systems have their maximum K_{eff} for a Co layer thickness between 0.15 and 0.25 nm and their easy-axis changes to the ip orientation at around 0.40 nm. However, in comparison to Co/Ni, the maximum K_{eff} is more than doubled with insertion layers, where $[\mathrm{Co}(0.15)/\mathrm{Ni}(0.4)/\mathrm{Pd}(0.6)]_9$ has a K_{eff} of $173 \pm 17\,\mathrm{kJ/m^3}$ and $[\mathrm{Co}(0.25)/\mathrm{Ni}(0.4)/\mathrm{Pt}(0.6)]_4$ of $201 \pm 20\,\mathrm{kJ/m^3}$. This increase in anisotropy can be mainly attributed to the lower magnetization M_{s} (see Fig. 4.5 a) and thus a smaller K_{shape} (Eq. 2.9). Additionally, the insertion layer tend to prevent intermixing at the Ni and Co interface, which might give rise to an increased interface magnetic anisotropy [340, 369, 382].

Generally, K_{u} mainly arises from interface effects in these systems [325–327, 357]. Thus, K_{u} should not be thickness-dependent. This is only observable in Fig. 4.5 d for $t_{\mathrm{Co}} > 0.2\,\mathrm{nm}$, where K_{u} saturates for all systems. Below this thickness, the Co layer is particularly influenced by roughness and non-continuous growth. Co/Ni MLs show larger K_{u} values despite the lower interface anisotropy terms of Co/Ni ($0.31\,\mathrm{mJ/m^2}$) [326] in comparison to Co/Pt ($0.50\,\mathrm{mJ/m^2}$) [325] and Co/Pd ($0.40\,\mathrm{mJ/m^2}$) [325]. This can be explained by the higher number of interfaces per thickness. If the seed and capping layers are excluded, a Co(0.2)/Ni(0.4)/Co(0.2)/Ni(0.4) stack has three interfaces and a thickness of 1.2 nm, while a Co(0.2)/Ni(0.4)/X(0.6) ML contains only two interfaces per 1.2 nm. Additionally, the smaller amount of repetitions increases the impact of the interfaces to the Pt and Pd seed and capping layer.

4.2.3 Multilayer Repetition Dependence

In a further study, the dependence of the magnetic properties on the repetition number N of the following three sample series is investigated: $[\mathrm{Co}(0.2)/\mathrm{Ni}(0.4)]_N$, $[\mathrm{Co}(0.2)/\mathrm{Ni}(0.4)/\mathrm{Pd}(0.6)]_N$, and $[\mathrm{Co}(0.2)/\mathrm{Ni}(0.4)/\mathrm{Pt}(0.6)]_N$. Based on the results of the Co layer thickness study in Sec. 4.2.2, $t_{\mathrm{Co}} = 0.2\,\mathrm{nm}$ is selected for all films. The thicknesses of Ni and Pd/Pt stay fixed at 0.4 and 0.6 nm, respectively. Figure 4.6 shows exemplary

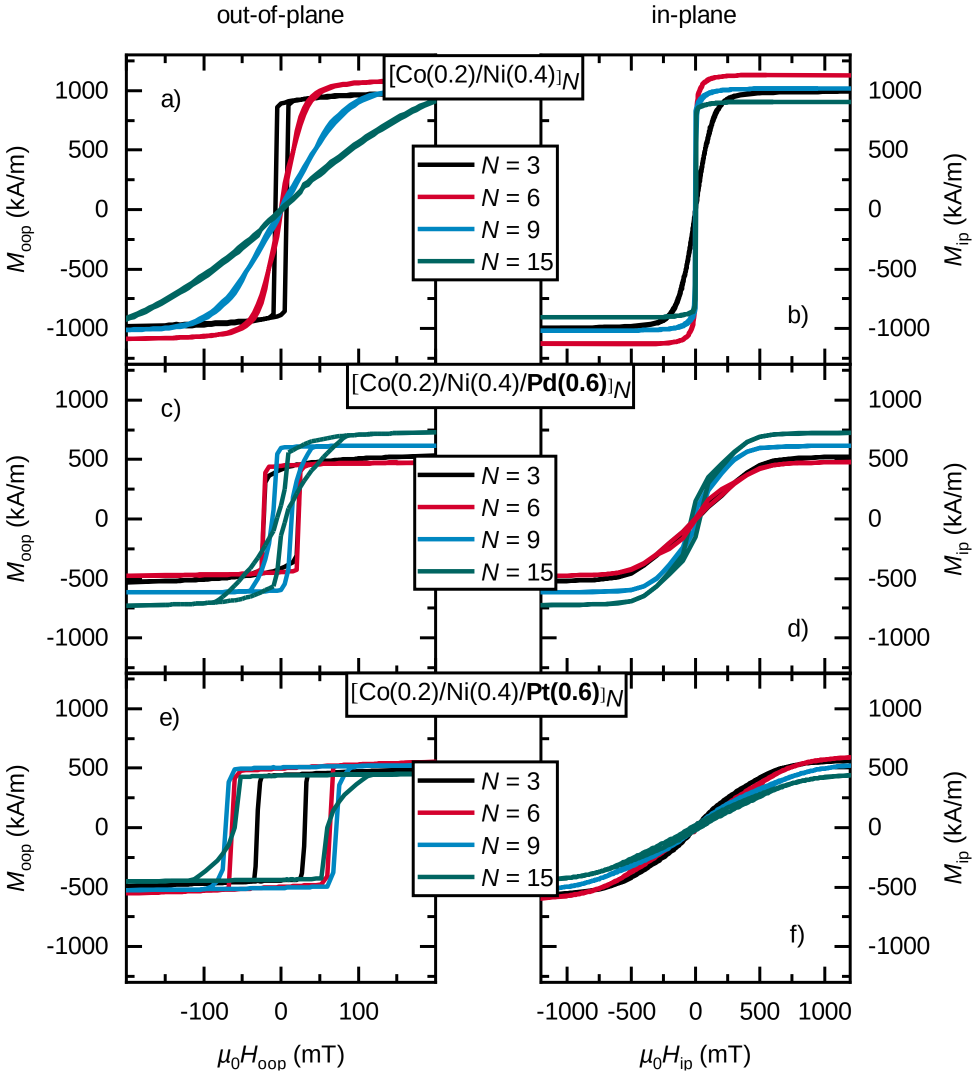

Figure 4.6: Multilayer repetition dependent *M*-*H* hysteresis loops. *M*-*H* hysteresis loops obtained in oop and ip geometry of $[\mathrm{Co}(0.2)/\mathrm{Ni}(0.4)]_N$ (a, b), $[\mathrm{Co}(0.2)/\mathrm{Ni}(0.4)/\mathrm{Pd}(0.6)]_N$ (c, d), and $[\mathrm{Co}(0.2)/\mathrm{Ni}(0.4)/\mathrm{Pt}(0.6)]_N$ (e, f) with varying repetition numbers N. The figure is also published in Ref. [257].

oop and ip *M*-*H* hysteresis loops of the three sample series. Based on the *M*-*H* data, the magnetic properties of the three sample series as a function of repetition number are extracted and summarized in Fig. 4.7.

The ratio of the M_s values between the three-sample series shown in Fig. 4.7 a stays more or less the same, as already described in Sec. 4.2.2. The lower M_s in all series for

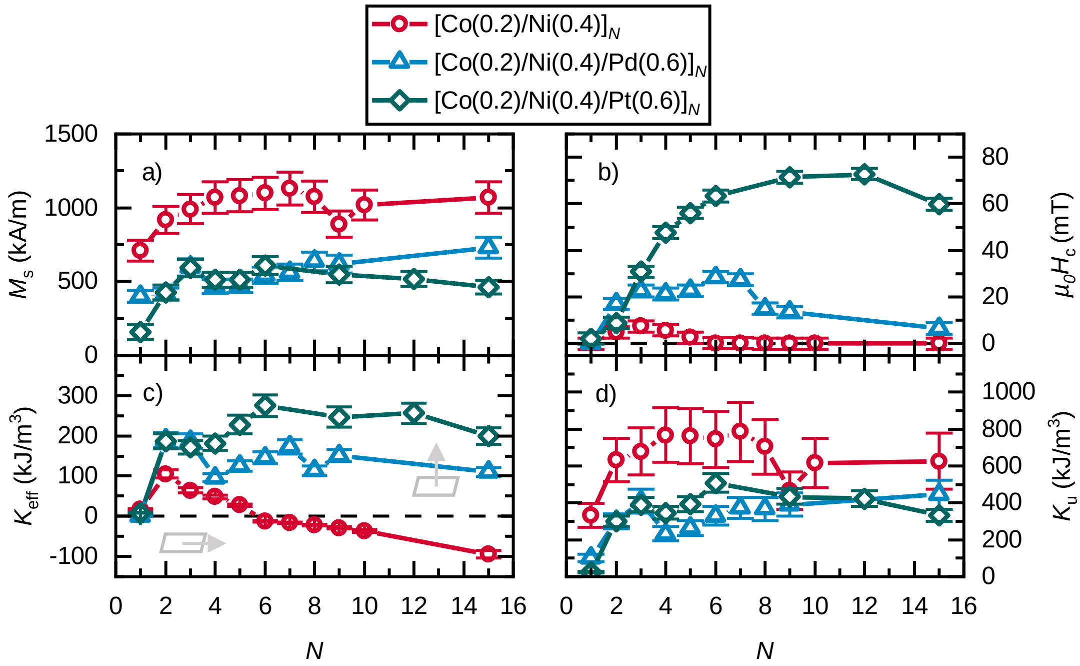

Figure 4.7: Multilayer repetition dependent magnetic values. Saturation magnetization M_s (a), coercive field H_c (b), effective anisotropy K_{eff} (c), and uniaxial anisotropy K_u (d) as function of the repetition number N. The figure is also published in Ref. [257].

$N \leq 3$ is again due to superparamagnetism. The Co/Ni multilayers exhibit an increase up to $N = 7$, in part due to the lower thickness per repetition N, as well as the decreasing relative effect of the non-magnetic Ni/Pt interface at the capping layer.

The vanishing H_c (Fig. 4.7 b) and K_{eff} values (Fig. 4.7 c) for $N \leq 2$ can be explained by the onset of superparamagnetism in ultra-thin films [383]. Otherwise, H_c scales with K_{eff} (Fig. 4.7 b, c).

In Fig. 4.7 c, the values of K_{eff} in Co/Ni MLs change sign between $N = 5$ and $N = 6$ and with it their easy-axes transition from oop to ip direction, which is mainly the result of increasing M_s (Fig. 4.7 a) and later of decreasing K_u (Fig. 4.7 d). There are two widely investigated approaches to delay this transition up to 10 repetitions: (i) increasing K_u by annealing [327] and seed layer optimization [327], or (ii) decreasing M_s (K_{shape}) by changing the ratio of Ni to Co [327]. Introducing a paramagnetic insertion layer does both. Considering the total film volume the magnetization is reduced and the intermixing and roughness decreases [340, 369, 382]. This leads to a contrary behavior of K_{eff} in Co/Ni/X MLs: their K_{eff} values stay mostly constant within the studied repetition numbers. The maximum effective magnetic anisotropy is also increased more than twofold from $105 \pm 10\,\mathrm{kJ/m^3}$ for [Co/Ni]$_3$ to $186 \pm 19\,\mathrm{kJ/m^3}$ for [Co/Ni/Pd]$_3$ and $275 \pm 28\,\mathrm{kJ/m^3}$ for [Co/Ni/Pt]$_6$.

The K_u values shown in Fig. 4.7 d increase for the Co/Ni MLs up to 4 repetitions to a maximum value of about $780{\pm}162\,\mathrm{kJ/m^3}$ and after 7 repetitions it starts to decrease. The large error bars arise from the quadratic error propagation of M_s. The behavior and values are in good agreement with the recent work of Arora et al. [327]. They showed that the moderate decrease of K_u for $N \geq 10$ can be explained by increasing roughness and intermixing with larger N. The decrease for repetition numbers below 3 can be again explained by the onset of superparamagnetism. A similar behavior for the sample series with insertion layers can be observed. The maximum K_u value of [Co/Ni/Pd]$_{15}$ and [Co/Ni/Pt]$_6$ amounts to $445{\pm}78\,\mathrm{kJ/m^3}$ and $507{\pm}51\,\mathrm{kJ/m^3}$, respectively, which is relatively small compared to $780{\pm}162\,\mathrm{kJ/m^3}$ of [Co/Ni]$_7$.

In addition, the equilibrium domain size is investigated by MFM after demagnetizing the samples. Figure 4.8 shows MFM images of the three sample series with different repetition numbers. It was not possible to measure images of [Co(0.2)/Ni(0.4)]$_N$ for N=9 and 15 due to the ip orientation of the easy-axis. The magnetic domain size depends on the ratio of the domain wall energy cost and the decreased dipolar energy (Sec. 2.4.1) [108]. Hence, the magnetic domain size D can be estimated depending on the total film thickness t by

$$D(t) = 0.95t \cdot \exp \frac{4\pi\sqrt{AK_\mathrm{u}}}{t\mu_0 M_\mathrm{s}^2}\,, \qquad \text{(2.22 revisited)}$$

whereas A and μ_0 are the magnetic exchange stiffness and the magnetic vacuum permeability, respectively. For $t << D$, D decreases exponentially with increasing t (Fig. 2.8). Thus, for all sample series, the domain sizes decrease with higher repetition number (total thicknesses t). Please note that a direct comparison of the measured domain sizes with its theoretical estimation is hardly possible due to the exponential dependency of Eq. 2.22 and the error range of the measured magnetic properties. Therefore, in the following, the evolution of the domain sizes for the sample series is discussed only qualitatively. In the first row of Fig. 4.8 a-c the domain sizes of MLs with $N = 3$ are quite similar despite of the differences in measured magnetic properties between Co/Ni and Co/Ni/X (see Fig. 4.7). The larger K_u and smaller t values of [Co/Ni]$_3$ are offset by the larger M_s in Eq. 2.22. For larger repetition numbers N, only the films with insertion layers can be compared. As already mentioned, the domain size is expected to decrease with increasing film thickness (for $t << D$), which is also observed in Fig. 4.8 b, d, f for Co/Ni/Pd and c, e, g for Co/Ni/Pt. A similar behavior

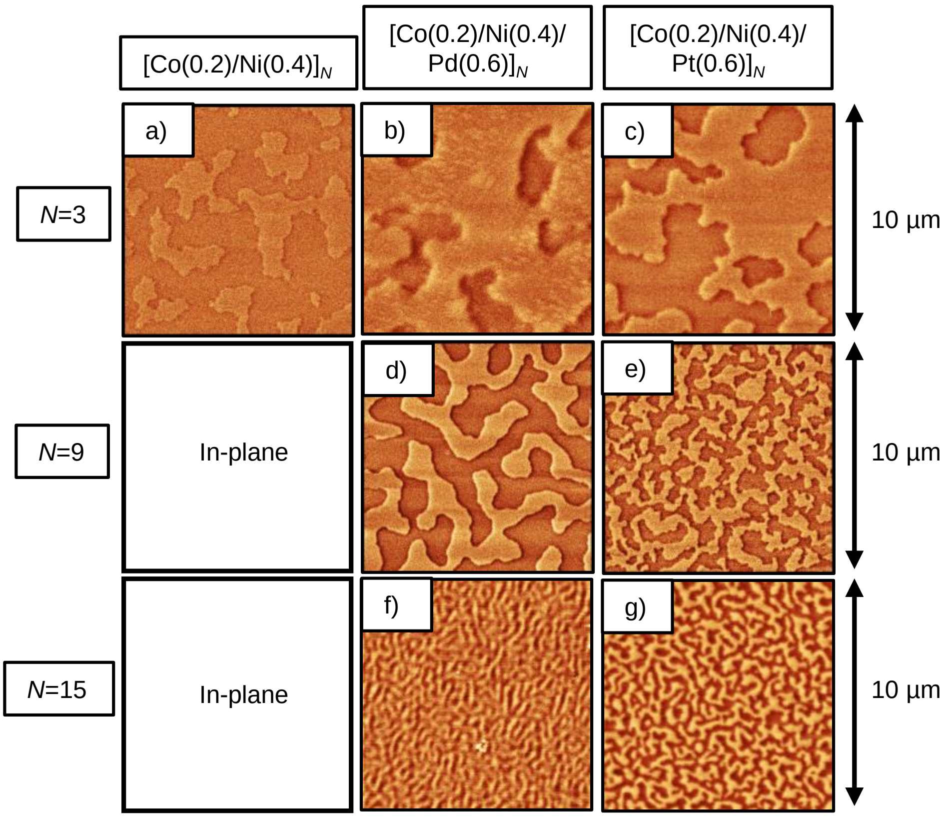

Figure 4.8: Multilayer repetition dependent magnetic domain structure. MFM images of $[Co(0.2)/Ni(0.4)]_N$ (a), $[Co(0.2)/Ni(0.4)/Pd(0.6)]_N$ (b, d, f), and $[Co(0.2)/Ni(0.4)/Pt(0.6)]_N$ (c, e, g) after sample demagnetization. The figure is also published in Ref. [257].

was already reported for Co/Ni [384, 385] and for Co/Pt [386] MLs. Despite a smaller K_u and larger M_s, $[Co/Ni/Pd]_9$ exhibits more sizeable domains, which could be a sign of a larger exchange stiffness A in Co/Ni/Pd MLs. For 15 repetitions, $[Co/Ni/Pt]_{15}$ shows slightly larger domains, which can be explained by the smaller M_s value compared to $[Co/Ni/Pd]_{15}$.

4.2.4 Insertion Layer Thickness Dependence

In order to examine the influence of the insertion layer thickness, two exemplary thicknesses are picked (t_X= 0.2 and 0.6) and investigated dependent on their repetition number N. Figure 4.9 illustrates the dependencies, while the data points of $[Co(0.2)/Ni(0.4)]_N$, $[Co(0.2)/Ni(0.4)/Pd(0.6)]_N$, and $[Co(0.2)/Ni(0.4)/Pt(0.6)]_N$ are equivalent to

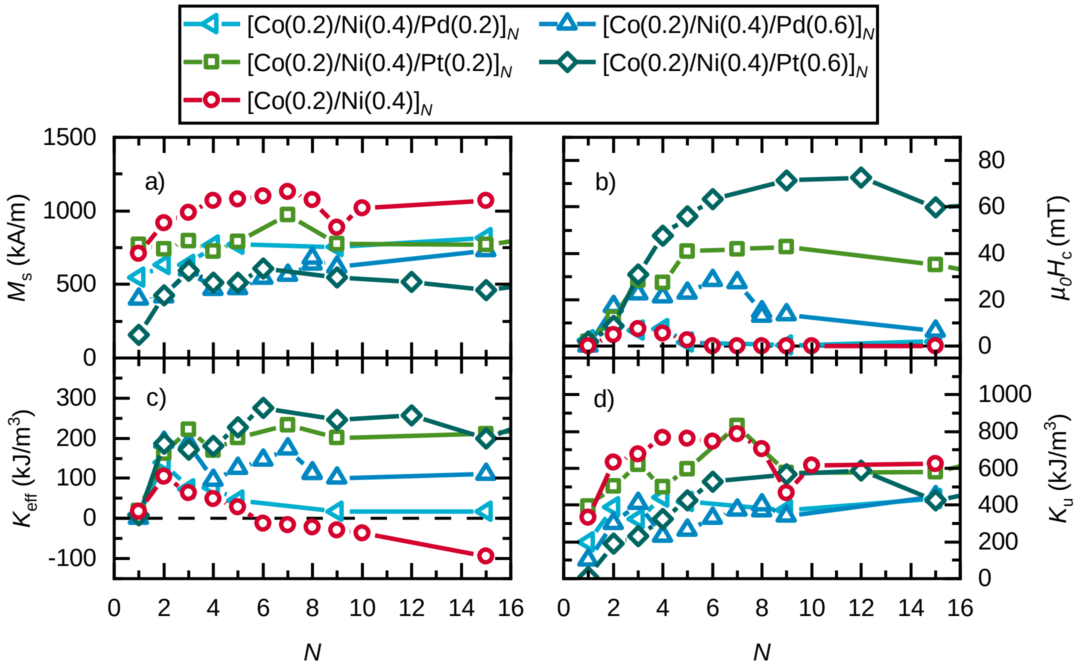

Figure 4.9: Insertion layer thickness and multilayer repetition dependent magnetic values. Saturation magnetization M_s (a), coercive field H_c (b), effective anisotropy K_{eff} (c), and uniaxial anisotropy K_u (d) as function of the repetition number N. In this figure, error bars are not displayed, due to clarity reasons.

the data displayed in Fig. 4.7. To improve clarity of the illustration, the error bars are not displayed. The errors behave in a similar manner as shown in Fig. 4.7.

The general response of the M_s values with increasing N was already described in the last section. Additionally, Fig. 4.9 a shows a positive offset of approximately 200 kA/m for the trilayer-based MLs with thinner insertion layers due to the larger ratio of ferromagnetic materials. The thinner insertion layers also introduce a negative offset of the H_c values of around 20 mT for both Pd and Pt (Fig. 4.9 b). The larger M_s of the thinner layers leads to a slightly worse K_{eff} in Fig. 4.9 c, due to a unchanged K_u (Fig. 4.9 d) but an increased K_{shape}. The reason for the relatively unchanged K_u of the thicker and thinner insertion layer samples is the constant number of interfaces. Especially for Pd insertion layers, a sufficient thickness is important, as the transition to an ip easy-axis with 5 or more repetitions in Fig. 4.9 c shows. Generally, the trilayer-based MLs with thinner insertion layers resemble the Co/Ni MLs more. The observed behavior confirms the increasing K_{eff} with the Pt thickness of Co/Ni/Pt MLs reported by Chen et al. [377].

4.2.5 Curie Temperatures of Co-Based Multilayers

Furthermore, the Curie temperature T_c for selected Co/Ni/X MLs is investigated. In order to extract T_c, the magnetization M of [Co/Ni]$_3$, [Co/Ni]$_9$, [Co/Ni/Pd]$_9$, and [Co/Ni/Pt]$_9$ are measured dependent on the temperature T (Fig. 4.10). All systems are saturated at 300 K and afterward measured with increasing T and an effective guiding field of 10 mT. The measurement geometry of all samples is in oop direction, except [Co/Ni]$_9$, which is measured in ip geometry, because of its ip easy-axis. T_c is estimated by the intersecting tangents method.

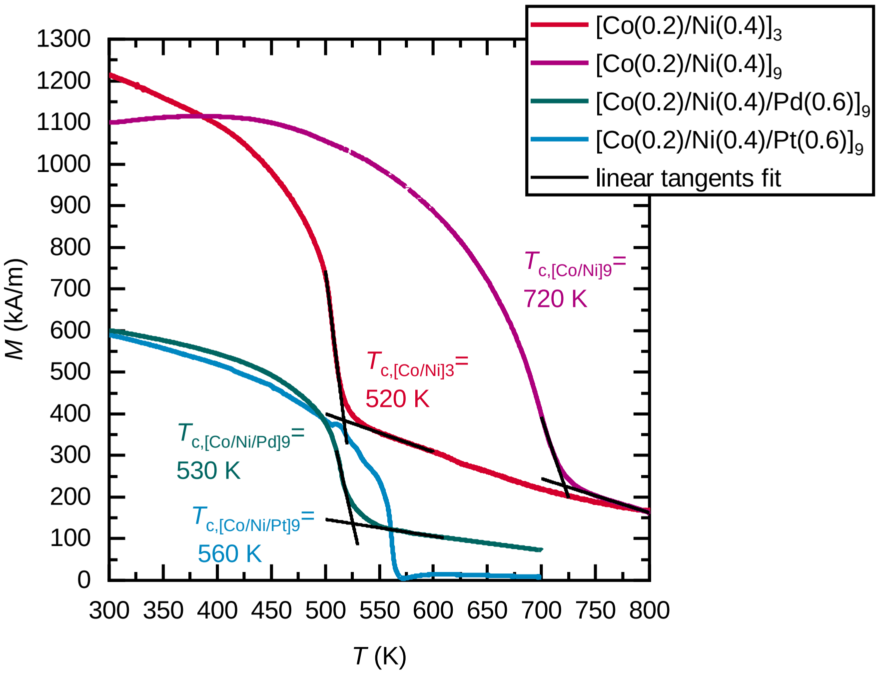

Figure 4.10: Curie temperatures of Co-based multilayers. Magnetization M against temperature T curve with a guiding field of 10 mT. The Curie temperatures are estimated by linear fits around the turning point. The figure is also published in Ref. [257].

All M-T curves, except for [Co/Ni/Pt]$_9$, do not drop fully to zero at their Curie temperature. Films measured oop might also lose magnetization due to decreasing K_u, which is induced by interfacial intermixing at these elevated measurement temperatures [377]. The Curie temperatures of [Co(0.2)/Ni(0.4)/Pd(0.6)]$_9$ and [Co(0.2)/Ni(0.4)/Pt(0.6)]$_9$ determined to 530 K and 560 K, respectively, are significantly lower than the T_c = 720 K of the [Co(0.2)/Ni(0.4)]$_9$ ML without insertion layers. The reduction in exchange energy caused by the insertion layers is mostly responsible for that. If

[Co(0.2)/Ni(0.4)]$_3$ is compared to the other samples, a T_c of 520 K is found, which is much lower than for the Co/Ni ML with 9 repetitions due to its smaller thickness. These values are in agreement with literature values. It was reported that the T_c of Co/Pt and Co/Pd MLs lies between 520 and 570 K [387, 388] depending on the ML composition, while the T_c of Co/Ni MLs can be as high as 950 K, similar to $Co_{33}Ni_{67}$ alloys [389].

4.2.6 Summary and Comparison to Other Ferromagnetic Multilayers

In this study, the influence of Pd and Pt insertion layers on the magnetic properties of Co/Ni MLs is investigated. It is shown that systems with and without insertion layers have a rather similar Co thickness dependence. An optimal Co layer thickness of $t_{Co} = 0.2\,nm$ is validated for all systems in order to achieve strong PMA. While K_{eff} is more than doubled, M_s and K_u decrease drastically with the insertion of Pd and Pt. The repetition number study reveals that K_{eff} can be increased over the whole measured range of repetition numbers (up to $N = 15$). This allows the extension of the transition from an oop to an ip easy-axis for larger repetition numbers for samples with insertion layers. MLs with Pt as insertion layer show the largest K_{eff} and H_c. The variation of the magnetic domain sizes is consistent with the corresponding magnetic properties of the three sample series. Furthermore, insertion of Pd and Pt decreases the Curie temperature for [Co/Ni]$_9$ from 720 K to 530 K and 560 K, respectively.

Concluding, Co/Ni MLs without insertion layers are not feasible for the proposed ECC medium (Sec. 4.1.3), due to their loss of PMA with large repetition numbers without seed layer optimization. Other than PMA, a large temperature independence is needed, at least up to the proposed writing temperature of 400-600 K. Therefore, the decrease in Curie temperature of the MLs with insertion layers is problematic. Nevertheless, [Co(0.2)/Ni(0.4)/Pt(0.6)]$_9$ exhibits the best compromise of the investigated MLs with a large PMA of 435 kJ/m^3 and an acceptable Curie temperature of 560 K. Thus, it is picked as the most promising ferromagnetic layer for the investigations of the envisioned exchange-coupled bilayer in Sec. 4.4.

4.3 Ferrimagnetic TbFeCo Alloys and Tb/FeCo Multilayers

Amorphous ferrimagnetic RE - 3d TM alloys provide high tunability of magnetic properties such as saturation magnetization and PMA [202, 390–395], and can exhibit zero magnetic moment at the compensation temperature T_{comp} depending on the alloy composition (Sec. 2.2.2). PMA is mainly associated to a chemical short-range order [396, 397], where RE-TM atom pairs prefer an oop direction (Sec. 2.2.3). These properties make them a compelling material candidate for a variety of applications. For instance, the use of ferrimagnetic RE-TM systems as pinning layers for soft ferromagnetic films is of high interest [100, 258, 398–404]. In this regard, the switching behavior of exchange-coupled soft and hard layers has been intensely studied and led to the term *Exchange-Spring Magnets* [398], which has further implications for spintronic devices such as spin valves [405–410] and magnetic tunnel junction devices [411], which is discussed in Sec. 4.4. Furthermore, AOS of magnetic domains in GdFeCo thin films induced by fs-laser pulses was discovered [260], and many intriguing works on the ultrafast magnetization reversal in TbFe(Co) followed [69, 262, 412, 413]. In addition, ferrimagnetic RE-TM materials have been utilized in THz technologies [275, 276, 414, 415], allowing thermomagnetic control of spintronic THz emitters [416].

Moreover, many studies have also been devoted to ferrimagnetic MLs because of their additional tunability of magnetic anisotropy depending on their individual layer thicknesses [397, 417–423]. Recently, also optical switching of the magnetization in a ferrimagnetic Tb/Co multilayer was investigated with an explicit focus on the annealing stability of the device [424, 425]. In addition, by tailoring the magnetic properties of Fe/Gd MLs, it was demonstrated that it is possible to stabilize various topologically protected spin objects such as skyrmions [128] and antiskyrmions [426] solely by dipolar interactions, which is further discussed in chapter 5. However, the proposed use as ECC medium for HAMR (Sec. 4.1.2) and the presented multitude of possible applications benefit or even require thermal stability. Despite the fact that RE-TM systems provide intriguing magnetic properties, they also exhibit irreversible changes upon annealing already occurring at temperatures as low as 450 K in amorphous TbFeCo [60, 203], which is much lower than the crystallization temperature [202, 427, 428]. On the other hand, it was also reported that annealing procedures at temperatures up to 500 K can be used to increase the PMA in TbFeCo films [429, 430].

In this section, the magnetic and structural properties of amorphous TbFeCo alloys and Tb/FeCo MLs are investigated. Motivated by the potential application for HAMR, the properties of selected films are also analyzed depending on the annealing temperatures. Having a detailed understanding of the underlying processes upon annealing is crucial for future storage and spintronic devices operating at elevated temperatures.

4.3.1 Deposition Technicalities and Experimental Details on the Magnetic and Structural Characterization of Tb-Based Ferrimagnets

The Tb-FeCo alloy and ML films are deposited at RT by magnetron (co-)sputtering (base pressure $< 10^{-8}$ mbar) from elemental targets. The sample holder rotates during the deposition to achieve a uniform film composition. The Ar pressure is kept constant at 5×10^{-3} mbar during the deposition process. The Tb, Fe, and Co deposition rates are 0.079, 0.060, and 0.014 nm/s, respectively. The films are prepared on Si(001) substrates with a 100-nm-thick thermally oxidized SiO_x layer. 2 nm of tantalum (Ta) and 5 nm of Pt are used as seed layer to enhance the adhesion and PMA of the ferrimagnet film [431, 432]. The system is capped by 5 nm Ta or Pt to prevent oxidation. The individual layer thicknesses are controlled using calibrated deposition rates.

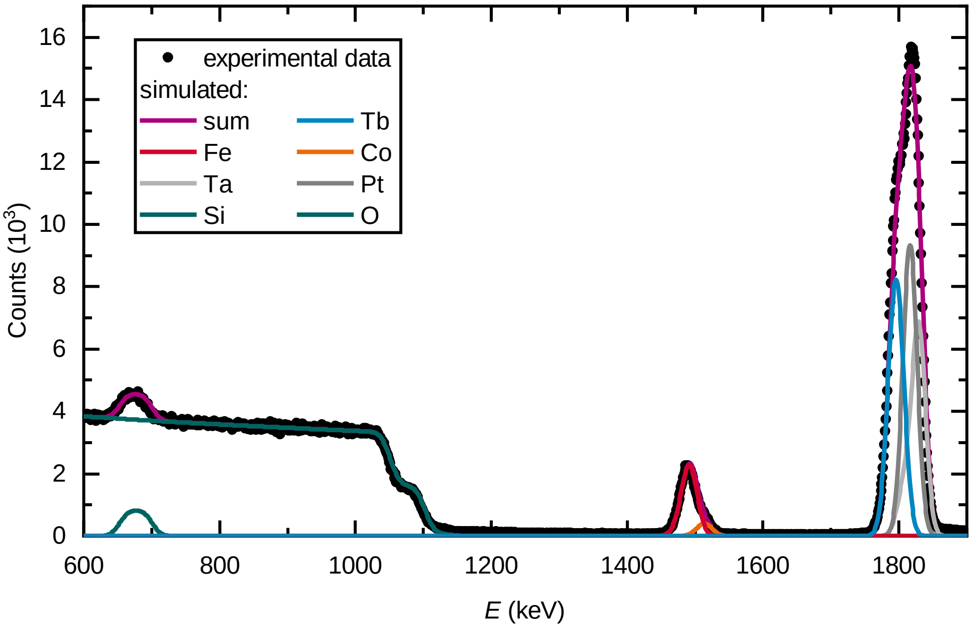

Figure 4.11: TbFeCo Rutherford backscattering spectrum. Exemplary Rutherford backscattering spectrum of $Tb_{28}(Fe_{85}Co_{15})_{72}$ (20 nm) analyzed by the software SIMNRA. The experimental and corresponding simulated spectra, confirming the composition, are shown.

The compositions and thicknesses of the alloys are confirmed by Rutherford backscattering spectrometry (RBS) using 1.7 MeV He^+ ions at a scatter angle of 170°. An exemplary RBS spectrum is shown in Fig. 4.11. The measured spectra are fitted by simulations of the film by the software SIMNRA. Although the overlapping Tb, Pt, and

Ta peaks hinder the analysis of the composition and thickness, the resulting values can be used to confirm the deposited film structure. Still, a deviation of the composition of ± 1 at.% and 10% of the film thickness is observed.

It is important to note that TbFeCo compounds are very sensitive to the smallest changes in their composition and deposition conditions [202, 396, 433–435]. This leads to deviations between different studies and even deposition runs. To investigate the thermal stability of the samples, the as-deposited samples are post-annealed in nitrogen atmosphere at a heating rate of 2 K/min up to 430, 570, 640, and 720 K.

The integral magnetic properties of the samples are investigated by SQUID-VSM. *M-H* hysteresis loops are captured in oop and ip geometry. It has been shown that edge effects can lead to artifacts in the measured *M-H* hysteresis loops [223] (Sec. 3.3.1). Thus, their occurrence is reduced by cutting all edges of the measured samples. In order to reveal the dominant sublattice of the investigated films, their remanent magnetization versus temperature (*M-T*) is measured. The samples are saturated at RT in an oop field of +7 T, cooled down while the field was still applied, and measured with a guiding field of +10 mT with increasing temperatures from 40 to 340 K. The effective magnetic anisotropy K_{eff} is determined from the integrated area difference between the oop and ip *M-H* hysteresis loops. MFM is used to receive information about the magnetic domain morphology at RT. To access the equilibrium domain size, the samples are demagnetized by decaying alternating magnetic fields.

In addition to the magnetic measurements, structural changes are investigated by four-point resistivity measurements. During these measurements, the samples are annealed in nitrogen atmosphere at a rate of 2 K/min up to 720 K. In Sec. 4.3.2 and 4.3.3 cross-section scanning transmission electron microscopy (STEM) and energy-dispersive X-ray spectroscopy (EDS) measurements are presented. A Jeol NeoArm system operating at 200 keV is used. The samples are mechanically thinned before measuring. The crystal structures of the films are characterized by X-ray diffractometry (XRD) using Cu-K_α radiation. The XRD patterns are measured in $\Theta - 2\Theta$ configuration with a 2 degree offset of the incident angle to avoid a too strong signal of the mono-crystalline Si substrate.

4.3.2 Composition Dependent Study on TbFeCo Alloys

As discussed in Sec. 4.1.3, the desired TbFeCo layer for a potential application in HAMR is Tb dominant with an observable compensation temperature above RT and a Curie temperature below 600 K. Previous studies about different TbFeCo compositions [202,

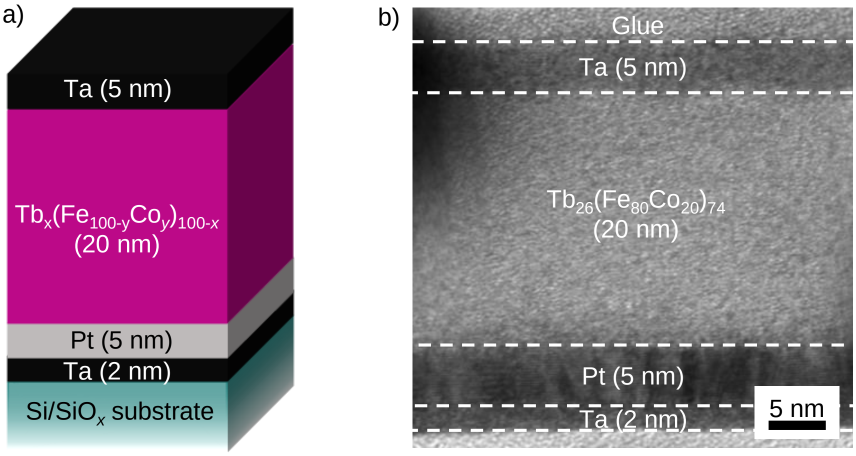

Figure 4.12: Layer stack of the investigated TbFeCo alloys. Schematic image illustrating the layer stack of $Tb_x(Fe_{100-y}Co_y)_{100-x}$ (20 nm) (a). Exemplary cross-section TEM image of a $Tb_{26}(Fe_{80}Co_{20})_{74}$ (20 nm) film (b).

436] are used, to make a preselection of possible compositions. However, due to the sensitivity of TbFeCo compounds to their deposition parameters [202, 396, 433], an independent evaluation has to be conducted to select the best possible composition. Therefore, $Tb_x(Fe_{100-y}Co_y)_{100-x}$ (20 nm) layers are investigated with Tb contents ranging from 18 to 30 at.% and Fe:Co ratios between 85:15 and 60:40. A schematic layer stack and an exemplary cross-section TEM image of $Tb_{26}(Fe_{80}Co_{20})_{74}$ (20 nm) are shown in Fig. 4.12. The TEM measurement confirms the amorphous nature of the TbFeCo sample as well as the thickness. In the following series, a change in Tb content is mainly used to influence the dominance of the different sublattices, while a larger Co ratio significantly increases the Curie temperature. A study of TbFeCo and the dependence of the Curie, crystallization, and compensation temperature on Tb, Co, and Fe content can be found in Ref. [202].

Figure 4.13 displays some selected oop and ip M-H hysteresis loops of 20-nm-thick TbFeCo alloys. Four samples with different Tb content are shown in oop (Fig. 4.13 a) and ip geometry (Fig. 4.13 b). All oop loops exhibit a rectangular shape and, therefore, a large PMA. The maximum saturation magnetization M_s is observed for $Tb_{18}(Fe_{70}Co_{30})_{82}$. Due to the non-strictly monotonous decrease in M_s, it can be assumed that the dominant sublattice is changing between the displayed compositions. Therefore, a compensation temperature at RT is expected for compositions between 24 and 26 at.% Tb, which is also

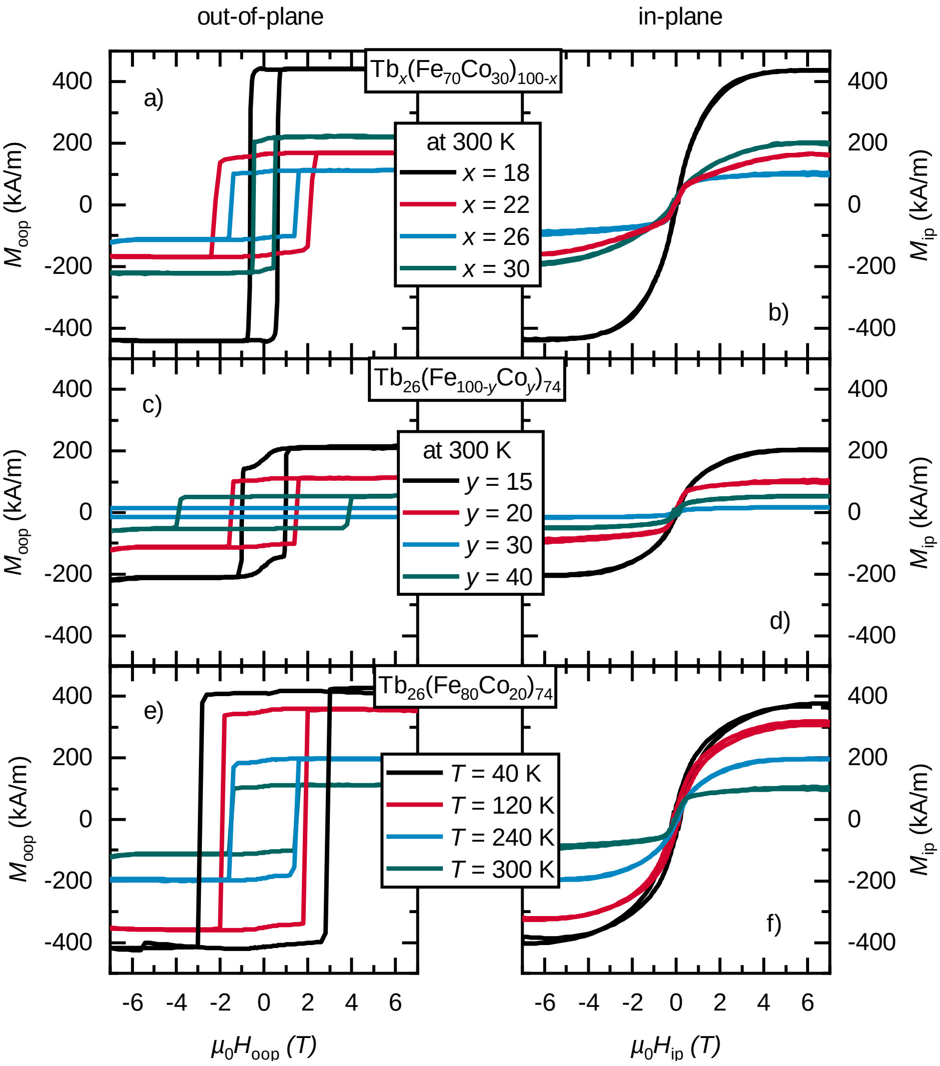

Figure 4.13: Selected TbFeCo *M*-*H* hysteresis loops. TbFeCo oop and ip *M*-*H* hysteresis loops dependent on the Tb content x in at.% (a, b), the Co to Fe ratio y in at.% (c, d), and the measurement temperature T (e, f).

confirmed by Fig. 4.14 a. It is also evident that the coercivity increases the closer the Tb content is to its compensation composition.

Figure 4.13 c and d focus on the dependency of the magnetic properties on the Co to Fe ratio y in at.%. Similar to the dependency on the Tb content in Fig. 4.13 a and b, an increase in Co decreases M_s up to a compensation composition around $y = 30$. In Fig. 4.14, it is shown that samples with 26 at.% are Tb dominant at RT. Therefore, the magnetization of the FeCo sublattice increases with Co content up to $y = 30$. This behavior is typical for FeCo alloys, which have a maximum M_s at a Co content of about 30 at.% [437]. At $y = 30$, the coercivity is too large to be measured with the maximum available magnetic field strength of $\pm 7\,\mathrm{T}$, which is, together with the low M_s, a clear sign for two nearly compensated sublattices. $Tb_{26}(Fe_{85}Co_{15})_{74}$ shows the only loop with a significant difference between its remanent and saturation magnetization. It has been shown that Co improves the squareness of TbFe alloys for certain compositions [436, 438]. For the rest of this work, the focus is on compositions with a Co ratio y of 30 and below. This is due to the massive increase of the Curie temperature for larger y [202], which is not desired for a potential HAMR application. A study of Co-rich TbFeCo thin films can be found in Ref. [439].

In Fig. 4.13 e and f, the temperature dependency of $Tb_{26}(Fe_{80}Co_{20})_{74}$ (20 nm) is shown. This composition is Tb dominant over the whole measured temperature range, which is apparent by the strictly monotonous decreasing M_s with T as shown by the M-T curve of Fig. 4.14 b. In contrast to the previous loops, the coercivity is not increasing the closer the system comes to a compensated state of the sublattices. Hence, the effect of decreasing coercivity with increasing temperatures is dominant in the shown parameter range. The ip loop at 40 K is also the only ip loop that exhibits a hysteresis. Overall, all loops shown in Fig. 4.13 display strong PMA, evident by the rectangular oop loops and hysteresis-free ip loops with large anisotropy fields. The results agree with previous composition studies on thin amorphous TbFeCo films [202, 436]. For the following investigations, the focus is on TbFeCo samples with a Fe:Co at.% ratio of 20:80 and 30:70. These compositions show an increased squareness with an acceptable low Curie temperature below 600 K [202].

In order to get a better understanding of which sublattice is dominant at what composition and temperature, M-T measurements are necessary. Figure 4.14 a and b display these measurements at a guiding field of 10 mT in oop configuration of TbFeCo samples with a Fe:Co ratio of 70:30 and 80:20, respectively. The Tb content x is varied between 18 and 30 at.% for both Fe:Co ratios. Additionally, the oop remanence M_r of the hysteresis loops of the corresponding samples and temperatures is extracted and plotted. Both the hysteresis loops and M-T measurements are conducted with the same sample and within the same measurement sequence. Therefore, typical errors in the magnetization values are equal. However, the two types of measurements display an offset, which can be explained by a measurement artifact [223]. In the hysteresis loops, this soft phase contribution is subtracted, which is not possible for M-T measurements. In this and all following M-T measurements, positive magnetization values correspond

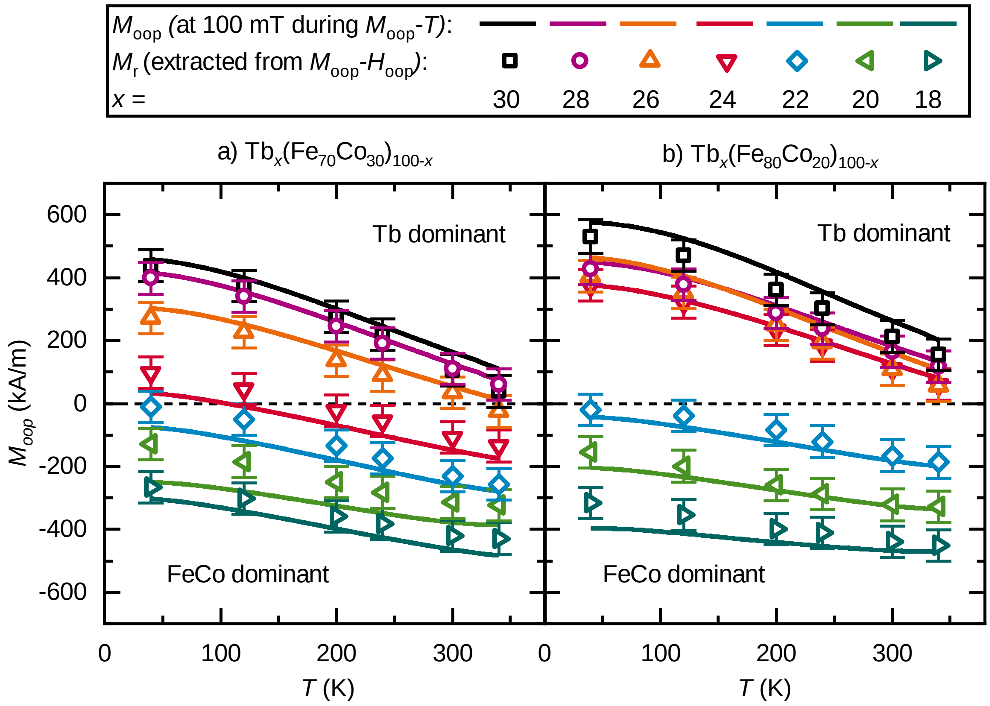

Figure 4.14: Temperature dependency of the magnetization of different TbFeCo compositions. M-T measurements at a guiding field of 10 mT in oop configuration of TbFeCo (20 nm) samples with a Fe:Co ratio of 70:30 (a) and 80:20 (b), and a varying Tb ratio between 18 and 30 at.%. Additionally, the oop remanence M_r of the hysteresis loops of the corresponding samples and temperatures is plotted.

to a Tb dominant state and negative ones to a FeCo dominant one. The graphs show the typical behavior of ferrimagnetic layers dependent on temperature, described in Sec. 2.2.2. A lower Tb content leads to a negative offset of the magnetization in both Fig. 4.14 a and b. In Fig. 4.14 a, this offset is systematic and constant with increasing Tb content, while Fig. 4.14 b shows an overlap of $x = 28$ and $x = 26$. Please note that the samples with a Tb content of 28, 26, and 24 at.% in Fig. 4.14 b were deposited within a different sputter run than the others and therefore their deposition parameters are not directly comparable. Hence, the samples with $x = 26$ and $x = 24$ show a slightly larger magnetization than expected within this series.

In Fig. 4.14 a samples with $x > 26$ are Tb dominant for the whole measured temperature range. The composition $Tb_{24}(Fe_{70}Co_{30})_{76}$ and $Tb_{26}(Fe_{70}Co_{30})_{74}$ exhibit a compensation temperature at roughly 120 and 320 K, respectively. The shown data in Fig. 4.14 b behaves similar. Samples with $x \geq 24$ are Tb dominant. Generally, the effective magnetization of the FeCo sublattice should increase with a larger Co ratio up

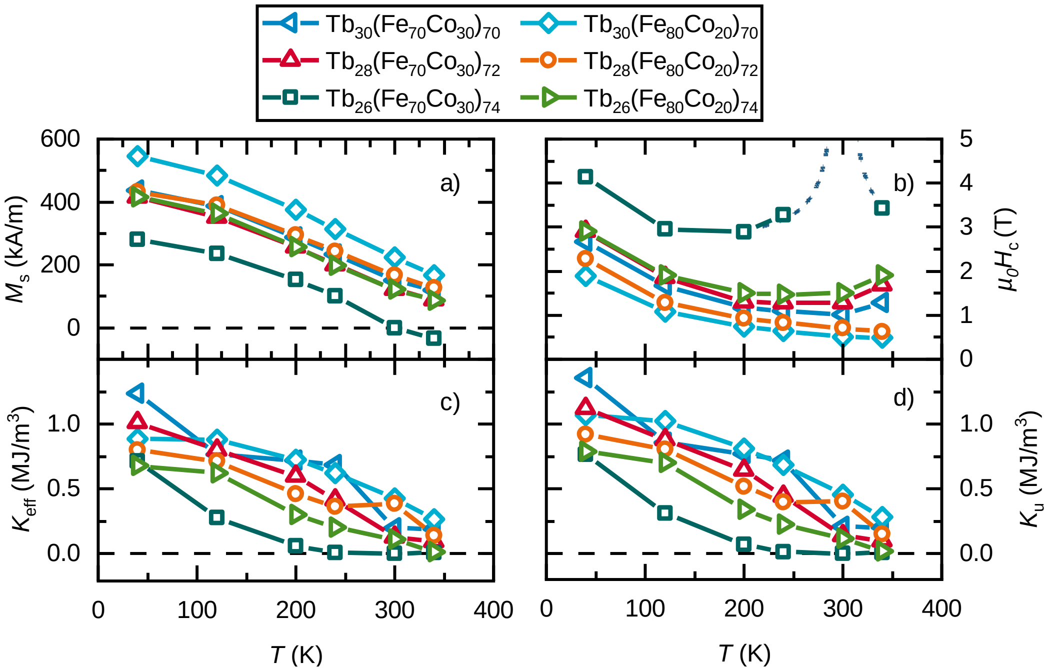

Figure 4.15: Temperature dependent magnetic values of different Tb dominant TbFeCo films. Saturation magnetization M_s (a), coercive field H_c (b), effective magnetic anisotropy K_{eff} (c), and uniaxial magnetic anisotropy K_u (d) as function of the temperature T. In this figure, error bars are not displayed, due to clarity reasons.

to 30 at.% [437], and thus the magnetization values of Fig. 4.14 b should show a positive offset in comparison to Fig. 4.14 a. This is only the case for the Tb dominant samples. Generally, the temperature dependence can be explained by the interatomic coupling J of the different atom types [59, 60, 79, 440]:

$$J_{\mathrm{Co-Co}} > J_{\mathrm{Co-Fe}} > J_{\mathrm{Fe-Fe}} > J_{\mathrm{Co-Tb}} > J_{\mathrm{Fe-Tb}} > J_{\mathrm{Tb-Tb}} \,. \tag{4.6}$$

With more Co, the temperature dependency of both sublattice decreases, and the Curie temperature increases.

Next, only samples with Tb content above 24 at.% are examined in more detail, due to the desired property of a compensation temperature below the Curie temperature but above RT for HAMR (Sec. 4.1.2). The saturation magnetization M_s, the coercive field H_c, the effective magnetic anisotropy K_{eff}, and the uniaxial magnetic anisotropy K_u are extracted from the measured oop and ip hysteresis loops and are displayed versus the measurement temperature T in Fig. 4.15.

The M_s values of all samples decrease with the measurement temperature T linearly (Fig. 4.15 a). Due to the squareness of the oop loops (Fig. 4.13), M_s and the remanence are almost identical. Thus, the shown trend is very similar to the M-T curves in Fig. 4.14. Only $\mathrm{Tb}_{26}(\mathrm{Fe}_{70}\mathrm{Co}_{30})_{74}$ exhibits a compensation temperature in the measured temperature range at approximately 300 K. Generally, samples with more Tb and less Co display larger M_s values.

Figure 4.15 b shows the coercive field H_c of the oop hysteresis loops. H_c tends to decrease with larger temperatures. However, this changes for temperatures close to the compensation temperature. Here, H_c increases. This is in particular the case for $\mathrm{Tb}_{26}(\mathrm{Fe}_{70}\mathrm{Co}_{30})_{74}$ at 300 K, where H_c is larger than the available field strength of 7 T (see also Fig. 4.13 c). In general, lower Tb and larger Co content increase H_c, which is the opposite behavior to M_s in Fig. 4.15 a. This behavior is described by the proportion

$$H_\mathrm{c} \propto \frac{1}{M_\mathrm{s}}\,, \tag{4.7}$$

under the assumption that the magnetic anisotropy energy values are constant (K_shape negligible for small M_s values) and that only the Zeeman energy changes with M_s and H. Hence, H_c diverges at the compensation temperature according to Eq. 4.7, which is illustrated by the fit shown as a dashed line in Fig. 4.15 b.

The effective magnetic anisotropy K_eff consists of the uniaxial magnetic anisotropy K_u and the magnetic shape anisotropy $K_\mathrm{shape} = \mu_0/2M_\mathrm{s}^2$ (Sec. 2.1.4):

$$K_\mathrm{eff} = K_\mathrm{u} - \frac{\mu_0}{2}M_\mathrm{s}^2. \tag{2.9 revisited}$$

It is calculated by integrating the area in between the oop and ip magnetization curves and decreases with T. For the presented values in Fig. 4.15 c, large Tb:FeCo ratios increase K_eff, while there is no clear trend for the different Co:Fe ratios. According to Eq. 2.9, the relatively small M_s^2, and the large K_u values, lead to very similar behavior for the shown K_u data in Fig. 4.15 d in comparison to the K_eff data in Fig. 4.15 c.

In order to further investigate TbFeCo as a potential candidate for HAMR, one composition is picked for annealing studies at temperatures above 340 K. The chosen composition is $\mathrm{Tb}_{28}(\mathrm{Fe}_{20}\mathrm{Co}_{80})_{72}$ (20 nm). It represents the best compromise between a Tb dominant sublattice (Fig. 4.14 b), a relatively high effective anisotropy of 257 kJ/m^3 (Fig. 4.15 c), a compensation temperature of 520 K (extrapolated from Fig. 4.14 b), and a low Curie temperature of about 600 K [202]. To measure the magnetization in oop

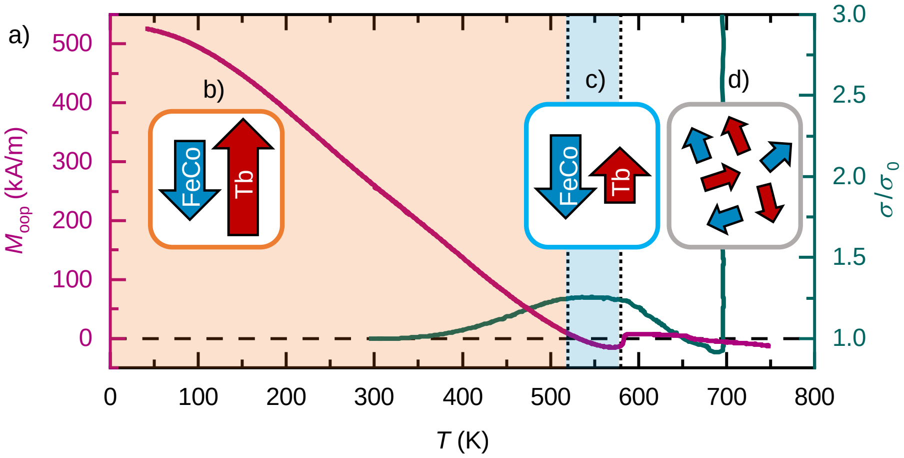

Figure 4.16: Sheet resistance, magnetization, and magnetic states of $Tb_{28}(Fe_{20}Co_{80})_{72}$ dependent on the temperature. The sheet resistance σ divided by the sheet resistance at RT σ_0 of $Tb_{28}(Fe_{20}Co_{80})_{72}$ together with the oop magnetization M_{oop} as a function of the annealing temperature T (a). The three different magnetic states, Tb dominant (b), FeCo dominant (c), and disordered/paramagnetic (d) are displayed in the corresponding temperature regions.

geometry above temperatures of 350 K, a special sample holder is necessary (Sec. 3.3.1). The high temperature M-T (300-750 K) measurement result is combined with the initial M-T (40-340 K) measurement of Fig. 4.14 in Fig. 4.16 a. The magnetization course confirms a compensation temperature at 520 K. Further, the Curie temperature is observable at 580 K. At temperatures above the Curie temperature, the magnetization stays close to zero until it starts to increase again at 650 K, possibly due to the formation of new crystalline phases with larger Curie temperatures. Dependent on the temperature, the different magnetic states of the sample are illustrated as insets in Fig. 4.16 b-d.

Additionally, the sheet resistance σ divided by the sheet resistance at RT σ_0 is measured while annealing and shown in Fig. 4.16 a. This measurement provides information about any structural changes within the film at these elevated temperatures. At 350 K, the resistance starts to increase with a maximum at around 570 K, which is associated with a structural relaxation of the film while still being amorphous [202–205]. The drop of resistivity at temperatures larger than 570 K is associated with the beginning of crystallization processes. At about 700 K, a sharp rise in resistivity is observed, which can be explained by the crystallization of additional phases, oxidation, formation of grains and grain boundaries, and the subsequent dewetting of the film. To confirm these described structural processes, cross-section TEM measurements are later shown in Sec. 4.3.3.

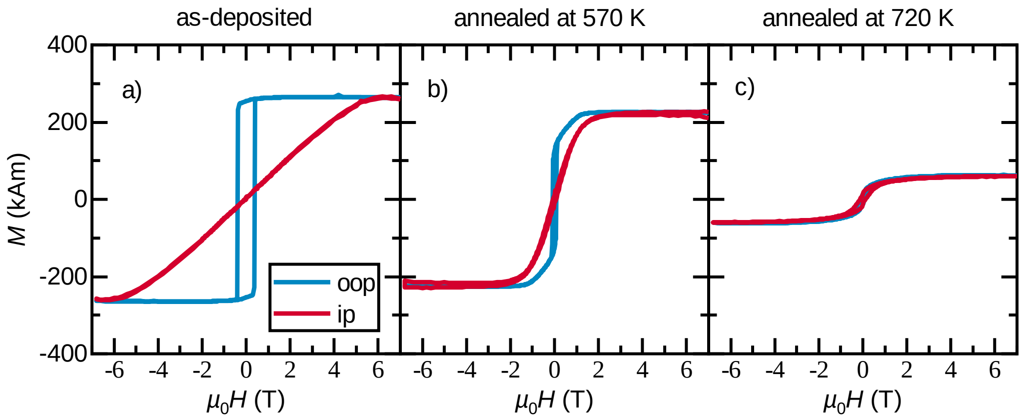

Figure 4.17: Hysteresis loops after annealing at different temperatures. *M-H* oop and ip hysteresis loops of $Tb_{28}(Fe_{20}Co_{80})_{72}$ measured at RT in the as-deposited state (a), after annealing at 570 K (b), and after annealing at 720 K (c).

While the magnetic properties fulfill the necessities for an application in an ECC media for HAMR, the structural changes at elevated temperatures need to be further examined. Irreversible changes in the recording medium at the writing temperature ($\approx$ 550 K) are not desired.

Therefore, the impact of the observed signs of severe structural changes at elevated temperatures in Fig. 4.16 is examined with regard to their magnetic properties. *M-H* hysteresis loops are captured of the as-deposited specimen, and after annealing the specimen at 570 and 720 K. The measurement temperature is 300 K for all three samples. In the as-deposited state, the sample shows a square loop with a strong PMA (Fig. 4.17 a). After annealing the sample, the coercivity in the oop direction drops close to zero (Fig. 4.17 b). While the much smaller area between the oop and ip loop points to a massive decrease in anisotropy, the saturation magnetization stays relatively constant. Figure 4.17 c displays a full loss in effective anisotropy at 720 K and a massive loss in saturation magnetization. These results denote irreversible magnetic changes due to the structural transformation indicated in Fig. 4.16. While the changes at 720 K are expected due to crystallization, which was reported in various works before [202, 205], the decreased effective anisotropy at temperatures below 600 K was only reported recently [203, 204].

In order to get a better understanding of the structural processes and the influence of the composition of the samples, various additional resistivity measurements are

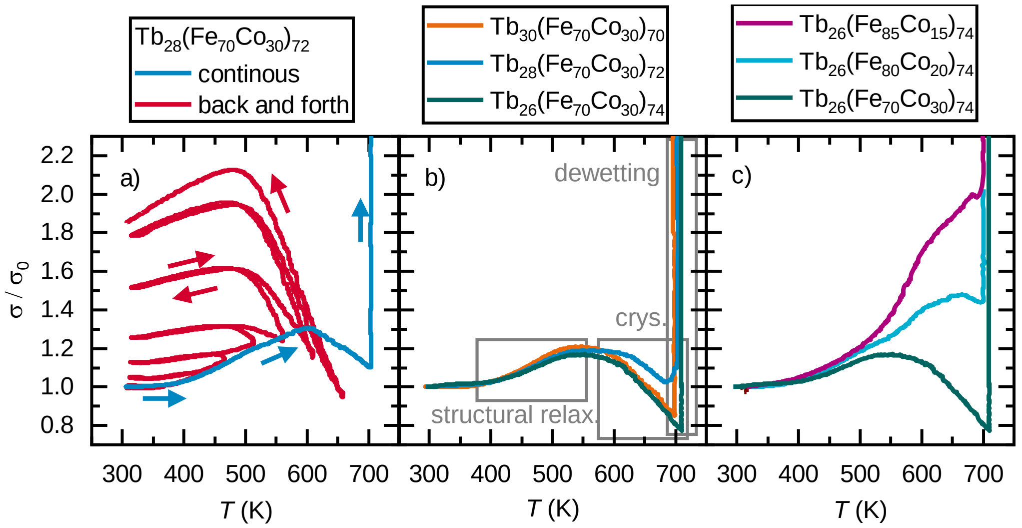

Figure 4.18: Sheet resistance studies on TbFeCo dependent on the temperature. Continuous and back and forth measurements of the normalized sheet resistance σ/σ_0 against temperature T (a). Comparison of the sheet resistance of TbFeCo with different Tb contents (b). Comparison of the sheet resistance of TbFeCo with different Co:Fe ratios (c).

conducted. Figure 4.18 a conveys the reversibility of the structural processes. The continuous heating process from 300 to 720 K at a heating speed of 2 K/min is compared to a "back and forth" measurement. Here, the sample is repeatedly cooled down after an increasing target temperature is reached. The target temperatures increase from 350 K in 50 K steps up to 650 K. The heating and cooling speed is 2 K/min. It is evident that the increased resistivity persists after the sample is cooled down. The resistivity even increases further for the "back and forth" measurement above a target temperature of 450 K, due to the longer time period at elevated temperatures. Despite the decreasing resistivity at temperatures above 600 K, the resistivity increases massively while cooling back down. This is probably caused by the inhomogeneity of a partially amorphous and partially crystalline film.

Figure 4.18 b and c compare TbFeCo films with different Tb, Co, and Fe content. There is no observable difference in the onset of the structural relaxation visible for different Tb content. The literature describes a slightly smaller crystallization temperature for larger amounts of Tb [202], which is partially visible in the starting temperature of the dewetting of the film. The influence of different Fe:Co ratios in Fig. 4.18 c is more severe. An increase of the crystallization temperature from 450 to 600 K is measured between $y = 15$ and $y = 30$ for $Tb_{28}(Fe_{100-y}Co_y)_{72}$ in [202]. In the displayed graph, the drop of resistivity is delayed from 550 to 700 K by decreasing the Co content.

To summarize, it is evident that the annealing of TbFeCo films above 400 K has irreversible effects on the structural and magnetic properties. This primarily stems from structural relaxation processes, which were reported before in [203, 204]. Figure 4.18 also shows that this cannot be easily tuned or prevented by a change in composition. Therefore, the next section investigates the possibility of an artificial multilayer structure to improve the annealing stability of Tb-FeCo thin films.

4.3.3 Comparison between TbFeCo Alloys and Corresponding Tb/FeCo Multilayers

Three different $[\mathrm{Tb}(t_{\mathrm{Tb}})/\mathrm{Fe}_{80}\mathrm{Co}_{20}(t_{\mathrm{FeCo}})]_N$ MLs are investigated with $t_{\mathrm{Tb}} = 0.40, 0.79, 1.27$ nm, $t_{\mathrm{FeCo}} = 0.37, 0.74, 1.23$ nm, and $N = 26, 13, 8$, respectively. The thicknesses and repetition numbers are chosen to replicate the corresponding composition and thickness of the 20-nm-thick $\mathrm{Tb}_{28}(\mathrm{Fe}_{80}\mathrm{Co}_{20})_{72}$ alloy thin film of Fig. 4.16. Note that the provided thicknesses are nominal thicknesses. A schematic of the ML stack and an exemplary STEM cross-section image of $[\mathrm{Tb}(1.27\,\mathrm{nm})/\mathrm{Fe}_{80}\mathrm{Co}_{20}(1.23\,\mathrm{nm})]_8$ is displayed in Fig. 4.19.

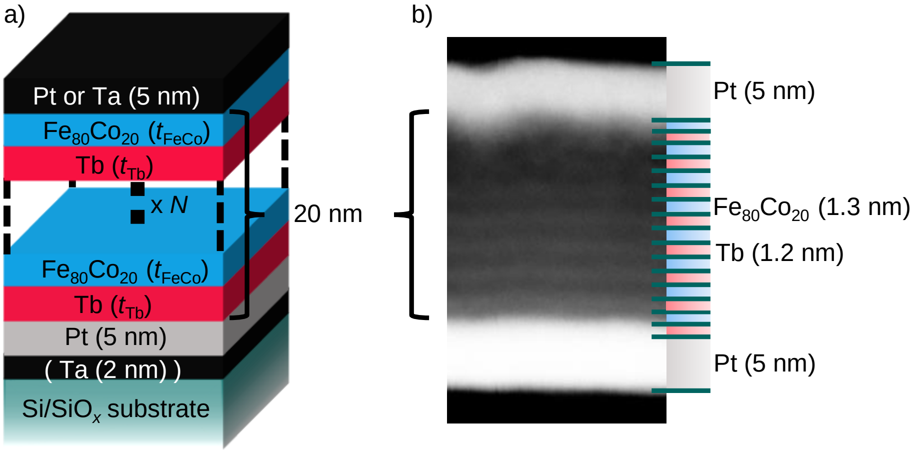

Figure 4.19: Layer stack of the investigated Tb/FeCo multilayers. Schematic image illustrating the layer stacking of $[\mathrm{Tb}(t_{\mathrm{Tb}})/\mathrm{Fe}_{80}\mathrm{Co}_{20}(t_{\mathrm{FeCo}})]_N$ (a). Exemplary cross-section STEM image of $[\mathrm{Tb}(1.27\,\mathrm{nm})/\mathrm{Fe}_{80}\mathrm{Co}_{20}(1.23\,\mathrm{nm})]_8$ (b).

The results of this subsection are published and summarized in *Heigl, M. et al. AIP Adv. 11, 085112 (2021)* [206].

Magnetic Properties

First, the magnetic properties of the prepared MLs and the alloy thin film are compared. All *M*-*H* hysteresis loops show strong PMA with an easy-axis of magnetization pointing oop, as is discussed later. The obtained *M*-*T* curves are plotted in Fig. 4.20. The TbFeCo alloy exhibits a declining absolute value of the magnetization M with temperature T, which indicates a Tb dominant system. There is no T_{comp} in the displayed temperature range. However, Fig. 4.16 shows a T_{comp} of 520 K for this alloy composition. The curves of the two MLs with thinner individual layers ($N = 26, 13$) match the curve of the alloy very well. The results of the alloy and the two thinner MLs are consistent with studies reported in the literature for similar systems [202].

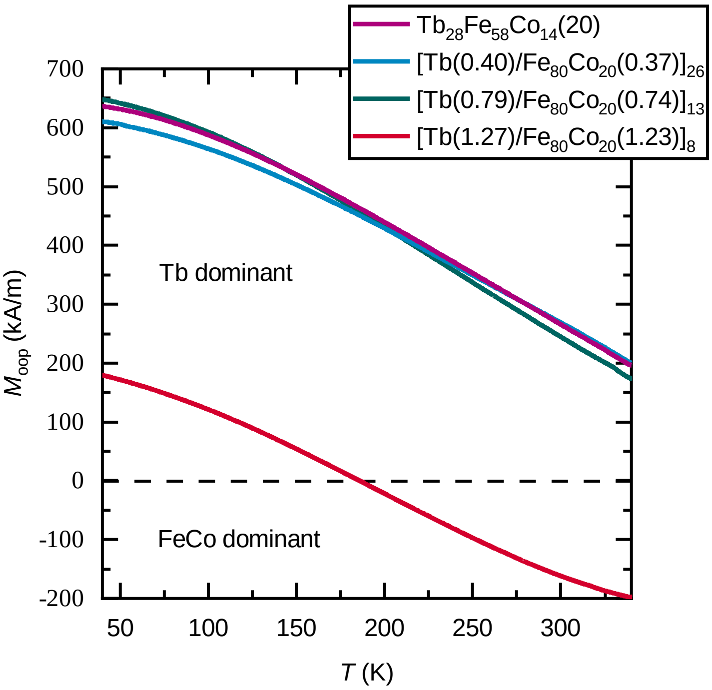

Figure 4.20: Magnetization versus temperature curves of different Tb-FeCo MLs and the corresponding alloy. Oop magnetization M_{oop} versus temperature T curves recorded with a guiding field of +10 mT. The curves of the two MLs with thinner individual layers ($N = 26, 13$) match the curve of the alloy very well and are Tb dominant over the whole measured T range. The ML with the thickest individual layers (> 1 nm) reveals a magnetic compensation point T_{comp} at 190 K. The figure is also published in Ref. [206].

The ML with the thickest individual layers shows a curve similar in shape but with a negative offset of roughly 400 kA/m. Due to the smaller effective Tb moment, this sample is only Tb dominant up to 190 K at which the two sublattices compensate each other (T_{comp}). At $T > 190\,\mathrm{K}$, the sample's FeCo sublattice is magnetically dominant.

It has been shown that interlayer intermixing plays an important role in Tb/Fe multilayers [441, 442]. If the individual layer thicknesses surpass the intermixing thicknesses, the RE-TM ratio is significantly modulated along the film normal. The threshold has been reported to be around 1 nm [418, 441]. This explains the discrepancy between $[\mathrm{Tb}(1.27)/\mathrm{Fe}_{80}\mathrm{Co}_{20}(1.23)]_8$ and the remaining samples. The effective Tb moment decreases, due to the formation of a Tb-rich alloy contribution (Tb>30 at.%) in the ML [275, 393]. This leads to a FeCo dominant sample at RT and the observed offset in the magnetization.

Figure 4.21 shows MFM images and corresponding *M-H* loops of the investigated samples depending on the annealing temperature. The MFM images in panel I are measured at RT in the as-deposited state after demagnetization. The images, which are shown in panel II and III, are obtained after annealing at 570 and 720 K, respectively, followed by demagnetization at RT. The corresponding *M-H* loops are shown underneath (panel IV-VI). The domain morphology in the equilibrium state can be used to make an assessment of changes in the magnetic properties, as the domain size depends on the uniaxial magnetic anisotropy K_{u}, saturation magnetization M_{S}, as well as the magnetic exchange stiffness A [108]. The magnetic domain size D can be estimated depending on the total film thickness t by (Sec. 2.4.1) [108]

$$D(t) = 0.95t \cdot \exp \frac{4\pi\sqrt{AK_{\mathrm{u}}}}{t\mu_0 M_{\mathrm{s}}^2}\ , \qquad \text{(2.22 revisited)}$$

whereas μ_0 is the magnetic vacuum permeability. All samples in the as-deposited state reveal square loops with an easy-axis of magnetization pointing in the oop direction (panels IV). In addition, only the sample with the thickest individual layers (Fig. 4.21 d IV) exhibits a pronounced hysteresis in the ip loop, indicating a more Tb-rich (Tb>30 at.%) part of the ML with an ip magnetic anisotropy. The M_{s} values of the loops are also comparable in all four samples before annealing with values between 180 and 290 kAm. It is important to note that the net magnetic moment in Fig. 4.21 d is FeCo dominant in contrast to the Tb dominant moments in Fig. 4.21 a-c, as revealed in Fig. 4.20. With the extracted K_{u} and M_{s} values (Fig. 4.22 a, d) from the *M-H* loops and using an A value of $10^{-12}\,\mathrm{J/m}$ from literature [443], the relation between the magnetic properties and the observed domain sizes can be confirmed via Eq. 2.22. The estimated domain sizes

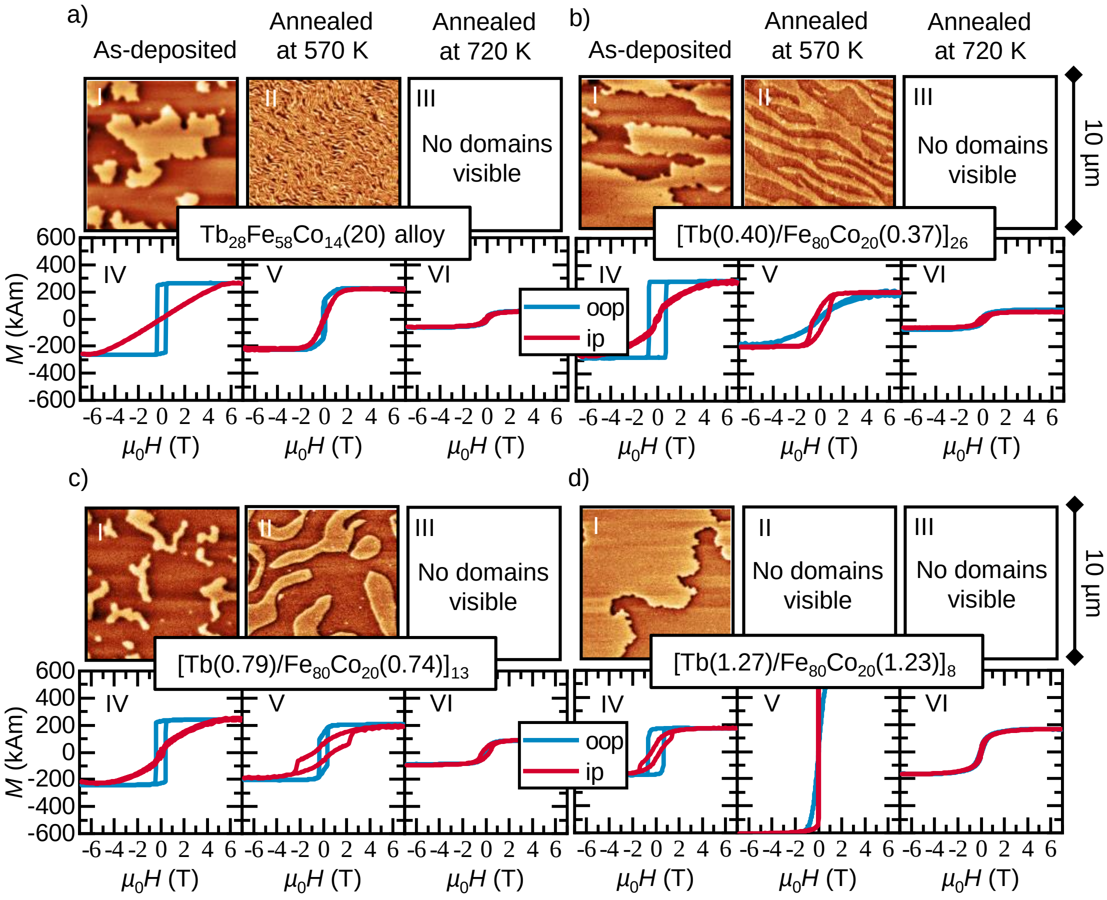

Figure 4.21: MFM images and the corresponding hysteresis loops of different Tb-FeCo multilayers and the corresponding alloy at different annealing temperatures. In the first row of a-d) MFM images are shown for three different annealing temperatures (panels I-III). The corresponding oop and ip *M-H* loops are shown in the panels IV-VI. The PMA of all samples decreases with annealing temperature. This is evident from both the size of the magnetic domains (panels I-III) and the *M-H* loops (panels IV-VI). The figure is also published in Ref. [206].

are between 3 and 7 µm which agrees well with the experimentally observed domain structure.

Next, the samples are annealed at 570 K. While the alloy sample shows a strong loss in PMA (Fig. 4.21 a V), the MLs with the lowest layer thicknesses still reveal an oop easy-axis magnetization (Fig. 4.21 b,c V). This behavior is also reflected in the magnetic domain morphology presented in the Fig. 4.21 a-c panel II. The domain size of the alloy sample decreases significantly more than observed for the MLs. By inspecting the *M-H* loops, it is clear that the pronounced loss in K_u is the main cause of the smaller domains

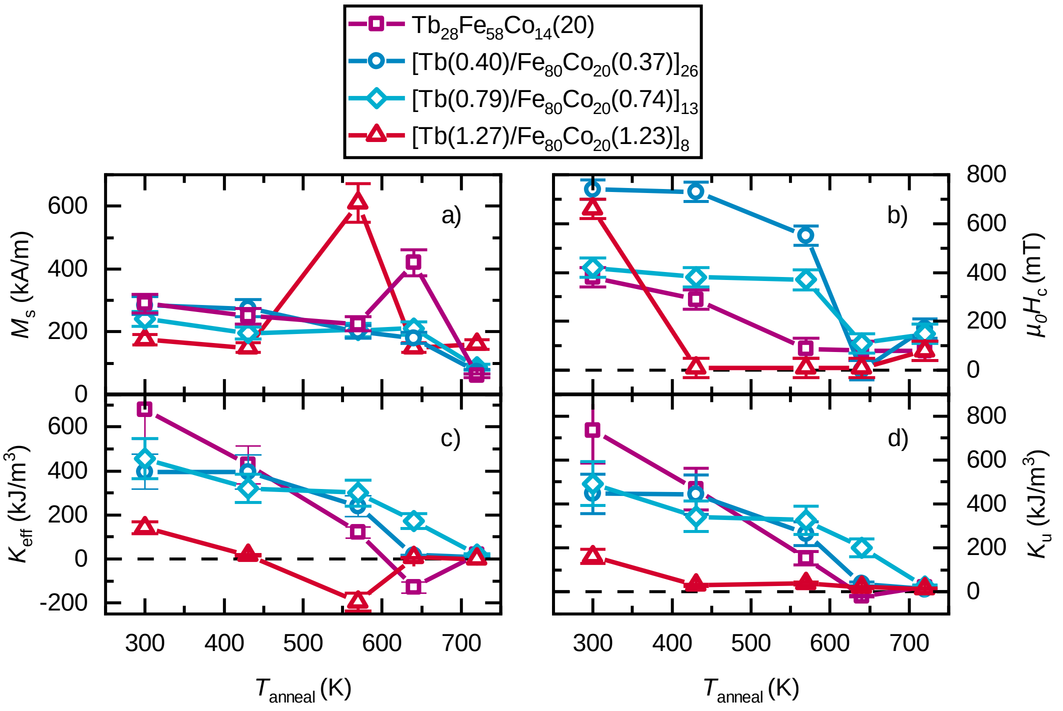

Figure 4.22: Annealing temperature dependent magnetic properties of the TbFeCo alloy and the multilayers. Saturation magnetization M_s (a), coercivity H_c (b), effective magnetic anisotropy K_{eff} (c), and uniaxial magnetic anisotropy K_u (d) as a function of annealing temperature T_{anneal} measured at RT. The ML structure delays the transition from an oop magnetic anisotropy direction to an ip direction (dashed line in c) from 640 K (alloy) to 720 K ([Tb/FeCo]$_{13}$). The magnetic properties of [Tb/FeCo]$_8$ differ greatly due to the individual layer thicknesses surpassing the critical intermixing thicknesses. The figure is also published in Ref. [206].

observed in the alloy sample. The decrease in domain size is less significant for the MLs and especially for [Tb/Fe]$_{13}$, due to a more resistant PMA. In contrast, the ML with the largest layer thicknesses, reveal a clear ip magnetic anisotropy (Fig. 4.21 d V) with an almost tripled M_s value. This drastic rise cannot be explained by selective oxidation of the RE or TM layer or by an increased moment from crystalline phases. In this state, the Tb and FeCo moments appear to be strongly decoupled and align parallel with the applied field. Due to the ip magnetization of the sample, no contrast can be detected by MFM imaging, which is only sensitive to oop magnetic stray field gradients.

Annealing at 720 K results for all samples in a complete loss in PMA as well as a substantial decrease in M_s. These effects are explained in more detail later.

In Fig. 4.22 the magnetic properties depending on the annealing temperature T_anneal are summarized. The saturation magnetization M_s (Fig. 4.22 a), the magnetic coercive field H_c (Fig. 4.22 b), and the effective magnetic anisotropy K_eff (Fig. 4.22 c) are extracted from the *M*-*H* loops. Positive K_eff values imply an oop magnetic easy-axis, negative ones an ip easy-axis. The uniaxial magnetic anisotropy K_u is calculated by

$$K_\mathrm{u} = K_\mathrm{eff} + \frac{\mu_0}{2} M_\mathrm{s}^2 \,, \tag{2.9 revisited}$$

with $\frac{\mu_0}{2} M_\mathrm{s}^2$ being the magnetic shape anisotropy (Sec. 2.1.4). As mentioned before, all specimens have a similar M_s before annealing. With increasing T_anneal, M_s of the alloy and the two MLs with thinner individual layers decreases. Only at 640 K, the alloy exhibits a peak to nearly double its initial M_s value. A similar peak can be found for the ML with the thickest individual layers at 570 K. These peaks correspond to the only negative values of K_eff in Fig. 4.22 c. As described previously for $[\mathrm{Tb/FeCo}]_8$ annealed at 570 K, the Tb and FeCo sublattices are assumed to be decoupled in this state, which is discussed in more detail later. The coercivity in Fig. 4.22 b generally decreases with T_anneal, while the coercive fields of $[\mathrm{Tb/FeCo}]_{26}$ and $[\mathrm{Tb/FeCo}]_{13}$ are more resilient to temperature.

The effective magnetic anisotropies of the as-deposited samples displayed in Fig. 4.22 c reveal a difference between the MLs and the alloy. Different studies on similar systems have reported an increase in M_s and K_eff for Tb(t_Tb<1 nm)/Fe($\mathrm{t_{Fe}}$<1 nm) ML structures in comparison to their alloy counterpart before annealing [397, 444]. The behavior of K_eff in Fig. 4.22 c partially resembles the coercivity in Fig. 4.22 b. It decreases for all specimens, while the slopes of $[\mathrm{Tb/FeCo}]_{26}$ and $[\mathrm{Tb/FeCo}]_{13}$ are smaller than the rest. The alloy and $[\mathrm{Tb/FeCo}]_8$ exhibit an effective ip anisotropy at 570 and 640 K, respectively, which is primarily a result of their large M_s value and resulting shape anisotropy. At larger T_anneal their K_eff values eventually also drop to zero. $[\mathrm{Tb/FeCo}]_8$ has a much smaller K_eff value than the other samples because of the previous discussed modulated Tb:FeCo ratio with Tb-rich layer parts. Figure 4.22 d displays the K_u values in dependence of the annealing temperature. With increasing individual layer thicknesses, the loss in PMA is delayed from 640 K of the alloy to 720 K of $[\mathrm{Tb/FeCo}]_{13}$. The individual layer thicknesses of $[\mathrm{Tb/FeCo}]_8$ are above the intermixing limit, resulting in a loss in PMA at already 420 K.

Structural Properties

Temperature-dependent resistivity measurements are performed to investigate the structural changes in the alloy and MLs. Figure 4.23 shows the evolution of the electric sheet resistance σ divided by the as-deposited sheet resistance $\sigma_{0,\mathrm{TbFeCo}}$ of the as-deposited $Tb_{28}(Fe_{20}Co_{80})_{72}$ alloy sample upon annealing at a rate of 2 K/min. To give a better overview of the magnetic changes, exemplary *M-H* loops of $[Tb/FeCo]_{26}$ are displayed above the resistivity curves. The loops are analogous to Fig. 4.21 b IV-VI. They are measured at RT, and the annealing temperature of the samples correspond to the temperature marked with dashed lines in the diagram. The two MLs with smaller

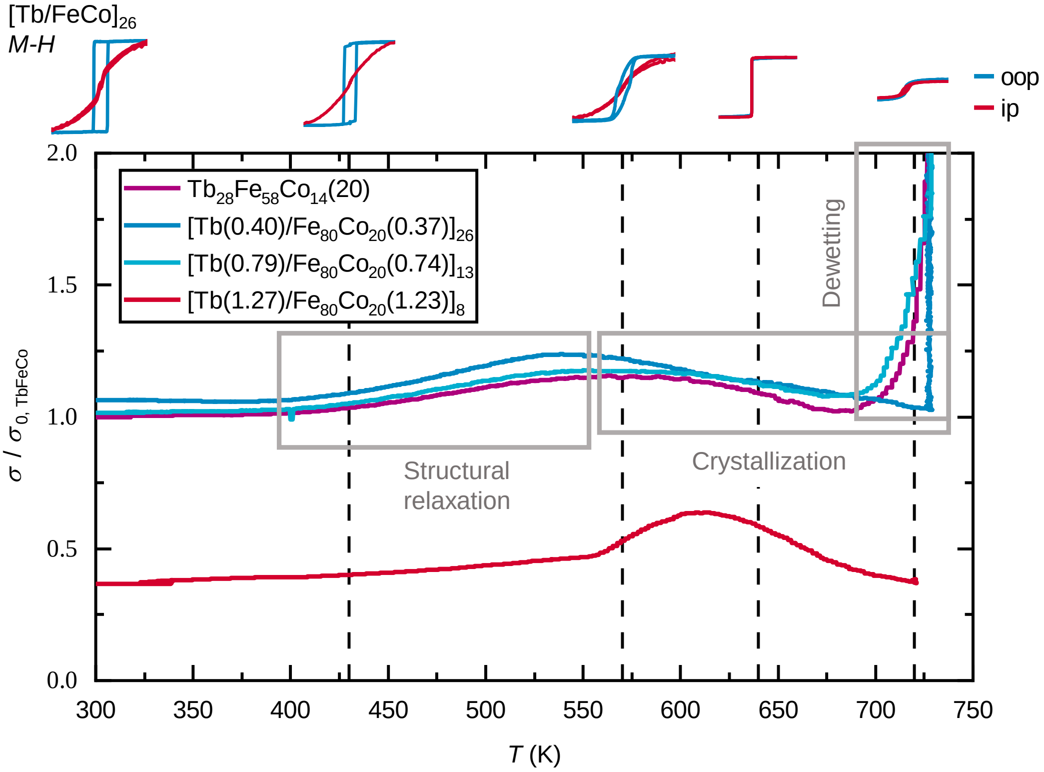

Figure 4.23: Comparison of the sheet resistance curves of Tb-FeCo multilayers and the alloy. The sheet resistance σ divided by the sheet resistance $\sigma_{0,\mathrm{TbFeCo}}$ of the $Tb_{28}(Fe_{20}Co_{80})_{72}$ alloy as a function of annealing temperature T for all four sample types. Exemplary, the *M-H* loops of the $[Tb/FeCo]_{26}$ ML are shown above their annealing temperatures marked by vertical dashed lines. The two MLs with thinner individual layers behave very similar to the alloy showing a bump at around 570 K, a decrease afterward, and a sharp rise above 700 K due to structural relaxation, crystallization, and dewetting. $[Tb/FeCo]_8$ exhibits an overall smaller resistivity and no sharp increase at 700 K. The figure is also published in Ref. [206].

repetition numbers behave very similarly to the alloy, exhibiting a relatively constant resistance up to 420 K. At higher temperatures, all samples show an increase in resistance with a maximum at around 570 K, which is often associated with structural relaxation of the film while still being amorphous [202–205]. This loss in chemical short-range order before crystallization is connected to the decrease of PMA discussed before. The drop of resistivity at temperatures larger than 570 K is associated with the beginning of diffusion and crystallization processes. All samples lose during these processes most of their remaining PMA. At about 700 K a sharp rise in resistivity is observed, which can be explained by the crystallization of additional phases, oxidation, and formation of voids and discontinuities, due to dewetting of the film. The magnetic properties drastically change at this point, revealing, besides a loss in PMA, a reduced magnetization (Fig. 4.22 a).

$[\mathrm{Tb/FeCo}]_8$ exhibits an overall smaller electrical resistivity due to its very FeCo dominated layers with lower electrical resistivities. The structural relaxation seems delayed in comparison to the other films' resistivity curves. This is typical for TbFeCo films with a larger FeCo ratio [203]. The curve is most likely a superposition of the more Tb-rich regions, which might exhibit a structural relaxation at similar temperatures as the other samples and the relaxation of FeCo-rich regions responsible for the larger bump at higher temperatures. Still, $[\mathrm{Tb/FeCo}]_8$ loses all its PMA already at 420 K, also because of the smaller initial PMA (Fig. 4.22 d). Further, the dewetting of the film is not observable in the resistivity curve and shifted to higher temperatures, possibly due to the FeCo-rich regions of the film.

In order to achieve a better understanding of the structure of the MLs and the structural modifications upon annealing, exemplarily, the $[\mathrm{Tb/FeCo}]_8$ ML is investigated by TEM in the as-deposited state and after annealing at 640 K. Figure 4.24 a shows a STEM cross-section image of the $[\mathrm{Tb/FeCo}]_8$ sample with the surface of the sample being on the left side. The two most bright layers on the left and right side represent the roughly 5-nm-thick Pt cover and seed layer. The contrast in-between confirms the underlying Tb/FeCo ML structure. The purple arrow indicates the EDS linescan used to generate the composition map presented in Fig. 4.24 b, and the x-axis of which is aligned to the STEM image in Fig. 4.24 a. Overall, the observed stack thickness of approximately 35 nm is slightly thicker than the intended 30 nm. The sputtered nominal $[\mathrm{Tb(1.27)/Fe_{80}Co_{20}(1.23)}]_8$ film reveals a modulation of the Tb and Fe ratio with a periodicity of 2.7 nm and relatively constant Co composition in the film. This means the periodicity is 0.2 nm larger as intended by the nominal thickness. The modulation of the

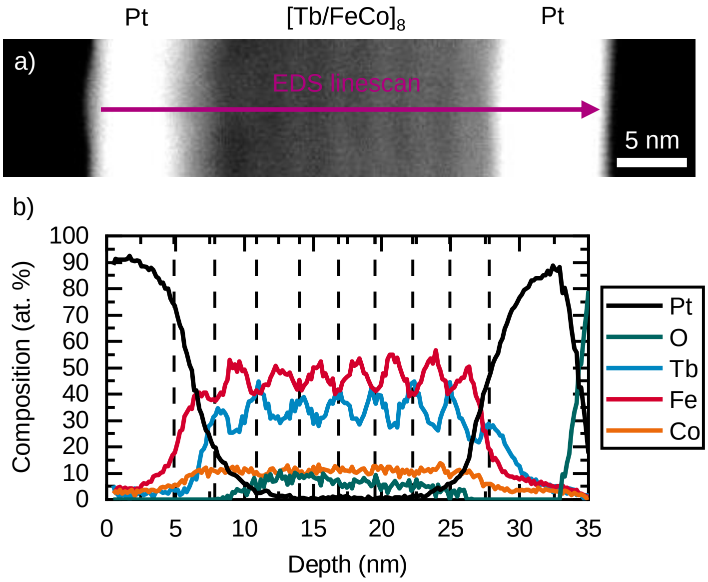

Figure 4.24: STEM study on a Tb/FeCo multilayer in the as-deposited state STEM cross-section image (a) and EDS scan along the line marked in a) (b) of [Tb(1.27)/$Fe_{80}Co_{20}$(1.23)]$_8$ in the as-deposited state confirming the ML structure. The figure is also published in Ref. [206].

Tb and Fe content also supports the previously reported intermixing lengths of around 1 nm in these kinds of films [418, 441]. The ML exhibits no sign of crystalline phases and appears to be amorphous in high-resolution TEM measurements (not shown). The modulation of the Tb and Fe content results in different compositions with $Tb_{48}Fe_{41}Co_{11}$ and $Tb_{26}Fe_{62}Co_{12}$ being the two extremes. This superposition of different compositions leads to an overall reduced Tb moment due to the reduced magnetization observed in Tb-rich alloy layers (Tb>30 at.%) [275, 393] agreeing with the experimental results. Also visible in the diagram is an oxygen contribution in the magnetic film, which probably enters during the preparation of the TEM sample. The sharp rise of oxygen on the right side arises from the SiO_x substrate. Please note that the Si contribution is not displayed.

Figure 4.25 shows a STEM cross-section image (a), an EDS linescan (b), and an additional high-resolution TEM image (c) of the [Tb/FeCo]$_8$ ML after annealing at 640 K. The ML structure of the film has fully vanished (Fig. 4.25 a, b) due to intermixing processes. Surprisingly, a nearly 20-nm-thick layer appears on top of the film. Figure 4.25 b reveals that this new layer is primarily a mixture of Fe-Co-O. Consequently, Fe and Co have diffused through the Pt capping layer during annealing and oxidized. The remaining alloy film in-between the Pt layers becomes Tb-rich, including a considerable amount of oxygen. While an annealing-induced phase

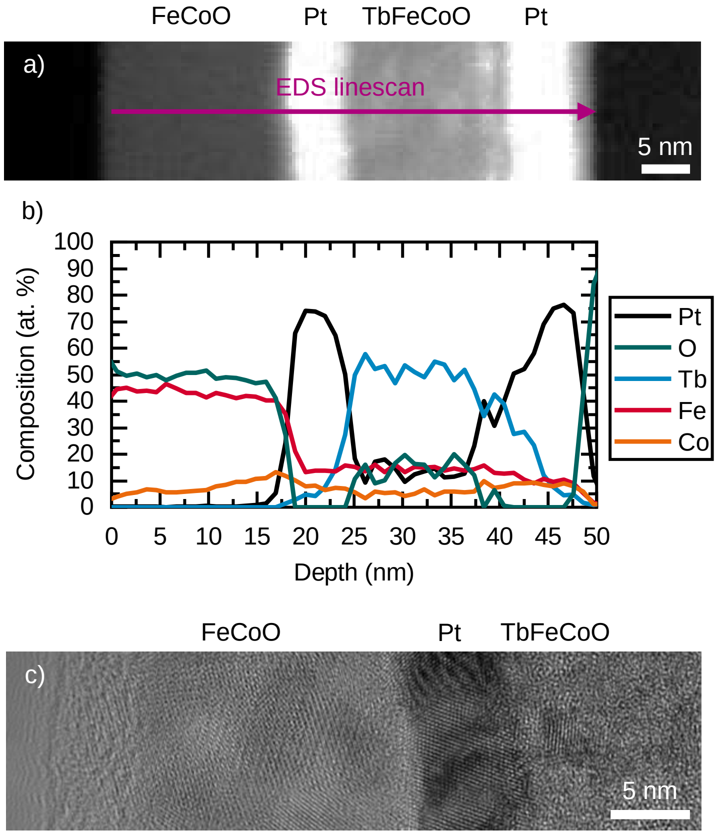

Figure 4.25: STEM and TEM studies of a Tb/FeCo multilayer after annealing at 640 K. STEM cross-section image (a), EDS scan along the line marked in a) (b), and high-resolution TEM image (c) of $[Tb(1.27)/Fe_{80}Co_{20}(1.23)]_8$ after annealing at 640 K revealing nano-crystalline phases in the oxidized FeCo layer. The figure is also published in Ref. [206].

separation has been observed before in these types of films [427, 445], this type of segregation is not expected.

To investigate the crystallinity of the layers, high-resolution TEM measurements are performed, and one of the resulting images of the upper region of the film is displayed in Fig. 4.25 c. Both the Pt and the Fe-Co-O layers show a variety of crystalline grains with different orientations. The lattice plane distance of some of the larger grains in the Fe-Co-O layer of 0.27 nm corresponds most likely to hematite (α-Fe_2O_3(100)-0.273 nm) [446]. This observed layer structure after annealing allows a clearer interpretation of the corresponding magnetic properties. As a result of strong diffusion, an Fe-Co-O layer has formed, which is well separated from the remaining Tb-rich alloy layer. This process results in a full loss in PMA (Fig. 4.22 d). The resulting Fe-Co-O layer is

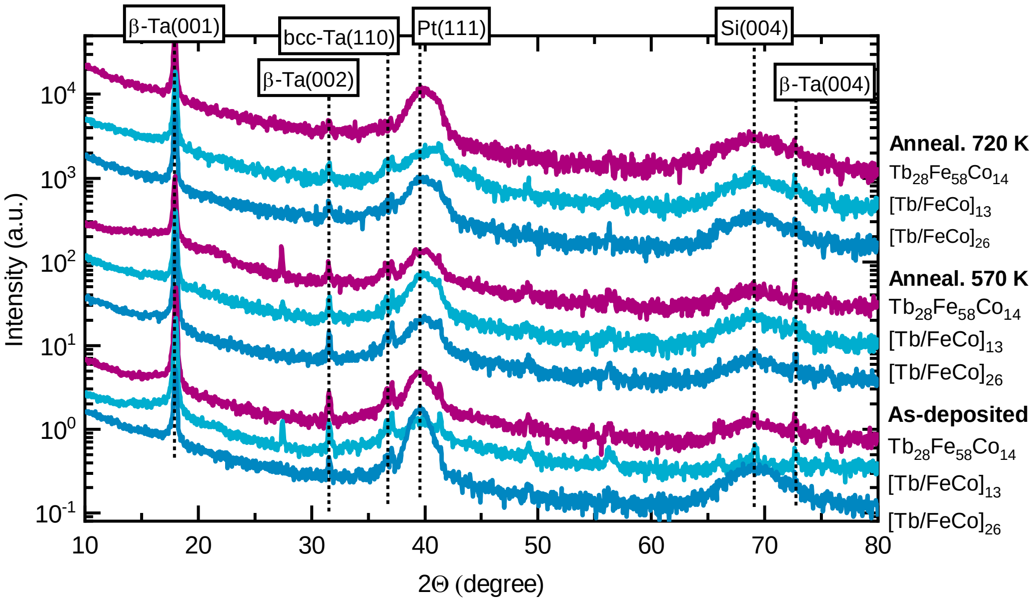

Figure 4.26: XRD scans of the as-deposited and annealed Tb-FeCo samples. XRD ($\Theta - 2\Theta$) scans of $Tb_{28}Fe_{58}Co_{14}$(20), $[Tb(0.40)/Fe_{80}Co_{20}(0.37)]_{26}$, and $[Tb(0.79)/Fe_{80}Co_{20}(0.74)]_{13}$ in the as-deposited state and after annealing at 570 and 720 K. There is no qualitative difference between the patterns of the pristine and the annealed samples. The figure is also published in Ref. [206].

expected to be mostly weakly ferromagnetic or even antiferromagnetic [447], while the ferrimagnetic Tb-rich alloy located in-between the Pt layers exhibits reduced magnetization. Both effects eventually result in a drastic reduction in net magnetization, as observed experimentally (Fig. 4.22 a). Due to the continuous nature of this process, it is possible that a state is obtained after annealing where the FeCo is already greatly separated and decoupled from the Tb but not yet fully oxidized. Additionally, the remaining TbFeCo alloy can still contribute a substantial magnetic moment. This causes a pronounced increase in saturation magnetization, as observed in Fig. 4.22 a at 570 K for the $[Tb/FeCo]_8$ ML and at 640 K for the alloy sample, respectively. Please note that this effect is also expected for the other two samples but was not observed, presumably due to the limited annealing steps.

In Fig. 4.26 XRD ($\Theta - 2\Theta$) patterns of $Tb_{28}Fe_{58}Co_{14}$(20), $[Tb(0.40)/Fe_{80}Co_{20}(0.37)]_{26}$, and $[Tb(0.79)/Fe_{80}Co_{20}(0.74)]_{13}$ in the as-deposited state and after annealing at 570 and 720 K are shown. Except for the peaks of the substrate, capping, and seed layers, no peaks of the film can be observed. This contradicts observations of α-FeCo (110) peaks found at annealing temperatures higher than 650 K in other reported studies [202, 203, 205, 448]. Also due to oxidation, Tb_2O_3 can be formed [203]. It can be concluded that the films are in all states amorphous or nano-crystalline, as confirmed by TEM studies.

4.3.4 Conclusion on the Feasibility of Amorphous Tb-FeCo Systems as Heat-Assisted-Magnetic-Recording Medium

20-nm-thick TbFeCo alloys with different compositions are studied, and a composition with large K_{eff}, a compensation temperature above RT, and a low Curie temperature is found as a potential candidate for ECC HAMR media. It is evident that the annealing of the investigated films above 400 K has irreversible effects on the structural properties. The magnetic characterization also reveals a decrease in PMA and coercivity with increasing annealing temperature. With four-point resistivity measurements, the annealing temperature is linked to the structural changes consisting of structural relaxation (loss in chemical short-range order), crystallization, and dewetting. It is shown that this cannot be tuned or prevented by a change in composition. Therefore, Tb/FeCo MLs are investigated next. $Tb_{28}(Fe_{20}Co_{80})_{72}(20)$, $[Tb(0.40)/Fe_{80}Co_{20}(0.37)]_{26}$, and $[Tb(0.79)/Fe_{80}Co_{20}(0.74)]_{13}$ show rather similar temperature dependent magnetization curves and their magnetically Tb dominant nature is confirmed. The thickest ML $[Tb(1.27)/Fe_{80}Co_{20}(1.23)]_8$ exhibits a very different behavior due to the composition modulation of the ML. It is demonstrated that the annealing stability of TbFeCo alloys can be enhanced by the introduction of an artificial ML structure. The loss in PMA can be delayed from 640 K for the TbFeCo alloy to 720 K for the $[Tb/FeCo]_{13}$ ML. Still, these improvements are not severe enough to argue for amorphous TbFeCo as a feasible HAMR medium because of the structural thermal instability. However, the insights provide a better understanding of the changes in the magnetic properties of Tb-FeCo alloys and MLs upon annealing and sets limits for their thermal stability, which will be important for future high-temperature spintronic devices based on amorphous RE-TM materials.

4.4 Exchange-Coupled Ferri-/Ferromagnetic Bilayers

Although the ferromagnetic Co/Ni/Pt MLs (Sec. 4.2) and the amorphous ferrimagnetic Tb-FeCo layers (Sec. 4.3) prove insufficient as HAMR medium, the concept of engineering exchange-coupled composites is still the most promising approach to meet current challenges in fabricating high energy density permanent magnets [449–451]. Furthermore, the investigation of exchange-coupled composites' reversal mechanism is important for future HAMR applications with more optimized individual layers. Already in 1991, Kneller and Hawig proposed to manufacture magnets with a magnetically hard and soft phase exchange-coupled at a mutual interface [85]. While the high magnetocrystalline anisotropy of the hard phase provides a high coercive field, the coupled soft phase should contribute to the energy density product by a high saturation magnetization. Due to the soft phase, the demagnetization curve shows a completely reversible part, which led to the term exchange-spring magnets.

Furthermore, exchange-coupled systems employing ferrimagnetic RE-3d TM alloys provide high tunability, interfacial exchange interaction, and zero magnetic moment at the compensation temperature T_{comp} [399–403, 436, 452–458], which is highly beneficial for many applications such as spin valves [405–410] and magnetic tunnel junction devices [411]. Below T_{comp}, the magnetic moment of the RE atoms dominates, which leads to an antiparallel alignment of the net magnetic moments of the ferrimagnetic layer when coupled to a ferromagnetic layer (Sec. 2.1.1). As a consequence, a positive horizontal shift of the hysteresis loop of the magnetically softer layer is typically observed after saturation in the positive field direction. In this configuration, a giant exchange bias shift of several Tesla has been reported for various nanoscale FI/FM bilayer systems, which can differ in the reversal behavior of the soft layer exhibiting either fully reversible or irreversible switching [97, 402, 459–462].

The micromagnetic simulations in *Vogler, C., Heigl, M. et al. Phys. Rev. B 102, 011429 (2020)* [258] based on the results in this section showed that a partial domain wall is formed at the FI/FM interface layer during the reversal of the FM. The minor loop becomes fully reversible if this domain wall generates a hard-axis field that overcomes the anisotropy field of the FM. It was further reported that the anisotropy and the bulk exchange of both layers, as well as the exchange coupling strength and the thickness of the FM play an important role in the reversibility of the FM.

This section experimentally explores the exchange interaction of TbFeCo/$[\mathrm{Co/Ni/Pt}]_N$ heterostructures for different measurement temperatures, Tb content, and ML repetition numbers N.

The film deposition is performed according to the already described processes of the individual layers. The heterostructures consist of a 20-nm-thick amorphous ferrimagnetic $\mathrm{Tb}_x(\mathrm{Fe}_{80}\mathrm{Co}_{20})_{100-x}$ layer and a ferromagnetic $[\mathrm{Co}(0.2\,\mathrm{nm})/\mathrm{Ni}(0.4\,\mathrm{nm})/\mathrm{Pt}(0.6\,\mathrm{nm})]_N$ ML on top (Fig. 4.27). In addition, 5-nm-thick Pt seed and cover layers are used. Furthermore, reference samples of the individual layers are prepared.

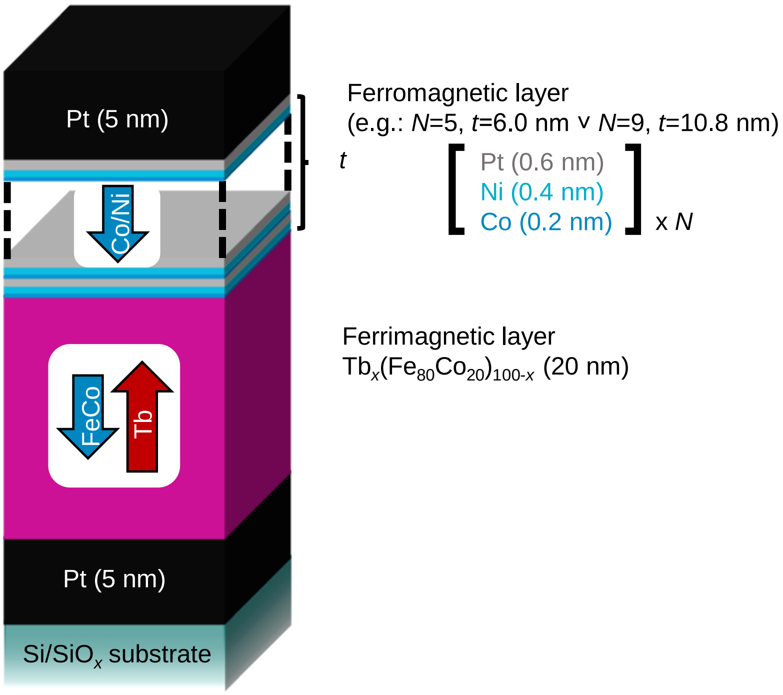

Figure 4.27: Layer stack of the investigated TbFeCo/[Co/Ni/Pt]$_N$ bilayers. The arrows inside the layers represent the parallel coupled moments of the multilayer to the FeCo sublattice inside the ferrimagnet.

The integral magnetic properties of the FI/FM heterostructures are investigated by SQUID-VSM magnetometry. Complementary, the complex reversal behavior is locally imaged by an ultra-high vacuum MFM operating in magnetic fields of up to 7 T at 40 K [463]. Details on the MFM data acquisition and data processing can be found in Ref. [227, 228].

4.4.1 Exchange-Coupled Systems Dependent on Temperature and Ferro-/Ferrimagnet Composition

First, the exemplary switching mechanism of the exchange-coupled $Tb_{28}(Fe_{80}Co_{20})_{72}(20)/[Co(0.2)/Ni(0.4)/Pt(0.6)]_9$ heterostructure is shown in Fig. 4.28. Figure 4.28 a displays the *M-H* loops of the two individual reference layers as well as the coupled heterostructure at 300 K. Both reference samples show strong PMA with coercive fields of about 1.5 T for the ferrimagnetic layer and 100 mT for the Co/Ni/Pt ML. As shown in Fig. 4.16, $Tb_{28}(Fe_{80}Co_{20})_{72}$ is Tb dominant up to 520 K. Thus, the two layers of the heterostructure are coupled antiparallel at zero field (Fig. 4.28 b I, III). Starting from a

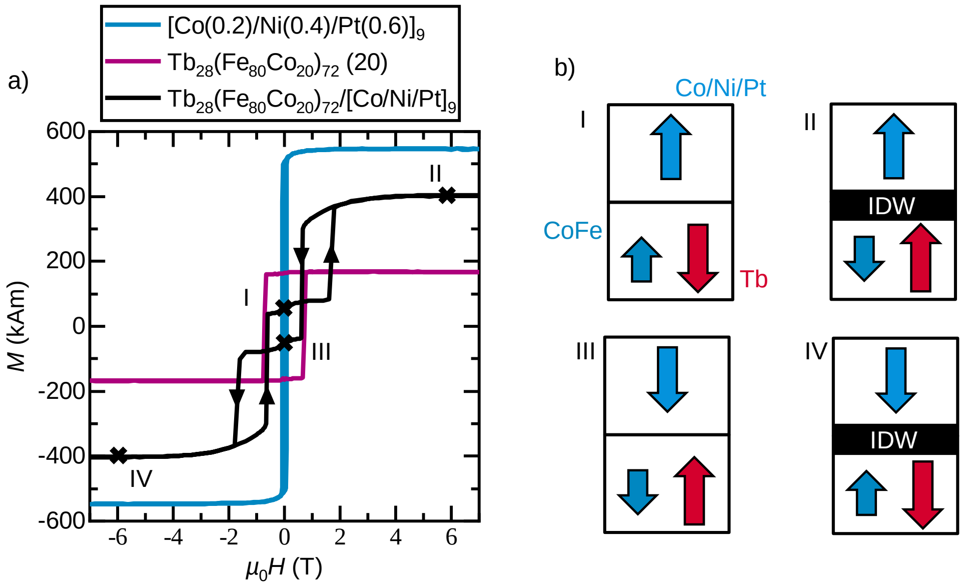

Figure 4.28: Hysteresis loops of the FI/FM bilayer and individual layers with the corresponding schematic magnetic states. Oop hysteresis loop of the FI/FM bilayer obtained at 300 K (a). The individual layers forming the heterostructures are displayed as well. Schematic images of the switching process (b). In the saturated state, the ferro- and ferrimagnetic layers align antiparallel under the formation of an interface domain wall (IDW).

positive magnetization M at zero field (I), by increasing the magnetic field H, the FI layer eventually switches at 2 T, due to the increasing Zeeman energy. An interface domain wall (IDW) is formed between the two layers, and the sample saturates with two magnetic parallel aligned layers (II). The continuous reversible increase of the magnetization at larger fields after the sharp switching can be attributed to the compression of the IDW [85, 94, 97]. For a decreasing external field H, the ferromagnetic layer switches eventually at 1.5 T in its relaxed antiparallel state (III). At a large opposite field of about -2 T, the magnetically hard FI switches again under the formation of an IDW. The switching mechanism of these kinds of FI/FM bilayers has been intensely studied and confirmed for very similar systems such as TbFe/[Co/Pt] [91, 97]. The exact switching of the individual layers has been observed by element-specific XMCD. Details about the microscopic reversal process are described later in Sec. 4.4.3.

Next, the temperature dependence of the heterostructure is explored. Figure 4.29 shows the same two-step switching mechanism for all the three measurement temperatures 40 K (a), 200 K (b), and 300 K (c). While the ferromagnetic layer stays mostly

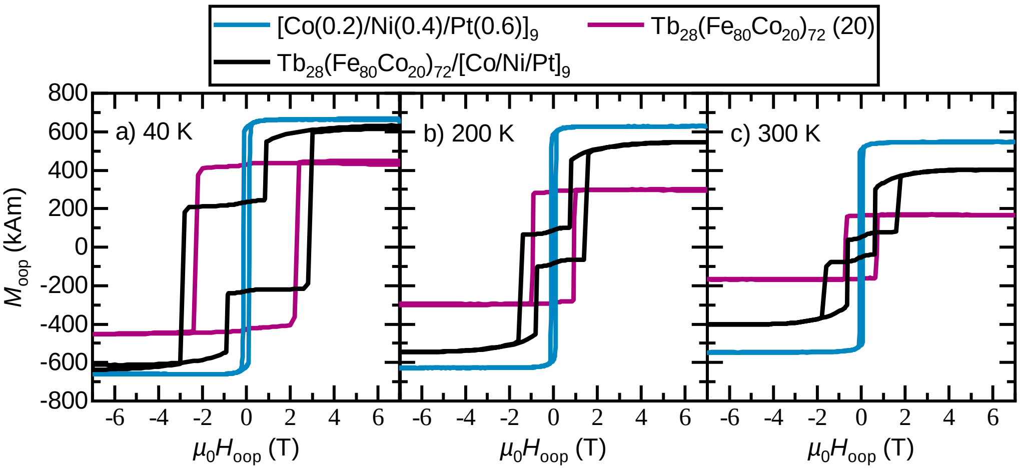

Figure 4.29: Hysteresis loops of the FI/FM bilayer and individual layers dependent on temperature. Oop hysteresis loop of the FI/FM bilayer obtained at 40 K (a), 200 K (b), and 300 K (c). The individual layers forming the heterostructures are displayed as well.

constant in its magnetic properties and only exhibits a slight decrease in M_s and H_c with temperature, the ferrimagnetic layer changes considerably. Both the M_s and H_c values of the FI lose more than half of their value from 40 to 300 K. For the heterostructure, the exchange bias field of the soft FM decreases with temperature. The saturation magnetization of the heterostructure lies within the values of the individual layers. Depending on which remanent moment per area is larger, the magnetization is positive or negative at zero field after positive/negative saturation. At 300 K, the Co/Ni/Pt ML moment is larger and a negative magnetization is measurable after saturation with a positive field (Fig. 4.29 c). At 200 and 40 K, the FI moment is larger (Fig. 4.29 b, a).

Figure 4.30 displays the *M*-*T* measurements of the individual layers and the heterostructure in oop geometry with a guiding field of +10 mT. Both the ferromagnetic and the ferrimagnetic layer magnetization amount decreases with temperature. However, the FI is more temperature-dependent and loses half its remanence between 40 and 340 K. The curve of the heterostructure can be seen as a sum of the individual layers, taking into account the thickness ratios of the two individual layers. The bilayer exhibits a compensation temperature at 270 K, where the moments of the two layers cancel each other out. Below this temperature, the ferrimagnetic alloy has a larger magnetic moment per area (Fig. 4.29 a, b). Above it, the ferromagnetic ML is the magnetically dominant one of the two layers (Fig. 4.29 c).

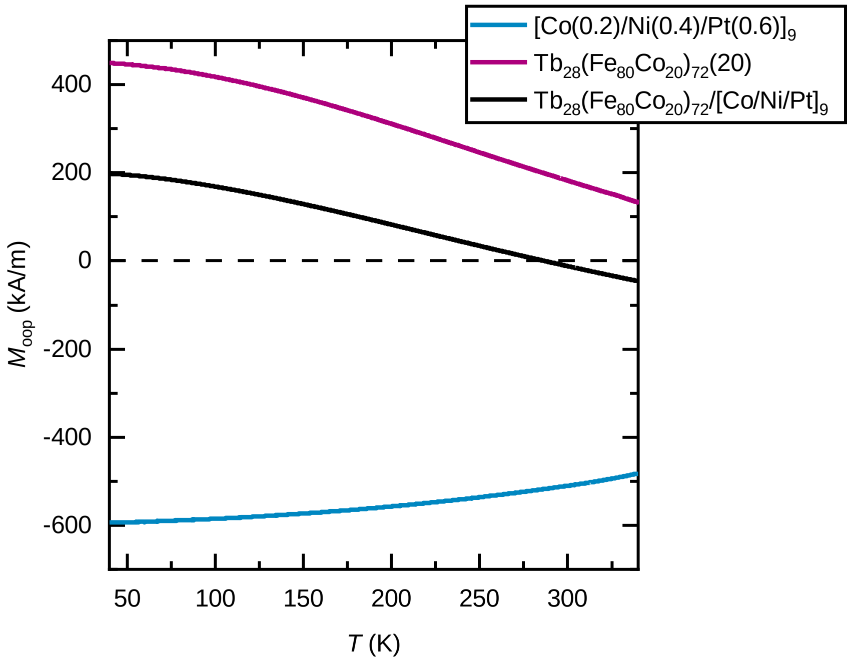

Figure 4.30: Magnetization versus temperature curves of a FI/FM bilayer and the individual reference layers. The magnetization M versus temperature T is recorded with a guiding field of +10 mT in oop geometry. The curve of the heterostructure can be seen as a sum of the individual layers, taking into account the thickness ratios of the two.

Further, the dependency of the exchange-coupling of the FI/FM bilayer is investigated dependent on the Tb content of the ferrimagnetic layer, while the ferromagnetic layer [Co(0.2)/Ni(0.4)/Pt(0.6)]$_9$ is not changed. Figure 4.31 displays oop M-H hysteresis loops of the heterostructures with a Tb content x of 24 at.% (a), 28 at.% (b), and 32 at.% (c) at RT. Additionally, the loops of the underlying individual layers are shown. All displayed FI compositions are Tb dominant at RT (Fig. 4.14). While the effective anisotropy increases with the Tb content, the coupling between the FM and the FI decreases [464]. This leads to a decrease in the exchange field, visible in the loops of the heterostructure. The effect of a stronger coupling for smaller x is also apparent in the shape of the loops. The FM rotates in a more continuous way with decreasing external fields if the coupling in-between the two layers is strong and the energy stored in the IDW is large (Fig. 4.14 a). A more sharp switching process can be observed for the sample with $x = 32$ exhibiting a weaker coupling (Fig. 4.14 c).

It is important to note that a three-stage switching process is also possible for FI/FM heterostructures, which is not shown but can be found, for example, in Ref. [436]. Coming

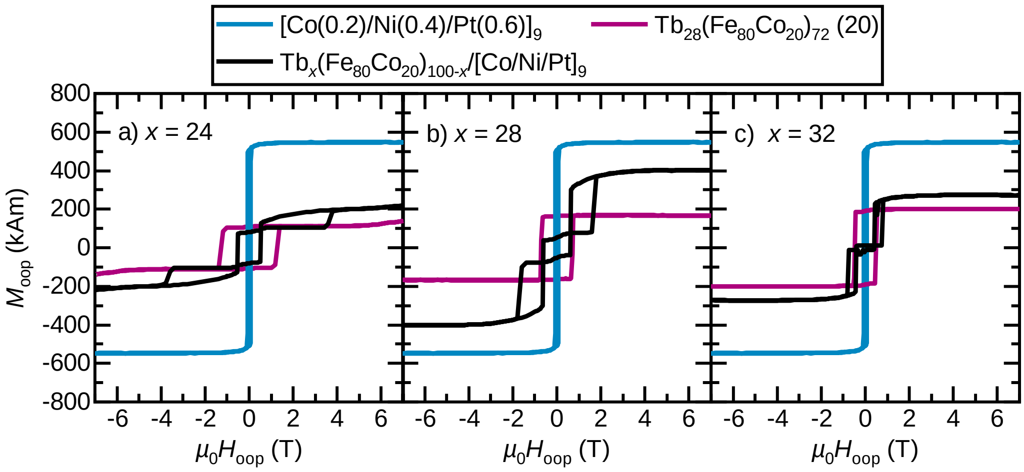

Figure 4.31: Hysteresis loops of the FI/FM bilayer and the individual layers dependent on the FI composition. Oop *M*-*H* hysteresis loops of the heterostructure and the individual layers with $x = 24$ (a), $x = 28$ (b), and $x = 32$ (c) at RT. All ferrimagnetic layers are Tb dominant. The hysteresis loops of the individual layers, which form the heterostructures, are displayed as well.

from saturation, the FI switches here first. If the external field further decreases, the whole system reverses its individual moments. If an increasing field is now applied in the opposite direction, the ferromagnetic layer switches in the new direction of the field, forming an IDW until the system saturates.

4.4.2 Magnetization Reversal Process Dependent on the Thickness of the Ferromagnet

Here, the dependency of the reversal process of the ferromagnetic layer on the thickness of the FM is investigated. Full *M*-*H* hysteresis loops, as well as minor loops of the exchange-coupled FI/FM systems, are shown in Fig. 4.32. Additionally, hysteresis loops of the reference samples consisting only of the FI or the FM are displayed. All measurements are recorded in oop geometry and at 40 K. Before the minor loops are captured, the bilayer is saturated in a +7 T field. Then, the magnetization of the ferromagnetic MLs is plotted as a function of the applied positive field, while the magnetization of the ferrimagnetic TbFeCo layer is saturated and still aligned with the positive field direction. Lowering the field reverses the magnetization of the ferromagnetic layer, which is driven by the strong antiferromagnetic coupling to the FI, as already mentioned. After the field reaches a value of zero, it is increased again. During this process, the magnetization of the so-called minor loop is recorded.

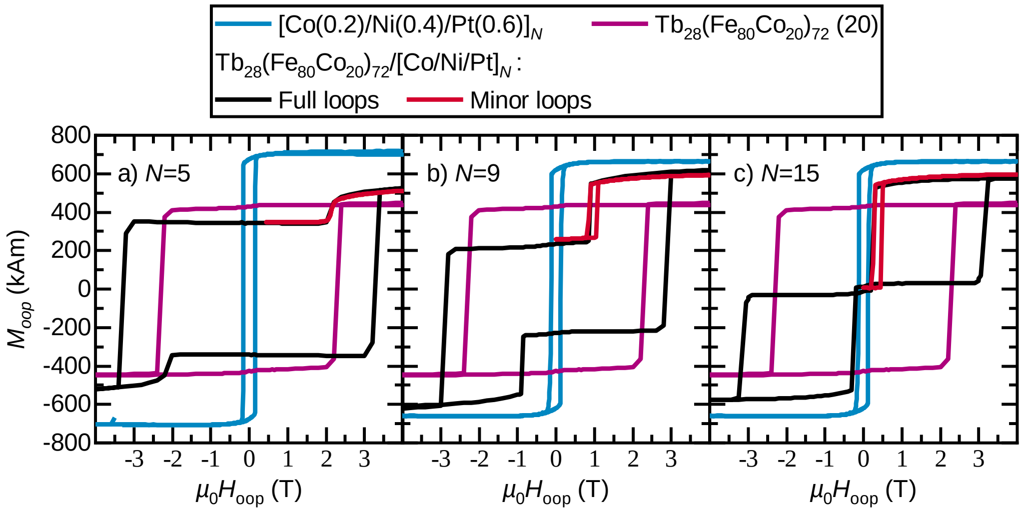

Figure 4.32: Hysteresis loops of the FI/FM bilayer and individual layers dependent on the repetition number of the ferromagnet. Oop hysteresis loops of $N = 5$ (a), $N = 9$ (b), and $N = 15$ (c). The individual layers forming the heterostructures and the minor loops are displayed as well.

All four reference samples show strong PMA with coercive fields of about 3 T and 200 mT for the ferrimagnetic layer and the Co/Ni/Pt MLs, respectively. For the exchanged-coupled FI/FM heterostructures, starting from saturation, by lowering the magnetic field, the ferromagnetic layer reverses due to the strong antiferromagnetic coupling. At a high opposite field of about -3 T, the magnetically hard FI layer eventually switches. It is observed that the field required for reversing the FM becomes larger with decreasing ML repetition number N (thickness), which is expected under the assumption that the interfacial exchange-coupling remains constant [258, 296]. The minor loops are captured to analyze the switching process of the softer FM layer and show two distinct switching mechanisms. While the FI/FM heterostructures with $N = 9$ and $N = 15$ exhibit a hysteretic reversal process (Fig. 4.32 b, c), the thinnest ferromagnetic layer reveals fully reversible and hysteresis free switching (Fig. 4.32 a).

To investigate this phenomenon further, additional heterostructures with a ML repetition number of $N = 3$ and $N = 7$ are fabricated. Figure 4.33 displays all heterostructures with varying repetition numbers N. The right half of the oop M-H hysteresis loops is compared in Fig. 4.33 a. The minor loops of the bilayers are normalized to the magnetization of the system with $N = 15$, and the value of the remanence is set arbitrarily to zero for better clarity in Fig. 4.33 b. The applied field required for the switching process becomes larger with decreasing N, which is expected for bilayers with

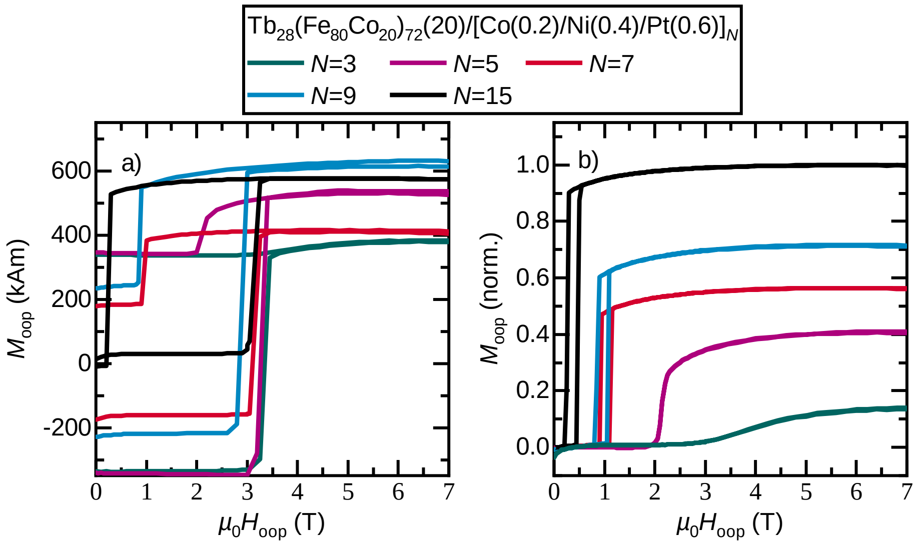

Figure 4.33: Hysteresis loops of the FI/FM bilayer and their minor loops dependent on the repetition number of the ferromagnet. Right half of the oop *M*-*H* hysteresis loops of the FI/FM bilayer dependent on the repetition number of the ferromagnet (a). Minor loops of the bilayers normalized to the magnetization of the system with $N = 15$. The value of the remanence is set arbitrarily to zero for better clarity (b).

a constant FM/FI interfacial exchange-coupling [97]. The critical FM thickness for the transition from hysteresis free to irreversible switching of [Co/Ni/Pt] MLs can now be determined more precisely. The transition happens between 5 and 7 ML repetitions.

These results were used as the experimental confirmation for the analytical model of the reversal process reported in *Vogler, C., Heigl, M. et al. Phys. Rev. B 102, 014429 (2020)* [258].

4.4.3 Microscopic Origin of the Magnetization Reversal Process

In this section, two specific FI/FM samples out of the previous sample series are studied, which exhibit two distinct cases of reversible and irreversible switching. The different underlying microscopic reversal processes are investigated using high-resolution MFM, which was provided by H. J. Hug's group from the EMPA and operated by A.-O. Mandru. Having a detailed understanding of such complex magnetization reversals is crucial for future spintronic and high-energy-density permanent magnet devices. The results of this section are published in *Heigl, M. et al. ACS Appl. Nano. Mater. 3, 9218 (2020)* [100].

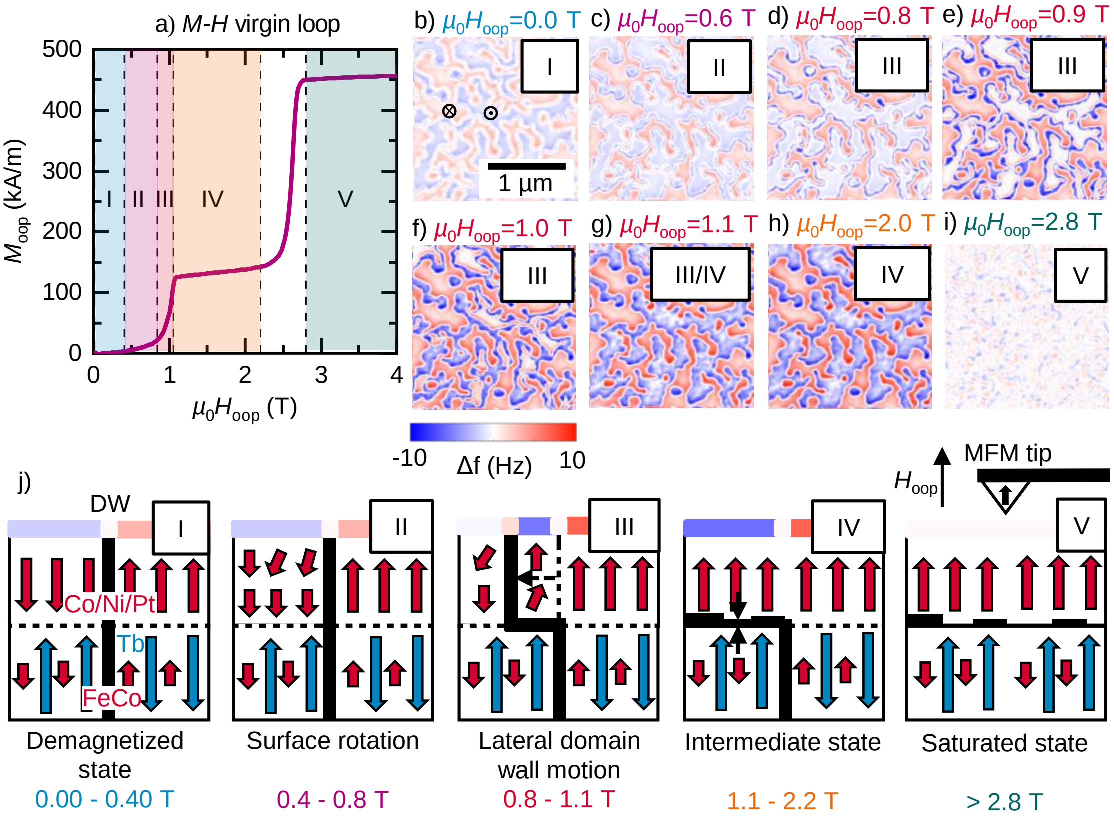

Figure 4.34: Microscopic origin of the irreversible magnetization switching for thick ferromagnetic layers. Virgin M_{oop}-H_{oop} curve of the FI/FM heterostructure with $N = 9$ starting from the demagnetized state (a). Five distinct field ranges are highlighted by different background colors. In b-i) in-field MFM images are displayed. Schematics of the magnetic states typical for the five field ranges are depicted in j).

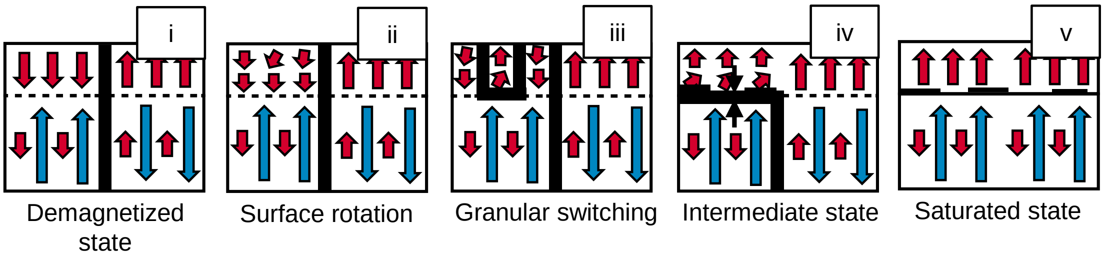

Figure 4.35: Schematic of fully reversible magnetization switching for thin ferromagnetic layers. Fully reversible switching via granular nucleation [228]. Both figures are also published in Ref. [100].

The underlying reversal mechanism for reversible switching was studied before in detail in a $[\mathrm{Co}(0.4)/\mathrm{Pt}(0.7)]_5$ ML exchange-coupled to ferrimagnetic $\mathrm{Tb}_{26.5}\mathrm{Fe}_{73.5}(20)$, which acts as a magnetically hard pinning layer. There, a nucleation-dominated magnetization reversal process was revealed, which is caused by grain-to-grain variations in magnetic anisotropy of the Co/Pt ML and an inhomogeneous exchange coupling to the magnetically harder TbFe layer [228]. Here, the focus is on studying the thicker ferromagnetic layer ($N = 9$) to extract the microscopic mechanisms leading to the transition from a non-hysteretic to hysteretic minor loop magnetization process when increasing the ferromagnet ML repetition number from $N = 5$ to $N = 9$. For this, the sample is demagnetized to acquire the virgin M_{oop}-H_{oop}-dependence at 40 K for fields raised from 0 to 4 T (Fig. 4.34 a). A different piece of the same sample in its as-grown state is used to acquire a series of MFM images at 40 K in fields from 0 to 2.8 T (Fig. 4.34 b-i). The magnetic domain structure in the as-grown state is presented in Fig. 4.34 b. In this state, the net magnetic moment of the ferrimagnetic layer and the magnetic moment of the ferromagnetic layer is aligned antiparallel, which is the ground state of this exchange-coupled FI/FM system. Because the tip magnetization is along the positive field direction (up), the domains appearing with a negative frequency shift contrast (blue domains) have a net up magnetization (parallel to that of the tip), while the red domains have a net down magnetization. The domains are separated by vertical domain walls going through both layers, as schematically displayed in Fig. 4.34 j, I. The magnetization loops acquired for the FI/FM heterostructure sample (black loop in Fig. 4.32 b and virgin loop displayed in Fig. 4.34 a) reveal that the Tb magnetic moment dominates the Co and Fe moments of the ferrimagnetic layer and also those of the ferromagnetic layer. Hence, the blue domains are locations characterized by an up magnetization of the FI and a down magnetization of the FM. When the field is increased to 0.6 T (Fig. 4.34 c) a slight increase in the MFM contrast is observed, which is compatible with a small rotation of the magnetic moments at the top of the FM away from the initial down direction toward the up direction schematically shown in Fig. 4.34 j, II. A more noticeable change becomes apparent at 0.8 T (Fig. 4.34 d): here, some dark blue spots occur at the domain walls, and the overall contrast is further increased. The latter is compatible with an increase in the rotation of the magnetic moments at the top of the ferromagnetic layer. The dark blue spots near the domain walls indicate the beginning of a lateral domain wall motion (Fig. 4.34 j, III) that becomes clearly visible in Figs. 4.34 e and 4.34 f for a field of 0.95 and 1 T, respectively. At about 1.05 T (Fig. 4.34 g), the ferromagnetic layer is almost fully reversed. The remaining MFM contrast then predominantly arises from the domains of the FI. For fields between 1.05 and 2 T, the MFM contrast increases

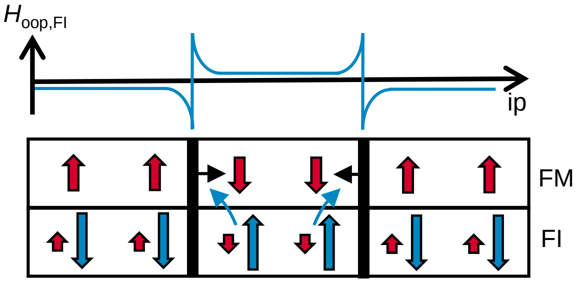

Figure 4.36: Cause of the stop of the domain wall propagation. Schematic showing the additional local field $H_{\mathrm{oop,FI}}$ arising from the ferrimagnetic layer, which ends the lateral domain wall propagation in the ferromagnet (Fig. 4.34 d-g)). The figure is also published in Ref. [100].

only very slightly, which is compatible with a vertical compression of the horizontal domain wall that has formed at the locations of the blue domains at the FI/FM interface (Fig. 4.34 j, IV). Note, however, that no further lateral domain wall motion occurs. This reflects the high coercivity of the FI. The last MFM image (Fig. 4.34 i) shows a state where all down domains in the FM have been reversed and an ip interfacial domain wall has formed (Fig. 4.34 j, V) [97]. The weak granular contrast is caused by variations of the z-component of the magnetic moment density arising for example from spatial film inhomogeneities (e.g., in the TbFeCo composition [69, 465]).

The details of the underlying reversal mechanism of the fully reversible switching case were already reported for a similar TbFe/[Co/Pt]$_5$ heterostructure [228]. There, a nucleation-dominated three-stage magnetization reversal process was revealed, which is caused by grain-to-grain variations in magnetic anisotropy of the Co/Pt ML and an inhomogeneous exchange-coupling to the magnetically hard TbFe layer. The reversal steps are schematically illustrated in Fig. 4.35. They consist of a rotation-dominated part of the ferromagnetic layer starting at the top surface of individual grains (ii) followed by the full reversal (iii) till saturation (iv). The last reversal step is again characterized by a rotation part of the ferrimagnetic domains till saturation (v).

The two reversal mechanisms could also be obtained by finite element simulations, which are shown in Sec. A.3.1. The simulations show the same microscopic origin and are in good agreement with the experimental results. The only difference is that the simulation exhibits no continuous lateral domain wall propagation with increasing fields. Due to limitations of the simulation and to keep the computational effort at an acceptable level, the simulation considers only a small area within an initially down FM magnetization. Thus, the magnetostatic energy arising from the up/down ferromagnetic and down/up ferrimagnetic domain pattern and the existence of an initial vertical domain wall inside the FI and FM is not considered. For this reason, the simulation reveals the switching of a low anisotropy grain followed by a rapid expansion of the reversed domain. In contrast, the MFM data recorded in fields from 0.8 to 1.05 T (Fig. 4.34 d-g) show steady states of the domain wall propagation, which cannot be observed in the simulation. The MFM images reveal that no domain reversal occurs inside the ferromagnetic down domain but that the reversal starts by the propagation of an already existing wall and that the propagating wall again becomes pinned for fields from 0.8 to 1.05 T. This can be explained by the up field arising from the ferrimagnetic up domains, which is strongest in the inside of the ferromagnetic down domain near its wall (Fig. 4.36). This stray field from the FI adds to the applied up external field and thus drives the propagation of the existing wall to a location inside the ferrimagnetic up domain, where the up stray field from the ferrimagnetic domain pattern is weaker. Because the simulation considers a ferromagnetic down domain only, this behavior cannot be modeled. The simulation, however, reveals that once a reversed domain exists, a rapid wall propagation follows. This explains why the field-interval, where a domain wall propagation is observed, remains small, i.e., about 0.2 T, which is compatible with the field on the surface of the ferrimagnetic layer near a domain wall.

4.5 Summary and Implications for Applications

The work of this chapter was initially motivated by the concept of a FI/FM bilayer as ECC media for HAMR (Sec. 4.1.2). Although the concept could have partially solved the magnetic recording quadrillema and improves many aspects of the latest FePt-based HAMR media, Sec. 4.2 and 4.3 describes the prevailing magnetic and structural issues of the proposed system at elevated temperatures.

Pd and Pt insertion layers in Co/Ni MLs were studied and improved the effective anisotropy of the systems (Sec. 4.2). This allowed Co/Ni-based MLs with large PMA, which are less dependent on the repetition number and the substrate. However, the insertion layers also decreased the Curie temperature, which made them less suited for applications in HAMR. Still, Co/Ni/Pd and Co/Ni/Pt MLs present a very intriguing system due to the described properties and large tunability for a variety of applications.

In Sec. 4.3 a magnetically suited TbFeCo composition for the ECC media concept was found for moderate temperatures. At temperatures above 400 K irreversible effects on the structural properties were found, which also influenced the magnetic properties. It was shown that this cannot be prevented by tuning the composition or by an artificial ML structure of the film. However, key insights on the structural and magnetic properties upon annealing were provided.

Even though the individual layers turned out to be unsuited for HAMR, the exchange-coupled bilayer made up of them was further investigated in Sec. 4.4. Other than measurements on the dependency on temperature and the FI composition, the focus was put on the FM thickness dependence. Two distinct magnetic reversal mechanisms were revealed. The reversal characteristics depend critically on the thickness of the ferromagnetic layer. By minor loop *M-H* measurements, an irreversible hysteretic switching process of the bilayer with $N > 6$ and a reversible switching for $N < 6$ was observed. The underlying microscopic origin is revealed by high-resolution MFM. For $N = 9$, the FM switches by ip domain wall propagation. In contrast, thinner ferromagnetic layers exhibit a nucleation-dominated reversal due to grain-to-grain variations in magnetic anisotropy of the Co/Ni/Pt ML and an inhomogeneous exchange-coupling with the magnetically hard TbFeCo layer. The coupled ferromagnetic layers of both systems were modeled by finite-element simulations with individual grains varying in K_u. The simulated macroscopic minor loops agreed very well with the experiments. The simulated MFM contrast of the thicker ferromagnetic layer revealed a dynamic process of the domain wall motion during switching in contrast to the experimentally observed magnetic relaxed states. This difference could be explained by the additional local field arising from the ferrimagnetic layer, which is absent in the model. With this exception, the simulations replicated the two switching mechanisms of both systems. High-resolution MFM, together with micromagnetic modeling, gave detailed insights into which magnetic system parameters are responsible for the complex magnetization reversal process of these exchange-coupled FI/FM bilayers. These insights are crucial for the realization of exchange-coupled high energy density permanent magnets and spintronic devices. The implications are not restricted to antiferromagnetically coupled FI/FM bilayers but are also valid for further exchange-coupled composite media [294, 466].

Chapter 5

Spin Textures in Ferrimagnetic Fe/Gd-Based Multilayers

Over the last decades, magnetic skyrmions have been one of the most actively investigated topics in the field of magnetism. A subgroup of these consists of dipolar-stabilized skyrmions, which are studied in this chapter. The stabilization via dipolar interaction exhibits a degree of freedom for its spin textures, which can enable the coexistence of a variety of different topologically protected spin objects, ranging from Bloch skyrmions with both chiralities to second-order antiskyrmions. Topologically protected spin objects are relevant for several applications, including information storage, unconventional computing, and sensor devices. The shown work in this chapter is part of the *Transregional Collaborative Research Center* (TRR 80): *From Electronic Correlations to Functionality*, funded by the DFG. Many of the shown LTEM images were captured at the CEITEC in the Czech Republic and are the result of a cooperation with M. Urbánek within the *Bavarian-Czech Academic Agency Project* (project no. 8E18B051). They were only possible thanks to the TEM operator M. Vaňatka. Further TEM measurements were conducted with the help of A. Ullrich at the University of Augsburg. The micromagnetic simulations supporting the experimental results in this chapter were carried out by S. Koraltan, R. Kraft, C. Abert, and C. Vogler, which are all part of D. Suess' group from the University of Vienna.

First, some of the numerous potential applications of skyrmions are outlined in Sec. 5.1. Afterward, Bloch skyrmions and topological trivial bubbles are presented, together with their dependency on the magnetic properties in Fe/Gd MLs (Sec. 5.2). These results are compared to previous work on this system. Section 5.3 describes the first observation of dipolar-stabilized first- and second-order antiskyrmions, which were prior exclusive to materials with D_{2d} or S_4 symmetry. These spin objects are stabilized together with Bloch skyrmions and bubbles in Fe/Gd-based MLs. More insights and a recipe for these novel magnetic quasi-particles are given thanks to the micromagnetic simulations from D. Suess' group. Brillouin light scattering (BLS) measurements were carried out by P. Che from D. Grundler's group from the EPFL in Switzerland. They were used to rule out DMI as the stabilization mechanism for the observed magnetic objects. To gain exact magnetic anisotropy values for the simulations, ferromagnetic resonance (FMR) measurements were carried out by A. Semisalaova from M. Farle's group from the University of Duisburg-Essen. The Master students T. Schmidt and J. Hintermayr helped with the evaluation of the data. This far-reaching cooperation led to the presented results in this section and the publication *Heigl, M. et al. Nat. Commun. 12, 2611 (2021)* [426]. In Sec. 5.4 an overview and comparison of different imaging techniques for the observed magnetic spin textures are given. The different appearances and deviations of techniques, including MFM, direct LTEM contrast, induction maps by LTEM, and DPC, are presented. This comparison was partially also described in the Master thesis of T. Schmidt. The high-resolution MFM images stem from Y. Feng of H. J. Hug's group from the EMPA in Switzerland. The results of the Master thesis of M. Seidler are summarized in Sec. 5.5. Here, the influence of ip magnetic fields and the substrate morphology on the magnetic textures is described. Post-deposition anisotropy engineering is used in Sec. 5.6 to imprint certain patterns of skyrmions. The work on ion radiation assisted by self-assembled nanospheres was carried out in close collaboration with M. Krupiński. Additionally, focused ion beam (FIB) was used to create an artificial domain pattern. The irradiation and TEM imaging of this section was carried out by J. Gaida of C. Ropers' group from the University of Göttingen. At last, a resume and outlook are given over the implications of the presented results in terms of future research and potential applications.

5.1 Challenges and Prospects of Skyrmion-Based Devices

For the longest time, magnetic objects have been used as information bits in tape storage or HDDs, accompanied by an ever-continuing drive for smaller stable spin textures. Hence, nanometric-sized structures that have an additional cause of stability are of immense interest for future data storage devices. Topologically protected skyrmions present such a structure, and their enormous potential created the field of *Skyrmion-Electronics* [173]. In this section, some skyrmionic devices are highlighted, particularly regarding the use of different coexisting skyrmion types. Other publications that review the potential of skyrmion-electronics and present multiple different application concepts are Ref. [173, 467–469].

5.1.1 The Racetrack Memory Concept

The concept of a domain wall (DW) racetrack memory was first proposed by S. S. P. Parkin in 2008 [470]. Here, similar to the HDDs discussed in Sec. 4.1.1, information is stored in DWs. However, to circumvent the use of moving parts and improve performance, the magnetic domains and their walls are moved while the read and write head is fixed. This is made possible by the use of short pulses of spin-polarized currents, which drive the DWs through a magnetic nanowire. A potential racetrack memory device is made up of many stacks of these quasi-one-dimensional nanowires, which enables drastically increased bit densities by the expansion in the third dimension. Unfortunately, this concept only showed limited practicality due to the flexibility of the DWs. They expand under torques provided by the applied currents and exhibit uncontrollable pinning at defects [471]. These limitations have been partially overcome by the use of DMI and STT in materials with strong PMA [472, 473], but could not be completely solved to compete with state-of-the-art data storage technologies [474].

Therefore, soon after their discovery in 2008, skyrmions were proposed as information carriers for the racetrack memory [475]. Their topological protection leads to a certain confined size and increased stability, which also helps to circumvent pinning to a certain extent [476]. However, skyrmions come with their own set of challenges, which still prevent an experimental demonstration of a fully functional electrically operating skyrmion racetrack memory device (Fig. 5.1). The topological properties also introduce the SkHE (Sec. 2.4.3). When skyrmions are driven by an applied current, they get deflected due to this effect. This reduces possible maximum propagation speeds or even leads to the erasure of skyrmions at the edge of the racetrack [477]. Many different approaches have been tested to circumvent this effect: B. Göbel et al. showed that an additional induced spin current by the spin Hall effect can suppress the SkHE [176]; the two sub-lattices in FIs [174] and AFs [175] (partially) cancel each others SkHE out; different skyrmion and spin object types show different or no SkHE at all (Sec. 2.4.3) [167]; and skyrmion-pairs cancel each others SkHE out in an antiferromagnetically exchange-coupled bilayer [177].

Furthermore, for writing and deleting skyrmions, many different options have been found over the years, ranging from magnetic fields and temperature stimuli [479–481] to electric currents [482–484], electric fields [485, 486], strain and heat induced by a

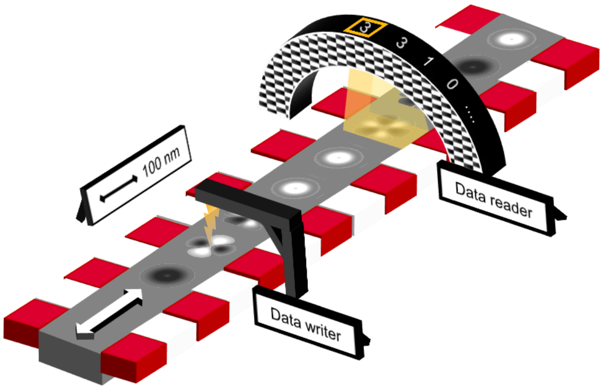

Figure 5.1: Illustration of a skyrmionic race track memory. Skyrmions are displayed as their LTEM contrast to improve the clarity of the illustration. The figure is also published in Ref. [478].

Surface Acoustic Wave (SAW) [487, 488], and optical excitation [145, 489]. There are also multiple options for a possible read operation, for example topological Hall resistivity measurements [490], MTJ setups [491, 492], or optical methods [493, 494]. An overview over all these methods can be found in Ref. [173].

Moreover, in the original skyrmion racetrack memory concept, information is stored by the distance between skyrmions. Due to defects and thermal fluctuation, there is a significant source of error, making it challenging to use [495]. To overcome this issue, binary information given by two different topologically protected spin objects was proposed [496–498].

The presented system in this chapter exhibits multiple coexisting topologically protected spin objects (Sec. 5.3). Therefore, it has the potential to store information as binary, ternary, or even quaternary information (counterclockwise Bloch skyrmion, clockwise Bloch skyrmion, first-order antiskyrmion, second-order antiskyrmion). While this multitude of different coexisting topologically protected spin objects increases the potential storage density, the presented system also has drawbacks for the potential application. Dipolar-stabilized skyrmions are usually around an order of magnitude larger (>100 nm) than DMI-stabilized ones (10-100 nm) [129]. Consequently, the storage density would be smaller for a system utilizing dipolar skyrmions instead of DMI skyrmions. Another problem is the relatively large thickness of the presented magnetic films. Thicker films mean more potential pinning sights, inhomogeneities, and larger necessary currents to drive the objects.

To summarize, the investigated systems in this chapter are great to study the different spin objects and to gain essential insights for future applications. However, ultimately other material systems with smaller coexisting spin objects have to be found for a potential commercially used racetrack memory device.

5.1.2 Skyrmions for Unconventional Computing

The physics of magnetic skyrmions can not only be exploited for the concept of the racetrack memory but also endow skyrmions with a huge potential as the smallest information carriers for unconventional computing. Over the last years, different concepts of skyrmion-based unconventional computing solutions have seen the light of day and could eventually surpass the racetrack memory concept as the primary motivation for the magnetic skyrmion research [7]. This trend has been driven by the gradually failing of the classic Von-Neumann computer architecture not meeting the demands of modern computing challenges. This architecture, used by most computers today, is fundamentally bottlenecked by the so-called *Memory Wall*. Due to the physical separation of the processing and memory unit (Fig. 5.2 a), the bandwidth between these two constraints the possible performance [6].

Further, the ever-growing interest in machine learning algorithms and artificial neural networks (ANNs) calls for computer architectures specifically designed for this purpose alone. One example of this is neuromorphic computing. It promises better power efficiency and faster operation speeds for neural network algorithms due to increased parallelization [499]. While the classic Von-Neumann computer architecture works mostly sequential with a relatively small number of large memory and complex processing units (Fig. 5.2 a), the brain-inspired neuromorphic design consists of a large number of highly interconnected simple computing (artificial neurons) and memory (artificial synapses) elements (Fig. 5.2 b) [500]. The neuromorphic architecture is designed to be as similar as possible to a to-compute ANN for optimal performance and energy efficiency. General for ANNs, each synapse transmits a signal from one neuron to another and has a *Weight* devoted to it. The weight represents the strength or importance of that connection and adjusts during the training process of the neural network. This training or learning process is usually done by feeding the network with data and its labels, similar to the data sets which should be analyzed in the future. The displayed network in Fig. 5.2 b consists of three neural layers: the input (top), output (bottom), and hidden (middle) layer. Depending on the complexity of the network, a multitude

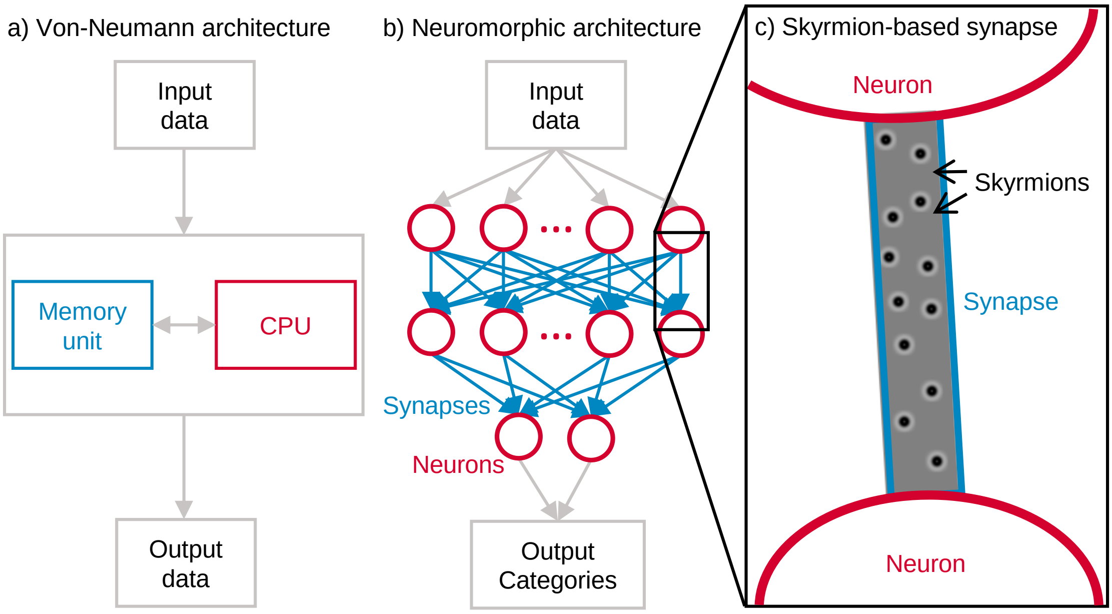

Figure 5.2: Illustration of different computer architectures and an artificial skyrmion-based synapse. a) Very simplified illustration of the classic Von-Neumann computer architecture. Algorithms are executed sequentially. b) Neuromorphic architecture with one input and one output neuron (computing element) layer at the top and bottom, respectively, and one hidden neuron layer in the middle. The neurons are connected by synapses (memory elements). c) Skyrmion-based artificial synapse. The number of skyrmions defines the resistivity and, with it, the weight of the connection. Skyrmions are displayed as their LTEM contrast to improve the clarity of the illustration.

of hidden neuron layers with different sizes are possible, as well as the possibility of traversing the layers multiple times.

Recently, magnetic skyrmions have been proposed as artificial synapse for neuromorphic computers [501–506]. Here, the number of skyrmions and the resulting Hall resistivity is used as the synaptic weights. Proof of concept devices have been presented that showed the electrical creation, detection, and deletion of skyrmions in a single device emulating the functions of an artificial synapse [504, 505]. A simulated skyrmion-based ANN device has been shown to reach a learning accuracy of $\sim 89\%$ for a supervised pattern recognition task [504]. The key advantages of skyrmion-based synaptic devices over the more established technologies, for example, resistive random-access memory (RRAM) [507], are the good linear weight distribution, longer endurance and retention, and less interference of the read and write operations. Although current RT skyrmions and consequently the devices using them are relatively large, skyrmion-based artificial synapses show huge potential.

Furthermore, skyrmionic neuron devices have been demonstrated. A neuron accumulates signals from all connected synapses and emits a pulse if a certain signal threshold is met [508]. This behavior was replicated by skyrmion dynamics on nanotracks [501, 509] and led to the first all-spin design proposed in Ref. [510] consisting of both skyrmionic neurons and synapses.

Beyond skyrmions in neuron-like computing devices, simple logic operations [511, 512] and transistor-like devices [513] have been demonstrated using skyrmions.

Alternatively to neuromorphic computing, reservoir and stochastic computing have to be mentioned as other unconventional computer architectures, which could potentially use skyrmions. In a reservoir computer, a medium with certain non-linear random properties, called reservoir, acts as a converter of an input signal into higher dimensional computational spaces [514]. The benefit of this architecture is the missing necessity of a training stage. The reservoir is not permanently changed in this approach, and only the read-out of the reservoir needs to be mapped to the desired output. Skyrmions and especially mixed states of coexisting spin objects and magnetic stripes are a good fit as reservoir media due to their complex interactions and internal degrees of freedom [515, 516].

Stochastic computing utilizes continuous streams of random bits for computations using probability instead of arithmetic [517]. Skyrmionic stochastic computing devices apply the thermally induced random motion of skyrmions to circumvent the prominent problem of correlated bit streams in stochastic computing [518, 519]. In current circuits, complex and hardware hungry operations are needed to reshuffle the signals of the bit streams in a pseudo-random way [520].

Skyrmionic Interconnections

One main concern that all the mentioned computer architectures share is the transferring of data among its integrated components. It was already mentioned that it is one of the bottlenecks of the Von-Neumann architecture [521] and also represents a challenge in the highly interconnected neuromorphic architectures [522]. R. Chen et al. [523] explored the concept of all-magnetic skyrmionic interconnects and illustrated this missing element of skyrmionic electronics. Here, the information is transferred similar to the racetrack memory via patterns of moving spin objects. In contrast to the racetrack memory

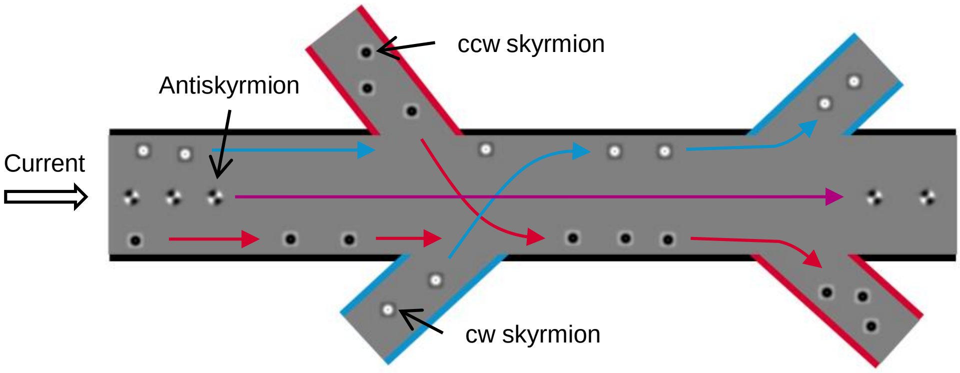

Figure 5.3: Illustration of a skyrmionic interconnection. Demonstration of topological multiplexing for three types of information carriers: counterclockwise (ccw) skyrmions, antiskyrmions, and clockwise (cw) skyrmions. All types of skyrmions are displayed as their LTEM contrast to improve the clarity of the illustration. Due to the skyrmion Hall effect, the different type of spin objects inherently chose the right path and output. The concept and illustration is inspired by Ref. [523].

concept, the SkHE of the spin objects is welcomed and used to achieve multiple parallel propagating spin object lanes. Depending on the type of spin objects, the SkHE inherently drives the object to one side of the nanotrack under an applied current (Fig. 5.3). These multiple lanes for different spin object types represent the topological multiplexing of signals. It conceptually resembles the wavelength and wave pipelining multiplexing in photonics [524] and silicon-based [525] interconnects.

In contrast to Ref. [523], Fig. 5.3 uses spin objects observed in this work. While all the previously mentioned concepts in this subsection do not necessarily benefit from different coexisting spin objects and are more concerned with the size of the used skyrmions, the multiplexing in skyrmion interconnects is not possible without coexisting spin objects with different topological charges. It has been shown that the so-called spin Hall angle of the SkHE in which a spin object is moving relative to an applied current is dependent on the helicity of the object [171]. Hence, counterclockwise (ccw) and clockwise (cw) Bloch skyrmions are driven to opposite sides of the nanotrack in Fig. 5.3. Interestingly, the helicity of antiskyrmions depends on their orientation. Consequently, their spin Hall angle varies with different orientations between the antiskyrmion and the applied current [172]. Under the assumption that the antiskyrmions do not rotate while being driven with a current, they can be moved without being deflected to the opposite sides of the nanotrack. Alternatively, skyrmioniums have been proposed as spin objects with zero total topological charge [154, 523]. The SkHE is also exploited to filter and output the different signals, as shown in Fig. 5.3.

5.1.3 Sensors Based on Skyrmions

Magnetic field sensors are essential for a variety of modern devices, ranging from the magnetic read heads needed for the data storage solutions discussed in Sec. 4.1.1 and 5.1.1 to acceleration sensors in cars and mobile phones [526]. Depending on the requirements of the magnetic sensor, different technologies are currently used. For example, Hall sensors do not necessarily exhibit a field range limit but show a relatively small sensitivity in comparison to XMR (magnetoresistance) sensors, including giant magnetoresistance (GMR), tunnel magnetoresistance (TMR), and anisotropic magnetoresistance (AMR) sensors [527]. To achieve a measurable XMR effect, magnetically soft thin films are used as free layers. Usually, their sensitivity is limited to ip magnetic fields of certain smaller field ranges [528]. Recently, magnetic vortices were proposed for magnetic field sensors with larger field ranges than classic XMR sensors [529]. To increase the measurable field ranges even further without sacrificing sensitivity, different PMA sensor concepts have been investigated for the last decades. Here, the TMR or GMR effects are also used, but with the hard-axis of the soft free layer acting as the sensing axis. Therefore, the sensor requires larger magnetic fields to be saturated [530, 531]. In this case, a pinning and pinned layer with PMA are needed. Synthetic AFs consisting of Co/Pt MLs have been proposed for this purpose [532].

Similar to vortex-based sensors, the topologically protected skyrmions can also be used for magnetoresistance sensors. In contrast to vortex-based or common XMR sensors, the proposed skyrmion-based sensor is sensitive to magnetic fields perpendicular to the sensing plane. One advantage of skyrmions is the absence of domain wall pinning, which decreases possible noise. It was already shown for vortices that their topologically protected textures lead to a significant reduction of signal noise [529]. Further, in comparison to vortex sensors, no elaborate nano-fabrication of magnetic discs is needed. However, nano-fabrication could be used to enlarge the window of stable skyrmions and, with it, the available measurable field range. The aspect of nano-fabrication on skyrmion-hosting layers is further explored in Sec. 5.6.1.

To realize such a skyrmion-based magnetic sensor, the oop components of the skyrmions are read out by a magnetoresistance stack. An example of such a stack is displayed in Fig. 5.4. Here, the skyrmion layer acts as the free layer, and a pinning and pinned layer with PMA, similar to other PMA sensors, is additionally needed. If an oop magnetic field is applied, the parallel aligned skyrmion centers grow, and the GMR increases. Skyrmion-based TMR sensors could also be realized accordingly. It is notable that the investigated dipolar-stabilized skyrmions of this work exhibit significant

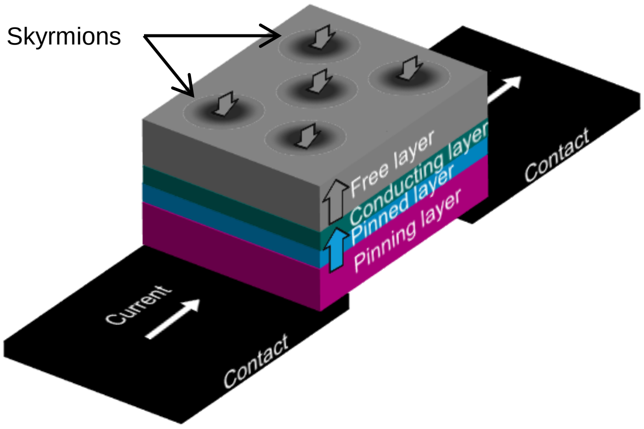

Figure 5.4: Illustration of a skyrmion-based GMR sensor concept. Skyrmions are displayed as their LTEM contrast to improve the clarity of the illustration. Thick arrows indicate the direction of the magnetic moments.

changes in size depending on the applied oop magnetic field [128]. This property makes them especially interesting for the proposed sensor in comparison to DMI skyrmions with relative finite sizes [533], which is also reflected in their possible length and linearity of the transfer curve. While skyrmions stabilized by DMI exhibit a small sensitivity to applied ip magnetic fields, the spin texture of dipolar skyrmions is significantly affected by them, which is investigated in Sec. 5.5. Here, the areas of ip magnetic components parallel to the applied field grow with the topological properties still being intact. Their behavior is very comparable to vortex-based sensors and could while being problematic for pure PMA sensors, also enable three-dimensional skyrmion-based magnetic sensors.

Furthermore, skyrmions have also been proposed for sensing low-current and low-voltage signals [534]. Here, the movement of a skyrmion on a nanotrack caused by a low current is read out by a MTJ. Thus, expensive voltage converters can potentially be avoided.

5.2 Skyrmion-Hosting Fe/Gd Multilayers

Many concepts to stabilize skyrmions exist, while the use of DMI being the most common [32–36, 124, 127]. An alternative approach is the use of the competition between long-range dipolar interaction, ferromagnetic exchange, and magnetic anisotropy. In this case, materials can not only host topological trivial bubbles (called type-2 bubbles)

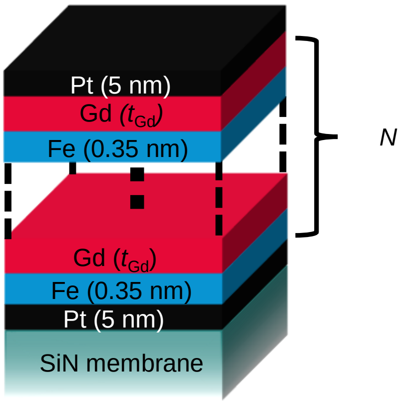

Figure 5.5: Schematic layer stack of Fe/Gd multilayers. Schematic image illustrating the layer stack of the Fe/Gd multilayers with different Gd thickness t_{Gd} and bilayer repetition numbers N.

but also topologically protected chiral magnetic bubbles (type-1), resembling magnetic Bloch skyrmions [128, 144–148]. These chiral bubbles or dipolar-stabilized skyrmions were intensively investigated in Fe/Gd multilayers by Montoya et al. [128, 149, 150]. In order to simplify the distinction in this chapter, type-1 bubbles are called *Skyrmions* and type-2 bubbles *Bubbles*.

In this section, the highly tunable system of amorphous ferrimagnetic Fe/Gd MLs is further investigated at different temperatures and magnetic fields. Spin textures are imaged by LTEM and the stability ranges of skyrmions, and bubbles are connected to the magnetic properties of the system. This lays the groundwork for further modifications of the ML in the following sections.

5.2.1 Method Details on the Deposition and Characterization of Fe/Gd Multilayers

The ML samples are prepared at room temperature by DC magnetron sputtering from elemental targets on 30-nm-thick SiN membranes for LTEM imaging and Si(001) substrates with a 100-nm-thick thermally oxidized SiO_x layer for magnetic characterization. The sputtering process is carried out using an Ar working pressure of 5×10^{-3} mbar in an ultra-high vacuum chamber (base pressure $< 10^{-8}$ mbar). A series of $[\mathrm{Fe}(0.35)/\mathrm{Gd}(\mathrm{t}_{\mathrm{Gd}})]_{80}$ (all thicknesses in nm) is prepared with the Gd thickness t_{Gd} ranging from 0.35 nm to 0.50 nm. A schematic illustration of the layer stack is given in Fig. 5.5. The layer stack is chosen accordingly to Montoya et al. who reported the existence of a skyrmion phase for $[\mathrm{Fe}(0.34)/\mathrm{Gd}(0.40)]_{80}$ at RT [128]. For all samples, 5-nm-thick Pt seed and cover layers are used to protect the films from corrosion. The thicknesses of the layers are estimated from the areal densities measured by a quartz balance before deposition. It is important to note that the deposition of layers in the sub-0.1-nm range is not precisely possible with this technique. Reproducibility can only be accomplished within one sputter run. It has been previously reported that the structure of these kinds of MLs exhibit strong intermixing [128].

The MLs are investigated by a variety of techniques at temperatures between 50 and 350 K. The integral magnetic properties of the MLs are probed by SQUID-VSM. *M*-*H* hysteresis loops are measured in oop and ip configuration for all samples at 50, 100, 150, 200, 250, 300, and 350 K. The M_s and H_a values are extracted. The magnetic domain morphology is imaged by LTEM using a FEI Titan and a JEOL NEOARM-200F system with a defocus of -2.5 mm in Fresnel mode. The temperature is controlled by the Gatan Double Tilt Liquid Nitrogen Cooling Holder Model 636 for the low-temperature measurements. The theoretical contrast of the spin textures is simulated by the Python program described in Sec. 3.3.3.

5.2.2 Magnetic Properties of Fe/Gd Multilayers

All measured *M*-*H* hysteresis loops of the $[\mathrm{Fe}(0.35)/\mathrm{Gd}(\mathrm{t_{Gd}})]_{80}$ MLs in oop and ip geometry for temperatures between 50 and 350 K are displayed in Fig. 5.6. Due to the decrease in saturation magnetization M_s with temperature T, it can be concluded that all Fe/Gd-based MLs are Gd dominant over all measured temperatures. This is also evident by the increase in magnetization M with thicker Gd layers. All films exhibit an increase of their ip anisotropy field H_a with increasing T. Thus, the effective anisotropy is also increasing with increasing temperatures T. This can be explained by the decreasing M_s and the therefore decreasing shape anisotropy $K_\mathrm{shape} = \mu_0/2M_\mathrm{s}^2$ (Sec. 2.1.4). The irreversible formation processes of cylindrical spin objects are indicated by the presence of an opening in the oop loop close to saturation [535]. This signature can be found in Fig. 5.6 a ($t_\mathrm{Gd} = 0.35$) at 150-250 K, in Fig. 5.6 c ($t_\mathrm{Gd} = 0.40$) at 300-350 K, in Fig. 5.6 e ($t_\mathrm{Gd} = 0.45$) at 350 K.

Figure 5.7 shows the dependence of M_s (a) and H_a (b) on T. The values are extracted from the shown *M*-*H* hysteresis loops in Fig. 5.6 and the error bars mainly account for uncorrected geometry effects of the samples during SQUID measurements (around ±10%). In Fig. 5.7 a a linear decrease in M_s with T is observed. Linear extrapolation determines expected compensation temperatures between 450 and 600 K for all four

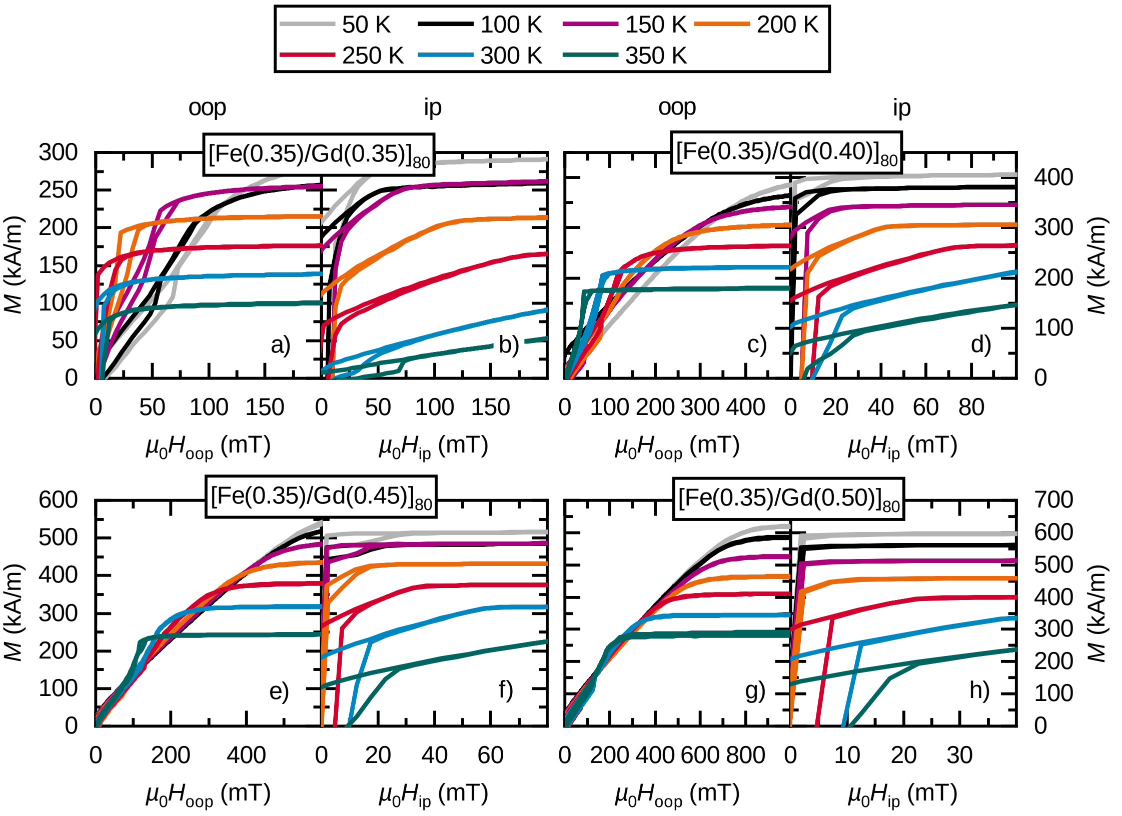

Figure 5.6: Hysteresis loops of Fe/Gd multilayers with different Gd layer thicknesses. *M*-*H* hysteresis loops of [Fe(0.35)/Gd(t_{Gd})]$_{80}$ MLs in oop and ip geometry at 50, 100, 150, 200, 250, 300, and 350 K. t_{Gd} = 0.35 nm (a, b), 0.40 nm (c, d), 0.45 nm (e, f), 0.50 nm (g, h).

samples. However, it has to be noted that irreversible structural changes, like the loss of the short-range order [536], as well as the onset of the Curie temperature [60] happen at lower temperatures or in this temperature region for Fe/Gd MLs. The sensitivity of RE TM alloys and MLs to temperature and the irreversible repercussion of their magnetic properties are conveyed for Tb-FeCo in Sec. 4.3. The difference in Gd thicknesses of the samples is evident by the offset between the four linear fits.

It is important to note that for the presented samples, it is not recommended to calculate magnetic anisotropy values from the *M*-*H* hysteresis loops. Their switching process is dominated by the exchange and dipolar energies due to their multidomain and stripe domain states, which is evident by the mostly small remanences in Fig. 5.6. Another technique to determine the magnetic anisotropies of a system is FMR. It is utilized in Sec. 5.3 but is skipped here in favor of the less laborious qualitatively

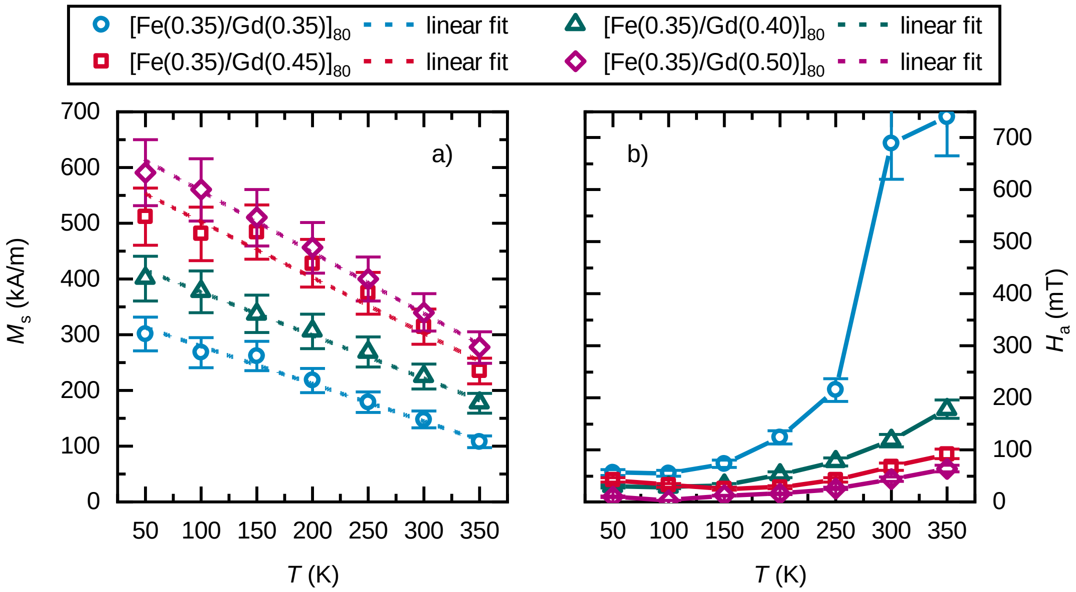

Figure 5.7: Magnetic values of Fe/Gd multilayers with different Gd layer thicknesses. Saturation magnetizations M_s fitted linearly (a) and in-plane anisotropy fields H_a against temperature T (b).

comparison of the change in the ip anisotropy fields H_a in Fig. 5.7 b. Larger H_a values indicate a more favorable oop magnetic orientation and therefore a larger uniaxial anisotropy or smaller shape anisotropy. In this regard, the decreasing M_s values lead to a decreasing shape anisotropy and increasing H_a values with temperature. This effect is especially elaborated for the low M_s values of [Fe(0.35)/Gd(0.35)]$_{80}$ at higher temperatures.

5.2.3 Observed Spin Objects and their Stability in Fe/Gd Multilayers

Using LTEM imaging, the spin texture of [Fe(0.35)/Gd(0.40)]$_{80}$ are imaged in this section. The images are acquired in 2.5 mm underfocus in Fresnel mode. In Fig. 5.8 a different types of magnetic stripe domains are shown at RT and zero magnetic field. The film exhibits three different kinds of stripe domains: broader dark stripes, broader bright stripes, and narrower stripes with less contrast and half the periodicity of the broader ones. This observation is similar to the stripe domains seen in previous works [128, 148]. A more detailed description of these kinds of domains is given in Ref. [537]. The mechanism to form this contrast is described in Sec. 3.3.3. Figure 5.8 b-d display the different stripes in more detail. The theoretical contrast of the spin textures in

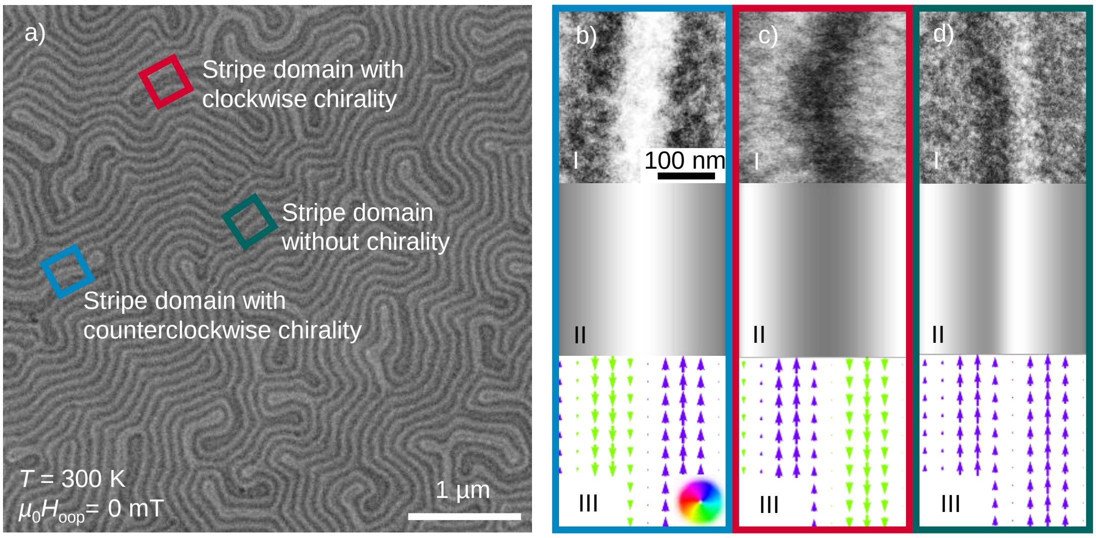

Figure 5.8: Different stripe domain types in Fe/Gd multilayers. Spin texture consisting of three different stripe types in [Fe(0.35)/Gd(0.40)]$_{80}$ at RT and zero magnetic field (a). The images b-d, I) show the measured zoomed-in stripe domains and b-d, II) display the simulated LTEM contrast caused by the theoretical spin textures shown in b-d, III). In b-d, III) the arrows and their color depict the directions of the ip components, with their sizes displaying the strengths. b) Stripes with chirality and a counterclockwise rotation. c) Stripes with chirality and clockwise rotation. d) Stripes without a chirality.

Fig. 5.8 b-d II is simulated by calculating the cross product of the two-dimensional ip components of the theoretical spin objects (Fig. 5.8 b-d III) and the incident electron beam multiplied by a deflection factor. The resulting smoothed histograms are plotted in Fig. 5.8 b-d II. Comparing the experimental results with the ideal theoretical contrasts, it can be confirmed that the bordering ip components are aligned mostly parallel to the stripes. Antiparallel ip moments on the opposite sides of the stripe result in larger high-contrast stripes (Fig. 5.8 b, c), while parallel aligned Bloch walls result in a narrower stripe pattern (Fig. 5.8 d). In other words, the broader stripes exhibit domain walls with a chirality, while the narrower ones exhibit no chirality. However, the underlying periodicity of the magnetic stripes is about 200 nm and the same for both types. The existence of only one underlying periodicity is also confirmed by the MFM measurements shown in Sec. 5.4.

Next, an oop magnetic field H_{oop} is applied to the sample. With an increasing field the stripe domains shrink in size and eventually only round spin objects are left at 90 mT. This state is shown in Fig 5.9 a. Three different coexisting spin objects exist. Panels I

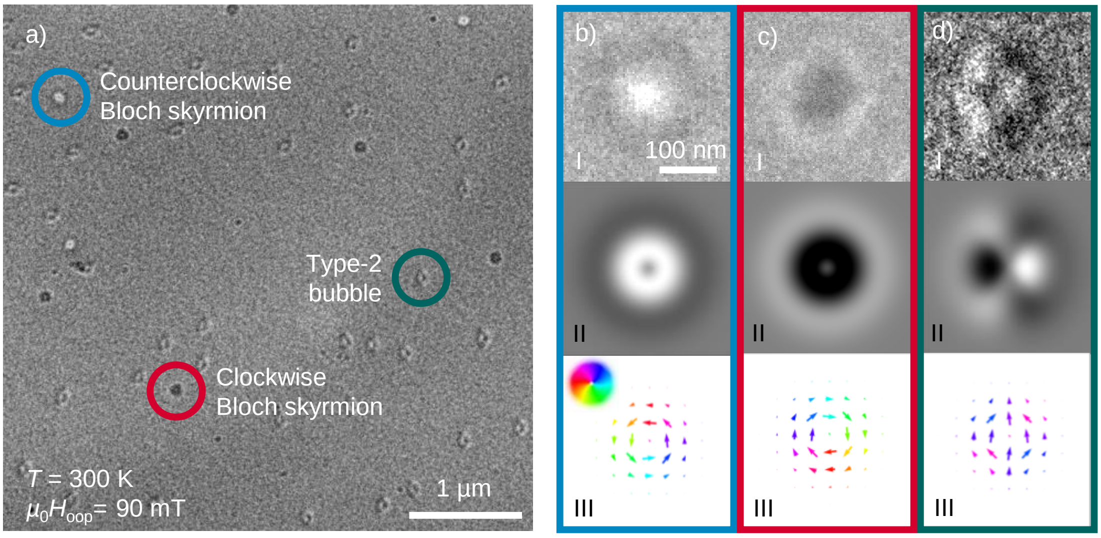

Figure 5.9: Spin object overview in Fe/Gd multilayers. a) Three different coexisting spin objects are visible in $[\mathrm{Fe}(0.35)/\mathrm{Gd}(0.40)]_{80}$ at RT and 90 mT. The images b-d, I) show the measured zoomed-in spin objects and b-d, II) display the simulated LTEM contrast caused by the theoretical spin textures shown in b-d, III). b) Bloch skyrmion with counter- and c) with clockwise rotation, and d) type-2 bubble.

of Fig. 5.9 b-d show the measured zoomed-in spin objects and panels II display the simulated LTEM contrast caused by the theoretical spin textures shown in panels III. The three different objects are ccw Bloch skyrmions (Fig. 5.9 b), cw Bloch skyrmions (Fig. 5.9 c), and topologically trivial type-2 bubbles (Fig. 5.9 d). They are well-known spin structures, which have been previously observed in similar Fe/Gd ML systems and other dipolar-stabilized systems [128, 144–148]. Type-2 bubbles differentiate themselves from skyrmions by domain walls consisting of both Néel- and Bloch-type pointing roughly in one ip direction. Because of this, they also exhibit no rotational symmetry. The elliptical shape in Fig. 5.9 d I and II arises from the one-fold symmetry of the spin configuration displayed in Fig. 5.9 d III. The size of the spin objects is similar to the periodicity of their underlying stripes with around 200 nm. Over the whole sample, the number of ccw and cw Bloch skyrmions seems to be equal due to the energetic degeneration of these two states. This was also observed in Ref. [128]. The number of bubbles at this specific field is larger, while there is no preferred orientation of the bubbles at first glance. Possible causes for a predominant orientation of stripes and bubbles in certain regions are explored in Sec. 5.5.3. The number of the different spin objects replicates the ratio of the different stripe types in Fig. 5.8. The transition from stripes to cylindrical spin objects as well as their stability ranges are investigated in the

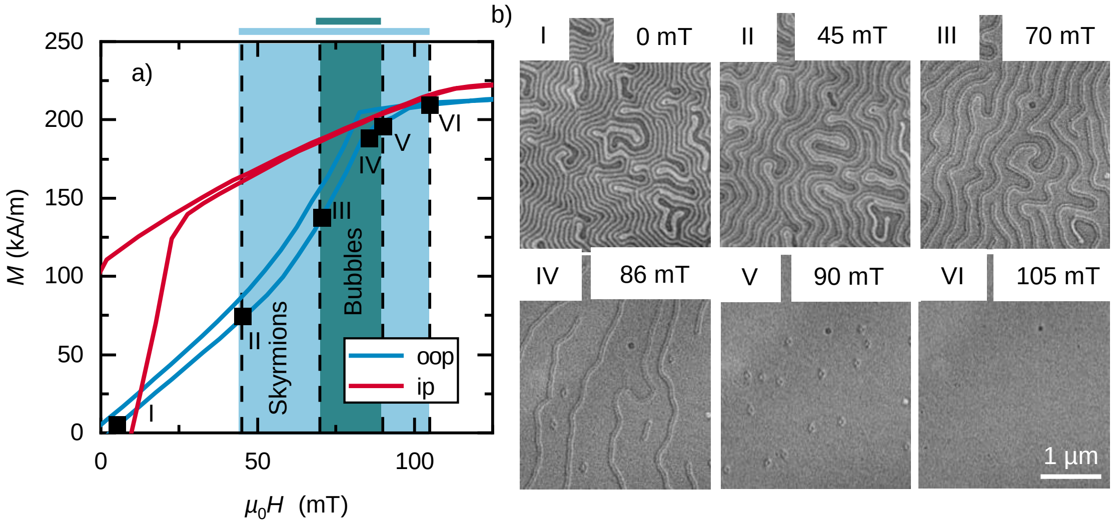

Figure 5.10: Stability ranges of the spin objects in Fe/Gd multilayers. a) Oop and ip *M*-*H* hysteresis loops of $[\mathrm{Fe}(0.35)/\mathrm{Gd}(0.40)]_{80}$ at RT. The colored regions mark the stability ranges of the spin objects coming from zero field. b) LTEM images of the sample at different oop magnetic fields, which are also marked in the oop loop in a). Panel I shows stripe domains with chirality (broader bright and dark stripes) and without (thinner stripes). At 45 mT disordered stripes coexist with Bloch skyrmions (II). Between 70 and 90 mT type-2 bubbles start to appear (III-V). In panel IV, all stripes disappeared, and skyrmions and bubbles coexist. At 105 mT only skyrmions are stable and observable (VI).

following Fig. 5.10. It explores the dependence of an applied oop magnetic field H_{oop} on the formation and stabilization of different spin objects using LTEM imaging and SQUID-VSM measurements. Figure 5.10 a shows the oop and ip *M*-*H* hysteresis loops of $[\mathrm{Fe}(0.35)/\mathrm{Gd}(0.40)]_{80}$ at RT. Moreover, corresponding LTEM images at different applied oop fields are presented in Fig. 5.10 b, which were captured at the same location while sweeping the field from zero toward magnetic saturation. The domain morphology and position of the different spin objects seem to be randomly distributed for every new field sweep starting from zero field after saturation. At the same time, the range of stability of the different spin objects stayed the same for every field sweep. Both the oop and ip hysteresis loops saturate at similar fields and have a saturation magnetization of around 220 kA/m, although their slopes differ greatly. The oop loop exhibits a linear parallel slope up to 45 mT. This can be connected to the reversible continuous growth of stripes parallel to the field. At 45 mT, the loop opens slightly more because of irreversible processes, like the formation and annihilation of cylindrical spin textures [535], which are, in this case, skyrmions. This opening stays relatively constant until the saturation of the film.

In the LTEM images, the different ranges of stability of the skyrmions and bubbles are identified. Starting from zero field, the film exhibits the three different kinds of stripe domains up to 45 mT. The different chiralities of the stripes determine the type of spin objects that can form under the oop magnetic field. When an oop field is applied, domains with magnetization parallel to the field grow at the expense of stripes antiparallel to the field. At 45 mT the first Bloch skyrmions start to form (Fig. 5.10 b II). They preferably arise from collapsed stripe domains with the same chirality. When the magnetic field is further increased to 70 mT, bubbles start to form out of the stripes without chirality (Fig. 5.10 b III). At 90 mT, the majority of stripes have vanished or shrank down to circular spin objects. The number of skyrmions stays constant from 70 mT while the number of bubbles further increases (Fig. 5.10 b, V). The number of topologically unprotected bubbles strongly decreases at larger fields than 90 mT. The final LTEM image is captured at 105 mT (Fig. 5.10 b VI). Only randomly distributed Bloch skyrmions are left. Their size decreased with increasing field down to around 100 nm, and they dissipate at fields slightly above 105 mT. It can be concluded that Bloch skyrmions are stable over a larger field range than bubbles due to their topological protection.

The field-dependent LTEM measurements are repeated for all samples of the series between 100 and 300 K. The resulting phase maps of the previously discussed sample $[\mathrm{Fe}(0.35)/\mathrm{Gd}(0.40)]_{80}$ and of $[\mathrm{Fe}(0.35)/\mathrm{Gd}(0.35)]_{80}$ dependent on the oop magnetic field H_{oop} and the temperature T are displayed in Fig. 5.11 a and b, respectively. The samples with the thicker Gd layers of 0.45 and 0.50 nm show only ip domains, due to their large magnetization and shape anisotropy (Fig. 5.7 a). Hence, their phase maps are not shown. The diagrams are constructed using the data from the LTEM measurements marked by the black dots. Selected images of the underlying LTEM measurements of $[\mathrm{Fe}(0.35)/\mathrm{Gd}(0.35)]_{80}$ and $[\mathrm{Fe}(0.35)/\mathrm{Gd}(0.40)]_{80}$ are displayed in Fig. A.2 and A.3, respectively. The area between the experimental data is filled under the assumption that stability transitions happen in the middle of the measured data points. As already mentioned, the domain morphology and position of the different spin objects seem to be randomly distributed for every new field sweep starting from zero field after saturation. At the same time, the range of stability of the different spin objects stayed the same for every field sweep. The phase map region of interest of $[\mathrm{Fe}(0.35)/\mathrm{Gd}(0.40)]_{80}$ at 300 K was discussed previously (Fig. 5.10). At lower temperatures, the magnetization

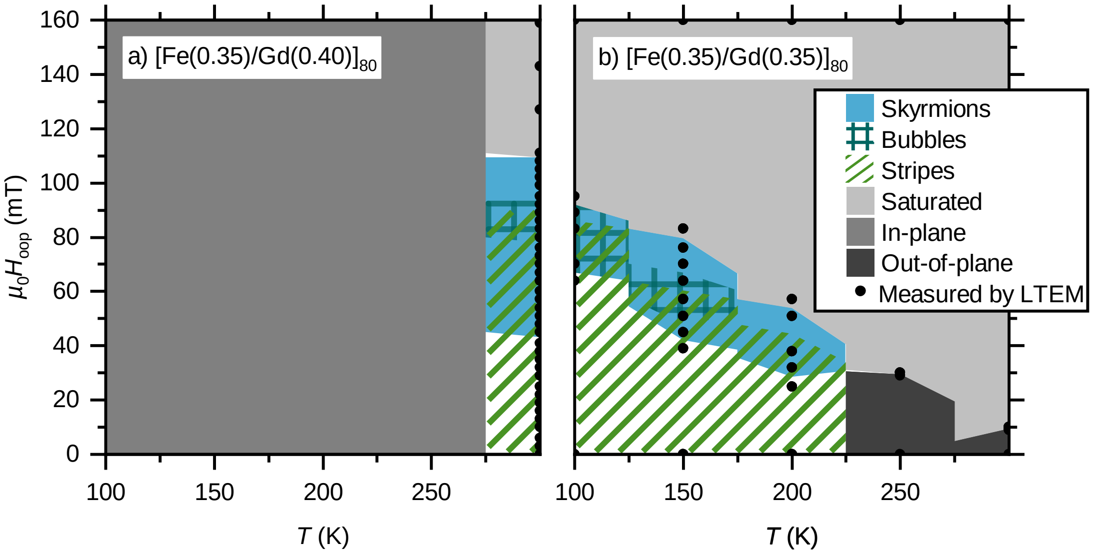

Figure 5.11: Phase maps of the spin objects in Fe/Gd multilayers. Magnetic field H_{oop} and temperature T dependence of the stability ranges of the different spin objects for [Fe(0.35)/Gd(0.40)]$_{80}$ (a) and [Fe(0.35)/Gd(0.35)]$_{80}$ (b). The diagram is constructed using the data from the LTEM measurements (black points).

and shape anisotropy increased, resulting in ip domains, similar to the samples with thicker Gd layers. The sample with the thinnest Gd layers with a thickness of 0.35 nm displays oop domains at 250 and 300 K. At 200 K, stripe domains and skyrmions can be observed. If the temperature is further decreased to 150 and 100 K, the stability window of skyrmions shifts to larger fields, and coexisting bubbles appear. It is evident that the stability range of bubbles is smaller than the one of skyrmions for both temperature and field. Generally, a skyrmion/stripe domain phase window between oop and ip domains can be observed when both Fig. 5.11 a and b are analyzed. In Sec. 2.4.1, Fig. 2.7 shows the different domain types dependent on the ratio of the magnetic uniaxial and shape anisotropy for a given sample thickness. While the uniaxial anisotropy K_u is not directly measured, it stems largely from the interfaces of the Fe and Gd layers and is therefore not strongly affected by changes in the Gd thickness. It can also be assumed that it stays relatively constant with temperature, which is later shown for a very similar system (see Fig. 5.16 d). The modest increase of K_u with temperature shown there is also confirmed by previous studies on Gd-rich Fe/Gd films [128, 538, 539]. The shape anisotropy is proportional to the second power of the saturation magnetization M_s (Sec. 2.1.4). Therefore, M_s is the primary parameter that influences the changes in domain types in the shown phase maps. If the phase window of stripe domains is compared to the M_s values presented in Fig. 5.7, M_s values between 210 and 270 kA/m are necessary to exhibit stripe domains and skyrmions in this system. While it was not possible to measure LTEM at elevated temperatures, a stripe domain and skyrmion phase for [Fe(0.35)/Gd(0.45)]$_{80}$ at 350 K can be predicted according to its M_s values, which is in agreement to the observed opening near saturation of the oop hysteresis loop shown in Fig. 5.6 e.

It is concluded that the effective magnetic anisotropy of Fe/Gd MLs needs to be carefully balanced by the thicknesses of the individual layers to achieve a magnetic stripe domain phase. The necessary ratios between the magnetic parameters and the film thickness t are elaborated in the magnetic domain theory section (Sec. 2.4.1) and the critical thickness for the onset of stripe domains is given by

$$t = 1.4 \cdot \sqrt{A}\frac{\mu_0 M_\mathrm{s}^2}{K_\mathrm{u}^{3/2}} \ . \qquad \text{(2.24 revisited)}$$

The vast thickness of the films enlarges the window of slightly negative effective anisotropies where stripe domains are energetically favorable (Fig. 2.4.1). Under the assumption that K_u and A are constant, the following can be concluded: (i) if M_s is too large at low temperatures or for thick Gd layers, ip domains are favored. (ii) if M_s is too low, oop domains are favored.

In conclusion, the stripe domains can be shrunk down to Bloch skyrmions and topological trivial type-2 bubbles by applying an oop magnetic field. The stability range of skyrmions is larger than the one of bubbles for both temperature and field. The spin objects tend to nucleate from stripe domains with the same chirality and need a larger applied field for larger M_s values. It is important to note that Montoya et al. observed that the nucleation mechanism of skyrmions from stripe domains differs depending on the ratio between K_u and M_s [128]. For large M_s values, stripes collapse into skyrmions, while for low M_s values, the stripes shrink down to skyrmions with an applied oop magnetic field. Conservation of the chirality during a transition from stripes to round spin objects is only given for the latter.

5.2.4 Achieving a Skyrmion Lattice

The previously studied film series succeeded in the stabilization of isolated skyrmions but did not show a dense skyrmion lattice. In this section, samples are displayed whose skyrmions are ordered in a dense hexagonal lattice at a certain applied oop magnetic

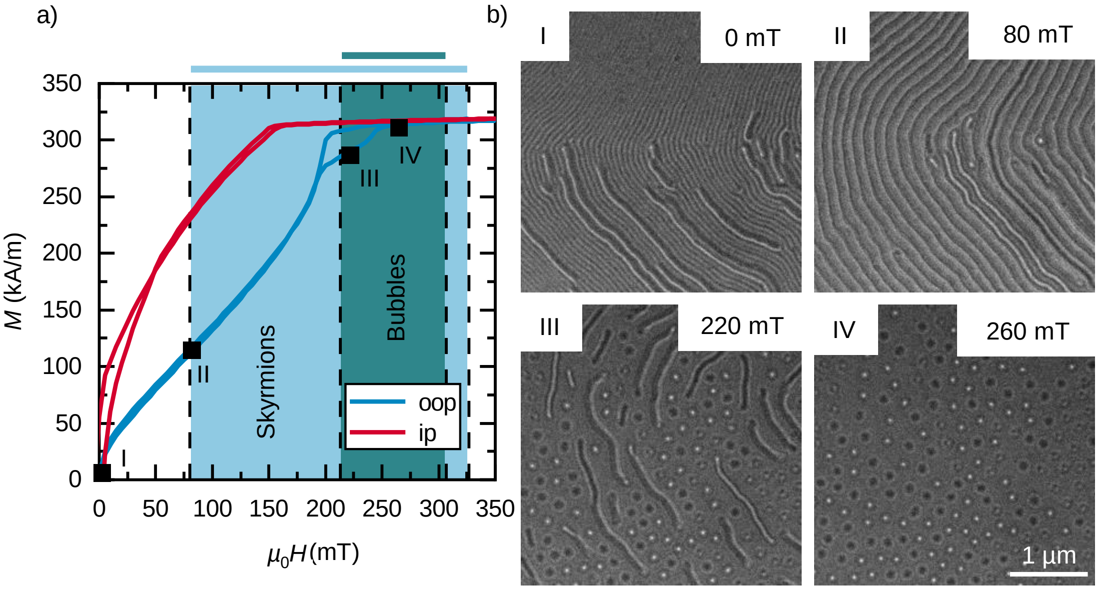

Figure 5.12: Hysteresis loops and LTEM images of a Fe/Gd multilayer with increased repetition number and a skyrmion lattice. a) Oop and ip *M*-*H* hysteresis loops of $[\mathrm{Fe}(0.35)/\mathrm{Gd}(0.40)]_{120}$ at RT. The colored regions mark the stability ranges of the spin objects coming from zero field. b) LTEM images of the sample at different oop magnetic fields, which are also marked in the oop loop in a). Panel I shows stripe domains. At 80 mT, the first Bloch skyrmions nucleate (II). Between 80 and 260 mT stripes collapse to skyrmions and a few bubbles (III). In panel IV, all stripes have disappeared, and a skyrmion-bubble-lattice has formed.

field. To accomplish this, skyrmions need to be the energetically most favorable state and not only a meta-stable phase between the transition from stripe domains to saturation, which was the case in Sec. 5.2.3. It has been shown experimentally that for Fe/Gd MLs, certain ratios of $M_\mathrm{s}^2/K_\mathrm{u}^{3/2}$ have to be met to achieve a skyrmion lattice for a given exchange constant A [128]. The requirements of the magnetic parameters are similar to the formation of stripe domains (Eq. 2.24), but the phase window is even smaller. It has also been shown that the phase window of skyrmion lattices grows with thicker films (higher repetition numbers) and larger M_s and K_u values.

Thus, samples with larger repetition numbers are fabricated. The exemplary measurement results of $[\mathrm{Fe}(0.35)/\mathrm{Gd}(0.40)]_{120}$ at RT are shown in Fig. 5.12. Overall, the behavior is similar to the sample discussed in Sec. 5.2.3, although the density and number of spin objects differ greatly between the samples. Panel I shows stripe domains. At 80 mT, the first Bloch skyrmions nucleate (II). Between 80 and 260 mT, the stripes collapse into skyrmions and bubbles (III). In panel IV, all stripes have disappeared, and a skyrmion-bubble-lattice has formed. If the loops of Fig. 5.10 a and Fig. 5.12 a

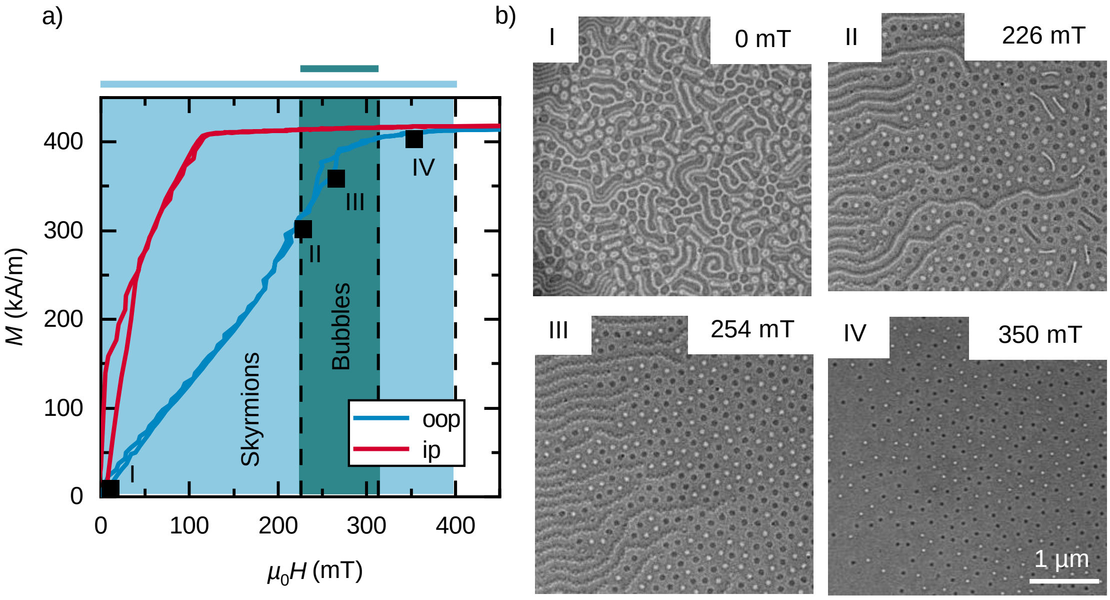

Figure 5.13: Hysteresis loops and LTEM images of a Fe/Gd multilayer with room temperature zero field skyrmions and a skyrmion lattice. a) Oop and ip M-H hysteresis loops of $[\mathrm{Fe}(0.35)/\mathrm{Gd}(0.50)]_{80}$ at RT. The colored regions mark the stability ranges of the spin objects coming from zero field. b) LTEM images of the sample at different oop magnetic fields, which are also marked in the oop loop in a). Panel I shows zero field skyrmions coexisting with stripe domains. At 226 mT, bubbles nucleate, and a skyrmion lattice starts to form, interrupted by remaining stripes (II). At 254 mT, a skyrmion and bubble lattice coexist (III). In panel IV, all bubbles have disappeared, and a skyrmion lattice has formed.

are compared, the larger M_s and H_a values are evident for the later. Additionally, a smaller remanence for both the oop and ip loops can be observed. Altogether, the larger thickness and the correct intrinsic magnetic properties give rise to the larger skyrmion window at larger oop magnetic fields and the existence of a hexagonal skyrmion lattice.

Another example for a skyrmion lattice is given in Fig. 5.13. Here, skyrmions are already stable at zero magnetic field, although no greater repetition number is used. The measured sample has the structure $[\mathrm{Fe}(0.35)/\mathrm{Gd}(0.50)]_{80}$. However, it has to be noted that this sample stems from a different series than the samples analyzed in Sec. 5.2.3 and therefore can not be directly compared. In comparison to Fig. 5.10 a and Fig. 5.12 a, Fig. 5.13 a exhibits even larger M_s and H_a values, while the remanences of the loops are small. It can be assumed that the large M_s and K_u values of this sample have the required ratio and an effective magnetic anisotropy close to zero is achieved. Further, the oop hysteresis loops lack an opening close to saturation and therefore the typical feature of the existence of cylindrical spin objects is missing [535]. Due to the fact that skyrmions exist at zero field coming directly from saturation (Fig. 5.13 b I), the skyrmions not only nucleated from collapsing stripe domains but also directly from the saturated state. Thus, the difference between the ascending and descending *M-H* curves is comparably small. If the field is increased from zero to 226 mT, the skyrmions start to shrink and more nucleate from stripe domains (II). At 254 mT, all stripes collapsed, and only a dense lattice of bubbles and skyrmions exists (III). It is clear that the skyrmions arrange in a hexagonal lattice. At 350 mT, all bubbles have vanished, and only skyrmions are left. From zero field to 350 mT a massive reduction in skyrmion size from roughly 200 to 70 nm is observed (Fig. 5.13 b).

In the presented study, the skyrmion lattice seems to be a stable state. In contrast, M.H. Seaberg et al. showed very recently spontaneous fluctuations of a skyrmion lattice in an almost identical system of $[\mathrm{Fe}(0.34)/\mathrm{Gd}(0.40)]_{100}$ [540]. Short-pulsed X-rays revealed that the skyrmion lattice oscillates with a relaxation time of a couple of nanoseconds and never entirely freezes into a static lattice at RT.

5.2.5 Conclusion about Spin Textures in Fe/Gd in Comparison to Previous Works

Stripes with and without chirality were observed in Fe/Gd MLs. Depending on the chirality of the stripes, bubbles and Bloch skyrmions nucleated and coexisted if an oop magnetic field is applied. Skyrmions proved to be more resilient toward temperature and oop magnetic fields due to their topological protection. A phase map for different Gd layer thicknesses, temperatures, and oop magnetic fields was created. This led to the confirmation that the ratio between the saturation magnetization and magnetic anisotropy values is crucial. Therefore, the results reported by Montoya et al. [128] could be validated. A skyrmion lattice was achieved for certain samples. In contrast to previous reports on Fe/Gd MLs, skyrmions were stabilized without an applied magnetic field at RT. Signs of spontaneous lattice fluctuations, which were reported in Ref. [540], were not observed.

These results establish the base for the further exploration of dipolar-stabilized spin textures and modifications of the Fe/Gd MLs.

5.3 First- and Second-Order Antiskyrmions in Fe/Gd-Based Multilayers

Next, the Fe/Gd MLs are modified by iridium (Ir) insertion layers to reduce the magnetic moment and anisotropy. This way, coexisting phases of first- and second-order antiskyrmions, Bloch skyrmions, and topological trivial bubbles are achieved. The stability of the different spin objects is studied in dependence on the oop magnetic field and temperature. From the experimental results, additionally supported by micromagnetic simulations, it can be concluded that the reduced magnetic moment and anisotropy support the formation of antiskyrmions via dipolar interaction. Moreover, the nucleation process of the antiskyrmions is analyzed experimentally and theoretically.

The findings show that antiskyrmions can be stabilized outside of bulk D_{2d} or S_4 crystals solely by dipolar interaction. Further, the shown measurements are the first experimental observation of second-order antiskyrmions. This easy-to-access range of different coexisting magnetic quasi-particles in thin films opens many possibilities for future studies on magnetic quasi-particle interaction and spin dynamics.

The results of this section are published in *Heigl, M. et al. Nat. Commun. 12, 2611 (2021)* [426].

5.3.1 Method Details on the Modification and Characterization of Fe/Gd-Based Multilayers with Insertion Layers

The ML samples are prepared at RT by DC magnetron sputtering from elemental targets on 30-nm-thick SiN membranes for LTEM imaging and Si(001) substrates with a 100-nm-thick thermally oxidized SiO_x layer for magnetic characterization. The sputtering process is carried out using an Ar working pressure of 5×10^{-3} mbar in an ultra-high vacuum chamber (base pressure $< 10^{-8}$ mbar). The composition $[Fe(0.35)/Gd(0.40)]_{80}$ from the series investigated in Sec. 5.2, which exhibits skyrmions at RT, is further modified by inserting 0.20-nm-thick Ir layers from the top and bottom. For all samples, 5-nm-thick Pt seed and cover layers are used to protect the films from corrosion. The thicknesses of the layers are estimated from the areal densities measured by a calibrated quartz balance before deposition. It is important to note that the deposition of layers in the sub-0.1-nm range is not precisely possible with this technique. A series of $[Fe(0.35)/Ir(0.20)/Gd(0.40)]_{N_{Ir}}/[Fe(0.35)/Gd(0.40)]_{80-2N_{Ir}}/[Fe(0.35)/Ir(0.20)/Gd(0.40)]_{N_{Ir}}$ MLs with different repetition numbers N_{Ir} of the Ir-containing layer stacks

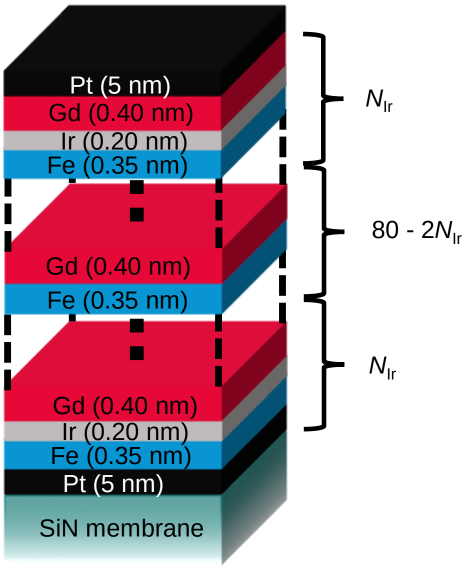

Figure 5.14: Schematic layer stack of Fe/Gd-based multilayers with Ir insertion layers. 0.20-nm-thick Ir layers are inserted from the top and bottom. The number of inserted Ir layers is changed, while the overall repetition number/number of Fe and Gd layers stayed constant. The figure is also published in Ref. [426].

($N_{\mathrm{Ir}} = 0, 2, 5, 10, 20, 40$) is prepared. Here, $N_{\mathrm{Ir}} = 0$ is equivalent to $[\mathrm{Fe}(0.35)/\mathrm{Gd}(0.40]_{80}$ and $N_{\mathrm{Ir}} = 40$ to $[\mathrm{Fe}(0.35)/\mathrm{Ir}(0.20)/\mathrm{Gd}(0.40)]_{80}$. A schematic of the $[\mathrm{Fe}(0.35)/\mathrm{Ir}(0.20)/\mathrm{Gd}(0.40)]_{N_{\mathrm{Ir}}}/[\mathrm{Fe}(0.35)/\mathrm{Gd}(0.40]_{80-2N_{\mathrm{Ir}}}/[\mathrm{Fe}(0.35)/\mathrm{Ir}(0.20)/\mathrm{Gd}(0.40)]_{N_{\mathrm{Ir}}}$ layer stack is displayed in Fig. 5.14.

Furthermore, samples with a modified position of the Ir insertion layer as well as different Ir thicknesses and insertion layer materials are fabricated and discussed in Sec. 5.3.9. $[\mathrm{Fe}/\mathrm{Gd}]_2/[[\mathrm{Fe}/\mathrm{Gd}]_6/\mathrm{Fe}/\mathrm{Ir}/\mathrm{Gd}]_{10}/[\mathrm{Fe}/\mathrm{Gd}]_8$ has an equivalent number of Ir layers as $N_{\mathrm{Ir}} = 5$ with a more even distribution of Ir throughout the ML stack. $[\mathrm{Ir}/\mathrm{Fe}/\mathrm{Gd}]_5/[\mathrm{Fe}/\mathrm{Gd}]_{76}/[\mathrm{Ir}/\mathrm{Fe}/\mathrm{Gd}]_5$ changes the stacking order of the trilayer and $[\mathrm{Fe}/\mathrm{Ir}(0.6)/\mathrm{Gd}]_5/[\mathrm{Fe}/\mathrm{Gd}]_{76}/[\mathrm{Fe}/\mathrm{Ir}(0.6)/\mathrm{Gd}]_5$ has an increased Ir thickness. The other used materials for the insertion layers are Pt, Cu, and Al.

The MLs are investigated by a variety of techniques at temperatures between 50 and 350 K. The integral magnetic properties of the MLs are probed by SQUID-VSM. M-H hysteresis loops are measured in oop and ip configuration for all samples at 50, 100, 150, 200, 250, 300, and 350 K and the M_s values are extracted.

The uniaxial magnetic anisotropy constant K_u is evaluated using FMR measurements performed with a Bruker spectrometer and a X-band resonator at a microwave frequency $f = 9.45\,\mathrm{GHz}$. FMR spectra are recorded in the temperature range 100-300 K for different orientations of the static magnetic field with respect to the Fe/Gd ML plane (polar angular dependence).

The interface Dzyaloshinskii-Moriya interaction (DMI) is extracted from non-reciprocal spin-wave dispersion using Brillouin light scattering (BLS) measurements. The wave-vector-resolved BLS in backscattering geometry is conducted at RT using a monochromatic continuous-wave solid-state laser with a wavelength of 473 nm [256]. Backscattered light is collected and processed with a six-pass Fabry–Perot interferometer TFP-2 (JRS Scientific Instruments). In this configuration, magnetostatic surface spin waves (MSSWs) are excited in the MLs [251]. By varying the incident angle, the wave vectors are tuned. MSSWs propagating along opposite directions lead to resonance peaks of Stokes and anti-Stokes signals in the BLS spectra. The two peaks are asymmetric in both peak intensity and frequency. The intensity difference is attributed to the non-reciprocity of MSSWs. The frequency difference originates from the asymmetry of the dispersion relations resulting from the interface DMI. The frequency difference is used to determine the interface DMI constant D according to Ref. [250].

The magnetic domain morphology is imaged by Lorentz TEM using a FEI Titan and a JEOL NEOARM-200F system with a defocus of -2.5 mm in Fresnel mode. The temperature is controlled by a Gatan Double Tilt Liquid Nitrogen Cooling Holder Model 636 for the low-temperature measurements. The theoretical contrast of the spin textures is simulated by the Python program described in Sec. 3.3.3.

Micromagnetic Simulations

The micromagnetic simulations are performed by using simulation codes based on both finite differences method, *magnum.af* [541] and hybrid finite- and boundary elements method, *magnum.fe* [542]. While the former is used to reproduce the experimental results and investigate the formation process of experimentally observed spin structures, the latter is employed to investigate the stability of isolated skyrmions and antiskyrmions by varying the material parameters of the system. In both cases the magnetization dynamics is investigated by means of numerical integration of the Landau-Lifshitz-Gilbert (LLG) equation [543–545]

$$\frac{\partial \boldsymbol{m}}{\partial t'} = -\frac{\gamma_\mathrm{gyro}}{1+\alpha_\mathrm{damp}^2}\boldsymbol{m} \times \boldsymbol{H}_\mathbf{eff} - \frac{\alpha_\mathrm{damp}\gamma_\mathrm{gyro}}{1+\alpha_\mathrm{damp}^2}\boldsymbol{m} \times \left(\boldsymbol{m} \times \boldsymbol{H}_\mathbf{eff}\right) \,, \tag{5.1}$$

where α_{damp} is the Gilbert damping constant, γ_{gyro} the reduced gyromagnetic ratio, $\boldsymbol{m}$ the magnetization unit vector, t' the time, and $\boldsymbol{H}_{\mathbf{eff}}$ the effective field term, which includes the considered energy contributions.

To reproduce the field driven magnetization dynamics in a Fe/Gd ML, a continuous film with a length l = 5 µm, width w = 5 µm and a thickness t = 62 nm is discretized in `magnum.af`. The cell volume is chosen according to the exchange length $l_{\mathrm{ex}} = 13\,\mathrm{nm}$ as $l_x \times l_y \times l_z = 10 \times 10 \times 8.85\,\mathrm{nm}^3$. First, each cell is randomly magnetized. Then, the structure is relaxed to its ground state at vanishing external fields, where the effective field term $\boldsymbol{H}_{\mathbf{eff}}$ is modeled in such a fashion that it includes only the micromagnetic exchange, uniaxial magnetic anisotropy, and demagnetization fields. To investigate the dynamics of the system, the sample is subject to the time-dependent Zeeman field, where $\boldsymbol{H}_{\mathrm{zee}} = H(t)\boldsymbol{e}_{\mathrm{oop}}$, with $\boldsymbol{e}_{\mathrm{oop}}$ being the unit vector in the oop direction. $\mu_0 H_{\mathrm{oop}}(t)$ is chosen to increase linearly from 0 mT to 200 mT over 40 ns. The role of DMI is investigated by repeating the simulations, where the DMI energy term is added into the effective field. In order to investigate the stability of an isolated spin object, `magnum.fe` is used. Here, a rectangular finite element mesh of dimensions $l = 300\,\mathrm{nm}$, $w = 300\,\mathrm{nm}$, and $t = 62\,\mathrm{nm}$ is utilized. A simple parameterization of the (anti-)skyrmions as initial magnetization state is chosen and the LLG is solved for 10 ns at high damping $\alpha_{\mathrm{damp}} = 1$ in the presence of Zeeman fields with magnitudes between 0 and 125 mT. To reproduce the effect of isolation in an infinite film, a very large oop uniaxial magnetic anisotropy constant $K_{\mathrm{u}} = 1\,\mathrm{MJ/m}^3$ is set in the outer region of a circle in the xy-plane with radius $r = 150\,\mathrm{nm}$, which is well above the (anti-)skyrmion size. M_{s} and K_{s} are varied and the integer topological charge N_{sk} of the final magnetization states is calculated, which is defined by

$$N_{\mathrm{Sk}} = \int \mathrm{d}^2 r \frac{1}{4\pi} \boldsymbol{m}(\boldsymbol{r}) \cdot \left[\frac{\partial \boldsymbol{m}(\boldsymbol{r})}{\partial x} \times \frac{\partial \boldsymbol{m}(\boldsymbol{r})}{\partial y} \right] . \qquad \text{(2.25 revisited)}$$

If N_{sk} of the relaxed magnetization state is $N_{\mathrm{sk}} = -1$, an antiskyrmion is stable for the particular pair of M_{s} and K_{u} values, while a skyrmion is assumed to be stable for $N_{\mathrm{sk}} = +1$.

5.3.2 Magnetic Properties of Fe/Gd-Based Multilayers with Ir Insertion Layers

All measured M-H hysteresis loops of the [Fe(0.35)/Ir(0.20)/Gd(0.40)]$_{N_{\mathrm{Ir}}}$/[Fe(0.35)/Gd(0.40)]$_{80-2N_{\mathrm{Ir}}}$/[Fe(0.35)/Ir(0.20)/Gd(0.40)]$_{N_{\mathrm{Ir}}}$ MLs in oop and ip geometry for

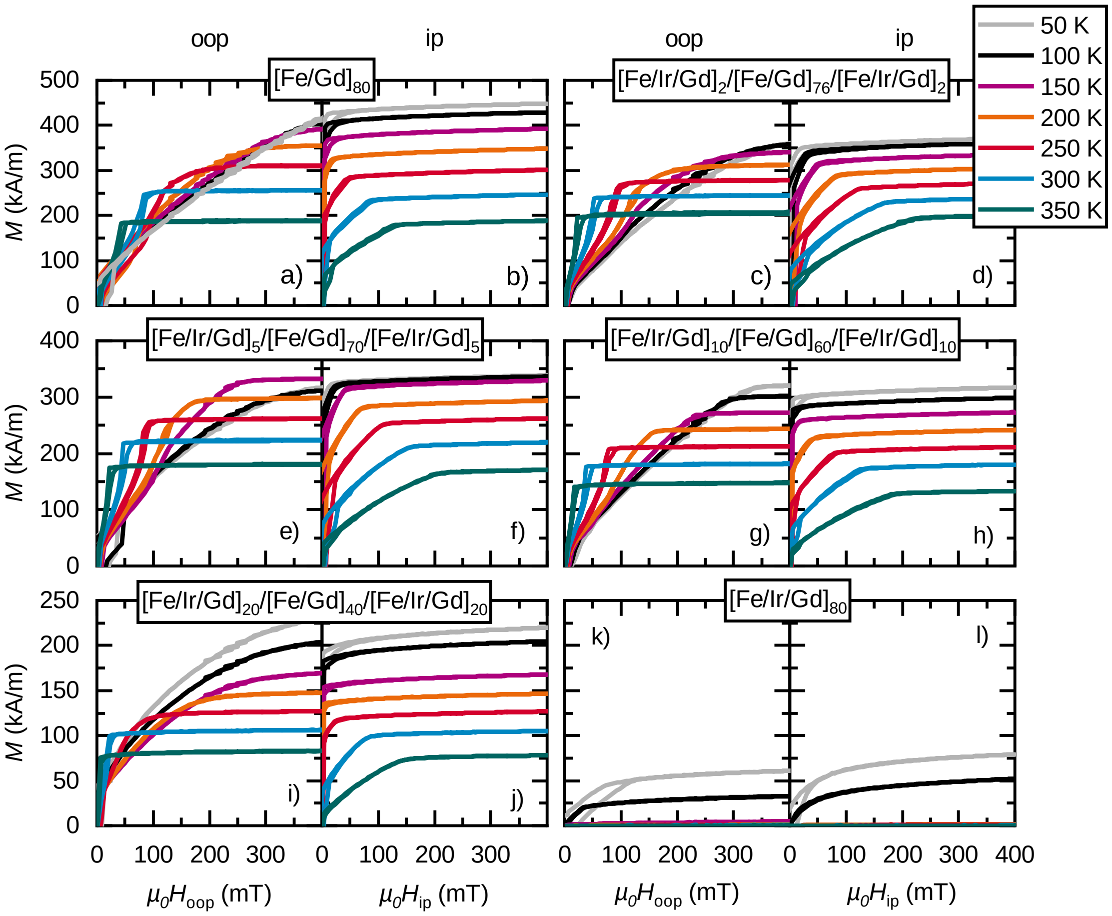

Figure 5.15: Hysteresis loops of Fe/Gd multilayers with different numbers of Ir insertion layers. *M-H* hysteresis loops of $[\mathrm{Fe}(0.35)/\mathrm{Ir}(0.20)/\mathrm{Gd}(0.40)]_{N_{\mathrm{Ir}}}/[\mathrm{Fe}(0.35)/\mathrm{Gd}(0.40)]_{80-2N_{\mathrm{Ir}}}/[\mathrm{Fe}(0.35)/\mathrm{Ir}(0.20)/\mathrm{Gd}(0.40)]_{N_{\mathrm{Ir}}}$ MLs in oop and ip geometry at 50, 100, 150, 200, 250, 300, and 350 K. N_{Ir} = 0 (a, b), 2 (c, d), 5 (e, f), 10 (g, h), 20 (i, J), 40 (k, l). The figure is also published in Ref. [426].

temperatures between 50 and 350 K are displayed in Fig. 5.15. Due to the decrease in saturation magnetization M_s with temperature, it can be concluded that all Fe/Gd-based MLs are Gd dominant over all measured temperatures. It is also evident that an increase in the number of insertion layers leads to a decrease in M_s, while the ip anisotropy fields H_a stay relatively constant. In Fig. 5.15 k and l the whole ML consists of the repeating trilayer Fe/Ir/Gd. Here, a significant magnetization can only be measured below 150 K. The formation of spin textures is indicated by the presence of an opening in the oop loop close to saturation [535]. This signature exists in Fig. 5.15 a ($N_{\mathrm{Ir}} = 0$) at 350-250 K, in c ($N_{\mathrm{Ir}} = 2$) at 350-200 K, in e ($N_{\mathrm{Ir}} = 5$) at 350-150 K, in g ($N_{\mathrm{Ir}} = 10$) at 350-200 K, in i

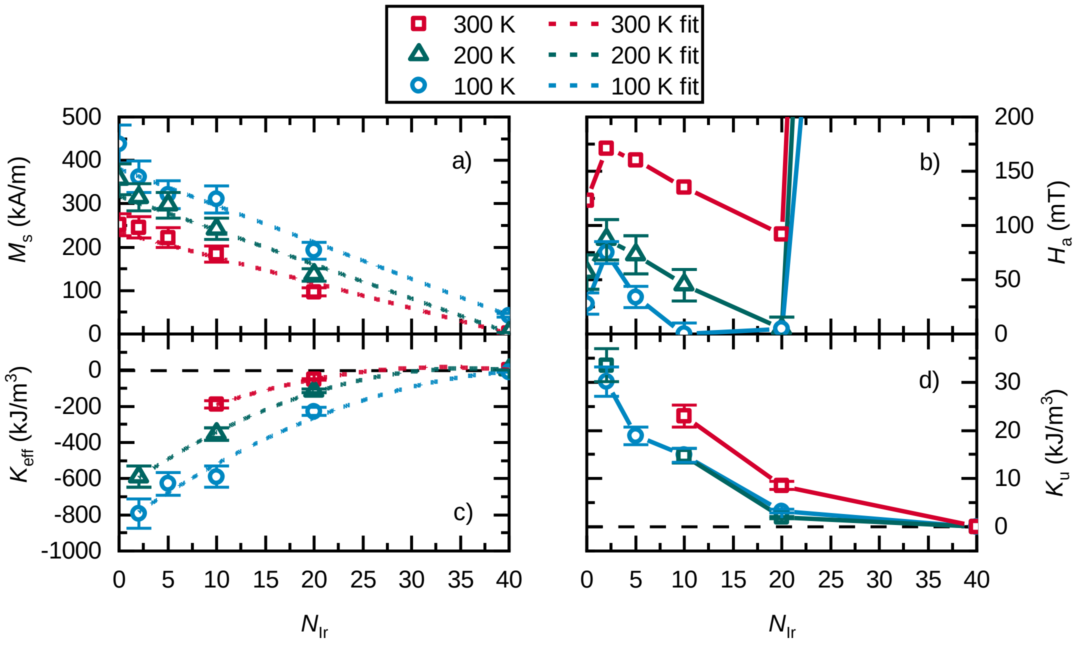

Figure 5.16: Magnetic values of Fe/Gd multilayers with different numbers of Ir insertion layers. The saturation magnetization M_s (a), the ip anisotropy field H_a (b), the effective magnetic anisotropy K_eff (c) and the uniaxial magnetic anisotropy K_u (d) as a function of the repetition number of Ir insertion layers N_Ir at 100, 200, and 300 K. The figure is also published in Ref. [426].

($N_\mathrm{Ir} = 20$) at 350-300 K. If these temperature ranges are compared to the stability ranges of skyrmions in the phase diagrams of Fig. 5.20, an excellent agreement can be found. It seems that the correct number of Ir insertion layers ($N_\mathrm{Ir} \approx 5$) increases the temperature window of stable spin objects. Hence, the underlying [Fe(0.35)/Gd(0.40)]$_{80}$ ML benefits from the lower magnetization achieved by the Ir insertion layers in terms of its skyrmion stability range. As discussed in the previous section, the saturation magnetization and anisotropy values are the crucial parameters to stabilize spin objects. Therefore, M_s and H_a are extracted from the shown hysteresis loops. Additionally, K_u is measured by FMR and K_eff is calculated by

$$K_\mathrm{eff} = K_\mathrm{u} + K_\mathrm{shape} = K_\mathrm{u} - \frac{\mu_0}{2} M_\mathrm{s}^2 \,. \qquad \text{(2.9 revisited)}$$

Please note that not all samples could be measured at every temperature with FMR.

Figure 5.16 shows the dependence of the saturation magnetization M_s (a), the ip anisotropy field H_a (b), the effective magnetic anisotropy K_eff (c), and the uniaxial anisotropy K_u (d) on the repetition number of Ir insertion layers N_Ir. The error bars account for uncorrected geometry effects of the samples during SQUID measurements (around ±10%). The insertion of Ir layers reduces linearly the saturation magnetization (Fig. 5.16 a). If all 80 layers have additional Ir insertion layers, M_s almost vanishes completely (N_{Ir}=40) as stated before. Thus, it can be concluded that Ir insertion layers reduce the total moment of the adjacent Fe and Gd layers to nearly zero. This can be explained by the additional induced moment in Ir by the adjacent Fe layer [546, 547], which is rather large in comparison to the typical induced moment of Gd in Ir [548]. Therefore, the overall magnetization of the Gd dominant system is reduced. It is also important to note that while the moment decreases with the increasing number of Ir insertion layers, the shape of the loops stays relatively similar. Larger H_a values indicate a more favorable oop magnetic orientation, which is partially confirmed by a comparison between Fig. 5.16 b and d. However, the small M_s values dominate H_a for $N_{Ir} = 20$. K_{eff} decreases quadratically, due to the linear decrease in M_s and its underlying shape anisotropy ($K_{shape} \propto M_s^2$). Furthermore, all samples reveal rather small K_u values, which decrease with increasing N_{Ir}, as displayed in Fig. 5.16 d. Generally, the temperature-dependent behavior is similar to the previously discussed Fe/Gd MLs in Fig. 5.7.

5.3.3 Different Spin Objects in Modified Fe/Gd Multilayers

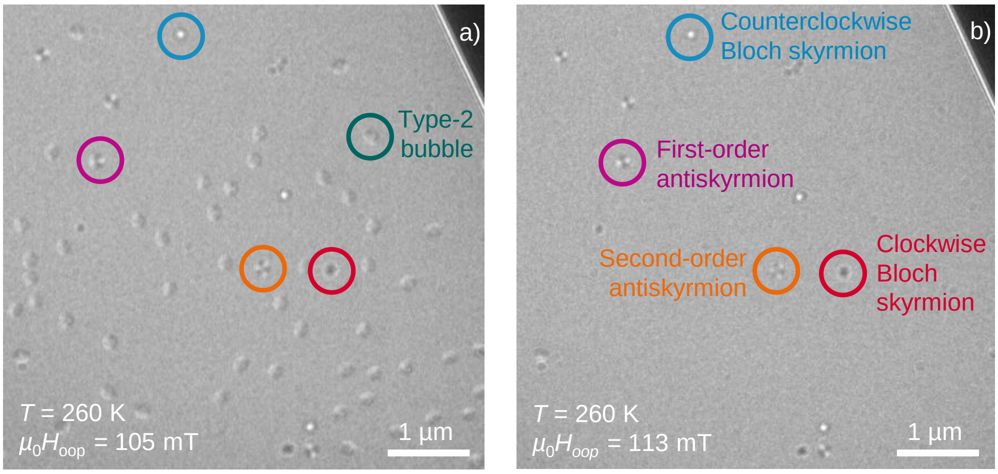

Figure 5.17: Variety of coexisting spin objects in a modified Fe/Gd multilayer. Underfocused LTEM image of $[Fe/Ir/Gd]_2/[Fe/Gd]_{76}/[Fe/Ir/Gd]_2$ taken in two different applied oop magnetic fields H_{oop} of 105 mT (a) and 113 mT (b) at the temperature T of 260 K. The figure is also published in Ref. [426].

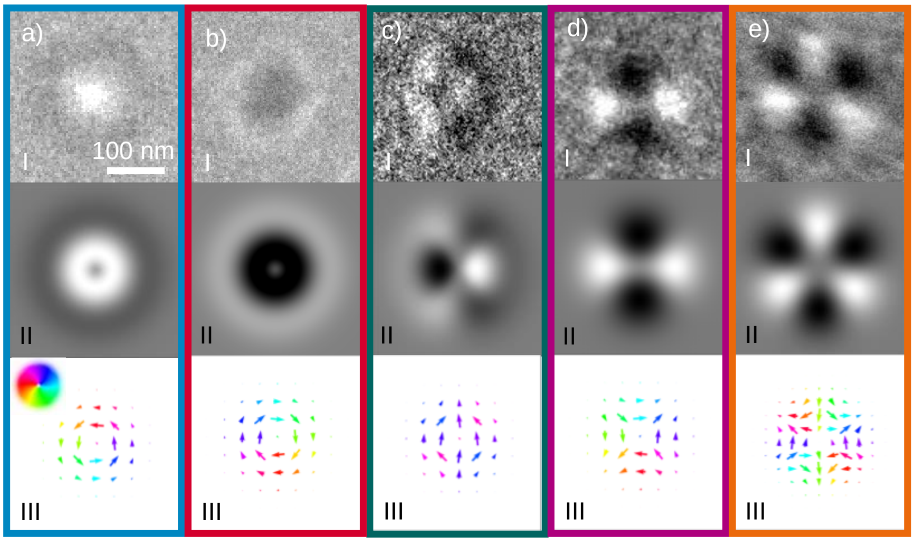

Figure 5.18: Spin object overview in modified Fe/Gd multilayers. Five different coexisting spin objects are in Fig. 5.17. Panels I show the measured zoomed-in spin objects and panels II display the simulated LTEM contrast caused by the theoretical spin textures shown in panels III. In panels III the arrows and their color depict the directions of the ip components, with their sizes displaying the strengths. Bloch skyrmion with counter- (a) and with clockwise rotation (b), type-2 bubble (c), first-order antiskyrmion (d), and second-order antiskyrmion (e). The figure is also published in Ref. [426].

Figure 5.17 displays exemplary LTEM images of the $[Fe/Ir/Gd]_2/[Fe/Gd]_{76}/[Fe/Ir/Gd]_2$ sample taken at 260 K in an applied oop magnetic field H_{oop} of 105 mT (a) and 113 mT (b). The images are acquired in 2.5 mm underfocus in Fresnel mode. Various coexisting spin objects are observed. In Fig. 5.18 the various spin objects are displayed in more detail (panel I), along with theoretical LTEM contrast images (panel II), and corresponding spin textures (panel III), showing a ccw Bloch skyrmion (a), a cw Bloch skyrmion (b), a type-2 bubble (c), a first-order antiskyrmion (d), and a second-order antiskyrmion (e). Comparing the experimental results with the theoretical ideal contrasts, it can be concluded that the samples exhibit up to five different spin objects at a time. While Bloch skyrmions and type-2 bubbles are well-known spin structures, which have been previously observed in similar Fe/Gd ML systems [128, 144–148] and in the previous section, first-order antiskyrmions have never been observed experimentally outside of compounds with D_{2d} or S_4 symmetry before. Additionally, second-order antiskyrmions, which exhibit a threefold symmetry instead of the twofold symmetry of first-order antiskyrmions, are observed. They have experimentally not been observed outside of these films. The different spin objects have similar sizes of around 200-250 nm in diameter. In addition, the second-order antiskyrmions appear to have the largest size due to the additional domain wall alteration between Bloch- and Néel-type.

In Fig. 5.17 a the five different spin objects are coexisting. The majority of them are topologically trivial type-2 bubbles. If the applied oop field is increased to 113 mT, the bubbles vanish, and only four different topologically protected spin objects remain. While the number of first-order antiskyrmions, counterclockwise skyrmions, and clockwise skyrmions seems to be relatively equal, only one second-order antiskyrmion is visible. This trend continues over the whole sample, with second-order antiskyrmions being extremely rare. The different spin objects are randomly distributed over the whole imaged area, revealing no preferred orientation, and appear at different locations after resetting the magnetic state. Jiang et al. [235] showed that Néel skyrmions exhibit no LTEM contrast when the film is normal to the electron beam. Considering this, the sample is tilted by up to 30 degrees revealing no indication of the existence of pure Néel-type spin objects.

5.3.4 Stability of the Observed Spin Objects in Modified Fe/Gd Multilayers

Using LTEM imaging and SQUID-VSM measurements, the dependence on an applied oop magnetic field and the temperature, which results in the formation and stabilization of different spin objects, is explored. Figure 5.19 a shows the oop and ip *M*-*H* hysteresis loops of $[\mathrm{Fe/Ir/Gd}]_2/[\mathrm{Fe/Gd}]_{76}/[\mathrm{Fe/Ir/Gd}]_2$ at 250 K. Moreover, corresponding LTEM images at different applied oop fields are presented in Fig. 5.19 b, which were captured at the same location while sweeping the field from zero toward magnetic saturation. Both the oop and ip hysteresis loops saturate at similar fields and have a saturation magnetization of around 270 kA/m, although their courses differ greatly. The oop loop exhibits a linear growth of magnetization with only a small opening up to around 60 mT. This can be connected to the reversible continuous growth of stripes parallel to the field. At larger fields, the hysteresis loop opens because of irreversible processes, like the formation and annihilation of cylindrical spin textures [535]. In the LTEM images, different ranges of stability of the different spin objects are identified.

Starting from zero field, the film exhibits three different kinds of stripe domains up to 63 mT: broader dark stripes, broader bright stripes, and narrower stripes with less contrast and half the periodicity of the broader stripes (Fig. 5.19 b, I). As described for Fig. 5.8, broader stripes exhibit domain walls with a chirality, while the narrower ones exhibit no chirality. However, the underlying periodicity of the magnetic stripes is about

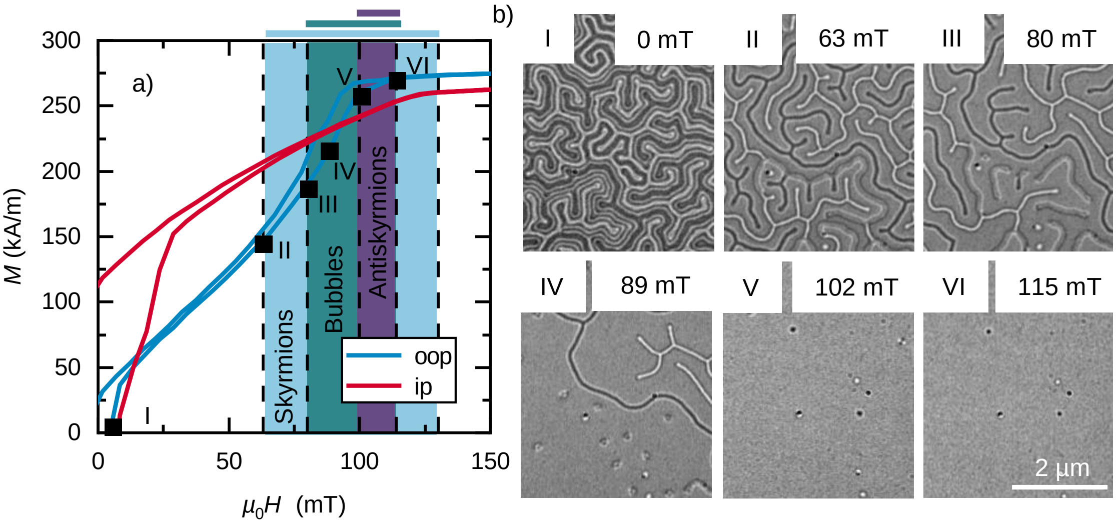

Figure 5.19: Stability ranges of the spin objects in modified Fe/Gd multilayers. Oop and ip M-H hysteresis loops of $[\mathrm{Fe/Ir/Gd}]_2/[\mathrm{Fe/Gd}]_{76}/[\mathrm{Fe/Ir/Gd}]_2$ at 250 K (a). The colored regions mark the stability ranges of the spin objects coming from zero field. LTEM images of the sample at different oop magnetic fields (b), which are also marked in the oop loop in a). Panel I shows stripe domains with chirality (broader bright and dark stripes) and without (thinner stripes). At 63 mT, stripes coexist with Bloch skyrmions (II). Between 80 and 89 mT, type-2 bubbles start to appear (III-IV). In panel V, all stripes disappeared, and antiskyrmions nucleated at 102 mT. Antiskyrmions, skyrmions, and bubbles coexist in this field range. At 115 mT, only skyrmions are stable and observable (VI). The figure is also published in Ref. [426].

250 nm and the same for both types. The existence of only one underlying periodicity for these kinds of samples is also confirmed by the MFM measurements in Sec. 5.4. The different chiralities of the stripes can determine the type of spin objects that potentially form under an applied oop magnetic field. When an oop field is applied, domains with magnetization parallel to the field grow at the expense of stripes antiparallel to the field. At 63 mT the first Bloch skyrmions start to form (Fig. 5.19 b, II). They preferably arise from collapsed stripe domains with the same chirality. Equal numbers of ccw (white) and cw (black) Bloch skyrmions appear when averaged over the whole sample. When the magnetic field is further increased to 80 mT, bubbles start to form out of the stripes without chirality (Fig. 5.19 b, III). At 89 mT, the majority of stripes has vanished or shrank down to circular spin objects. The number of skyrmions stayed constant from 80 mT while the number of bubbles further increased (Fig. 5.19 b, IV). The first isolated antiskyrmions appear at 102 mT when all remaining stripes have vanished (Fig. 5.19 b, V). The number of topologically unprotected bubbles is also strongly reduced at these higher fields. The last displayed LTEM image is captured at 115 mT (Fig. 5.19 b, VI). Only

randomly distributed Bloch skyrmions are left. Their size decreased with increasing field down to around 100 nm, and they dissipate at around 130 mT. All six panels also show microstructural defects as black dots, which are slightly smaller than the skyrmions and unaffected by the magnetic field. In Fig. 5.19 b, II-V one of the counterclockwise skyrmion is pinned to one of these defects. It can be concluded that Bloch skyrmions are stable over the most extensive field range, while bubbles and antiskyrmions only exist in somewhat limited field ranges.

5.3.5 Phase Diagrams for Different Numbers of Ir Insertion Layers

The procedure of Fig. 5.19 is repeated for all samples of the series and different temperatures between 100 and 300 K. The observed stability ranges of the different spin objects are displayed in Fig. 5.20 dependent on the oop magnetic field H_{oop} and temperature T. The diagram is constructed using the data from the LTEM measurements marked by the black dots. The area between the experimental data is filled under the assumption that stability transitions happen in the middle of the measured data points.

The underlying LTEM images, which show significant features, are displayed in Sec. A.2.2. As already mentioned, the domain morphology and position of the different spin objects seem to be randomly distributed for every new field sweep starting from zero field after saturation. At the same time, the range of stability of the different spin objects stays the same for every field sweep. Similar to Fig. 5.11, stripe domains are necessary for the potential nucleation of spin objects. In all phase diagrams of Fig. 5.20, no pure antiskyrmion phase is observable. Antiskyrmions always coexist with Bloch skyrmions and sometimes with type-2 bubbles. It is also evident that the stability range of antiskyrmions is smaller than the one of skyrmions for both temperature and field for all samples. Bubbles occur at larger temperature ranges, while they seem more susceptible to magnetic fields. Thus, the parameter range for antiskyrmion nucleation is smaller than the one of bubbles. However, if antiskyrmions nucleate, they are more stable than bubbles due to their topological protection. For five of the six samples, it is possible to stabilize antiskyrmions even at room temperature.

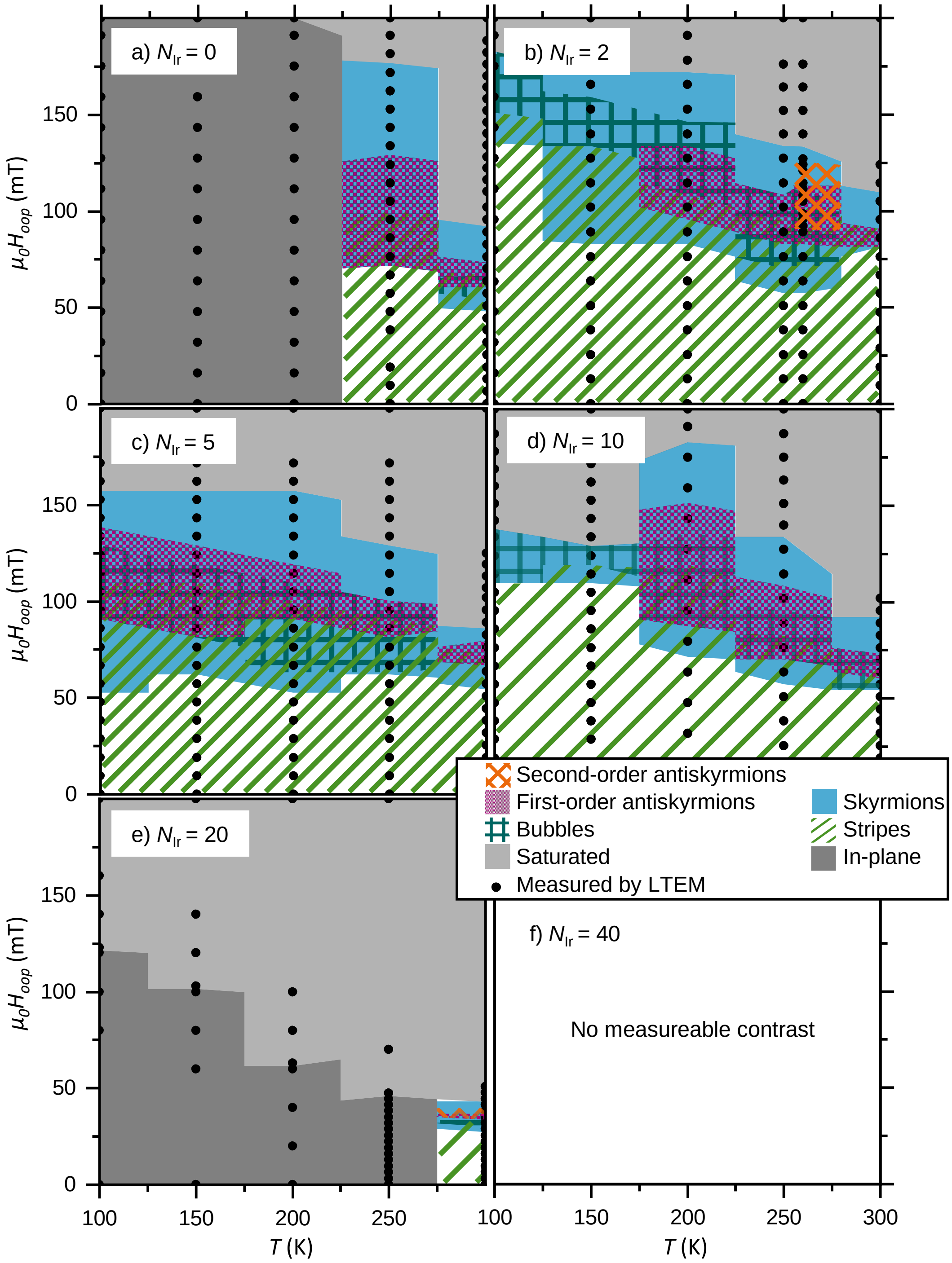

Figure 5.20: Phase diagrams of the spin objects in modified Fe/Gd multilayers. Magnetic field H_{oop} and temperature T dependence of the stability ranges of the spin objects. The figure is also published in Ref. [426].

While first-order antiskyrmions exist in every sample of the series besides $N_{\mathrm{Ir}} = 40$ at a wide range of temperatures, second-order antiskyrmions are only observed at 260 K in $N_{\mathrm{Ir}} = 2$ (Fig. 5.20 b) and at 300 K in $N_{\mathrm{Ir}} = 20$ (Fig. 5.20 e). In all cases, they are quite rare in comparison to the other spin objects. Because of that, their existence can not be ruled out at other temperatures and fields. Interestingly, if second-order antiskyrmions occur, they are stable at larger fields than first-order antiskyrmions. For $N_{\mathrm{Ir}} = 40$ no magnetic LTEM contrast is observable due to the low magnetization of the sample (see Fig. 5.20 f).

5.3.6 Micromagnetic Modeling of the Antiskyrmion-Hosting System

Micromagnetic simulations are performed based on the finite differences method, where the magnetization dynamics are investigated by means of numerical integration of the LLG equation to reproduce the experimental findings. Here, only the magnetic exchange, uniaxial magnetic anisotropy, demagnetization, and Zeeman fields are considered, using an exchange stiffness constant $A = 6\,\mathrm{pJ/m}$, an uniaxial magnetic anisotropy constant $K_{\mathrm{u}} = 22\,\mathrm{kJ/m^3}$, a saturation magnetization $M_{\mathrm{s}} = 225\,\mathrm{kA/m}$, and a film thickness of 62 nm as material parameters, which is in the range of the experimental values (Fig. 5.16). In order to confirm the dipole-dipole interaction as stabilization mechanism for antiskyrmions, no DMI was included in the simulations. The results are displayed in Fig. 5.21.

The simulations do not show significant differences in their spin configuration along the film thickness. Figure 5.21 a-d show the domain morphology at a larger scale with the color illustrating the oop component of the magnetization. Figure 5.21 e-g display enlarged images with black vectors showing the x- and y-components of the magnetization. Figure 5.21 a and e display the relaxed magnetization state at zero field showing stripes with different chiralities bristled with Bloch lines. In Fig. 5.21 b an external oop magnetic field of $\mu_0 H_{\mathrm{oop}} = 50\,\mathrm{mT}$ is applied and the stripes start to shrink in size forming skyrmions. An external magnetic field of $\mu_0 H_{\mathrm{oop}} = 88\,\mathrm{mT}$ reveals the coexistence of type-2 bubbles, Bloch skyrmions with both cw and ccw chiralities, and antiskyrmions (Fig. 5.21 c, f). In Fig. 5.21 d and g only topologically protected spin structures (skyrmions/antiskyrmions) remain at 95 mT. The micromagnetic simulations are in excellent agreement with the experimental observations (Fig. 5.19). They exhibit the same coexistence of bubbles, skyrmions, and antiskyrmions with a decreasing density of bubbles for larger applied fields.

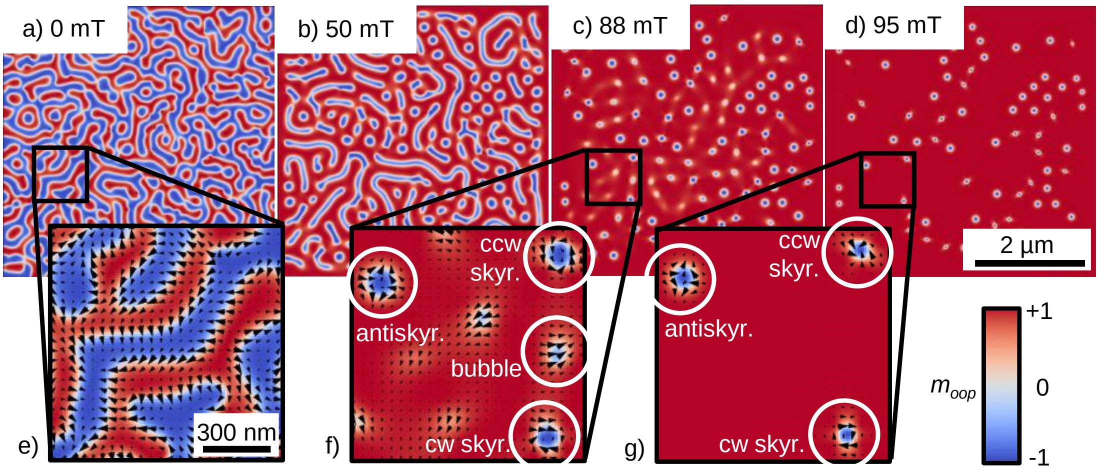

Figure 5.21: Micromagnetic simulations of the domain morphology in modified Fe/Gd multilayers. The domain morphology is simulated using magnetic parameters close to the sample $[\mathrm{Fe/Ir/Gd}]_2/[\mathrm{Fe/Gd}]_{76}/[\mathrm{Fe/Ir/Gd}]_2$. The domain morphology at a larger scale with the color illustrating the z- component of the magnetization (a-d). Enlarged images with black vectors showing the x- and y- components of the magnetization (e-g). The relaxed magnetization state at zero field, showing stripes with different chiralities bristled with Bloch lines (a, e). An external magnetic field of $\mu_0 H_{\mathrm{oop}} = 50\,\mathrm{mT}$ is applied, stripes and skyrmions are coexisting (b). An external magnetic field of $\mu_0 H_{\mathrm{oop}} = 88\,\mathrm{mT}$ reveals the coexistence of type-2 bubbles, Bloch skyrmions with both cw and ccw chiralities, and antiskyrmions (c, f). Only topologically protected spin structures (skyrmions/antiskyrmions) remain at 95 mT (d, g). The figure is also published in Ref. [426].

In order to exclude the possibility that the spin textures are stable in the micromagnetic simulations because of numerical errors and simulation artifacts, energy barrier simulations are performed by applying a full micromagnetic model [545, 549, 550]. The minimum energy paths with and without DMI to annihilate an antiskyrmion are calculated to obtain a saturated magnetic configuration along the oop direction and to transform an antiskyrmion into a skyrmion. The former is shown in Fig. 5.22 a and the latter in Fig. 5.22 b. All simulations show a clear energy barrier, reflecting the metastable nature of the antiskyrmion state. It is also observed that other energetically more favorable states need to be overcome in order to transform to skyrmions or the saturated state, making these transformations very costly from an energetic point-of-view. It has to be mentioned that, due to the change of the topological number N_{sk} from -1 to 1, Bloch like states are formed, and a micromagnetic treatment with a mesh size larger than the lattice constant underestimates the atomistic barrier [498].

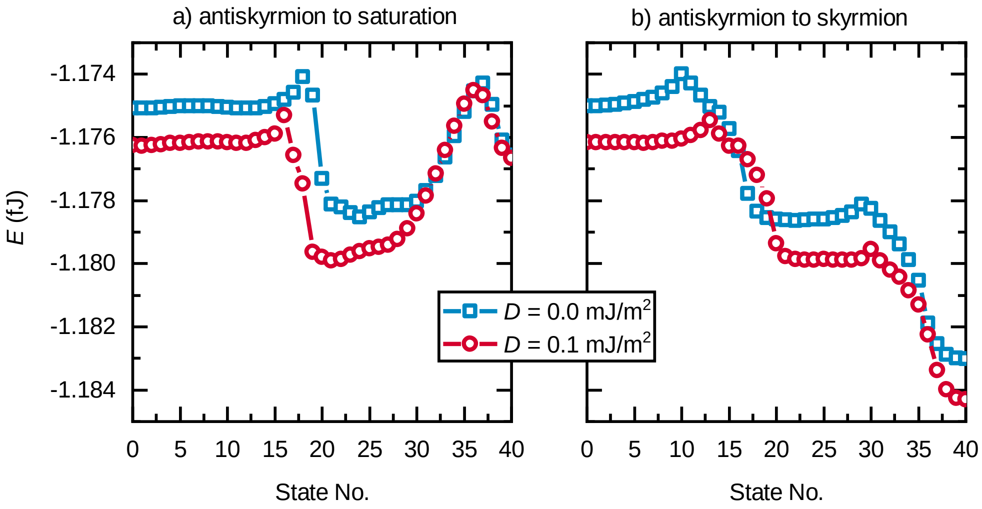

Figure 5.22: Micromagnetic simulations of the energy barriers between (anti-)skyrmion and saturation. Minimum energy paths to annihilate an antiskyrmion by saturation (a) and by transformation to a Bloch skyrmion (b). Both show a clear energy barrier for a DMI value D of 0.0 and 0.1 mJ/m^2, reflecting the metastable nature of the antiskyrmion state. The figure is also published in Ref. [426].

5.3.7 Nucleation of Antiskyrmions

In order to learn how to achieve an antiskyrmion state, the nucleation process of an antiskyrmion is investigated in more detail, both with LTEM imaging and micromagnetic simulations. Figure 5.23 a-e show a specific location of the [Fe/Ir/Gd]$_2$/[Fe/Gd]$_{76}$/[Fe/Ir/Gd]$_2$ sample at 200 K where an antiskyrmion eventually forms. The distinct feature that in all samples at $T < 250$ K antiskyrmions always nucleate from a crossing point of three stripes is observed. One of these crossing points is displayed in Fig. 5.23 a. Three stripes without a chirality meet, and due to the resulting ip components, one stable Bloch line emerges, resulting in contrast very similar to an antiskyrmion. With increasing field, the stripes shrink down, and one of them disconnects at 86 mT (Fig. 5.23 b). At 95 mT the Bloch line remains only connected to the very end of a single stripe. This stripe decreases in size until an isolated antiskyrmion is left at 105 mT (Fig. 5.23 d). The antiskyrmion shrinks with increasing field at 124 mT (Fig. 5.23 e). It is important to note that these crossing points of three stripes also exist in samples that do not exhibit antiskyrmions. Also, not all triple crossings of stripes with Bloch lines necessarily nucleate antiskyrmions if antiskyrmions exist. While the starting chirality of the crossing stripes does not seem to play a role, with increasing fields, the antiskyrmion always nucleated at the end of a stripe without chirality resembling a Bloch line. Very similar

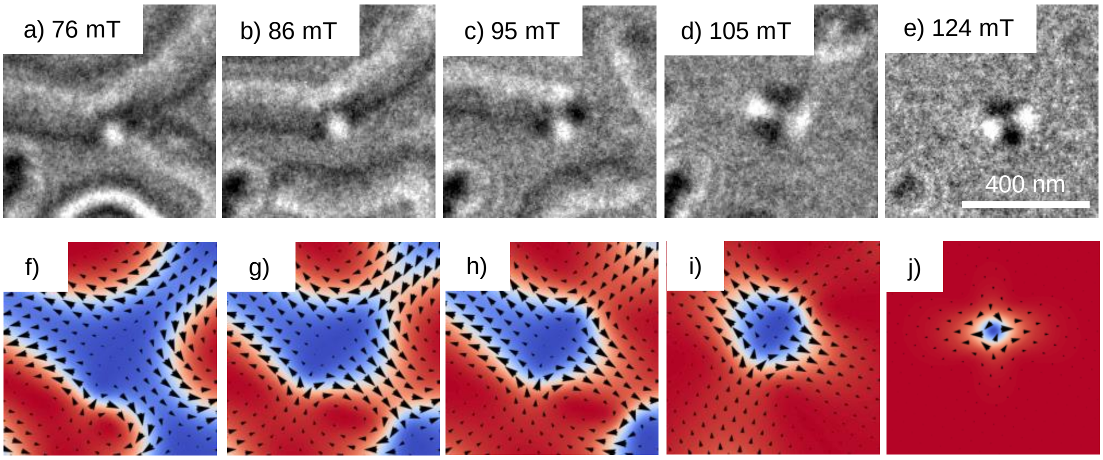

Figure 5.23: Nucleation process of antiskyrmions. Nucleation process of an antiskyrmion starting from a crossing point of three stripes without a chirality imaged by LTEM (a). The images stem from a skyrmion-hosting sample with $N_{\mathrm{Ir}} = 2$ at 200 K. b) and c) show the crossing point with only two and one stripe connected after the field is increased to 86 and 95 mT, respectively. The crossing point resembles a Bloch line and acts as the nucleation point of the antiskyrmion after the final stripe shrinks down at 105 mT (d). The antiskyrmion shrinks with an increasing field at 124 mT (e). As a comparison, the nucleation process in the micromagnetic simulations is displayed in f-j). The simulation parameters are the same as in Fig. 5.21. A very similar process is observed here. The figure is also published in Ref. [426].

nucleation processes can be found in the micromagnetic simulation, as displayed in Fig. 5.23 f-j. The process also starts at a crossing point of three stripes (Fig. 5.23 f) and ends with an isolated antiskyrmion (Fig. 5.23 i,h). In the simulation, antiskyrmions exclusively originate from these triple crossing points for saturation magnetization values between 175 kA/m and 325 kA/m using a K_{u} value of 22 kJ/m^3. This behavior agrees well with the experimental data.

Additionally, micromagnetic simulations of the nucleation process of a ccw Bloch skyrmion, a cw Bloch skyrmion, a first-order antiskyrmion, and a second-order antiskyrmion can be found in Fig. A.14 a, b, c, and d, respectively. Please note that only the nucleation processes of the Bloch skyrmions and the first-order antiskyrmion could be observed experimentally. Due to the rarity of second-order antiskyrmions and no possibility to predict possible nucleation spots, imaging of the formation process was not achieved.

5.3.8 Antiskyrmion Recipe

To get a better understanding of the necessary parameter space to stabilize the different spin objects, the relevant magnetic properties are measured. M_s is extracted from magnetometry measurements, while FMR measurements are carried out to determine the K_u values. Due to the inclusion of heavy metal materials in the form of Ir in the MLs, an interface DMI contribution has to be considered. It was also shown that bulk DMI can even exist in inhomogeneous ferrimagnetic alloys [551]. The DMI constant D is measured by Brillouin light scattering (BLS) [250]. The Fe/Gd ML without Ir shows no measurable DMI, while the ML with five Ir layers at the top and bottom ($N_\mathrm{Ir} = 5$) exhibits a D value of $(0.10 \pm 0.01)\,\mathrm{mJ/m^2}$. This value is more than an order of magnitude smaller than typical values for DMI-stabilized skyrmions [552]. Previous works [128, 149] established that the ratio of K_u and M_s is crucial for the formation of stripe domains and skyrmions [109, 553].

In Fig. 5.24 the M_s and K_u values are plotted for temperatures between 100 and 300 K. The corresponding topologically protected spin objects, which are experimentally observed, are marked. In addition, results reported by Montoya et al. [128] obtained for similar systems are included exhibiting exclusively Bloch skyrmions at higher M_s values (blue triangles). The purple squares correspond to samples that showed antiskyrmions under the investigated applied oop magnetic fields. These antiskyrmions always coexist with skyrmions and sometimes with bubbles. Blue and white squares correspond to the existence of sole skyrmions and ip domains without further spin objects, respectively. Figure 5.24 reveals the importance of low M_s values satisfying the condition $\frac{1}{2}\mu_0 M_\mathrm{s}^2 > K_\mathrm{u}$ for stabilizing (anti-)skyrmions.

In order to get an understanding of how M_s and K_u affect the underlying spin texture, additional micromagnetic simulations are performed. The simulations are carried out with zero DMI and a constant film thickness of 62 nm. The starting spin configuration for the simulations is an isolated Bloch skyrmion and an isolated antiskyrmion. Their stability is probed at different applied oop fields between 0 and 125 mT. The regions where these spin objects are at least stable at one of the fields are marked by color in Fig. 5.24. The purple region marks the parameter range in which the initial antiskyrmion stays stable. The blue region marks parameters in which the skyrmion is stable. The underlying diagrams for specific fields are displayed in the appendix (Fig. A.15). It is important to note that the simulations do not convey the possible formation path of (anti-)skyrmions. This leads to stable skyrmions and antiskyrmions at very low K_u values, while experimentally, this parameter range leads to pure in-plane domains

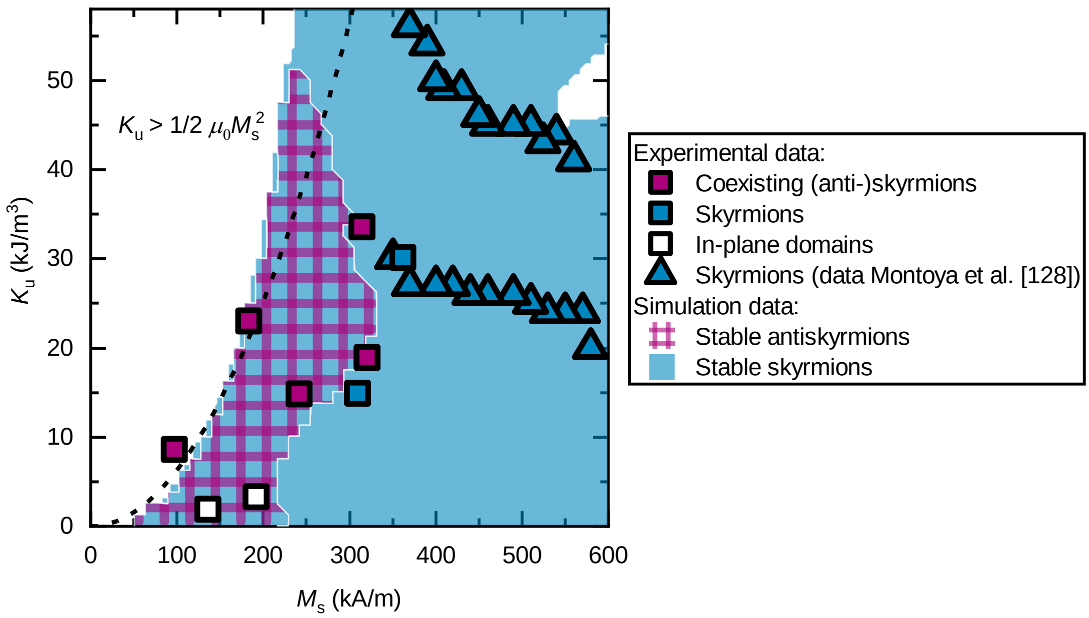

Figure 5.24: Phase diagram of antiskyrmions and skyrmions. The diagram includes both experimental and simulation results depending on the uniaxial magnetic anisotropy K_u and saturation magnetization M_s. The squares correspond to LTEM measurements that show antiskyrmions and skyrmions coexisting (purple), solely skyrmions (blue), and no visible spin objects (white) and their K_u and M_s values at the measured temperature. The triangles are experimental data points reported by Montoya et al. [128] obtained for similar Fe/Gd systems, which show exclusively skyrmions. The colored areas of the diagram correspond to the parameter regions in which skyrmions (blue) and antiskyrmions (purple) are stable in the simulations. In the white regions, neither of them is stable. The dashed line shows $K_u = \frac{1}{2}\mu_0 M_s^2$. The figure is also published in Ref. [426].

instead of stripe domains which are necessary to form the described spin objects (white squares). The simulations reveal a pocket in the phase diagram at small K_u and M_s where antiskyrmions are at least metastable. In agreement with the experiments, there is no exclusive antiskyrmion phase. The simulations also show that various spin objects exist if the magnetic shape anisotropy ($\frac{1}{2}\mu_0 M_s^2$) is larger than K_u (right side of the dashed line). The simulation matches the experimental data very well, revealing a delicate balance of interactions that is achieved for the samples by the insertion of Ir layers moving the samples' parameters further to a novel phase region of metastable antiskyrmions. By making use of a different composition of Fe/Gd layers and the introduction of Ir insertion layers, the experiments show particularly low values for M_s and K_u, an aspect of crucial importance.

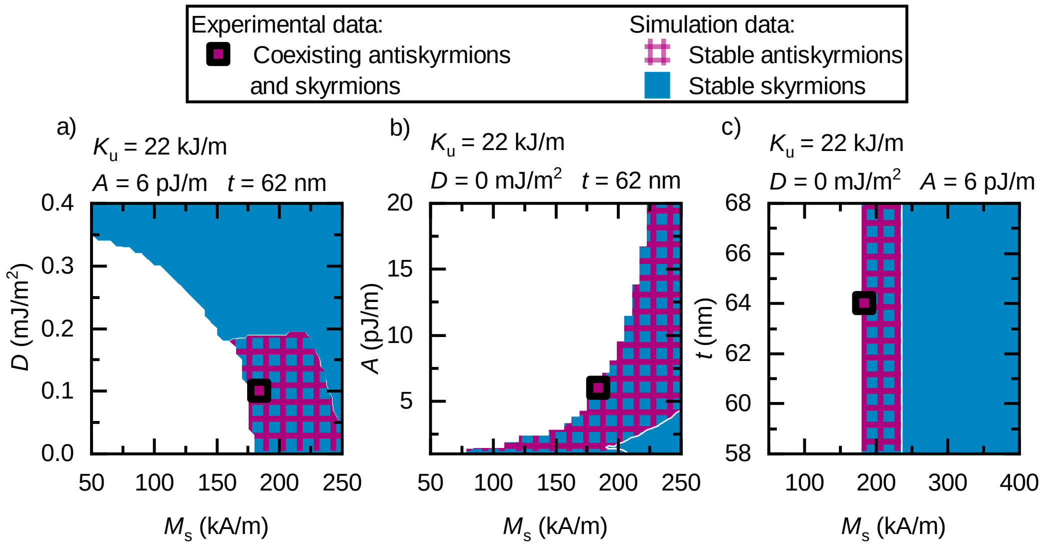

Figure 5.25: Micromagnetic simulations of the stability phase maps of an antiskyrmion and a skyrmion at different magnetic parameters. The colored areas of the diagram correspond to the parameter regions in which skyrmions (blue) and antiskyrmions (purple) are stable in the simulations dependent on the DMI value D (a), exchange stiffness constant A (b), and the thickness t (c) against the saturation magnetization M_S. In the white regions, neither of them is stable. The purple square represents the experimentally observed coexisting antiskyrmions and skyrmions in the range of the given parameters.

For different thicknesses, exchange stiffness constants, and DMI values, additional simulations are conducted (Fig. 5.25), showing only a minor impact on the formation and stability of the spin objects in the analyzed parameter range. However, for DMI values greater than 0.2 mJ/m^2 antiskyrmions no longer exist, and skyrmions dominate. Figure 5.25 shows that the other magnetic values also lie in the right regime where antiskyrmions can be nucleated and stabilized. The purple square corresponds to the experimental measurement of $[Fe/Ir/Gd]_5/[Fe/Gd]_{70}/[Fe/Ir/Gd]_5$ at 100 K, which showed coexisting skyrmions and antiskyrmions. Figure 5.25 a shows that a DMI value higher than $D = 0.2\,\mathrm{mJ/m^2}$ leads to a system where the antiskyrmion is no longer a stable configuration, and skyrmions dominate. Additionally, exchange interactions influence the window of stable antiskyrmions, as shown in Fig. 5.25 b. Increasing M_s values need also a larger exchange stiffness constants A to stabilize antiskyrmions. These simulations have been performed without DMI and an uniaxial magnetic anisotropy constant $K_u = 22\,\mathrm{kJ/m^3}$ is used. To show that the total thickness of the investigated samples does not influence the stability of the antiskyrmions, the thickness of the magnetic material is varied together with M_s (Fig. 5.25 c). Further material parameters are chosen as $A = 6\,\mathrm{pJ/m}$, $D = 0\,\mathrm{mJ/m^2}$, and $K_u = 22\,\mathrm{kJ/m^3}$. It is evident that the thickness in the simulated and fabricated range does not lead to any deviations from the described antiskyrmion recipe.

5.3.9 Fe/Gd Multilayers with Different Insertion Layers

In order to further investigate the influence of the Ir insertion layers on the Fe/Gd MLs, additional layer stacks with modified insertion layer positions, thicknesses, and materials are studied. Six different layer stacks are fabricated, and the measured *M-H* oop and ip hysteresis loops of the MLs are displayed for temperatures between 50 and 350 K in Fig. 5.26. Please note that these samples are not directly comparable to the samples investigated before because they are not part of the same deposition run.

The sample displayed in Fig. 5.26 a and b has the same amount of Ir insertion layers as $[\mathrm{Fe/Ir/Gd}]_5/[\mathrm{Fe/Gd}]_{76}/[\mathrm{Fe/Ir/Gd}]_5$. However, their Ir layers are distributed homogeneously over the whole sample thickness. The sample of Fig. 5.26 c and d has a change in the order of the underlying trilayer of the ML. Here, Fe is deposited on top of the Ir layer and Gd on top of the Fe layer. Figure 5.26 e and f display loops of a sample with three times the thickness of Ir (0.6 nm) in comparison to the thickness of previous Ir layers (0.2 nm). These three samples with Ir insertion layers behave all relatively similarly and show openings close to their saturation at different fields and temperatures. Due to the similar M_s values and shapes of the loops in Fig. 5.26 a and b in comparison to Fig. 5.15 e and f, no direct magnetic difference for a different distribution of the Ir insertion layers can be found. However, the order of the individual layers plays a significant role, which is apparent in direct comparison to Fig. 5.26 c and d. More magnetization is induced in Ir grown on top of Fe than beneath it. Therefore, the sample of Fig. 5.26 a and b exhibits a larger M_s value than the sample of Fig. 5.26 c and d. The influence of the stacking order of Fe/Ir is described in more detail in Ref. [554]. It is also evident that thicker Ir layers in Fig. 5.26 e and f lead to a larger induced moment by the adjacent Fe layer and therefore to a smaller M_s in the Gd dominant ML. For these thin individual layers, an increased induced moment with an increase in thickness is expected due to direct ferromagnetic interaction [554, 555].

Figure 5.26 g-l shows samples with Pt, Cu, or Al as insertion layers. Please note that the magnetization scale of the samples with Cu and Al is different from the sample with Pt insertion layers. While Pt displays similar properties as Ir as an insertion layer, Cu and Al lead to no reduction in the M_s values. This can be explained by the strong

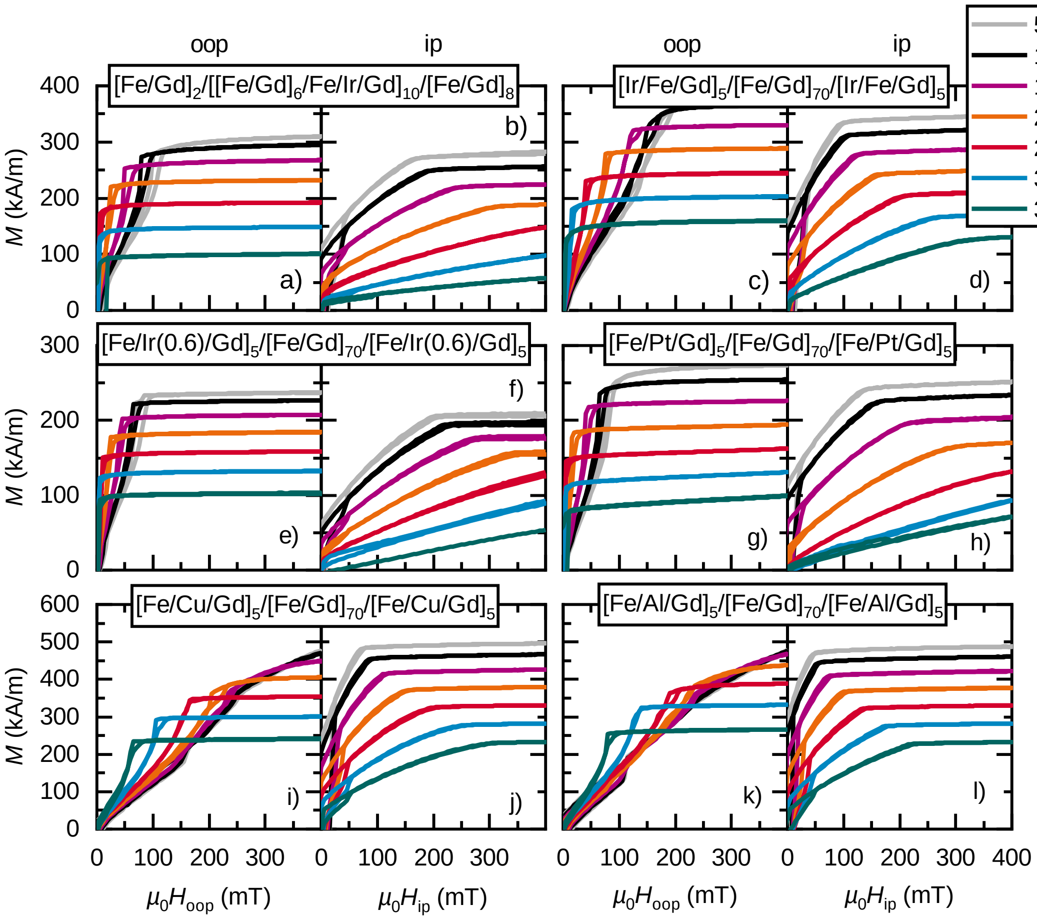

Figure 5.26: Hysteresis loops of Fe/Gd multilayers with different insertion layer positions, thicknesses, and materials. *M*-*H* hysteresis loops of a layer stack with homogeneously distributed Ir layers (a, b), Ir layers at the bottom of the underlying trilayer (c, d), Ir layers with three times the thickness (0.6 nm) (e, f), Pt insertion layers (g, h), Cu insertion layers (i, j), and Al insertion layers (k, l).

spin-orbit coupling of Ir and Pt, which is absent in Cu and Al. However, Cu and Al still exhibit induced moment due to the proximity effect, although it is typically comparably small [556, 557].

Exemplary LTEM images of the samples with Pt and Al insertion layers are displayed in Fig. A.9. The spin texture of the sample with Cu shows a nearly identical behavior as the Al sample and is therefore not shown. The RT measurements show coexisting antiskyrmions and skyrmions in the sample with Pt and only skyrmions and bubbles in the sample with Al insertion layers. This observation confirms the antiskyrmion recipe of the previous subsection (Fig. 5.24). Under the assumption that the magnetic parameters, like exchange stiffness and DMI, are comparable, only samples with M_s values roughly beneath 300 kA/m can stabilize antiskyrmions (Fig. 5.24), which is not the case for the sample with Al insertion layers (Fig. 5.26 k, l).

5.3.10 Conclusion about Antiskyrmions in Fe/Gd-Based Multilayers

This section demonstrates the possibility of stabilizing antiskyrmions primarily by dipole-dipole interaction at RT. For the first time, second-order antiskyrmions are experimentally observed, and first-order antiskyrmions are stabilized outside of $\mathrm{D_{2d}}$ Heusler or S4 schreibersite compounds. The novel spin objects are imaged by LTEM and coexist in Fe/Gd-based multilayers together with Bloch skyrmions and topological trivial type-2 bubbles. Phase diagrams of the spin objects are created in dependence on the oop magnetic field, temperature, saturation magnetization, and uniaxial magnetic anisotropy. Micromagnetic simulations confirmed the phase pocket of metastable antiskyrmions for low saturation magnetization and uniaxial magnetic anisotropy values satisfying the condition $\frac{1}{2}\mu_0 M_\mathrm{s}^2 > K_\mathrm{u}$. The phase pocket is confirmed for Fe/Gd MLs and Fe/Gd MLs modified by Ir and Pt insertion layers. Further, the nucleation process of antiskyrmions reveals the necessity of a crossing point of three magnetic stripe domains to form an isolated antiskyrmion with an oop magnetic field. This discovery significantly simplifies future investigations of antiskyrmions. Additionally, the coexisting phases of different topologically protected spin objects provide great potential for further studies on quasi-particle interactions, spin dynamics, as well as for possible future applications in spintronics.

5.4 Comparison between Different Imaging Techniques

Up until now, the spin textures of this chapter are only imaged by LTEM in the Fresnel mode. However, there are other imaging options with their own advantages and disadvantages, which are presented in this section by exemplary measurements of Fe/Gd-based MLs. The different techniques are already introduced in Sec. 3.3.

5.4.1 Imaging of Spin Textures by Magnetic Force Microscopy

First, magnetic force microscopy (MFM) is presented as an imaging technique for the previously described spin textures. Figure 5.27 displays a comparison between LTEM in the Fresnel mode (a-d) and MFM (e-h) of $[\mathrm{Fe}(0.35)/\mathrm{Gd}(0.40)]_{120}$ at RT. The MFM measurements are carried out at the University of Augsburg with a Bruker Dimension

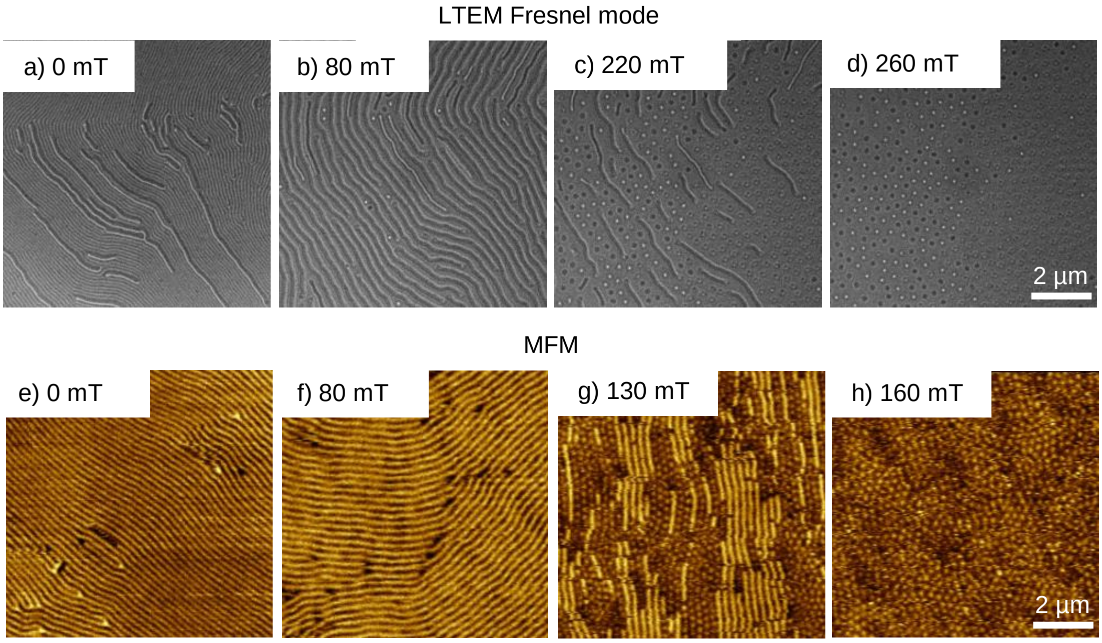

Figure 5.27: Comparison between ambient MFM and LTEM Fresnel imaging. LTEM images of $[\mathrm{Fe}(0.35)/\mathrm{Gd}(0.40)]_{120}$ at RT and at different applied oop magnetic fields (a-d). MFM images of the same sample also at RT and at different applied oop magnetic fields (e-h).

FastScan microscope under ambient conditions. This system has no built-in option to apply magnetic fields. Therefore, permanent magnets and spacers are used. To change the applied magnetic field, the measurement is stopped, and the setup is modified with other magnets or spacers. Hence, the measured areas of the MFM images differ. This makes it impossible to image continuous transformations of certain spin textures with changing magnetic fields. Further, MFM visualizes the stray fields at the surface of the magnetic sample. Therefore, only contrast between different magnetic oop components or ip divergences of the magnetization is detectable. Hence, a stripe pattern is visible, but the different chiralities of the stripes are not (Fig. 5.27 e-g). In a direct comparison, it is evident that the periodicity of the MFM stripes agrees very well with the larger black and white stripes of the LTEM images (Fig. 5.27 a, b). Similarly, the contrast in Fig. 5.27 g and h reveals round magnetic objects without any further ip information. While the stray field of Bloch skyrmions and bubbles theoretically differs (Fig. 5.28 b, c), the resolution of the shown measurements is not able to resolve these small variations. The direct comparison to the LTEM images in Fig. 5.27 c and d reveals that Bloch skyrmions and bubbles can coexist in this sample in the measured state. However, they are not distinguishable by the shown MFM measurements, and therefore no statement can be made about which kinds of spin objects are depicted in Fig. 5.27 g and h. Another significant difference between the MFM and LTEM measurements is the necessary strength of the magnetic field to achieve certain spin texture states. While a skyrmion bubble lattice is achieved at around 260 mT in the LTEM measurement, only 160 mT are necessary during the MFM measurement. There are multiple possible reasons for this discrepancy. On the one hand, the measurement temperatures differ. While both measurements are carried out at ambient temperatures, a difference of up to 10 K can occur. The large temperature influence on the magnetic properties of these samples was already discussed in the previous sections. On the other hand, the measurements of the magnetic field and its calibration could be incorrect to a certain degree. Also, while both samples were deposited during the same sputter run, their substrate, as well as their position inside the sputter chamber, differ. Therefore, the samples could show slightly different magnetic properties. Further, the LTEM SiN membrane and its morphology make a difference, which is further investigated in Sec. 5.5.3.

Overall, ambient MFM can be used as a fast and comparably cheap way to obtain first information about the domain morphology of a sample and the possible existence of spin objects. However, it can not replace LTEM due to its lack of information about the ip magnetization components.

Next, a high-resolution MFM at the EMPA in Switzerland is used to image the different spin objects in $[\mathrm{Fe/Ir/Gd}]_{10}/[\mathrm{Fe/Gd}]_{60}/[\mathrm{Fe/Ir/Gd}]_{10}$. In Fig. 5.28 a the result of a RT measurement at an applied oop magnetic field of 46 mT is shown. The equivalent LTEM measurements of this sample with different oop fields at RT are shown in Fig. A.7 a-d. Figure 5.28 b-d display three different measured zoomed-in spin objects (I), the simulated oop stray fields taken at 9 nm above the sample surface (II), and the underlying theoretical spin textures (III). In Fig. 5.28 b-d III, the arrows and their color depict the directions of the ip components, with their sizes displaying the strengths. The agreement between the simulated oop stray field and the measured contrast confirms the distinguishability of Bloch skyrmions, type-2 bubbles, and first-order antiskyrmions with high-resolution MFM. Please note that the rotation direction of Bloch skyrmions can not be determined by MFM.

In summary, high-resolution MFM is a suitable tool to image and differentiate dipolar-stabilized spin objects. The imaging of skyrmions with MFM is quite common [165, 558]. However, the differentiation of different types of skyrmions and spin objects is difficult and only possible due to the relatively large sizes of the presented spin objects

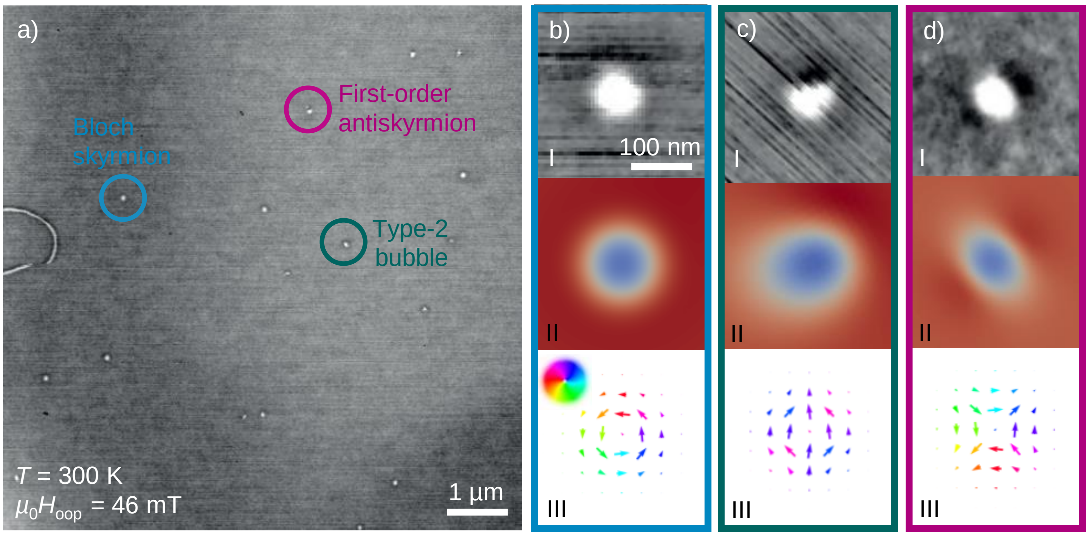

Figure 5.28: Spin objects imaged by high-resolution MFM. High-resolution MFM image of $[\mathrm{Fe/Ir/Gd}]_{10}/[\mathrm{Fe/Gd}]_{60}/[\mathrm{Fe/Ir/Gd}]_{10}$ with an applied oop magnetic field H_{oop} of 46 mT at $T = 300\,\mathrm{K}$ (a). b-d, I) display the measured zoomed-in spin objects. b-d, II) show the simulated oop stray fields taken at 9 nm above the sample surface caused by the theoretical spin textures shown in b-d, III). In b-d, III) the arrows and their color depict the directions of the ip components, with their sizes displaying the strengths. Bloch skyrmion (b), type-2 bubble (c), and first-order antiskyrmion (d).

in comparison to DMI skyrmions with radii below 100 nm. While high-resolution MFM imaging is not necessarily less work-intensive than LTEM imaging, it represents a great alternative. This applies in particular if the deposition on a membrane is not an option or in situ contacting during the measurement is required. Additionally, MFM is sensitive to the moments at the surface of the sample, while LTEM provides information from the superposition of all moments along its thickness. This is particularly interesting if the spin texture is inhomogeneous along the thickness. Therefore, a combination of LTEM and high-resolution MFM provides a possible way to image 3D spin textures to a certain extent. A similar method of combining surface and transmission imaging tools was used to confirm the existence of hopfions [156].

5.4.2 Imaging with Different Lorentz Transmission Electron Microscope Techniques

Additionally to the Fresnel mode, LTEM offers multiple other modes and techniques to image magnetic textures, as presented in Sec. 3.3.3. The most prominently used technique is the creation of magnetic induction maps with Fresnel images.

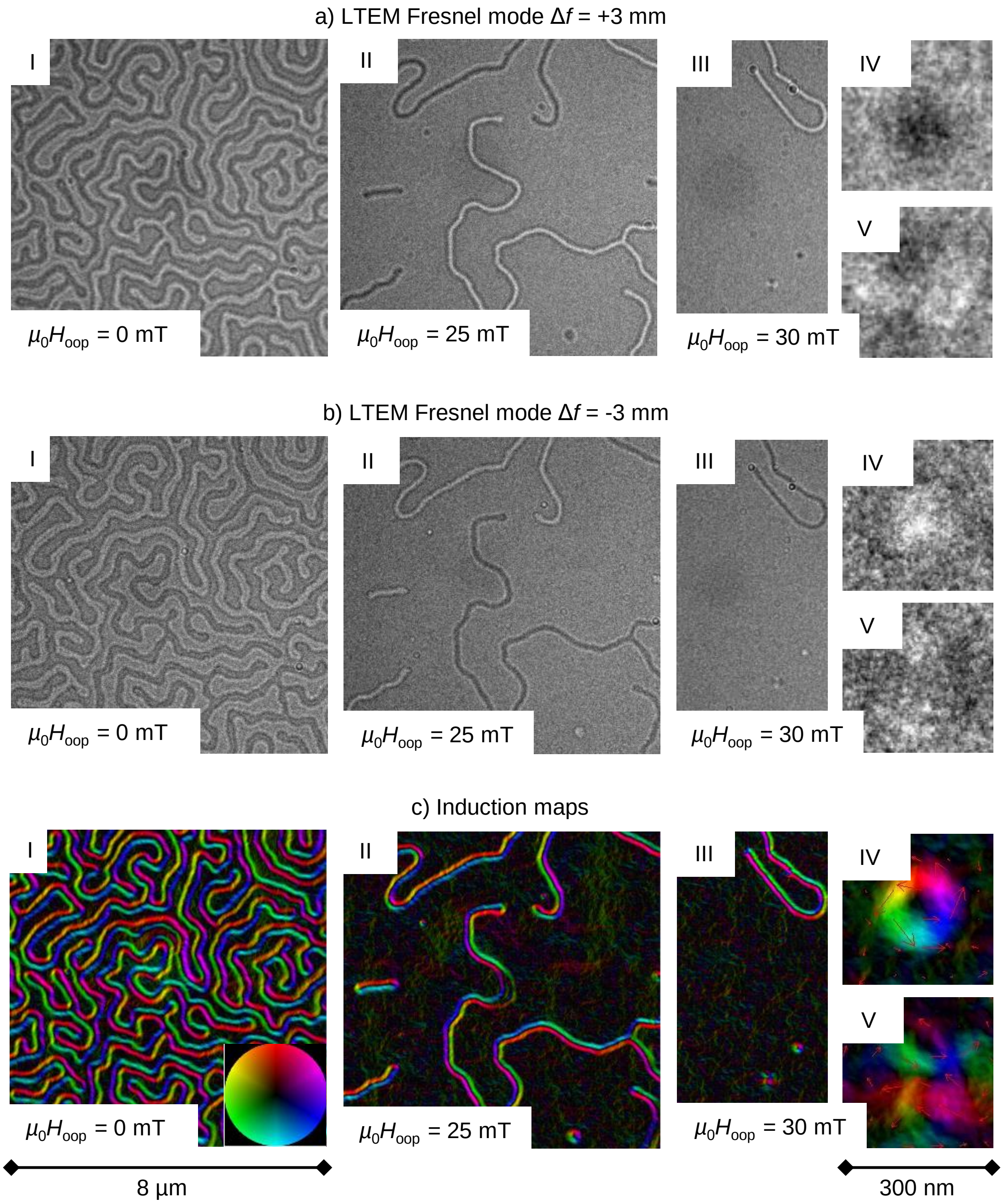

Figure 5.29: Exemplary magnetic induction maps and the underlying LTEM Fresnel images at different magnetic fields. LTEM Fresnel images of $[Fe/Ir/Gd]_{20}/[Fe/Gd]_{40}/[Fe/Ir/Gd]_{20}$ in an overfocus of 3 mm (a) and an underfocus of -3 mm (b) at an applied oop magnetic field of 0 mT (I), 25 mT (II), and 30 mT (III). Zoomed-in images of a counterclockwise skyrmion (IV) and antiskyrmion (V). c) shows the resulting color coded induction maps.

Here, a series of Fresnel LTEM images at different focal lengths are used to calculate magnetic induction maps by the transport of intensity equation. Figure 5.29 displays the magnetic induction map and its underlying LTEM images of $[\mathrm{Fe/Ir/Gd}]_{20}/[\mathrm{Fe/Gd}]_{40}/[\mathrm{Fe/Ir/Gd}]_{20}$ at the two different defocus values of $\Delta f = +3$ and -3 mm at RT and different applied oop magnetic fields. An additional image in focus is used to filter contrast caused by structural features (not shown). Please note that images with additional defocus values can improve the quality of the resulting induction map. However, all images need to be precisely aligned with one another, which is challenging due to shifts in the imaged area, rotation, and magnification with different defocus values. Figure 5.29 a and b are identical besides the inverted contrasts. Panels I-III are all taken from slightly different areas of the sample. Panel IV and V show the zoomed-in image of a counterclockwise skyrmion and an antiskyrmion, respectively. The resulting induction maps in Fig. 5.29 c use a color code to indicate the direction of their ip magnetic components. The ip direction corresponds to the position of a given color in the color wheel in the bottom right corner of panel I. In panel II, a skyrmion is visible in the bottom right corner. Additionally, smaller round objects with a similar color gradient are observed. They are artifacts caused by structural inhomogeneities or contaminations. The broadening of the stripe in the middle of panel II originates from a slight movement of the stripe while the focus was changed. The coexisting skyrmion and antiskyrmion in panel III are also imaged and zoomed-in in panel IV and V, respectively. While the counterclockwise Bloch type of the skyrmion is clearly visible in the induction map, the imaged ip components of the antiskyrmion are less conclusive. Here, the underlying resolution limit of the Fresnel mode (Sec. 3.3.3), as well as the small magnetic signal of the sample, take their toll.

However, the advantage of the depiction of LTEM images as induction maps is clear: the ip moments are directly visualized, and there is no need to interpret a certain pattern of contrast. However, more than double the amount of data needs to be captured and analyzed in comparison to pure Fresnel images. Further, the sample needs to be magnetically stable and show no domain changes while the focus values are changed.

Another option to directly image the ip magnetic moments with TEM is the differential phase contrast (DPC) mode (Sec. 3.3.3). Figure 5.30 shows a Fresnel LTEM image (a) and a image captured in the DPC mode (b) of $[\mathrm{Fe}(0.35)/\mathrm{Gd}(0.40)]_{80}$ at RT and zero field in a direct comparison. The colors of the DPC image depict the ip magnetic components direction and correspond to the color wheel in the top right. All stripes in the shown images exhibit one chirality, which is evident in both images. While, in theory,

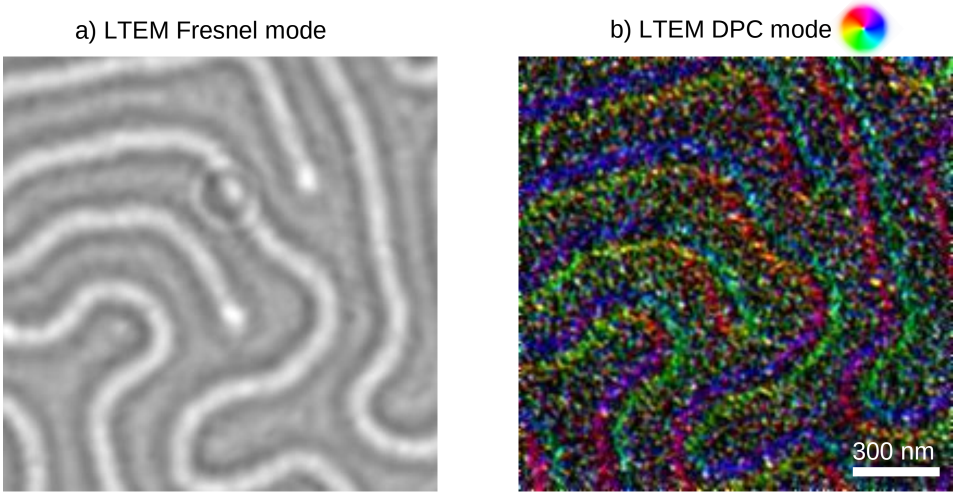

Figure 5.30: Magnetic stripe domains visualized by the differential phase contrast mode in comparison to the LTEM Fresnel mode. Stripe domains of [Fe(0.35/Gd(0.40)]$_{80}$ imaged by LTEM in the Fresnel mode (a). The same area imaged by the differential phase contrast mode (DPC) (b). The colors depict the ip magnetic components direction corresponding to the color wheel.

DPC provides one order of magnitude better resolution than the Fresnel mode [242], DPC fails to probably image the presented sample due to the structural inhomogeneities. In general, DPC is better suited for monocrystalline samples [559]. Other disadvantages of DPC are the long measuring times and large amounts of created data, especially in comparison to the Fresnel mode.

5.5 Influence of an In-Plane Magnetic Field on Spin Textures

In 2020, J. Jena et al. demonstrated the coexistence of antiskyrmions and skyrmions in D_{2d} symmetry systems and, with it, the importance of ip fields to nucleate specific spin objects [140]. In the same year, Peng et al. showed the controlled transformation of antiskyrmions, skyrmions, and bubbles with ip fields in a similar system [141]. Further, Je et al. demonstrated the controlled nucleation of bubble or skyrmion lattices by an applied ip field in Fe/Gd MLs [560].

Hence, an ip magnetic field is a promising instrument to manipulate and transform coexisting spin objects, which is further investigated for Fe/Gd MLs with Ir insertion layers in this section. In particular, three samples are used: [Fe/Ir/Gd]$_{20}$/[Fe/Gd]$_{40}$/[Fe/Ir/Gd]$_{20}$, which was previously discussed in Sec. 5.3, and two not-yet-discussed [Fe/Ir/Gd(t$_{\mathrm{Gd}}$)]$_{5}$/[Fe/Gd(t$_{\mathrm{Gd}}$)]$_{70}$/[Fe/Ir/Gd(t$_{\mathrm{Gd}}$)]$_{5}$ samples with t_{Gd} =0.40 and 0.45 nm,

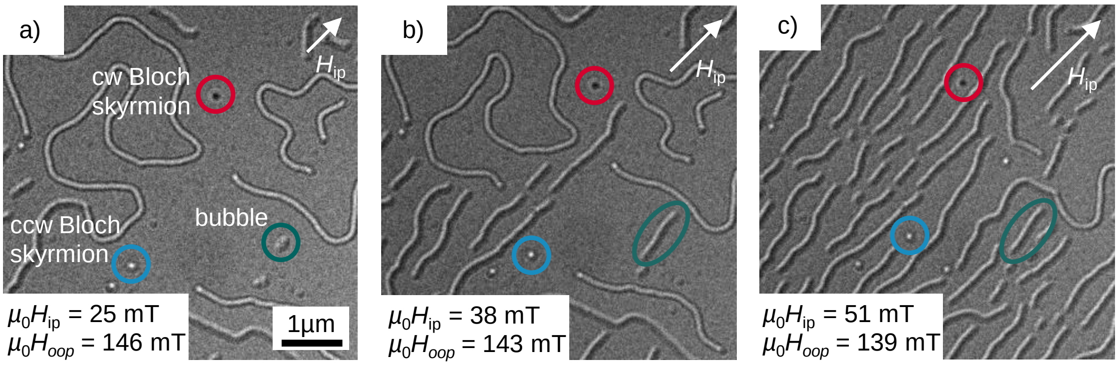

Figure 5.31: Influence of an in-plane magnetic field on the magnetic textures. LTEM images of [Fe/Ir/Gd(0.4)]$_5$/[Fe/Gd(0.4)]$_{70}$/[Fe/Ir/Gd(0.4)]$_5$ at different ip and oop fields at RT. The oop field component H_{oop} is decreasing with increasing tilt angle, while the ip field component H_{ip} is increasing (a-c). The corresponding tilt angles are 10 ° (a), 15 ° (b) and 20 ° (c). Spin textures without a chirality align with the ip field, while textures with a chirality shrink down or are relatively unaffected.

which do not exhibit antiskyrmions due to their too large saturation magnetization. The exact composition and sputter parameters can be found in Sec. A.4. Please note that these samples stem from a different deposition series and are therefore not directly comparable to the previous samples with the same or similar compositions. *M*-*H* hysteresis loops and LTEM measurements without an ip field of the new samples can be found in the appendix in Fig. A.1 and Fig. A.10, respectively.

Figure 5.31 shows the influence of an ip magnetic field on the different stripe domains and spin objects in [Fe/Ir/Gd(0.4)]$_5$/[Fe/Gd(0.4)]$_{70}$/[Fe/Ir/Gd(0.4)]$_5$. The measurement is carried out at RT, and the effective oop and ip magnetic fields are changed between Fig. 5.31 a, b, and c by tilting the sample holder. Generally, the oop field component decreases with an increasing tilt angle, while the ip field component increases. Figure 5.31 a, b, and c correspond to tilting angles of 10, 15, and 20°.

At low ip fields and tilt angles, no change to the initial spin texture state is visible. Stripe domains with and without chirality, Bloch skyrmions, and bubbles coexist (Fig. 5.31 a). If the ip field component is further increased, additional stripe domains without a chirality nucleate, while stripes with a chirality shrink in size (Fig. 5.31 b, c). Bubbles orientate with the field or grow to stripes without a chirality. Generally, stripes without a chirality align with the ip field, while stripes with a chirality do not. Skyrmions seem to be not affected by the applied ip fields. The different responses of spin textures with or without chiralities can be explained by their spin configurations. Spin textures without a chirality have a direction in which the majority of ip magnetization components point, while textures with a chirality do not have that. Therefore, the Zeeman energy is only decreased for correctly aligned spin textures without a chirality and does not change for differently aligned spin textures with a chirality. It has to be noted that due to the simultaneous change in the oop and ip magnetic field components, the changes in the spin textures can not necessarily be attributed to one or the other. However, changes in the orientation of the different spin textures can solely be attributed to the ip field. The ip rotation of stripe domains without a chirality depending on the various energy contributions was previously studied for 65-nm-thick FeGa samples in Ref. [561]. Generally, the sensitivity of a sample with respect to an ip field can be identified by the ip *M*-*H* hysteresis loop and its slope.

The measurements in the following subsections use a constant oop field while the ip field is varied. This can be achieved by increasing the applied magnetic field accordingly to the tilt angle to counterbalance the reduction of the oop field component.

5.5.1 Transformation of Spin Objects by an In-Plane Magnetic Field

Next, the influence of an ip magnetic field on the different spin objects is investigated, in particular, the stability ranges at a constant oop field and an increasing ip field.

Figure 5.32 a shows coexisting skyrmions and an antiskyrmion in $[Fe/Ir/Gd]_{20}$/$[Fe/Gd]_{40}$/$[Fe/Ir/Gd]_{20}$ at RT and an applied oop magnetic field of 31 mT. Here, the antiskyrmion stays stable up to an ip field of 11 mT. At this field it transforms to a bubble (Fig. 5.32 b). The observed Bloch skyrmions transform to bubbles at an ip field of 26 mT

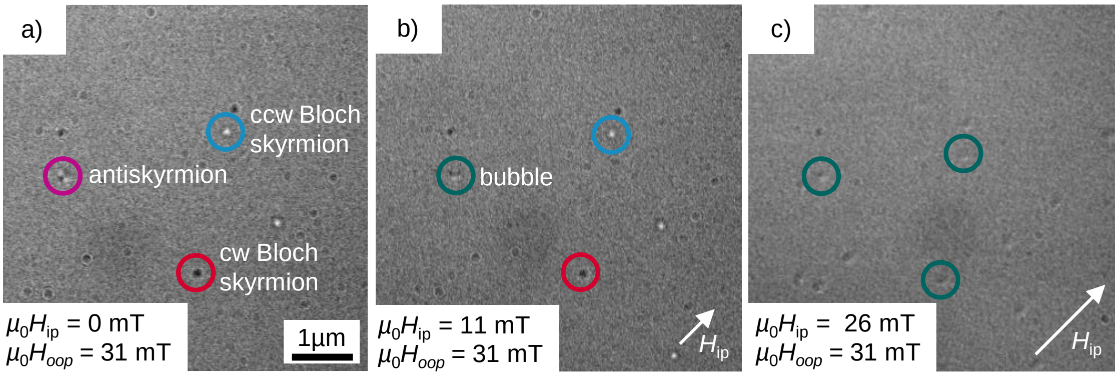

Figure 5.32: Influence of an in-plane magnetic field on different spin objects. LTEM images of $[Fe/Ir/Gd]_{20}$/$[Fe/Gd]_{40}$/$[Fe/Ir/Gd]_{20}$ at different ip and oop fields at RT. Antiskyrmions and skyrmions are coexisting (a). At an ip field of 11 mT the antiskyrmion transforms to a bubble (b). At 26 mT all spin objects have transformed to bubbles, which are aligned with the ip field (c).

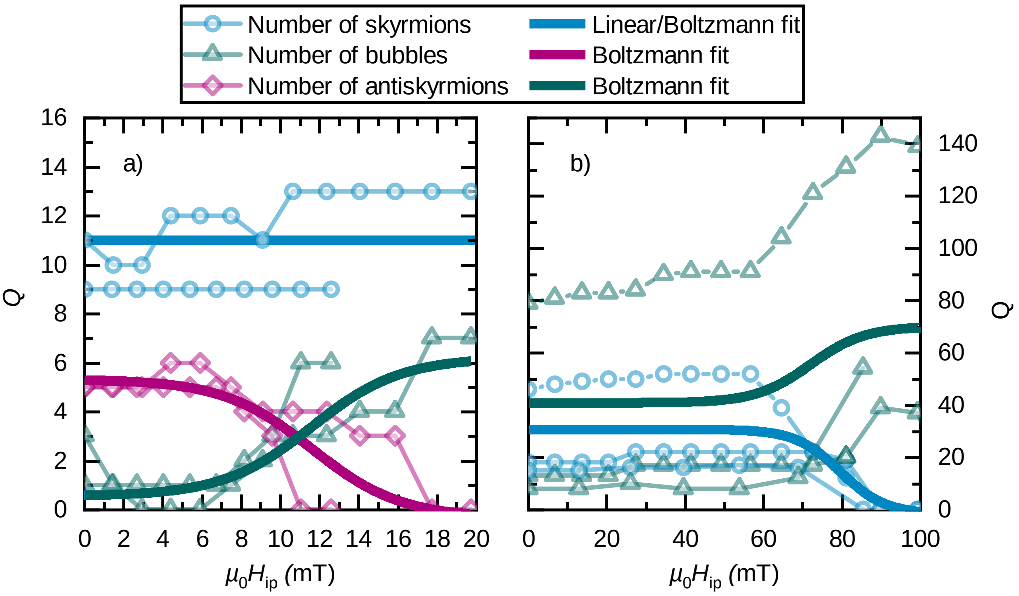

Figure 5.33: Quantity of the different spin objects dependent on the applied in-plane magnetic field. Quantity of skyrmions, bubbles, and antiskyrmions Q against the increasing ip field H_{ip} of two measurement series of $[\mathrm{Fe/Ir/Gd}]_{20}/[\mathrm{Fe/Gd}]_{40}/[\mathrm{Fe/Ir/Gd}]_{20}$ at a constant oop field of 31 mT at RT (a). The sum of the number of antiskyrmions and bubbles of both series is fitted by a Boltzmann function with a center at 11 mT. The number of skyrmions stays constant in the shown field range illustrated by the linear fit. The quantity of skyrmions and bubbles of $[\mathrm{Fe/Ir/Gd(0.4)}]_5/[\mathrm{Fe/Gd(0.4)}]_{70}/[\mathrm{Fe/Ir/Gd(0.4)}]_5$ against the increasing ip field at a constant oop field of 160 mT at RT (b). The transition from skyrmions to bubbles happens here at 75 mT.

(Fig. 5.32 c). All bubbles are aligned with the ip field in this state.

To quantify these transitions, multiple ip field sweeps are carried out, and the existence ranges of the different spin objects are tracked. For the sample $[\mathrm{Fe/Ir/Gd}]_{20}/[\mathrm{Fe/Gd}]_{40}/[\mathrm{Fe/Ir/Gd}]_{20}$ two measurements are carried out with ip fields ranging from 0 to 13 mT and 0 to 20 mT at RT. The oop field is fixed at 31 mT. The number of skyrmions, bubbles, and antiskyrmions is tracked and plotted in Fig. 5.33 a. Analogously, the number of skyrmions and bubbles is counted in $[\mathrm{Fe/Ir/Gd(0.4)}]_5/[\mathrm{Fe/Gd(0.4)}]_{70}/[\mathrm{Fe/Ir/Gd(0.4)}]_5$ for three increasing ip field sweeps and a fixed oop field of 160 mT at RT (Fig. 5.33 b). The increase or decrease in the number of spin objects is fitted by a Boltzmann fit. Figure 5.33 a confirms the observation in Fig. 5.32. The antiskyrmions transform to bubbles at approximately 11 mT, while the skyrmions stay stable up to fields larger than 20 mT. Figure 5.33 b shows a similar behavior for the transformation of skyrmions to bubbles. Here, the transition happens at around 75 mT. At ip fields above 100 mT the film saturates in the ip direction of the field (Fig. A.1 b).

Summarizing the stability ranges of the spin objects, topologically trivial bubbles are the preferred state at large ip fields. Skyrmions are more resilient to an ip magnetic field than antiskyrmions and therefore transform to bubbles at a larger ip field. Contradicting to Ref. [141], no transformation to skyrmions or antiskyrmions could be achieved consistently. The reason for this is that bubbles represent a stable state in the presented system. In Ref. [141] bubbles are only stable under an applied ip field and can therefore be exploited as a transitory spin configuration between skyrmions and antiskyrmions.

5.5.2 Rotation and Deformation of Spin Objects by an In-Plane Magnetic Field

Spin objects are also affected by the ip field before they transform to a different state. These early deformations and reorientations are studied in this subsection.

Figure 5.34 shows the rotation of existing bubbles with an increasing ip field in $[\mathrm{Fe/Ir/Gd(0.4)}]_5/[\mathrm{Fe/Gd(0.4)}]_{70}/[\mathrm{Fe/Ir/Gd(0.4)}]_5$ at RT and an applied oop magnetic field of 165 mT. The bubbles continuously rotate from a seemingly random orientation to the direction of the ip field without any significant changes in their size. The skyrmions are not affected in this field range. After the ip field is removed, the bubbles stay in their new orientation. It is, therefore, possible to selectively control the orientation of bubbles

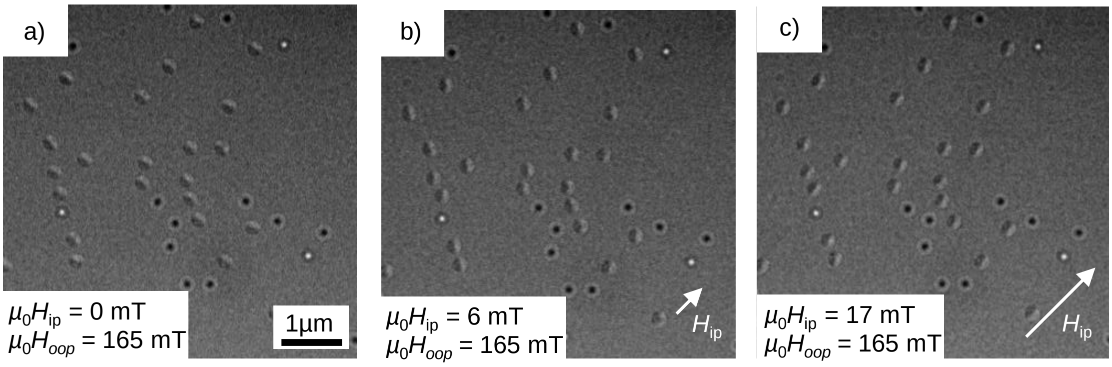

Figure 5.34: Influence of an in-plane magnetic field on the type-2 bubble orientation. LTEM images of $[\mathrm{Fe/Ir/Gd(0.4)}]_5/[\mathrm{Fe/Gd(0.4)}]_{70}/[\mathrm{Fe/Ir/Gd(0.4)}]_5$ at different ip fields and at RT. The oop field is fixed at 165 mT. The bubbles align with the increasing ip field. Skyrmions seem to be unaffected.

with ip fields.

Next, the spin objects are investigated in more detail right before they are transformed by the ip field. Thus, a zoomed-in image in this state is displayed in Fig. 5.35 panel IV. The underlying spin object is shown as the theoretical in-plane components of the spin configuration in panel I. The theoretical deformation of the spin object by an ip field is displayed in panel II together with the resulting simulated LTEM contrast in panel III. The experimental and simulated results (panel IV, III) agree very well.

Figure 5.35 a and b display the deformation of Bloch skyrmions. The experimental data stems from $[\mathrm{Fe/Ir/Gd(0.4)}]_5/[\mathrm{Fe/Gd(0.4)}]_{70}/[\mathrm{Fe/Ir/Gd(0.4)}]_5$ at an oop and ip field of 160 and 60 mT, respectively. The area of the skyrmion whose ip components pointing in the direction of the ip field H_{ip} grows, which pushes the center of the skyrmion to the side and elongates the skyrmion in the direction of H_{ip} (Fig. 5.35 a, b, II). This can also be seen in the contrast images in panel III and IV. A similar elongation of the skyrmion size with ip fields was simulated and experimentally observed for Bloch skyrmions [562] and for Néel skyrmions [563].

Figure 5.35 c shows the effect on bubbles compared to the experimental data of $[\mathrm{Fe/Ir/Gd(0.4)}]_5/[\mathrm{Fe/Gd(0.4)}]_{70}/[\mathrm{Fe/Ir/Gd(0.4)}]_5$ at an oop and ip field of 160 and 90 mT, respectively. The orientation of the bubble is chosen to be in the direction of H_{ip}, due to the reorientation of bubbles with H_{ip} at much smaller fields (Fig. 5.34). Here, the ip field also leads to an elongation of the bubble in the field direction, while the basic magnetic configuration stays the same.

Finally, the influence of an ip field on antiskyrmions is investigated in Fig. 5.35 d. A LTEM image of $[\mathrm{Fe/Ir/Gd}]_{20}/[\mathrm{Fe/Gd}]_{40}/[\mathrm{Fe/Ir/Gd}]_{20}$ is shown in panel IV at an oop and ip field of 31 and 13 mT, respectively. Again, the ip field increases the region's size with the same orientation (panel II). Therefore, the contrast of the left side of the antiskyrmion is washed out and enlarged, while the right side is relatively unaffected.

It is important to note that all the shown deformations in Fig. 5.35 are fully reversible in contrast to the reorientations of the bubbles in Fig. 5.34. Additionally to the reported studies on the deformation of skyrmions by ip magnetic fields [562, 563], the deformation of skyrmions by strain, due to the corresponding change in the anisotropy contributions, was previously studied [564], as well as the deformations during the current-driven motion of skyrmions [565–567]. The change of skyrmions from their circular shape is a characteristic feature used to analyze their stability [565].

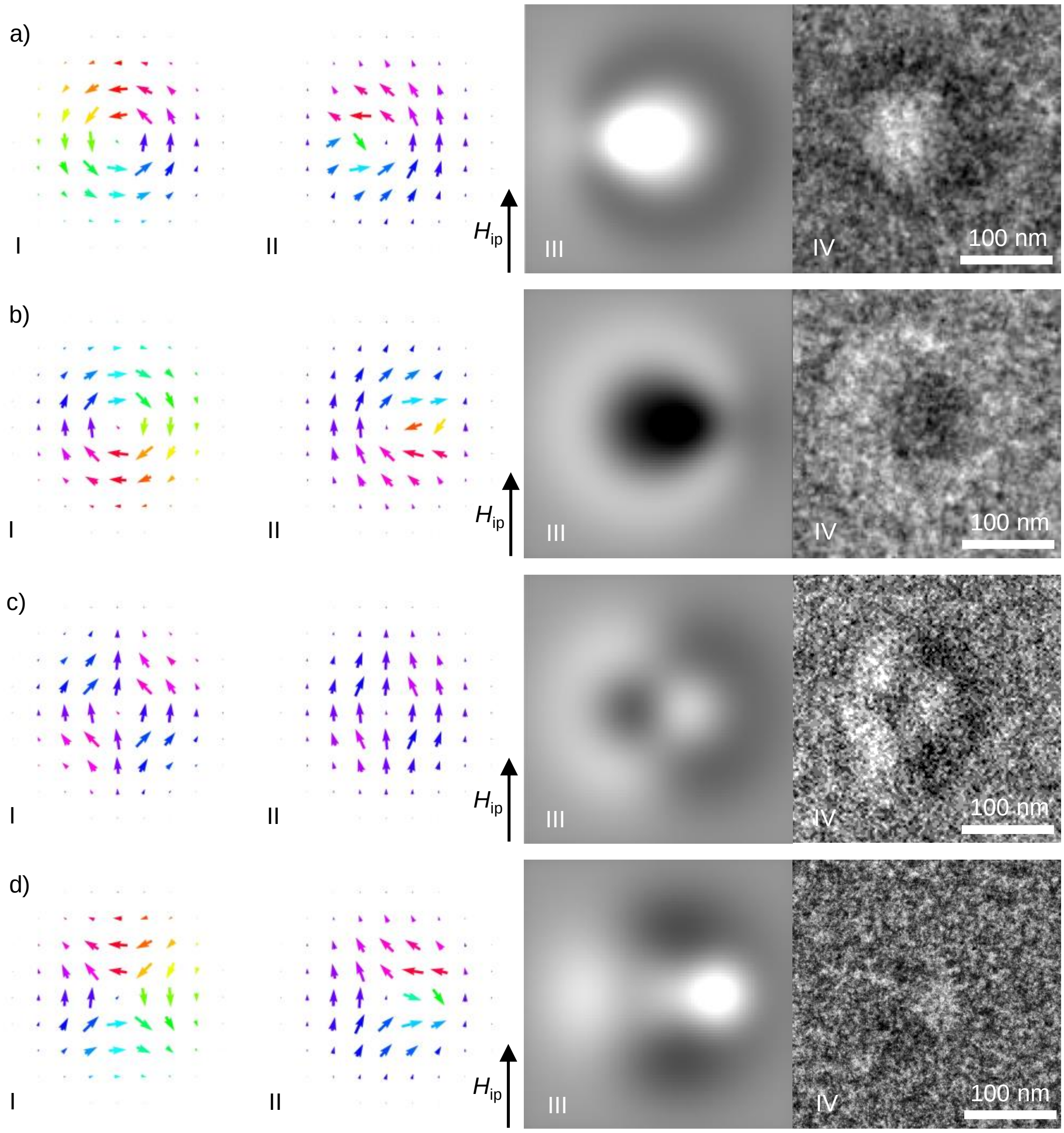

Figure 5.35: Influence of an in-plane magnetic field on the moment configuration of the different spin objects. A counterclockwise Bloch skyrmion (a), a clockwise Bloch skyrmion (b), a bubble (c), and an antiskyrmions (d) are shown. The initial theoretical ip spin configuration (panels I) is influenced by an ip magnetic field H_{ip} in panel II. The arrows and their color depict the directions of the ip components, with their sizes displaying the strengths. Panels III display the simulated and panels IV the experimentally observed contrast of the different spin objects imaged by LTEM and deformed by an ip field.

Furthermore, it was shown that the maximum skyrmion velocity is limited by the skyrmion surface tension and deformation [567]. Therefore, studies on this property are crucial for future applications like the racetrack memory.

5.5.3 Influence of the Surface Morphology of the Membrane

Now that the effects of an ip magnetic field are better understood, another phenomenon of the LTEM images can be investigated: the inhomogeneity of the spin textures throughout the investigated membranes.

Figure 5.36 a displays such differences in the type of spin textures depending on the location on the membrane. This LTEM measurement of $[\mathrm{Fe/Ir/Gd(0.45)}]_5$/ $[\mathrm{Fe/Gd(0.45)}]_{70}$/$[\mathrm{Fe/Ir/Gd(0.45)}]_5$ is carried out at zero field, a tilt angle of -1.4°, and at RT after it was saturated with an oop field of above 600 mT. While the top area mostly exhibits maze-like stripes with chiralities, the bottom area shows more parallel stripes without a chirality. If the membrane is tilted to 0°, saturated, and measured at zero field, the areas of the different stripe types shift (Fig. 5.36 b). Please note that it has been ensured that the sample is imaged in the eucentric height, and therefore the imaged areas of Fig. 5.36 a-c are identical, although different tilt angles are used. If the procedure is repeated for a tilt angle of +1.4°, the stripe types shift even further away from their initial position (Fig. 5.36 c). As discussed at the beginning of this section, stripes without a chirality are energetically most favorable if their orientation is along potential ip magnetic field components. Thus, it can be concluded from the observations in Fig. 5.36 that the applied magnetic field exhibits different ip field components for different areas

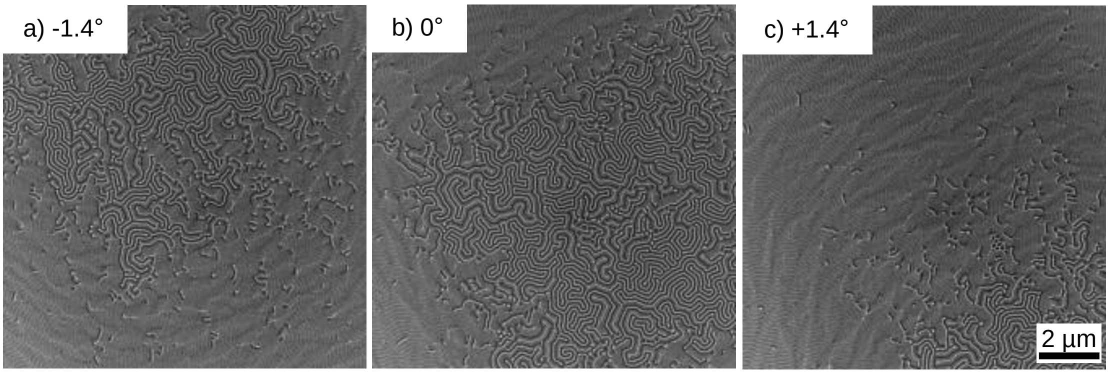

Figure 5.36: Inhomogeneity of spin textures dependent on the tilt angle. LTEM images measured at RT without an applied magnetic field. The images are captured after being saturated at a -1.4° (a), 0° (b), or +1.4° (c) tilt angle.

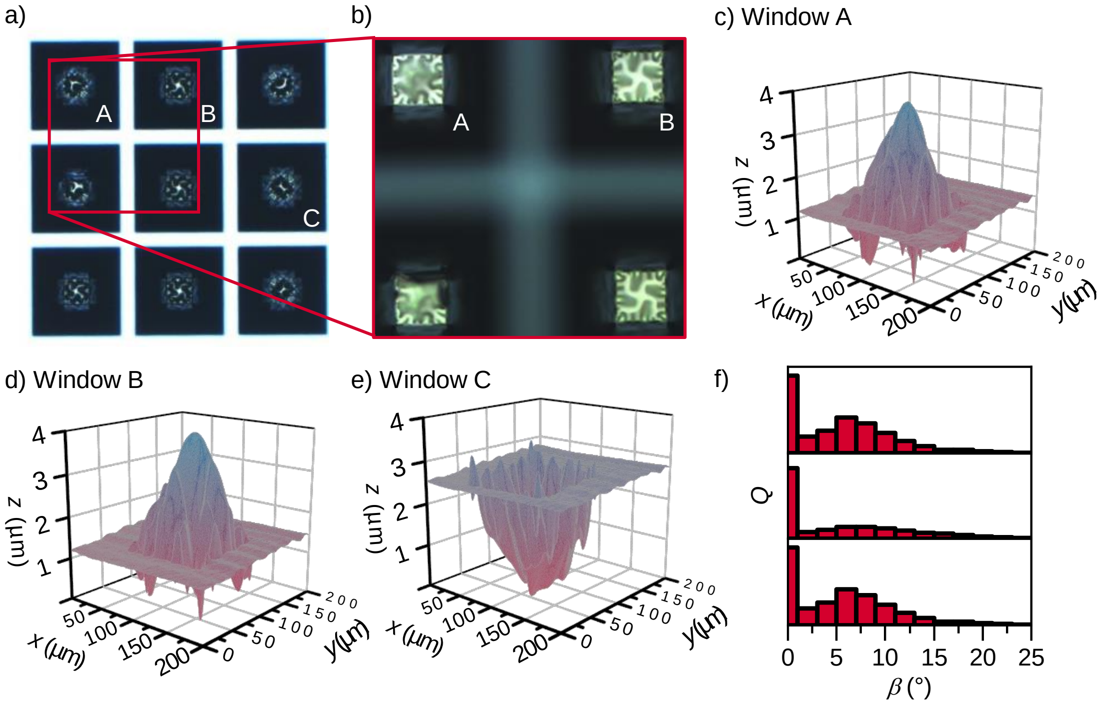

Figure 5.37: Images and information of the membrane morphology. Optical microscopy measurements show the nine membranes of a LTEM sample of $[Fe/Ir/Gd(0.45)]_5/[Fe/Gd(0.45)]_{70}/[Fe/Ir/Gd(0.45)]_5$ (a, b). The height profiles of window A, B, and C are measured with a laser microscope (c-e). The histogram of the occurring tilt angles β of the membrane surface display a Gaussian distribution with a maximum around 7°.

of the membrane, which can be manipulated by the tilt angle. Therefore, the membrane seems to be not flat and shows distortion angles in the range of a few degrees.

In order to further investigate this phenomenon, optical and laser microscopy is utilized in Fig. 5.37. A typical sample is made up of nine membrane windows with an area of 100 µm × 100 µm. An image of these nine windows of a LTEM sample of $[Fe/Ir/Gd(0.45)]_5/[Fe/Gd(0.45)]_{70}/[Fe/Ir/Gd(0.45)]_5$ is shown in Fig. 5.37 a. The height profiles of windows A, B, and C are closer investigated in the following. Figure 5.37 b shows an enlarged section. Here, the membrane windows clearly exhibit some morphology. To quantify this, laser microscopy measurements are used. The results of the three windows A, B, and C are displayed in Fig. 5.37 c-e. Please note that the z-axis is scaled differently from the x- and y-axes. All three membranes show a maximum height difference of approximately 3 µm. The resulting tilt angles β are

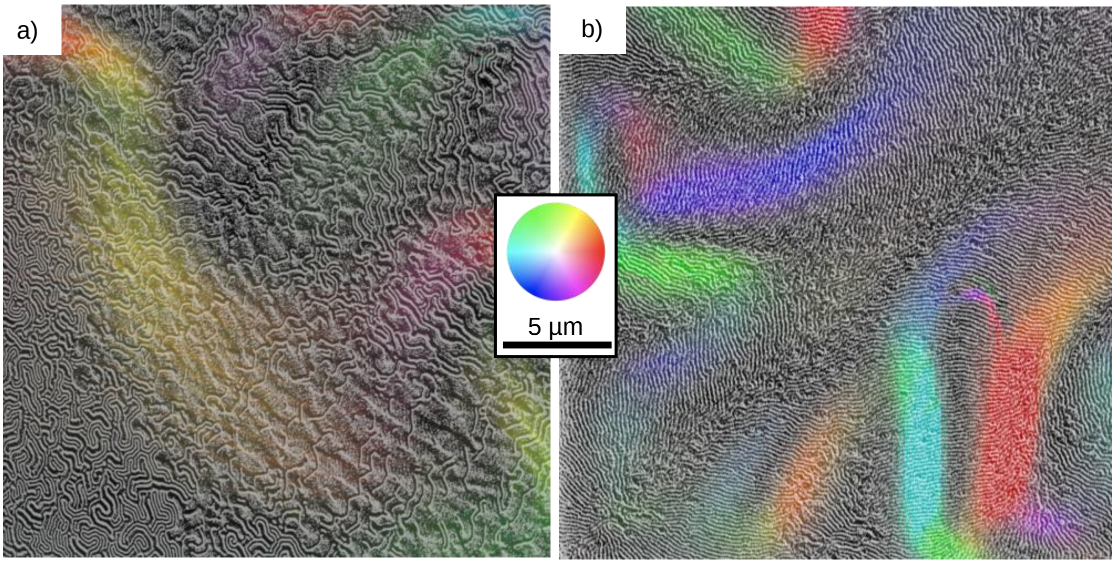

Figure 5.38: Spin textures correlating with the membrane morphology. Stitched large scale LTEM image of window A (a) and B (b) of $[Fe/Ir/Gd(0.45)]_5/[Fe/Gd(0.45)]_{70}/[Fe/Ir/Gd(0.45)]_5$ at zero field and RT after being saturated at a tilt angle of zero. The superimposed colors depict the direction of the tilt and their intensity the size of the tilt angle.

calculated from the gradient of the surface and plotted as a histogram in Fig. 5.37 f. While the maximum of the histogram at 0° stems mostly from the area surrounding the membrane and can be ignored, the Gaussian distribution of the angle β has its maximum around 7°.

Due to the large magnification of the LTEM, which is for the shown images usually around ×4000, the influence of the membrane morphology at a grander scale is hardly visible. On the other hand, measurements with much smaller magnifications are unable to image the spin textures. Therefore, a multitude of LTEM images is stitched together to create a better overview of the whole membrane's domain morphology. The images are captured at zero field and RT after the sample is saturated at a tilt angle of zero. Figure 5.38 displays a sector of these stitched LTEM images together with the superimposed information about the tilt angles of the membranes. The colors depict the direction of the tilt and their intensity, the size of the tilt angle. Figure 5.38 a and b show window A and B of the $[Fe/Ir/Gd(0.45)]_5/[Fe/Gd(0.45)]_{70}/[Fe/Ir/Gd(0.45)]_5$ sample, respectively. It is clearly visible that the stripes without a chirality align with the local tilt of the membrane. Due to the nearly perfect agreement of the tilt direction and the alignment of the stripes, possible differences in the local anisotropy due to strain can be ruled out as a cause for the inhomogeneity of the spin textures. Also, stripes with chiralities exist preferably in areas with no or small tilt angles.

The strong effect of the domain morphology explains retrospectively the large difference between the MFM and LTEM measurements in Sec. 5.4. The samples measured with MFM have a rigid Si/SiO$_x$ substrate and, therefore, no deformation of the surface. Further, the cause of the clearly defined areas of skyrmion and bubble lattices in Sec. 5.2.4 is now known. It has to be noted that the shown *M*-*H* hysteresis loops in this work are all measured on Si/SiO$_x$ substrate samples and therefore do not show the influence of the membrane morphology.

The cause of the deformation of the membrane is its thinness of 30 nm and the elastic stress induced by the deposited film, which is in the range of 60-80 nm. Thicker membranes could solve this problem at the expense of contrast of the LTEM measurements. Other options include a change in seed layers and/or deposition parameters.

5.6 Post-Deposition Anisotropy Engineering

In this chapter, a variety of spin objects and their host systems were presented. While the possible nucleation points could be predicted from their domain morphology at zero field (Sec. 5.3.7), a controlled and reproducible creation of certain skyrmion types at certain spots is not achieved. Having defined nucleation centers for spin objects on a sample is crucial for most applications as well as for statistical studies on them. It was shown that the magnetic anisotropy is one crucial parameter to control the nucleation and stability of skyrmions. Therefore, this section presents some first results on local anisotropy engineering to locally control the nucleation of spin objects.

One way to influence the magnetic anisotropy ex-situ is ion radiation (Sec. 3.1.2). It was shown that this method is suitable to locally control the magnetic properties of systems [568]. Therefore, $[\mathrm{Fe}(0.35)/\mathrm{Gd}(0.45)]_{80}$ samples are irradiated with different doses of He^{+} ions. Figure 5.39 shows MFM (a-d) and corresponding oop and ip *M*-*H* hysteresis measurements (e-h) before (a, e) and after irradiation with a dose of $1 \cdot 10^{14}\,\mathrm{at/cm^2}$ (b, f), $3 \cdot 10^{14}\,\mathrm{at/cm^2}$ (c, g), and $2 \cdot 10^{15}\,\mathrm{at/cm^2}$ (d, h). While the effects of the two lower doses (Fig. 5.39 b/f, c/g) are relatively minor in comparison to the initial state (Fig. 5.39 a/e), the largest dose leads to a loss of nearly all PMA. This is evident

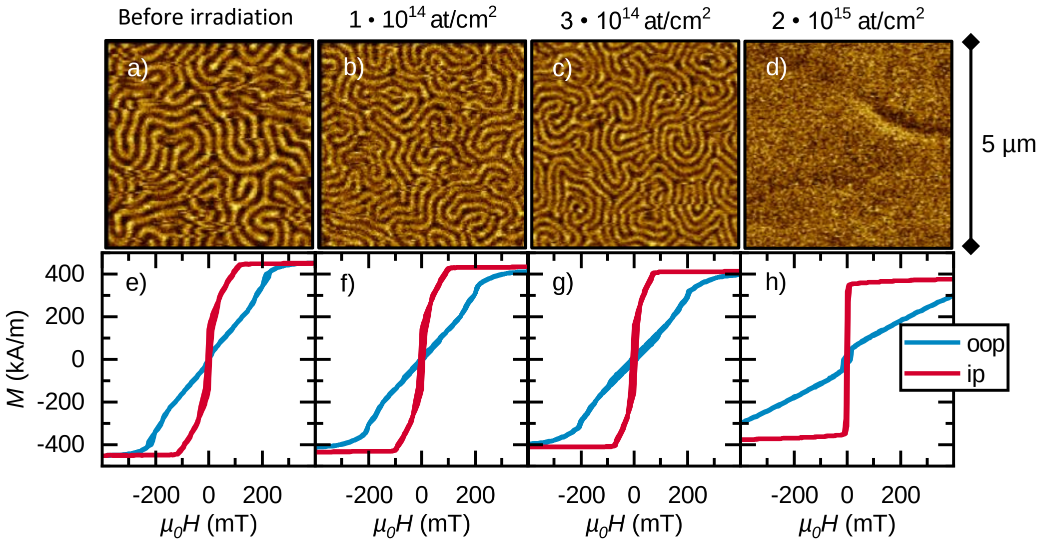

Figure 5.39: Hysteresis loops and MFM measurements depending on ion irradiation doses. MFM measurements at zero field and RT before (a) and after irradiation with certain doses (b-d). Corresponding oop and ip *M*-*H* hysteresis loops (e-h).

by the change from a maze stripe domain pattern (Fig. 5.39 a-c) to one dark and bright line, which is the typical phenotype of an ip domain wall (Fig. 5.39 d). Accordingly, the anisotropy field of the oop hysteresis loop increases drastically from Fig. 5.39 g to h, resulting in a magnetic ip easy axis due to the shape anisotropy. During this loss of the oop magnetic anisotropy, the saturation magnetization of the sample shows no significant change (Fig. 5.39 g, h). Similar results were reported on Co/Pt MLs [569]. The ions induce intermixing between the individual layers and, therefore, reduce interface magnetic anisotropy effects.

In the following, this controlled ex-situ reduction of the oop magnetic anisotropy is used, together with irradiation masks, to achieve an artificially engineered anisotropy pattern in the Fe/Gd MLs.

5.6.1 Patterning by Self-Assembled Nanospheres

One possibility to achieve an irradiation mask, which covers the whole sample and has a hexagonal pattern with a similar scale as the observed skyrmion lattices (Sec. 5.2.4), is the use of self-assembled nanospheres. This method has been used in the past, together with ion irradiation, to modulate the properties of magnetic films and imprint artificial hexagonal patterns [570–572]. In 2016, an artificial dense lattice of magnetic bubbles was

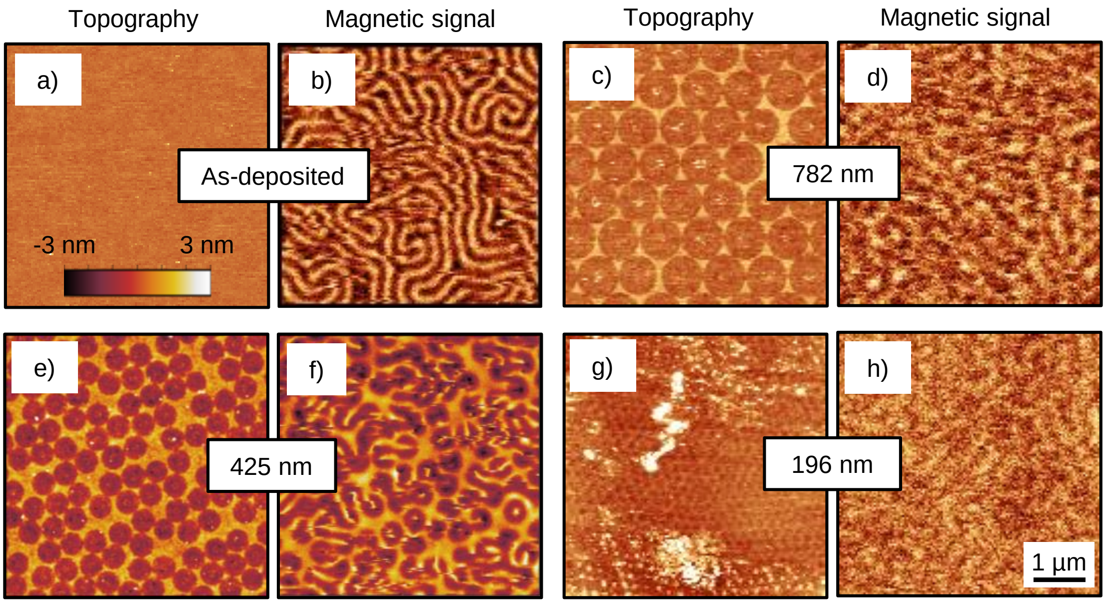

Figure 5.40: MFM images after irradiation with different nanosphere masks. Topographic and magnetic signal of MFM measurements in the as-deposited state (a,b) and after irradiation and removing of the sphere mask with sphere diameters of 782 nm (c, d), 425 nm (e, f), and 196 nm (g, h).

created in Co/Pt MLs in this way [573].

Figure 5.40 shows MFM images of $[\mathrm{Fe}(0.35)/\mathrm{Gd}(0.45)]_{80}$ samples in the as-deposited state and after irradiation with a dose of $2 \cdot 10^{15}$ at/cm^2. While the sample in Fig. 5.40 a and b had no nanosphere protection layer, the rest had a monolayer of nanospheres on top with sphere diameters of 782 nm (c, d), 425 nm (e, f), and 196 nm (g, h). Both the topographic (a, c, e, g) and the magnetic signal (b, d, f, h) of the MFM measurement of the same area are displayed for every sample in Fig. 5.40. The as-deposited sample has no significant topography or roughness (Fig. 5.40 a) and shows the typical stripe maze domains in Fig. 5.40 b analogously to Fig. 5.39 a.

The topographic signal of the samples with masks reveals the nanosphere pattern, which was present during the irradiation process. Please note that the images are measured after the nanosphere layer is removed. However, parts of the capping layer are removed by the lift-off process, too. This is confirmed by the roughly 1-3 nm deep pattern (Fig. 5.40 c, e, g).

In Fig. 5.40 d the domain morphology of the sample with 782 nm large nanospheres shows shorter and more separated stripes in comparison to the initial domain pattern

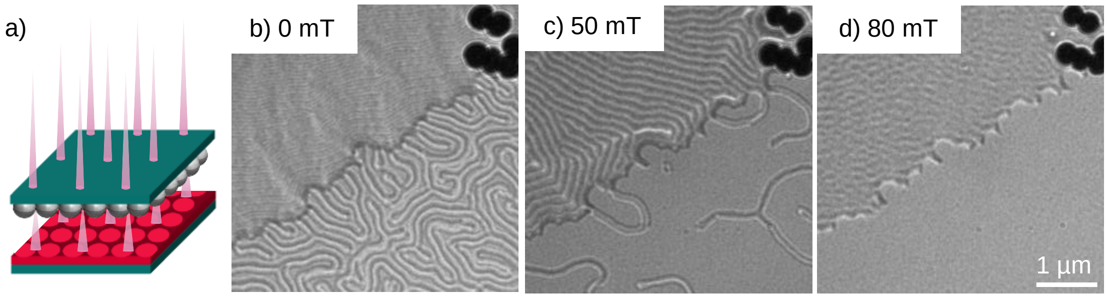

Figure 5.41: Irradiation with a nanosphere membrane mask and LTEM measurements of the resulting patterned film. Illustration of the irradiation process with a nanosphere membrane as a mask (a). LTEM images of the irradiated magnetic film at an applied oop magnetic field of 0 mT (b), 50 mT (c), and 60 mT (d). The bottom right half was covered by the nanosphere mask. In the top right corner remaining nanospheres are visible.

of the sample (Fig. 5.40 b). As expected, stripe domains represent no stable state in the irradiated areas. Therefore, the stripes are cut off every 782 nm. Due to the relatively large unaltered areas in comparison to the approximately 200 nm periodicity of the stripes, stripes with a length of around 700 nm seem more favorable than round spin objects in this state. The use of 425 nm-large nanospheres is the most promising approach to achieve an artificial hexagonal skyrmion lattice (Fig. 5.40 f). Here, multiple isolated round spin objects and stripes coexist. Hence, the spheres still seem to be a little bit too large to achieve a pure artificial spin object pattern. It is important to note that the existing round spin objects are stable without an applied oop magnetic field at RT. The domain pattern of the 196 nm-large nanospheres in Fig. 5.40 h is similar to Fig. 5.40 d. The initial stripe pattern is separated and washed out. Due to the too small nanospheres in comparison to the initial stripe periodicity, it is more comparable to a continuous change of the magnetic properties than a local pattern of the film.

Figure 5.40 f proved that it is possible to achieve an artificial spin object pattern by ion irradiation using a nanosphere-covered sample. However, a determination of the type of spin object is not possible with the presented MFM measurements. LTEM measurements would provide the ability to determine the type of the spin objects, as well as the option to continuously apply magnetic fields for further investigations. However, the lift-off process of the nanospheres described in Sec. 3.1.2 is not suited for the used TEM membranes. Therefore, a different technique has to be developed, which still utilizes the sphere monolayer as an irradiation mask. Instead of applying the nanospheres directly onto the magnetic film, a second TEM membrane is used. It is covered with the sphere monolayer and put on top of the membrane with the magnetic film during irradiation. The spheres of the mask membrane face the magnetic film to reduce shadow effects. An illustration of this setup is given in Fig. 5.41 a. Furthermore, simulations showed that the transmission of a 30-nm-thick SiN membrane weakens the irradiation dose only slightly. After the irradiation process, the mask membrane is removed, and the membrane with the magnetic film is imaged by LTEM. Three of the resulting images of $[\mathrm{Fe}(0.35)/\mathrm{Gd}(0.45)]_{80}$ with a 425 nm nanosphere mask are shown in Fig 5.41 b-d. A few of the nanospheres of the mask membrane are stuck to the magnetic film and are visible in the top right corner of the three images. The imaged region was chosen because only half the area was covered by the nanosphere mask. Hence, two very distinct regions with different magnetic properties are visible. The bottom right corner was covered with nanosphere, while the top left corner only had the insignificant protection of the membrane without spheres. In Fig. 5.41 b the top left corner lost a significant portion of its PMA anisotropy. It still shows stripe domains with a small periodicity and needs much larger fields than the bottom part of the image to be saturated (Fig. 5.41 c, d). In contrast, the bottom right is very similar to the initial state of the system (Fig. 5.40 b). At 50 mT skyrmions and bubbles are observable (Fig. 5.40 c) and at 80 mT the area saturates. Besides the border between the two areas, no pattern from the nanospheres is visible. The reason for this is the shadow effect, which results in a very small and spread-out dose of irradiation, which affects the full magnetic film.

To prevent these shadow effects and achieve a hexagonal modulated film on TEM membranes, radio frequency (RF)-plasma etching can be used to reduce the size of the spheres on the mask membrane. Thereby smaller sphere sizes with the initial positions and ordering can be achieved [572, 574, 575]. Further, studies on the dependency of the type of the spin objects on the size of the spheres can be conducted by this technique.

5.6.2 Imprinting a Domain Pattern by a Focused Ion Beam

Another possibility to imprint artificial domain patterns by reducing the PMA is the use of a focused ion beam (FIB). It was shown that focused gallium ion beam irradiation can lead to structural and magnetic phase transitions in metastable FeNi thin films and therefore changes in its magnetic anisotropy [576]. The possibility to create magnetic patterns with continuous magnetization transition was also demonstrated. Analogously, FIB was used to locally reduce the uniaxial magnetic anisotropy in Co/Pd MLs and create artificial stripe domains [577]. Very recently, FIB was also utilized to create a

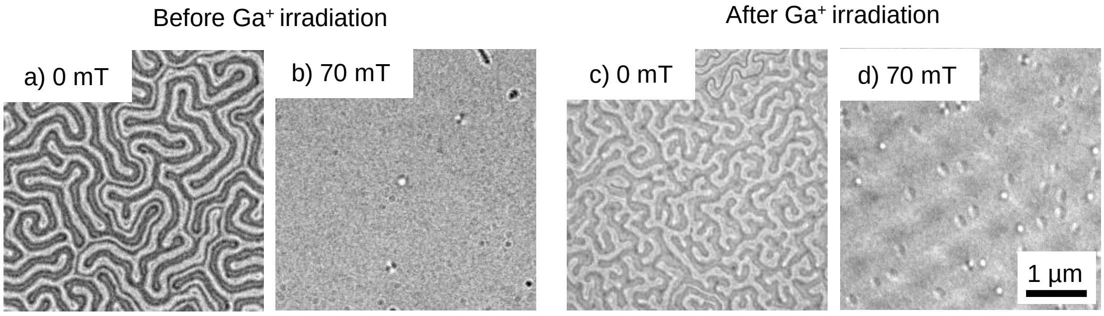

Figure 5.42: Imprinted check pattern by focused ion beam irradiation. LTEM images of $[\mathrm{Fe/Ir/Gd}]_5/[\mathrm{Fe/Gd}]_{70}/[\mathrm{Fe/Ir/Gd}]_5$ in the as-deposited state at RT without a magnetic field (a) and at 70 mT (b). Corresponding LTEM images of a check pattern after irradiation of the same sample by a focused Ga^+ beam at RT, measured at 0 mT (c) and 70 mT (d).

hexagonal grit of artificial skyrmion nucleation spots [578].

The first results of artificially imprinted magnetic patterns in $[\mathrm{Fe/Ir/Gd(0.4)}]_5/[\mathrm{Fe/Gd(0.4)}]_{70}/[\mathrm{Fe/Ir/Gd(0.4)}]_5$ are shown in Fig. 5.42. Figure 5.42 a and b correspond to the images in Fig. A.6 and show the sample before irradiation at 0 and 70 mT, respectively. The images show a typical randomly orientated maze domain morphology without any applied magnetic field (Fig. 5.42 a). With an applied opp field of 70 mT, (anti-)skyrmions and stripes are visible (Fig. 5.42 b). In Fig. 5.42 c and d, a square pattern is irradiated on the sample by a small dose of Ga^+ ions. After irradiation, the domains align with the pattern at zero field (Fig. 5.42 c). In Fig. 5.42 d, the density of spin objects with an applied field is greatly increased in comparison to Fig. 5.42 b. Additionally, bubbles exist now at the corners of the pattern.

5.7 Summary and Outlook in Context of Future Experiments and Applications

First, the existence of Bloch skyrmions and bubbles in Fe/Gd MLs was demonstrated (Sec. 5.2). The observation of Montoya et al. [128] could be confirmed: the saturation magnetization and magnetic anisotropy values are crucial parameters for the stabilization of dipolar-stabilized Bloch skyrmions, and a delicate balance needs to be adjusted to stabilize individual skyrmions or skyrmion lattices. The skyrmion lattice state was demonstrated for two different sample compositions.

The modification of the Fe/Gd ML with different insertion layers leads to the stabilization of first- and second-order antiskyrmions primarily by dipole-dipole interaction (Sec. 5.3). This was the first experimental observation of second-order antiskyrmions and the first observation of first-order antiskyrmions outside of materials with D_{2d} or S_4 symmetry. These novel spin objects coexist in Fe/Gd-based multilayers together with Bloch skyrmions and topological trivial type-2 bubbles. Phase diagrams of the spin objects were created depending on the applied oop magnetic field, temperature, saturation magnetization, and uniaxial magnetic anisotropy. Micromagnetic simulations confirmed the phase pocket of metastable antiskyrmions for low saturation magnetization and uniaxial magnetic anisotropy values satisfying the condition $\frac{1}{2}\mu_0 M_s^2 > K_u$. Furthermore, the nucleation process of antiskyrmions was investigated and revealed that a crossing point of three magnetic stripe domains is necessary to form an isolated antiskyrmion with an oop magnetic field at low temperatures.

Different techniques were presented to image the observed spin objects (Sec. 5.4). While the possibility to differentiate between skyrmions, bubbles, and antiskyrmions by MFM was demonstrated, the advantages of LTEM predominated. Induction maps and DPC measurements were presented as additional techniques to improve the clarity and the resolution of the LTEM measurements.

In Sec. 5.5 the influence of ip magnetic fields on the observed magnetic textures was studied. Here, the stability ranges of the different spin textures depending on the strength of the ip field were analyzed. It was shown that textures without a chirality align with the field direction and stay stable for larger ip fields, while textures with a chirality are relatively unaffected until they vanish. On closer inspection, all spin objects showed certain deformations before they are annihilated by the increasing ip field. Additionally, the effect of the membrane morphology on the magnetic textures was studied.

At last, post-deposition techniques to locally change the magnetic anisotropy of the samples were presented (Sec. 5.6). Patterning by ion irradiation with a self-assembled nanosphere mask or by a FIB system showed great potential to create custom spin object lattices or domain patterns.

The chapter represents significant advances in the research of dipolar-stabilized spin objects. In particular, the discovery of antiskyrmions outside of complex crystals with D_{2d} or S_4 symmetry significantly simplifies future investigations of antiskyrmions. Additionally, the coexisting phases of different topologically protected spin objects provide great potential for further studies on quasi-particle interactions, spin dynamics, as well as for possible future applications in spintronics. The presented local anisotropy engineering tools further pave the way for the targeted control of the spin objects' nucleation and motion.

The next logical step is the investigation of the dynamic properties of the presented spin objects. The current-induced motion of dipolar-stabilized skyrmions was demonstrated by Montoya et al. in Fe/Gd MLs [579]. They showed that the magnetic textures exhibit a motion under a current density of around $108\,\mathrm{A/m^2}$, but failed to show motion of individual skyrmions due to limitations in their magnetic field range. Moving antiskyrmions with currents is discussed heavily in theoretical works [132, 172] but was not realized experimentally until now. Antiskyrmions are expected to have no Hall angle under the right orientation with respect to the current [172]. Skyrmions and antiskyrmions in dipolar systems are also predicted to show fascinating interactions under injected driving charge currents: spontaneous formations of bi-(anti-)skyrmions, pair annihilation of a skyrmion and an antiskyrmion, and forced separation of bi-skyrmions [132]. With the coexistence of all the different spin objects, the here presented system is the ideal candidate to investigate and compare different current-induced motions and interactions.

Implications for Potential Applications

Section 5.1 described a range of possible applications of skyrmions. In particular, the coexisting phases of different topologically protected spin objects provide great potential for the racetrack memory (Sec. 5.1.1) and the skyrmionic interconnection (Sec. 5.1.2). With multiple available coexisting spin objects, the information in such a racetrack device can be stored in a binary, ternary, or quaternary way. The knowledge gained about the different nucleation processes can be used to create artificially designed nucleation spots by local anisotropy engineering. Further, the writing of custom magnetic domain patterns with FIB (Sec. 5.6.2) represents one possibility to fabricate defined tracks for the spin objects in a continuous film. To further elaborate on these concepts, the current-induced dynamics of the different spin objects have to be investigated, in particular in combination with FIB-modified films.

The density of the potentially stored data or the data throughput is one of the key metrics for the feasibility of the proposed technologies. In this regard, the presented spin objects are not competitive due to their large sizes with diameters above 100 nm. Here, new systems have to be found. The provided antiskyrmion recipe (Sec. 5.3) together with the general theory on skyrmion size [129] has a huge potential in this regard.

While the currently investigated skyrmion-based unconventional computing devices work with only one skyrmion type (Sec. 5.1.2), coexisting different types, which interact in complex ways, could elevate these concepts to their next stage.

The investigations also showed that the studied primarily dipolar-stabilized spin objects significantly change their size dependent on the applied oop magnetic field while still being topologically protected. This property makes them especially interesting for the proposed skyrmion-based sensors (Sec. 5.1.3). To achieve a maximum signal of the proposed sensor, a hexagonal closely-packed lattice is desired. This skyrmion lattice was achieved for Fe/Gd MLs at RT (Sec. 5.2.4) and can be created artificially by ion irradiation with a self-assembled nanosphere mask (Sec. 5.6.1).

Chapter 6

Conclusion

In this work, the challenges of modern and future data storage solutions are tackled by investigating ferrimagnetic systems as potential building blocks.

After the essential fundamentals of the occurring magnetic phenomena and the used experimental techniques were laid out, two distinct chapters explore different ferrimagnetic systems and their potential applications.

In chapter 4 ferrimagnetic and ferromagnetic films are exchange-coupled and studied as potential composite media for magnetic recording technologies. However, the individual ferrimagnetic layer turned out to be unsuited for the desired magnetic recording technology due to irreversible structural changes at the required operating temperatures. Nevertheless, new insights are gained about the complex magnetization reversal processes of ferrimagnetic and ferromagnetic exchange-coupled bilayer structures. Further, the results of the individual layers are potentially interesting for other applications, like magneto-resistive random access memories or all-optical-switching-based storage devices.

Chapter 5 focuses on the nucleation, stability, and behavior of different dipolar-stabilized spin textures in Fe/Gd-based multilayers with implications for a variety of possible applications in data storage, unconventional computing, or sensor devices. The first experimental observation of second-order antiskyrmions was made, and a recipe was developed to stabilize antiskyrmions in a wide range of other material systems. Furthermore, the first steps toward controlled nucleation of the different spin objects were made.

While chapter 4 offers interesting fundamental insights on ferro- and ferrimagnetic thin film systems, the investigations in terms of the desired usage as a magnetic recording medium led to a dead end. In contrast, chapter 5 represents only a starting point. The research interest in skyrmions has been at a constant high level since their discovery in

2009 [32]. The recent observation of coexisting skyrmions and antiskyrmions in 2020 [140, 141], together with the newly found application of skyrmions in unconventional computing [503–505], only further fueled the excitement of the magnetic community in this regard. The presented novel recipe of antiskyrmions, which are stabilized by magnetic dipole-dipole interaction, represents a new playground for future research in this area. The wide range of theoretical predictions of the dynamics and interaction of the different spin objects [132, 172] is only a foreshadowing of the experimental results to come. It is not unlikely that the continuously ongoing research in this area will soon lead to the breakthrough of magnetic skyrmions in commercially available applications.

Appendix A

Attachments

In this chapter, additional measurement and simulation data are shown, which are not essential but complementary to the presented results. Further, lists are given with all samples used in this work. These samples lists include the sample name, composition, and the section they are presented in, plus the deposition parameters in the caption of the sample list.

A.1 Additional SQUID-VSM Measurements

Figure A.1 shows *M*-*H* oop and ip hysteresis loops of the samples investigated in Sec. 5.5. The samples compositions are [Fe/Ir/Gd(t_{Gd})]$_5$/[Fe/Gd(t_{Gd})]$_{70}$/[Fe/Ir/Gd(t_{Gd})]$_5$ with t_{Gd} =0.40 (a, b) and 0.45 nm (c, d).

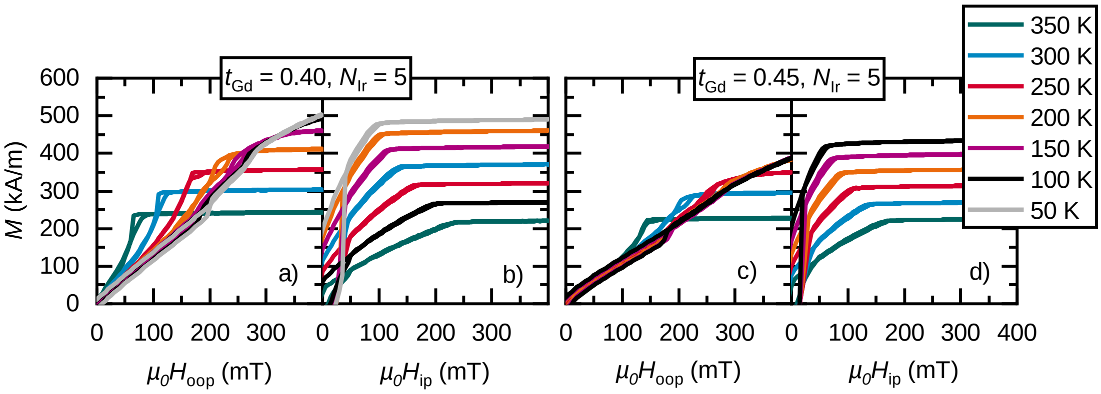

Figure A.1: Hysteresis loops of Fe/Gd-based multilayers for the applied ip magnetic field studies. *M*-*H* oop and ip hysteresis loops of [Fe/Ir/Gd(t_{Gd})]$_5$/[Fe/Gd(t_{Gd})]$_{70}$/ [Fe/Ir/Gd(t_{Gd})]$_5$ samples with t_{Gd} =0.40 (a, b) and 0.45 nm (c, d). a) and c) display the oop, b) and d) the ip loops.

A.2 Additional LTEM Measurements

In addition to the results in chapter 5, selected LTEM images of the discussed samples at various temperatures and oop magnetic fields are shown in this section.

A.2.1 Complementary to Sec. 5.2

The presented LTEM images are used to create the spin object phase maps in Fig. 5.11.

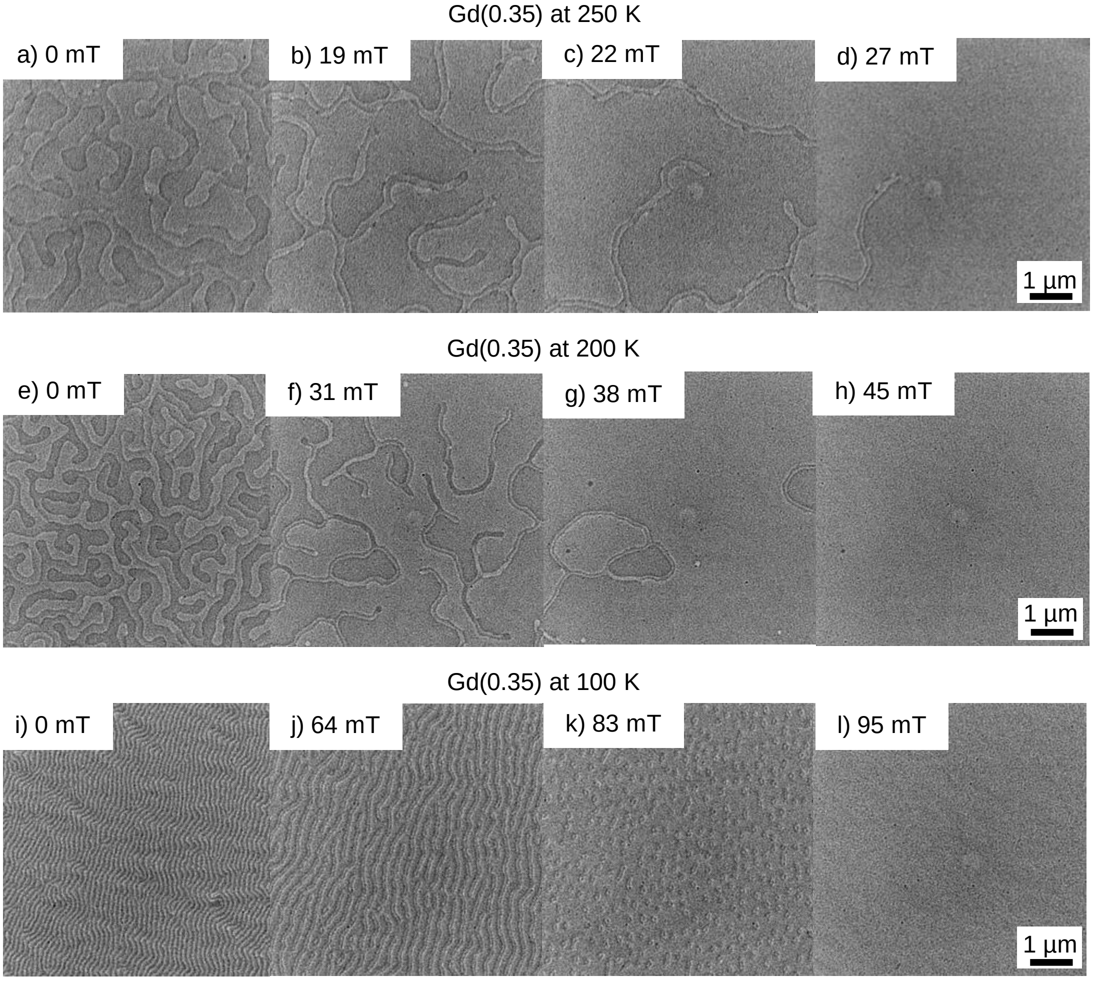

Figure A.2: Selected LTEM images of [Fe(0.35)/Gd(0.35)]$_{80}$. LTEM measurements at 250 K (a-d), 200 K (e-h), and 100 K (i-l). At 300 K also only oop domains exist, which are larger than the domains in a-d (not shown).

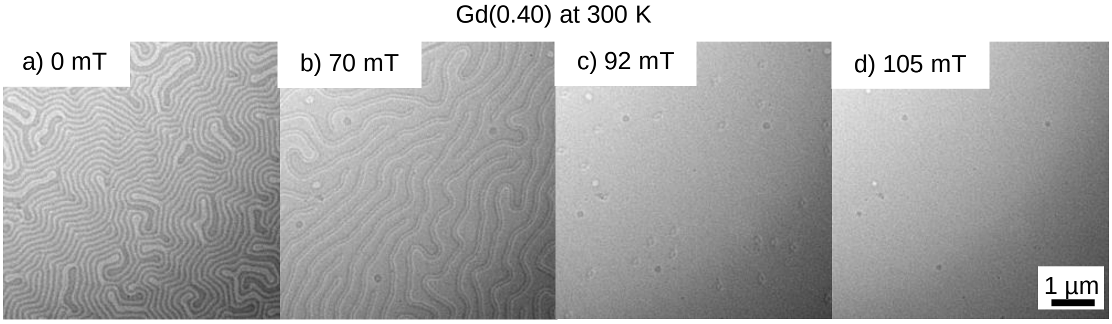

Figure A.3: Selected LTEM images of [Fe(0.35)/Gd(0.40)]$_{80}$. LTEM measurements at 300 K (a-d). At lower temperatures only ip domains exist (not shown).

In Fig. A.2-A.3 LTEM images of the studied samples in Sec. 5.2 are provided at the relevant temperatures. Figure A.2 a-d shows the oop magnetic domains without any spin objects of [Fe(0.35)/Gd(0.35)]$_{80}$ at 250 K. At higher temperatures the size of the oop domains increases and no spin objects are observable (not shown). At lower temperatures the sample exhibits both bubbles and skyrmions (Fig. A.2 e-l). Figure A.3 a-d shows the nucleation of skyrmions and bubbles in [Fe(0.35)/Gd(0.40)]$_{80}$ at 300 K. At lower temperatures only ip domains exist (not shown).

A.2.2 Complementary to Sec. 5.3

In Fig. A.4-A.8 LTEM images of all studied samples in Sec. 5.3 are provided. The presented LTEM images are used to create the spin object phase maps in Fig. 5.20.

Figure A.4 a-h shows the nucleation process of antiskyrmions and various other spin objects without Ir insertion layers in [Fe/Gd]$_{80}$ at 300 K (Fig. A.4 a-d) and 250 K (Fig. A.4 e-h). At lower temperatures, no spin objects are observable in this sample (Fig. A.4 i-p). Figure A.5 displays the nucleation of bubbles and skyrmions in [Fe/Ir/Gd]$_2$/[Fe/Gd]$_{76}$/[Fe/Ir/Gd]$_2$ at 300 K (a-d), 260 K (e-h), 200 K (i-l), and 100 K (m-p). Additionally, first-order antiskyrmions can be observed at 300, 260, and 200 K. Second-order antiskyrmions only nucleate at 260 K (e-h). Figure A.6 shows LTEM images of the [Fe/Ir/Gd]$_5$/[Fe/Gd]$_{70}$/[Fe/Ir/Gd]$_5$ ML at different temperatures. Over the whole temperature range, antiskyrmions and skyrmions exist. Figure A.7 shows LTEM images of the [Fe/Ir/Gd]$_{10}$/[Fe/Gd]$_{60}$/[Fe/Ir/Gd]$_{10}$ ML at different temperatures. Skyrmions exist at every measured temperature, antiskyrmions only between 200 and 300 K (a-l). Figure A.8 shows LTEM images of the [Fe/Ir/Gd]$_{20}$/[Fe/Gd]$_{40}$/[Fe/Ir/Gd]$_{20}$ ML at 300 K. The contrast is weaker for this sample because of the reduced magnetic moment (Fig. 5.16 a). Although Fig. A.8 a exhibits only magnetic stripes with chirality at

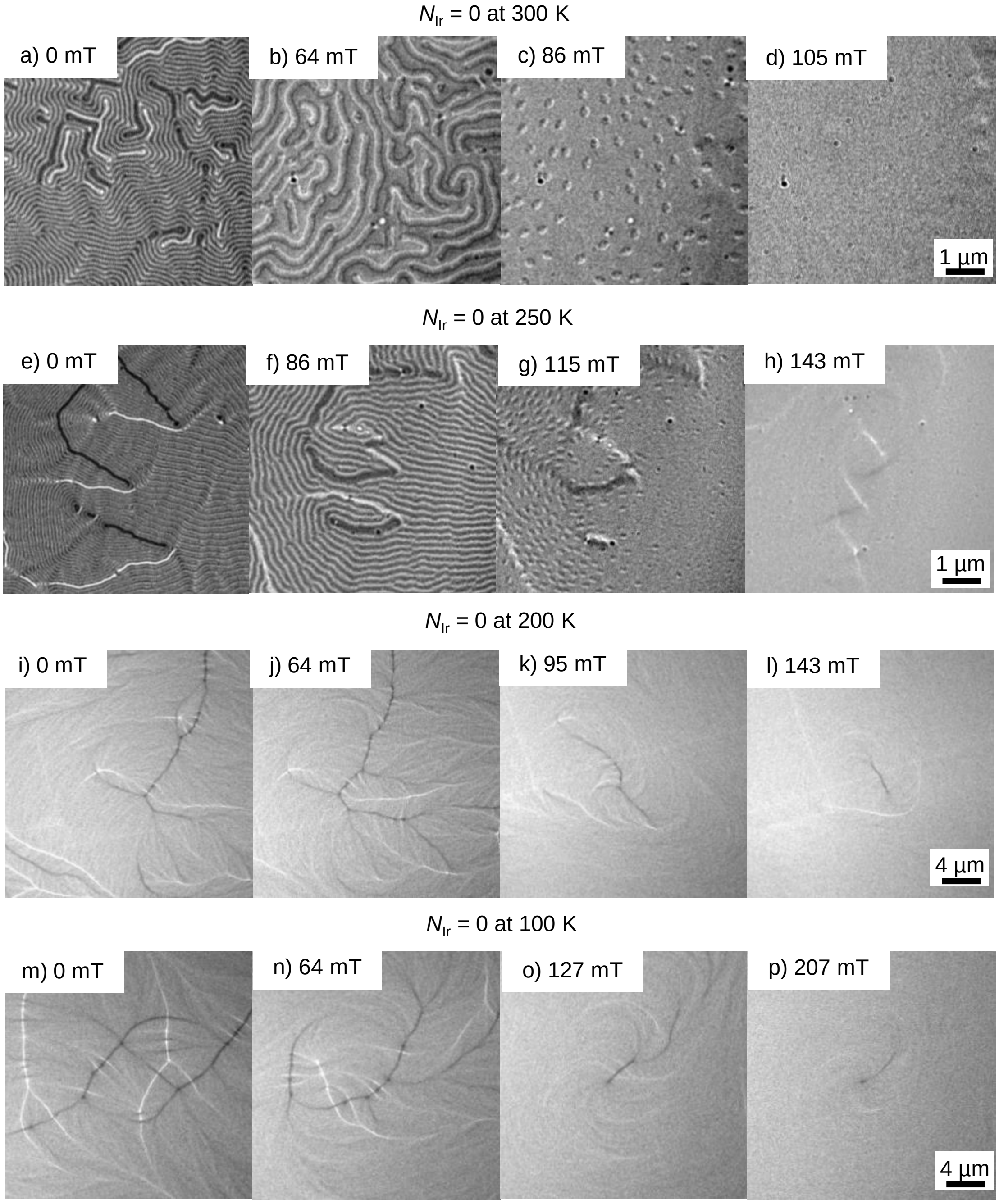

Figure A.4: Selected LTEM images of [Fe/Gd]$_{80}$ without Ir insertion layers. Please note that the scale changes for the last two rows. Despite the missing Ir layers, antiskyrmions are observable at 300 K.

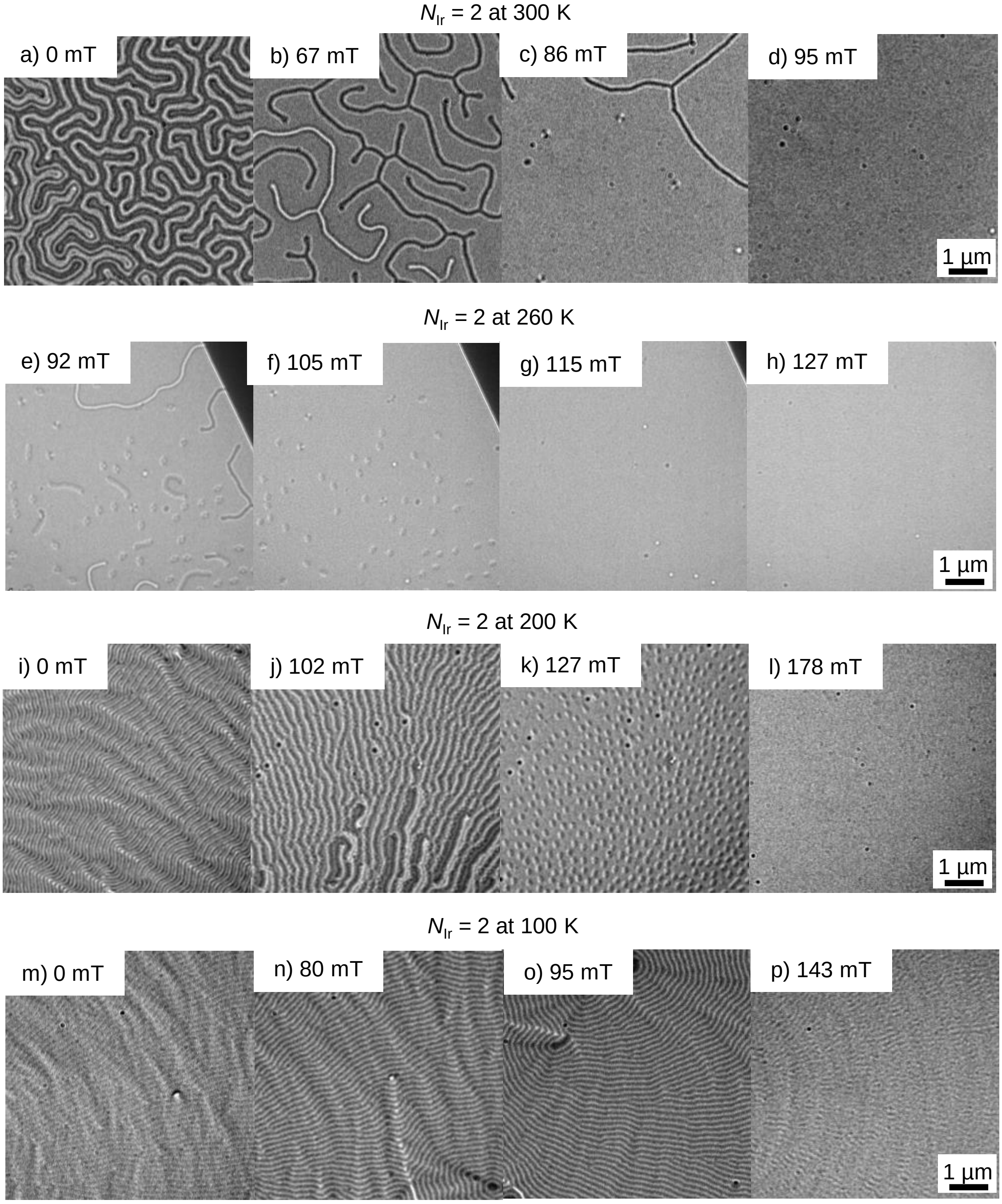

Figure A.5: Selected LTEM images of [Fe/Ir/Gd]$_2$/[Fe/Gd]$_{76}$/[Fe/Ir/Gd]$_2$. First-order antiskyrmions exist at 300 K (a-d), 260 K (e-h), and 200 K (i-l). The nucleation of a second-order antiskyrmion can be observed at 260 K (e-h).

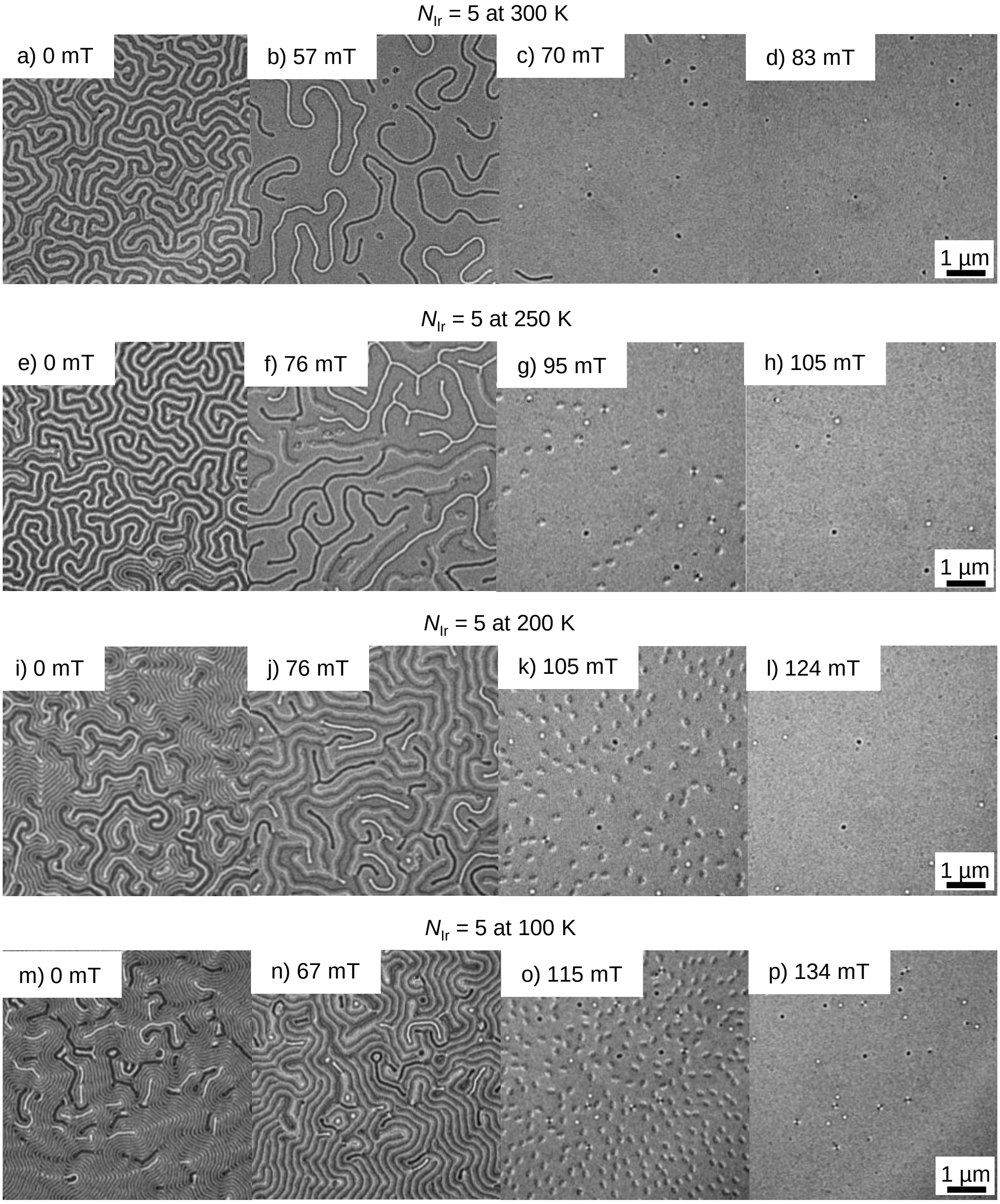

Figure A.6: Selected LTEM images of [Fe/Ir/Gd]$_5$/[Fe/Gd]$_{70}$/[Fe/Ir/Gd]$_5$. A video of the changing spin texture of this sample at 250 K is available at youtu.be/97nUhTelTxA.

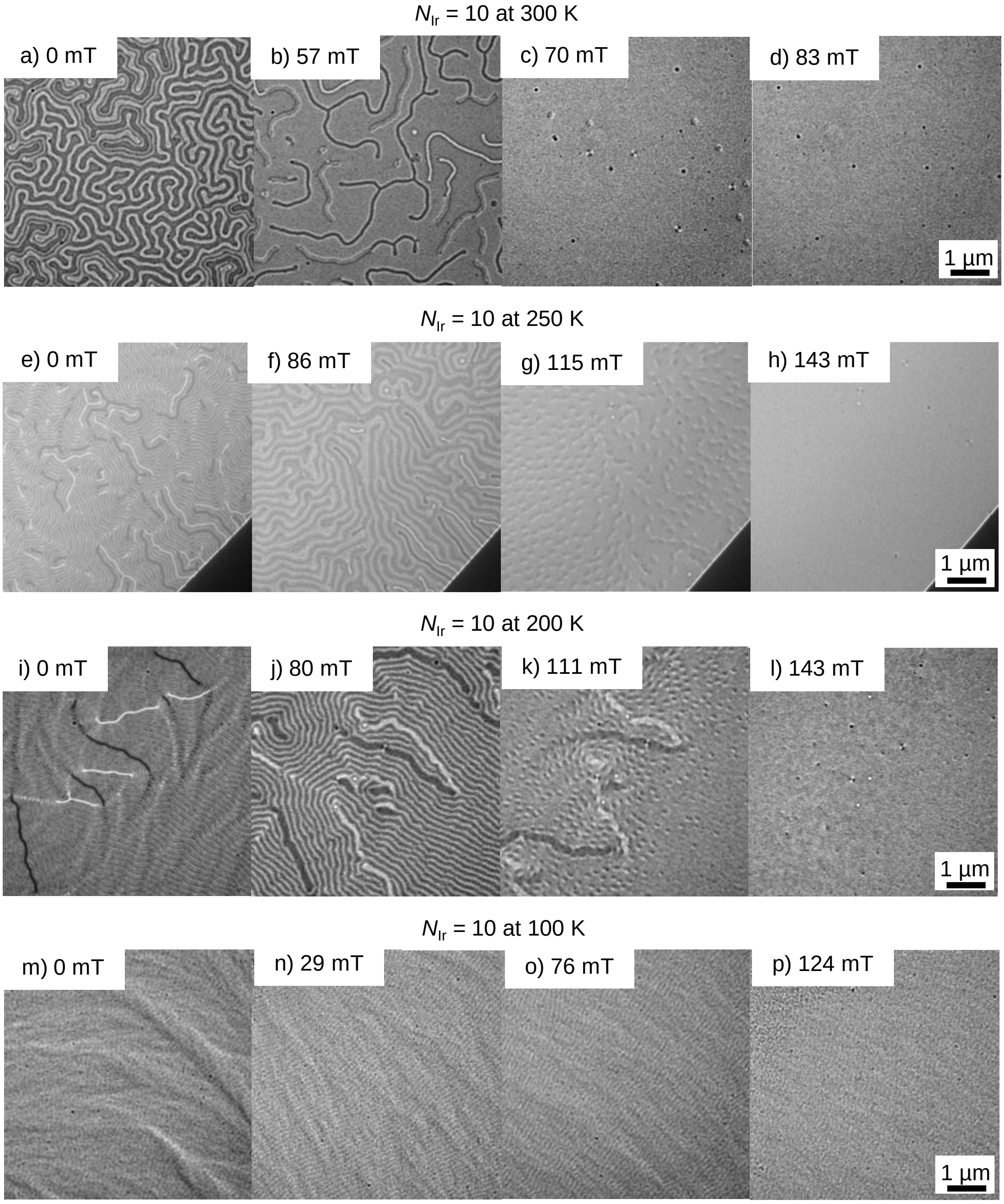

Figure A.7: Selected LTEM images of [Fe/Ir/Gd]$_{10}$/[Fe/Gd]$_{60}$/[Fe/Ir/Gd]$_{10}$. First-order antiskyrmions exist between 200 and 300 K (a-l).

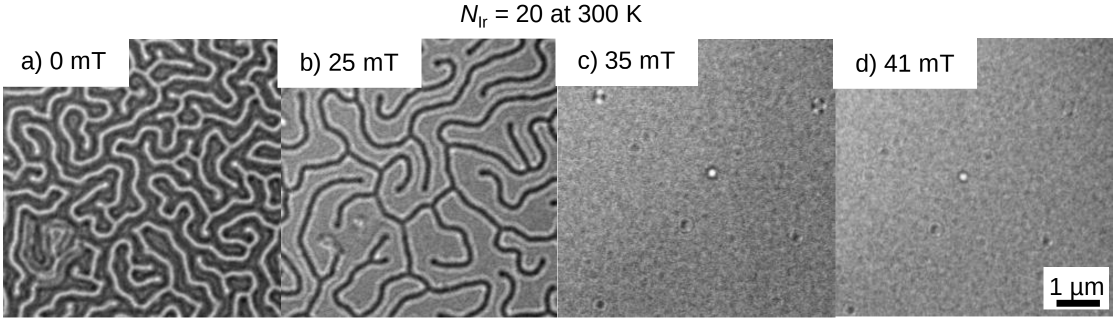

Figure A.8: Selected LTEM images of [Fe/Ir/Gd]$_{20}$/[Fe/Gd]$_{40}$/[Fe/Ir/Gd]$_{20}$. A video of the changing spin texture of this sample at 300 K is available at youtu.be/VYAM1K1Ucpg. The LTEM measurements at lower temperatures showed only ip domains and are not displayed.

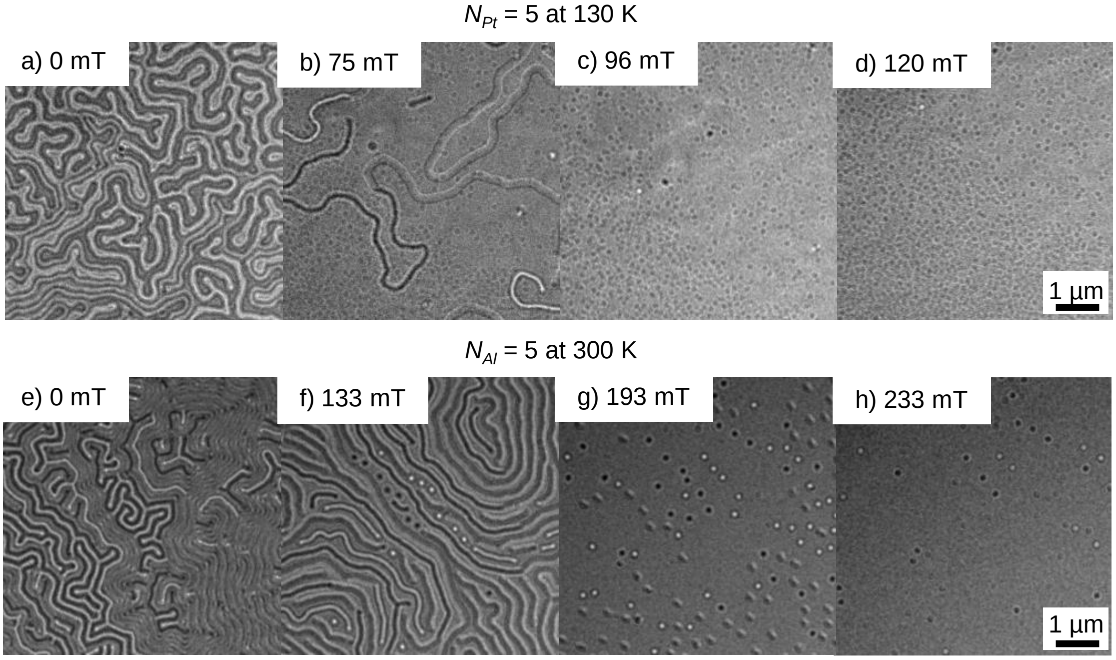

Figure A.9: Selected LTEM images of Fe/Gd MLs with different insertion layers. LTEM measurements of [Fe/Pt/Gd]$_5$/[Fe/Gd]$_{70}$/[Fe/Pt/Gd]$_5$ at 130 K and [Fe/Al/Gd]$_5$/[Fe/Gd]$_{70}$/[Fe/Al/Gd]$_5$ at 300 K.

zero field, Fig. A.8 b shows bubbles at 32 mT. At 35 mT skyrmions and antiskyrmions start to nucleate while the bubbles vanish (Fig. A.8 c).

Figure A.9 displays exemplary LTEM measurements of Fe/Gd-based MLs with Pt and Al insertion layers instead of Ir. Their magnetic properties are discussed in Sec. 5.3.9.

While antiskyrmions can be stabilized with Pt insertion layers at 130 K (Fig. A.9 a-d), only skyrmions and bubbles are observable in Al (Fig. A.9 e-h).

A.2.3 Complementary to Sec. 5.5

Section 5.5 focuses on the influence of ip magnetic fields and therefore only shows LTEM measurements with both oop and ip magnetic fields applied to the sample. Therefore, Fig. A.10 displays the domain morphology of the used samples without any ip field components at 300 K. Additionally, the $[\mathrm{Fe/Ir/Gd}]_{20}/[\mathrm{Fe/Gd}]_{40}/[\mathrm{Fe/Ir/Gd}]_{20}$ ML is used, which was shown in Fig. A.8. The other used compositions are $[\mathrm{Fe/Ir/Gd(t_{Gd})}]_5/[\mathrm{Fe/Gd(t_{Gd})}]_{70}/[\mathrm{Fe/Ir/Gd(t_{Gd})}]_5$ samples with t_{Gd} =0.40 (Fig. A.10 a-d) and 0.45 nm (Fig. A.10 e-g), which do not exhibit antiskyrmions due to their too large saturation magnetization (Fig. A.1). However, the sample with t_{Gd} =0.45 nm exhibits a dense skyrmion/bubble lattice at 300 K (Fig. A.10 e-g).

t_{Gd}=0.40 nm N_{Ir} = 5 at 300 K

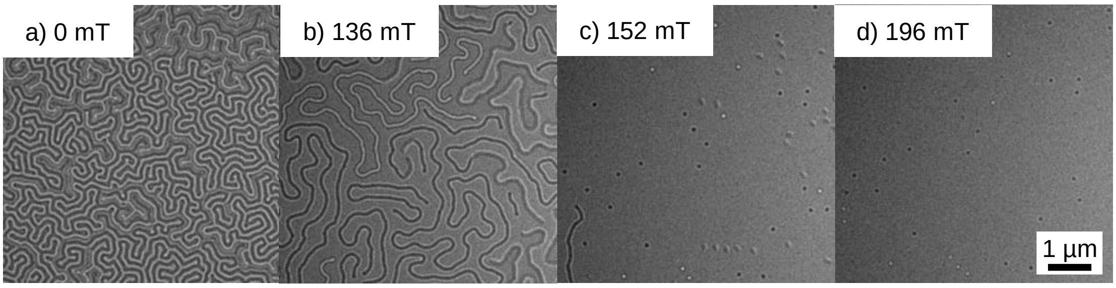

t_{Gd}=0.45 nm N_{Ir} = 5 at 300 K

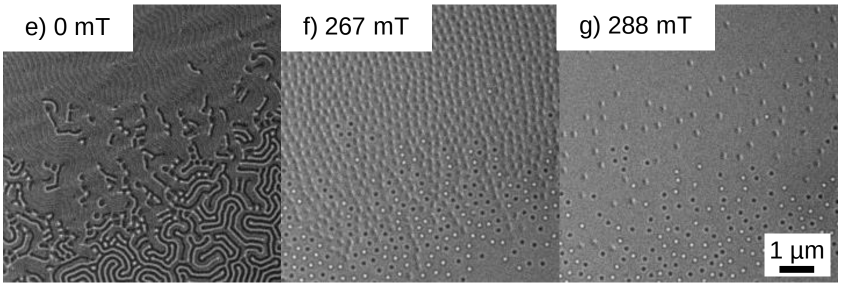

Figure A.10: Selected LTEM images of $[\mathrm{Fe/Ir/Gd}]_5/[\mathrm{Fe/Gd}]_{70}/[\mathrm{Fe/Ir/Gd}]_5$ with different Gd thickness. The MLs with t_{Gd} =0.40 (a-d) and 0.45 nm (e-g) exhibit both skyrmions and bubbles at 300 K. The latter shows a dense skyrmion/bubble lattice.

A.3 Additional Micromagnetic Simulations

The micromagnetic simulations supporting the experimental results in this work were carried out by S. Koraltan, C. Vogler, R. Kraft, and C. Abert, which are all part of D. Suess' group from the University of Vienna. In the following, additional simulations are shown, which complement the respective experimental results.

A.3.1 Complementary to Sec. 4.4

In this section, finite-element simulation results obtained with the finite-elements package *magnum.fe* [580] are presented. This is to reproduce the different minor loop behaviors observed for thin and thick FM layers and from that gain a more fundamental understanding of the relevant physics governing the experimental observations.

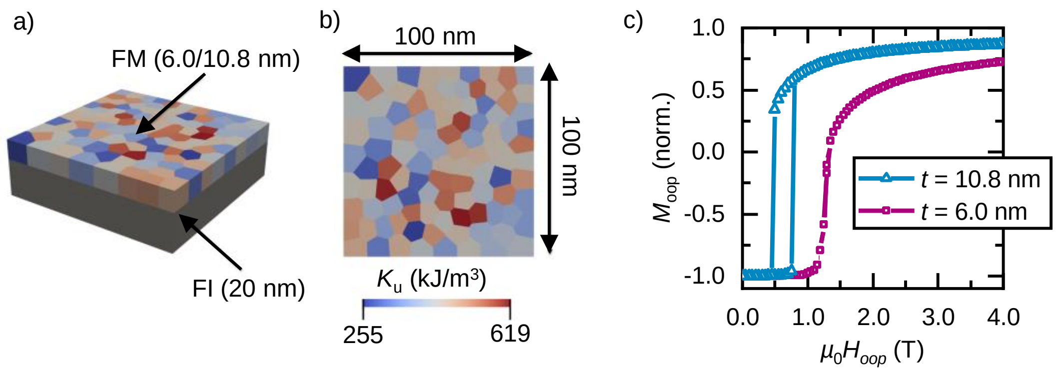

Figure A.11: Model and minor loops of the micromagnetic simulations of the FI/FM bilayer. Model of the simulated FI/FM bilayer structure (a). The lateral dimension of the model and the thickness of the layers are given. The average grain diameter is 10 nm and the discretization length is 2 nm. The color code shows the effective magnetic anisotropy, which is assumed to be normally distributed over the grains in the FM layer (b). Simulated macroscopic minor loops of the FM layer coupled to the FI for two different FM thicknesses of 6 nm ($N = 5$, purple line and squares) and 10.8 nm ($N = 9$, blue line and triangles) (c). The figure is also published in Ref. [100].

As shown in Fig. A.11 a and b, the model consists of 100 nm × 100 nm films with a 20 nm-thick FI layer and FM layers of 6.0 or 10.8 nm thickness, corresponding to the two different repetition numbers of $N = 5$ and $N = 9$, respectively. The structures consist of grains having an average diameter of 10 nm, generated by Voronoi tessellation. Due to the required small discretization length of 2 nm and the resulting large computational effort, the lateral dimensions are kept at 100 nm × 100 nm, which is considerably smaller

Table A.1: Material parameters used for the micromagnetic simulations of the investigated FI/FM heterostructures. K_u is the uniaxial magnetic anisotropy constant, M_s is the saturation magnetization, A is the exchange coupling in the bulk, J is the interface exchange coupling between the antiferromagnetically coupled layers, α_damp is the damping constant, l and w are the lateral size of the geometry and t is the thickness of the layers. The anisotropy axis is tilted by 1 ° against the oop direction in both layers to avoid metastable states.

Layer	**Ferrimagnet**	**Ferromagnet**
K_u (kJ/m^3)	1168	$255 - 619$
M_s (kA/m)	517	668
A (pJ/m)	10.0	10.0
J (mJ/m^2)	-0.1 to -33.8	
α_damp	1.0	1.0
$\angle_{K_\mathrm{eff},e_\mathrm{oop}}$ (°)	1.0	1.0
l&w (nm)	100.0	100.0
t (nm)	20.0	6.0 / 10.8

than the typical domain structures observed by MFM, displayed in Fig. 4.34 b-i. However, given that single grains with a lateral length of 50 nm were well approximated with a spin chain model in a previous work [228], a homogeneous magnetization within this distance in the ip direction can be assumed. Hence, the lateral film dimensions for the simulation work are justified. The grains of the model are fully exchange-coupled in the lateral directions. The uniaxial magnetic anisotropy K_u is normally distributed with a mean of 430 kJ/m^3 and a standard deviation of 75 kJ/m^3 (total range of 255 to 619 kJ/m^3), and the ratio $J_\mathrm{iex}/K_\mathrm{eff,FM}$ of interface exchange constant between the two layers and the respective effective magnetic anisotropy constant of the FM is kept constant at -0.1 µm (color code in Fig. A.11 a, b). All other material parameters are given in Table A.1.

The assumptions of a strong variation in the magnetic anisotropy of the FM layer and simultaneously in the interface-exchange constant at the FI/FM interface are based on previous results reported in Ref. [228, 258]. In Ref. [228], a hysteresis-free minor loop was found for a similar heterostructure with a thin FM layer of 5.5 nm and in Ref. [258], the relevant parameters and a condition for hysteresis-free minor loops were derived.

For the modeling, the ground state of the heterostructure with the FI layer magnetization pointing in the upwards oop direction and that of the FM layer pointing in the downwards oop direction is considered. Subsequently, the field magnitude is increased step-wise in 50 mT increments up to 4 T and then decreased back to 0 T. After each field step, the micromagnetic state of the system is relaxed for 1 ns. Note that the

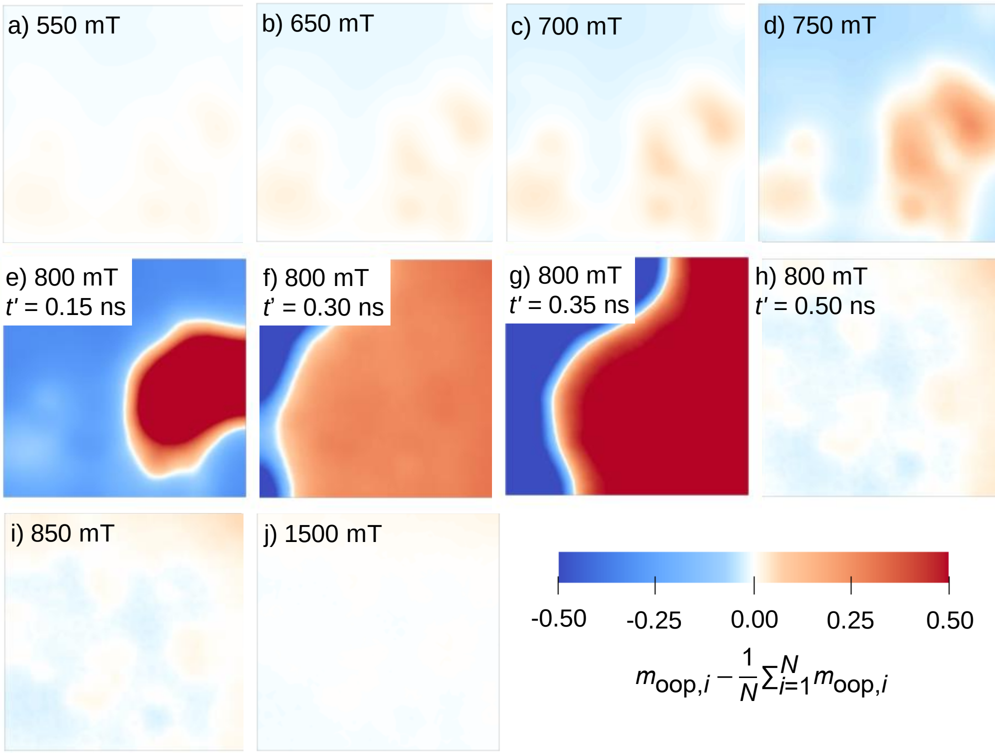

Figure A.12: Simulated MFM contrast of the bilayer with the thicker FM layer. Simulated MFM contrast of the thicker FM layer of 10.8 nm ($N = 9$) during its reversal for representative chosen applied oop magnetic fields. The color code represents the quantity in Eq A.1. e-h) show the dynamic process of the domain wall motion during switching at 800 mT and not the relaxed magnetization state, as indicated by the simulation time. The figure is also published in Ref. [100].

variation of the applied field in the simulations is performed much faster than that used during the experiments. However, because of the high damping constant ($\alpha_{\mathrm{damp}} = 1.0$) used for the simulations, a stationary state is obtained within 1 ns, such that the modeled loops are representative of the experimental loops.

Figure A.11 c displays minor loops of heterostructures with a thick ($N = 9$) and thin ($N = 5$) FM layer. While the loop for the thick FM layer shows a lower switching field of about 580 mT and a hysteresis width of around 300 mT, the switching field for the thin FM layer is higher than 1 T and hysteresis is absent. This reproduces the experimentally observed switching behavior of the FM layer (Fig. 4.33 b). Note that for the modeling, the only parameter changed is the thickness of the FM layer.

To gain a more fundamental understanding of the reversal process of the ferromagnetic layer and to understand the MFM contrast evolution with the field (Fig. 4.34 b-i), the quantity

$$m_{\text{oop},i} - \frac{1}{N}\sum_{i=1}^{N} m_{\text{oop},i}, \tag{A.1}$$

is plotted, with $m_{\text{oop},i}$ being the oop component of the normalized magnetization of node i of the finite-element discretization and with the sum running over all N nodes of the surface mesh on the top of the FM. Note that because a homogeneous magnetic moment distribution does not generate a stray field and hence has no MFM contrast, the average m_{oop} component is subtracted in equation A.1 to facilitate the comparison of the simulation results with MFM data. Figure A.12 displays the computed field evolution of the contrast for the sample with thicker FM layer ($N = 9$, 10.8 nm-thick). At low positive fields, the top FM layer couples antiparallel to the bottom FI. Therefore, in Fig. A.12 a-d, a weak contrast appears, which can be attributed to a difference in the canting of the magnetic moments in the individual grains with different magnetic anisotropy. The moments in grains with small anisotropy show more canting than those in grains with higher anisotropy. The contrast further increases with increasing applied oop field. Note that the simulation is performed only for the domain with an up magnetization of the FI layer and a down magnetization of the FM layer because the opposite domain with an up FM magnetization would not be affected by an applied field well below the coercivity of the FI layer. The simulation thus reveals a continuous rise of the up magnetization of the FM down domain and hence a decrease of the magnetization difference between the FM down and up domains. Therefore, the field arising from the pattern of domains in the FM that is antiparallel to that of the FI layer is reduced, and consequently, the MFM contrast is increased. This explains the small increase in contrast observed when comparing the MFM images from Fig. 4.34 b and c.

At a field of about 800 mT, a domain wall forms throughout the whole film, starting from the grain with the lowest anisotropy, as illustrated in Fig. A.12 e-h. The domain wall propagates through the film until all parts have switched parallel to the field (and parallel to the FI net magnetization), which is a fully irreversible process in agreement with the experimental results. Note that since in the relaxed magnetization state at 800 mT the domain wall propagation cannot be seen, Fig. A.12 e-h) shows the dynamic process at 800 mT, as indicated by the simulation time in the upper right corner. In order to compare the simulation results with the observed MFM data, some limitations of the simulation work need to be further elaborated. To keep the computational effort at an acceptable level, the simulation considers only a small area within an initially down FM magnetization. Thus, the magnetostatic energy arising from the up/down FM and down/up FI domain pattern and the existence of an initial vertical domain wall inside the FI and FM is not considered. For this reason, the simulation reveals the switching of a low anisotropy grain followed by a rapid expansion of the reversal domain. In contrast, the MFM data recorded in fields from 0.8 to 1.05 T (Fig. 4.34 d-g) show steady states of the domain wall propagation that cannot be observed in the model used for simulation.

After the FM has switched, the contrast becomes abruptly weak and decreases with increasing external field, as displayed in Fig. A.12 i-j. Note that again only the FM magnetization inside an initial FM down domain is considered. The simulation shows that the grain-to-grain variation of the up magnetic moment is reduced with increasing up field, which corresponds to a compression of the ip domain wall that has formed at the FI/FM interface. Hence, the up magnetic moment of the FM layer is increased, approaching that of a FM domain with an initial up magnetization. The down/up field from the FM layer that weakened the up/down field of the domains inside the FI layer thus becomes gradually smaller. This explains the small increase of the MFM contrast observed when the field is increased from 1.05 to 2 T (Figs. 4.34 g and 4.34 h).

Note that the magnetization process observed here for the thicker FM layer is fundamentally different from that observed in the work of Ref. [228] for a thinner FM layer. For this reason, the modeling is also performed for the thinner FM layer using the parameters describing the FI/FM heterostructure samples fabricated here. The results are displayed in Fig. A.13. Again the modeling is performed for a film area with an initial down FM magnetization. As in the work of Ref. [228] a three-stage magnetization process is observed. Stage 1 (Fig. A.13 a-c) is characterized by a rotation of the initial down magnetic moments near the top of the FM layer towards the up direction of the applied field. In stage 2 (Fig. A.13 d-g), the magnetic moments of isolated grains switch towards the up direction to improve the alignment of the magnetic moments to the applied field. The angle between the magnetic moments and the field is then smaller for the moments near the top of the FM film and larger for the moments near the FI/FM interface. Because this switching process depends on the properties of individual grains, a large grain-to-grain variation occurs. In stage 3 (Fig. A.13 h-l) all grains have switched to have a predominately up magnetization. The contrast drops as the horizontal domain wall at the FI/FM interface is compressed, and the local variation of the domain wall thickness is decreased. As observed by MFM in the work of Ref. [228], no lateral propagation of a vertical domain wall inside the FM layer occurs, but a three-stage

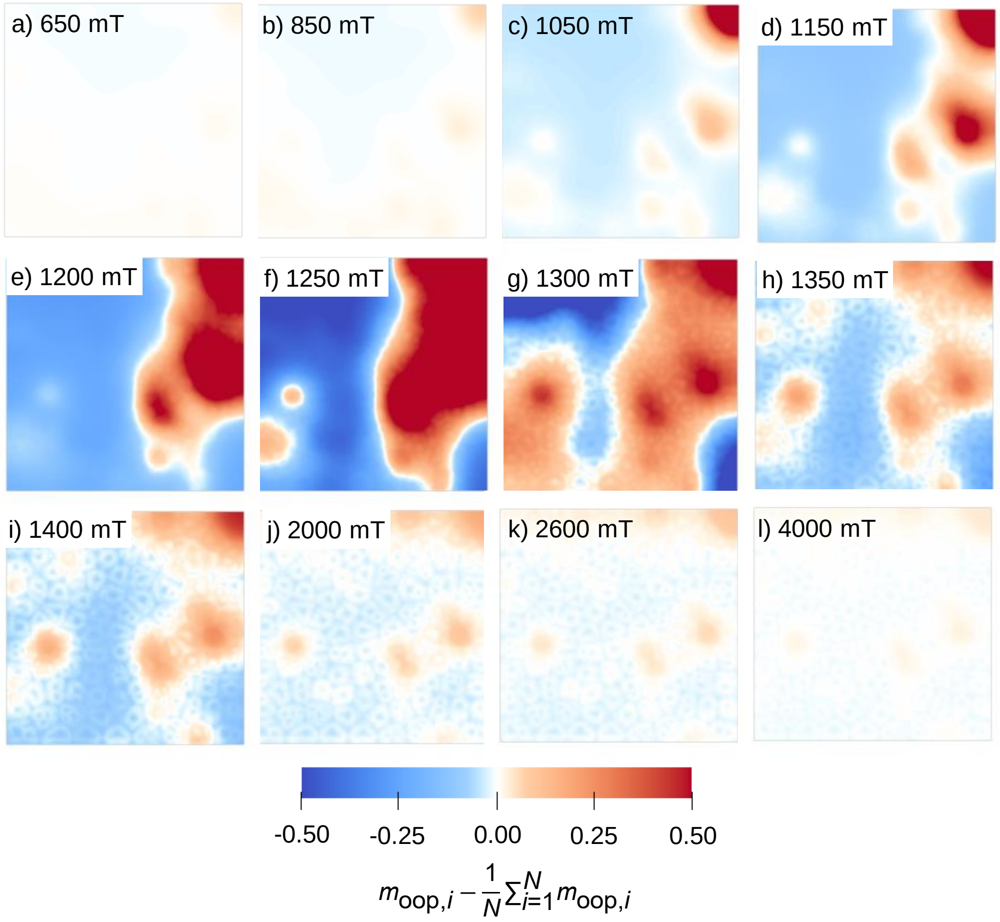

Figure A.13: Simulated MFM contrast of the bilayer with the thinner FM layer. Simulated MFM contrast of the thinner FM layer of 6.0 nm ($N = 5$) during its reversal for representative chosen applied oop magnetic fields. The color code represents the quantity of Eq A.1. The figure is also published in Ref. [100].

magnetization process takes place for each individual grain. The reversal process is hysteresis-free (purple curve with squares in Fig. A.11 c).

The condition for hysteresis-free switching derived in Ref. [258] can be applied here. Using the parameters listed in Table A.1 for the thicker FM layer clearly reveals that 90 % of the grains in the heterostructure remain above the threshold for hysteresis-free switching ($K_{\mathrm{uni}} \leq 330\,\mathrm{kJ/m^3}$), while for the system with the thinner FM the threshold value is $K_{\mathrm{uni}} \leq 418\,\mathrm{kJ/m^3}$. This means that 40% of the grains are below the threshold and hence show a hysteresis-free process. For the thinner FI/FM heterostructure with $N = 5$, this means that almost half of the FM grains show a gradual, hysteresis-free rotation of the magnetization. Based on this behavior and the small thickness of the FM, short vertical domain walls can form, as schematically illustrated in Fig. 4.35, and the observed three-stage process with a local rearrangement of domains in the switching process occurs. In contrast, in the thick FM layer with $N = 9$, almost all grains show irreversible hysteretic reversal. An abrupt switch of individual grains would generate several large vertical domain walls, which is energetically unfavorable due to the thickness of the FM. This is the reason why only one domain wall is observed, which is independent of the granular structure, propagating through the FM layer and causing irreversible switching of the macroscopic minor loop.

A.3.2 Complementary to Sec. 5.3

In addition to Fig. 5.23, micromagnetic simulations of the nucleation process of a ccw Bloch skyrmion, a cw Bloch skyrmion, a first-order antiskyrmion, and a second-order antiskyrmion can be found in Fig. A.14 a, b, c, and d, respectively. Please note that only the nucleation process of the Bloch skyrmions and the first-order antiskyrmion could be observed experimentally. Due to the rarity of second-order antiskyrmions and no possibility to predict possible nucleation spots, imaging of the formation process was not achieved. Figure A.14 illustrates the magnetization states at chosen magnitudes of the applied Zeeman field during the formation of the spin objects. The simulation parameters are selected according to Sec. 5.3.1 for a, b, and c. In Fig. A.14 d a weak DMI of $D = 0.1\,\mathrm{mJ/m^2}$ is used. The DMI energy is modeled in the micromagnetic simulations as

$$E_{\mathrm{DMI}} = \int_{\Omega_m} D\left[\boldsymbol{m} \cdot \nabla(\boldsymbol{e}_d \cdot \boldsymbol{m}) - (\nabla \cdot \boldsymbol{m})(\boldsymbol{e}_d \cdot \boldsymbol{m})\mathrm{d}\boldsymbol{x}\right], \tag{A.2}$$

where Ω_m is the magnetic region, $\boldsymbol{e}_d = (0,\ 0,\ 1)$, D is the DMI constant, and $\boldsymbol{m}$ is the normalized magnetization vector. Comparing the two systems, with and without DMI, the nucleation of the skyrmions and antiskyrmions takes place in similar manner at comparable field magnitudes. Each snapshot is sliced from the simulation output, such that the provided images illustrate a close up look at the particular spin objects within an area of $l_x \times l_y = 500 \times 500\,\mathrm{nm^2}$. The black vectors are showing the ip components of the magnetization, while the color illustrates the oop component. It is noteworthy that in the micromagnetic investigations, the second-order antiskyrmions only appear in the presence of weak DMI, where $D = 0.1\,\mathrm{mJ/m^2}$. However, they are really rare and their presence can not be ruled out in systems without DMI. The simulations were carried out

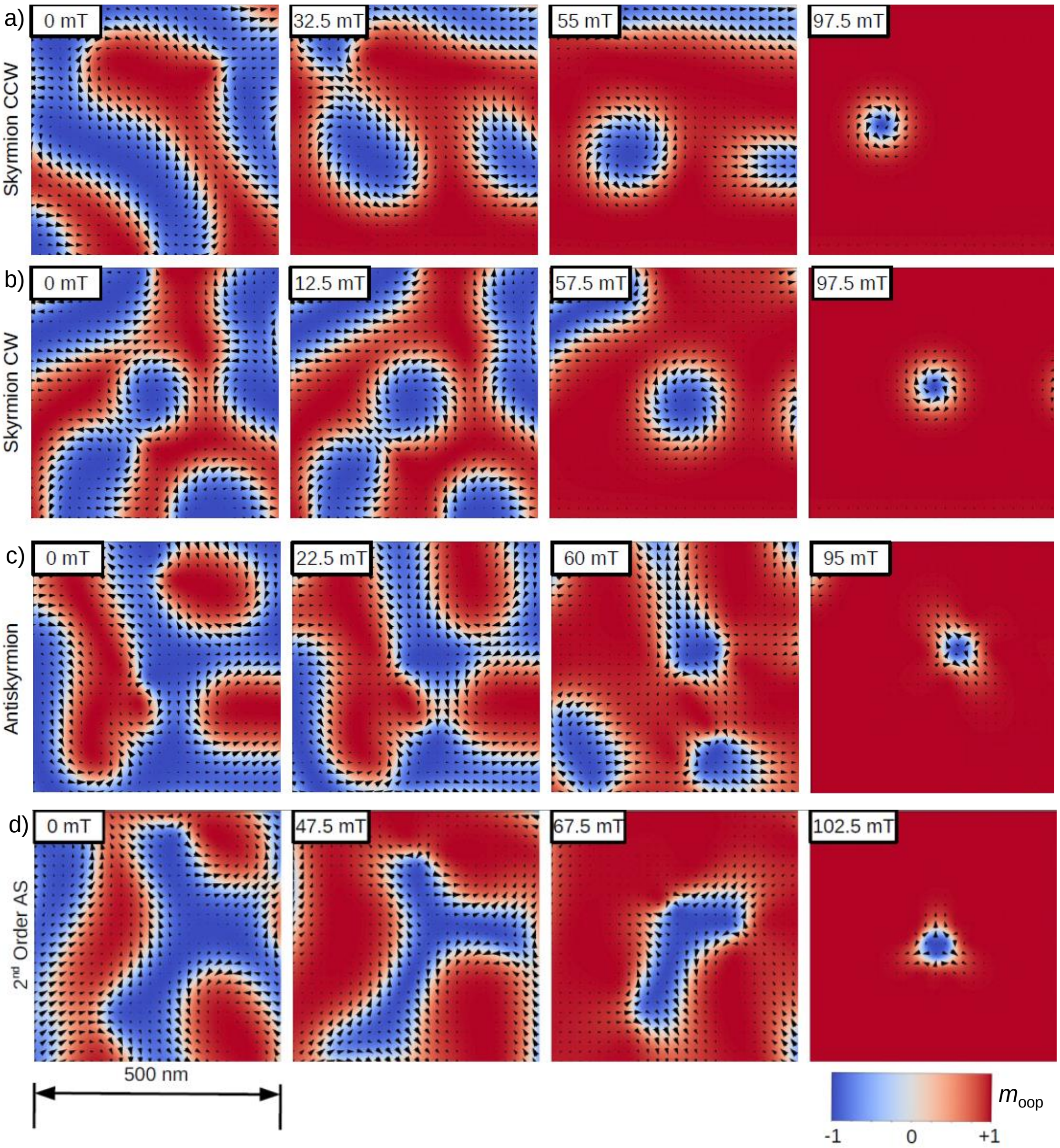

Figure A.14: Micromagnetic simulations of nucleation processes of different spin objects. Formation process of a counterclockwise (ccw) Bloch skyrmion (a), a clockwise (cw) Bloch skyrmion (b), a first-order antiskyrmion (c), and a second-order antiskyrmion (d). The figure is also published in Ref. [426].

by S. Koraltan and are also published in Ref. [426].

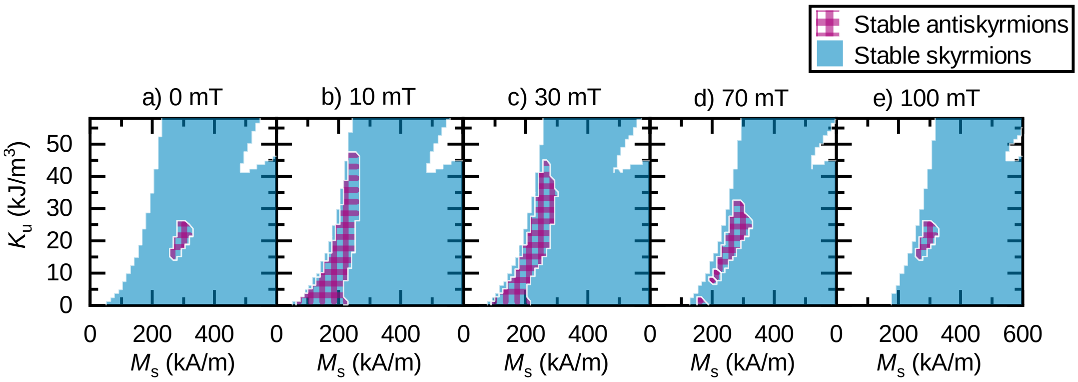

Figure A.15: Micromagnetic simulations of the stability phase maps of an antiskyrmion and a skyrmion at different oop fields. The colored areas of the diagram correspond to the parameter regions in which skyrmions (blue) and antiskyrmions (purple) are stable in the simulations dependent on the uniaxial anisotropy K_u and the saturation magnetization M_s. In the white regions neither of them are stable. The figure is also published in Ref. [426].

In order to investigate the stability of skyrmions and antiskyrmions in infinite films, their magnetization dynamics in a confined system are investigated where a rough parametrization is chosen as the start configuration. Furthermore, to avoid the decay of the topological structure by moving out of the confined system, a high anisotropy of $K_u = 1\,\mathrm{MJ/m^3}$ in the outer ring of the simulated structure is set. If this anisotropy barrier is placed at a sufficient distance from the topological structure, this procedure is assumed to accurately account for possible annihilation processes in infinite films while keeping the computational cost at a feasible level.

Figure A.15 illustrates the obtained stability phase maps of an antiskyrmion and a Bloch skyrmion for a system free of DMI at different Zeeman fields. To obtain these results, the Zeeman fields are applied constantly for 10 ns, while solving the LLG (Eq. 5.1), in a system where a parametrization of an antiskyrmion or a Bloch skyrmion is the initial magnetic configuration. The exchange stiffness constant is chosen as constant at $A = 6\,\mathrm{pJ/m}$. The final magnetization state $\boldsymbol{m}(10\,\mathrm{ns})$ is then evaluated by means of the finite element method and the integer topological charge N_sk is calculated integrating Eq. 2.25 over the entire volume, and dividing the result by the thickness of the sample, which is 62 nm.

A.4 Lists of Samples

In the following, all samples used for the presented results in this work are listed by sample name, composition, and the section they are presented in. Please note that this is only a small fraction of the actually deposited samples. The samples were prepared at RT by DC magnetron (co-)sputtering from elemental targets. All samples were fabricated in the BesTec system described in Sec. 3.1.1. The provided thicknesses are for the most part nominal thicknesses. The individual layer thicknesses were adjusted by the deposition rate, which was controlled by a calibrated quartz balance. The thicknesses and compositions of the 20-nm-thick alloys were partially checked by RBS according to Sec. 3.2.1. The ML structure of samples was confirmed by cross-section TEM (Sec. 3.2.7). The tables are sorted by the corresponding sections the samples were used at. The deposition parameters are stated in the caption of the tables.

Table A.2: Sample list for Sec. 4.2. All deposited samples used for the presented results in Sec. 4.2 are listed. Thickness are given in nanometer. The deposition angle was fixed at 17.5°. The maximum base pressure was always below 10^{-8} mbar. The working Ar pressure was kept constant at 5.0×10^{-3} mbar. The sputtering rates of Co, Ni, Pt, and Pd were set to 0.02, 0.03, 0.05, and 0.05 nm/s, respectively. The samples were prepared on Si(100) substrates with a 100-nm-thick thermally oxidized SiO_x layer.

Name	Composition	Used in
B170201_7	$Pt(5)/[Co(0.10)/Ni(0.4)]_3/Pt(5)$	Sec. 4.2.2
B170201_8	$Pt(5)/[Co(0.15)/Ni(0.4)]_3/Pt(5)$	Sec. 4.2.2
B161206_3	$Pt(5)/[Co(0.20)/Ni(0.4)]_3/Pt(5)$	Sec. 4.2.2
B170201_9	$Pt(5)/[Co(0.25)/Ni(0.4)]_3/Pt(5)$	Sec. 4.2.2
B170201_10	$Pt(5)/[Co(0.30)/Ni(0.4)]_3/Pt(5)$	Sec. 4.2.2
B181025_3	$Pt(5)/[Co(0.40)/Ni(0.4)]_3/Pt(5)$	Sec. 4.2.2
B170516_3	$Pt(5)/[Co(0.50)/Ni(0.4)]_3/Pt(5)$	Sec. 4.2.2
B171017_2	$Pd(5)/[Co(0.10)/Ni(0.4)/Pd(0.6)]_9/Pd(5)$	Sec. 4.2.2
B180628_2	$Pd(5)/[Co(0.15)/Ni(0.4)/Pd(0.6)]_9/Pd(5)$	Sec. 4.2.2
B171016_2	$Pd(5)/[Co(0.20)/Ni(0.4)/Pd(0.6)]_9/Pd(5)$	Sec. 4.2.2
B180628_1	$Pd(5)/[Co(0.25)/Ni(0.4)/Pd(0.6)]_9/Pd(5)$	Sec. 4.2.2
B171016_9	$Pd(5)/[Co(0.30)/Ni(0.4)/Pd(0.6)]_9/Pd(5)$	Sec. 4.2.2
B171016_10	$Pd(5)/[Co(0.40)/Ni(0.4)/Pd(0.6)]_9/Pd(5)$	Sec. 4.2.2
B171017_1	$Pd(5)/[Co(0.50)/Ni(0.4)/Pd(0.6)]_9/Pd(5)$	Sec. 4.2.2
B170410_5	$Pt(5)/[Co(0.10)/Ni(0.4)/Pt(0.6)]_4/Pt(5)$	Sec. 4.2.2
B170410_6	$Pt(5)/[Co(0.15)/Ni(0.4)/Pt(0.6)]_4/Pt(5)$	Sec. 4.2.2

B170324_4	Pt(5)/[Co(0.20)/Ni(0.4)/Pt(0.6)]$_4$/Pt(5)	Sec. 4.2.2
B170410_7	Pt(5)/[Co(0.25)/Ni(0.4)/Pt(0.6)]$_4$/Pt(5)	Sec. 4.2.2
B170410_8	Pt(5)/[Co(0.30)/Ni(0.4)/Pt(0.6)]$_4$/Pt(5)	Sec. 4.2.2
B181025_4	Pt(5)/[Co(0.40)/Ni(0.4)/Pt(0.6)]$_4$/Pt(5)	Sec. 4.2.2
B181025_5	Pt(5)/[Co(0.50)/Ni(0.4)/Pt(0.6)]$_4$/Pt(5)	Sec. 4.2.2
B181025_1	Pt(5)/[Co(0.2)/Ni(0.4)]$_1$/Pt(5)	Sec. 4.2.3
B161206_4	Pt(5)/[Co(0.2)/Ni(0.4)]$_2$/Pt(5)	Sec. 4.2.3
B161206_3	Pt(5)/[Co(0.2)/Ni(0.4)]$_3$/Pt(5)	Sec. 4.2.3
B161206_2	Pt(5)/[Co(0.2)/Ni(0.4)]$_4$/Pt(5)	Sec. 4.2.3
B161206_1	Pt(5)/[Co(0.2)/Ni(0.4)]$_5$/Pt(5)	Sec. 4.2.3
B161206_5	Pt(5)/[Co(0.2)/Ni(0.4)]$_6$/Pt(5)	Sec. 4.2.3
B161208_1	Pt(5)/[Co(0.2)/Ni(0.4)]$_7$/Pt(5)	Sec. 4.2.3
B161208_2	Pt(5)/[Co(0.2)/Ni(0.4)]$_8$/Pt(5)	Sec. 4.2.3
B181025_2	Pt(5)/[Co(0.2)/Ni(0.4)]$_9$/Pt(5)	Sec. 4.2.3
B160706_2	Pt(5)/[Co(0.2)/Ni(0.4)]$_{10}$/Pt(5)	Sec. 4.2.3
B160706_3	Pt(5)/[Co(0.2)/Ni(0.4)]$_{15}$/Pt(5)	Sec. 4.2.3
B181025_6	Pd(5)/[Co(0.2)/Ni(0.4)/Pd(0.6)]$_1$/Pd(5)	Sec. 4.2.3
B170516_5	Pd(5)/[Co(0.2)/Ni(0.4)/Pd(0.6)]$_2$/Pd(5)	Sec. 4.2.3
B170516_6	Pd(5)/[Co(0.2)/Ni(0.4)/Pd(0.6)]$_3$/Pd(5)	Sec. 4.2.3
B170516_7	Pd(5)/[Co(0.2)/Ni(0.4)/Pd(0.6)]$_4$/Pd(5)	Sec. 4.2.3
B170516_8	Pd(5)/[Co(0.2)/Ni(0.4)/Pd(0.6)]$_5$/Pd(5)	Sec. 4.2.3
B180628_3	Pd(5)/[Co(0.2)/Ni(0.4)/Pd(0.6)]$_6$/Pd(5)	Sec. 4.2.3
B180628_4	Pd(5)/[Co(0.2)/Ni(0.4)/Pd(0.6)]$_7$/Pd(5)	Sec. 4.2.3
B170518_1	Pd(5)/[Co(0.2)/Ni(0.4)/Pd(0.6)]$_8$/Pd(5)	Sec. 4.2.3
B171016_2	Pd(5)/[Co(0.2)/Ni(0.4)/Pd(0.6)]$_9$/Pd(5)	Sec. 4.2.3
B171016_3	Pd(5)/[Co(0.2)/Ni(0.4)/Pd(0.6)]$_{15}$/Pd(5)	Sec. 4.2.3
B170324_1	Pt(5)/[Co(0.2)/Ni(0.4)/Pt(0.6)]$_1$/Pt(5)	Sec. 4.2.3
B170324_2	Pt(5)/[Co(0.2)/Ni(0.4)/Pt(0.6)]$_2$/Pt(5)	Sec. 4.2.3
B170324_3	Pt(5)/[Co(0.2)/Ni(0.4)/Pt(0.6)]$_3$/Pt(5)	Sec. 4.2.3
B170324_4	Pt(5)/[Co(0.2)/Ni(0.4)/Pt(0.6)]$_4$/Pt(5)	Sec. 4.2.3
B170324_5	Pt(5)/[Co(0.2)/Ni(0.4)/Pt(0.6)]$_5$/Pt(5)	Sec. 4.2.3
B170324_6	Pt(5)/[Co(0.2)/Ni(0.4)/Pt(0.6)]$_6$/Pt(5)	Sec. 4.2.3
B170515_3	Pt(5)/[Co(0.2)/Ni(0.4)/Pt(0.6)]$_9$/Pt(5)	Sec. 4.2.3
B170515_4	Pt(5)/[Co(0.2)/Ni(0.4)/Pt(0.6)]$_{12}$/Pt(5)	Sec. 4.2.3
B170410_1	Pt(5)/[Co(0.2)/Ni(0.4)/Pt(0.6)]$_{15}$/Pt(5)	Sec. 4.2.3
B171017_3	Pd(5)/[Co(0.2)/Ni(0.4)/Pd(0.2)]$_1$/Pd(5)	Sec. 4.2.4

B171016_4	Pd(5)/[Co(0.2)/Ni(0.4)/Pd(0.2)]$_{2}$/Pd(5)	Sec. 4.2.4
B171016_5	Pd(5)/[Co(0.2)/Ni(0.4)/Pd(0.2)]$_{3}$/Pd(5)	Sec. 4.2.4
B171016_6	Pd(5)/[Co(0.2)/Ni(0.4)/Pd(0.2)]$_{4}$/Pd(5)	Sec. 4.2.4
B171016_7	Pd(5)/[Co(0.2)/Ni(0.4)/Pd(0.2)]$_{5}$/Pd(5)	Sec. 4.2.4
B171016_8	Pd(5)/[Co(0.2)/Ni(0.4)/Pd(0.2)]$_{9}$/Pd(5)	Sec. 4.2.4
B181025_10	Pd(5)/[Co(0.2)/Ni(0.4)/Pd(0.2)]$_{15}$/Pd(5)	Sec. 4.2.4
B181025_7	Pt(5)/[Co(0.2)/Ni(0.4)/Pt(0.2)]$_{1}$/Pt(5)	Sec. 4.2.4
B181025_8	Pt(5)/[Co(0.2)/Ni(0.4)/Pt(0.2)]$_{2}$/Pt(5)	Sec. 4.2.4
B170515_7	Pt(5)/[Co(0.2)/Ni(0.4)/Pt(0.2)]$_{3}$/Pt(5)	Sec. 4.2.4
B170410_2	Pt(5)/[Co(0.2)/Ni(0.4)/Pt(0.2)]$_{4}$/Pt(5)	Sec. 4.2.4
B170515_8	Pt(5)/[Co(0.2)/Ni(0.4)/Pt(0.2)]$_{5}$/Pt(5)	Sec. 4.2.4
B170515_9	Pt(5)/[Co(0.2)/Ni(0.4)/Pt(0.2)]$_{7}$/Pt(5)	Sec. 4.2.4
B170515_10	Pt(5)/[Co(0.2)/Ni(0.4)/Pt(0.2)]$_{9}$/Pt(5)	Sec. 4.2.4
B170516_1	Pt(5)/[Co(0.2)/Ni(0.4)/Pt(0.2)]$_{15}$/Pt(5)	Sec. 4.2.4

Table A.3: Sample list for Sec. 4.3. All deposited samples used for the presented results in Sec. 4.3 are listed. Thickness are given in nanometer. The deposition angle was fixed at 17.5°. The maximum base pressure was always below 10^{-8} mbar. The working Ar pressure was kept constant at 5.0×10^{-3} mbar. The sputtering rates of Ta, Pt, and Tb were fixed at 0.05, 0.05, and 0.06 nm/s, respectively. Depending on the desired composition, the rates of Tb and Co were set between 0.05 - 0.10 nm/s and 0.01 - 0.08 nm/s, respectively. The samples were prepared on Si(100) substrates with a 100-nm-thick thermally oxidized SiO_x layer.

Name	**Composition**	**Used in**
B170131_2	Pt(5)/Tb$_{18}$(Fe$_{70}$Co$_{30}$)$_{82}$(20)/Pt(5)	Sec. 4.3.2
B170206_2	Pt(5)/Tb$_{20}$(Fe$_{70}$Co$_{30}$)$_{80}$(20)/Pt(5)	Sec. 4.3.2
B170207_3	Pt(5)/Tb$_{22}$(Fe$_{70}$Co$_{30}$)$_{78}$(20)/Pt(5)	Sec. 4.3.2
B170207_7	Pt(5)/Tb$_{24}$(Fe$_{70}$Co$_{30}$)$_{76}$(20)/Pt(5)	Sec. 4.3.2
B170523_2	Ta(2)/Pt(5)/Tb$_{26}$(Fe$_{70}$Co$_{30}$)$_{74}$(20)/Ta(5)	Sec. 4.3.2
B170518_5	Ta(2)/Pt(5)/Tb$_{28}$(Fe$_{70}$Co$_{30}$)$_{72}$(20)/Ta(5)	Sec. 4.3.2
B170523_4	Ta(2)/Pt(5)/Tb$_{30}$(Fe$_{70}$Co$_{30}$)$_{70}$(20)/Ta(5)	Sec. 4.3.2
B180131_5	Ta(2)/Pt(5)/Tb$_{18}$(Fe$_{80}$Co$_{20}$)$_{82}$(20)/Ta(5)	Sec. 4.3.2
B170206_4	Pt(5)/Tb$_{20}$(Fe$_{80}$Co$_{20}$)$_{80}$(20)/Pt(5)	Sec. 4.3.2
B170207_1	Pt(5)/Tb$_{22}$(Fe$_{80}$Co$_{20}$)$_{78}$(20)/Pt(5)	Sec. 4.3.2
B170207_5	Pt(5)/Tb$_{24}$(Fe$_{80}$Co$_{20}$)$_{76}$(20)/Pt(5)	Sec. 4.3.2
B180201_3	Ta(2)/Pt(5)/Tb$_{26}$(Fe$_{80}$Co$_{20}$)$_{74}$(20)/Ta(5)	Sec. 4.3.2
B180201_4	Ta(2)/Pt(5)/Tb$_{28}$(Fe$_{80}$Co$_{20}$)$_{72}$(20)/Ta(5)	Sec. 4.3.2

B180201_5	Ta(2)/Pt(5)/Tb$_{30}$(Fe$_{80}$Co$_{20}$)$_{70}$(20)/Ta(5)	Sec. 4.3.2
B170523_8	Pt(5)/Tb$_{26}$(Fe$_{85}$Co$_{15}$)$_{70}$(20)/Pt(5)	Sec. 4.3.2
B180328_4	Ta(2)/Pt(5)/[Tb(0.40)/Fe$_{70}$Co$_{30}$(0.37)]$_{26}$/Ta(5)	Sec. 4.3.3
B180328_5	Ta(2)/Pt(5)/[Tb(0.79)/Fe$_{70}$Co$_{30}$(0.74)]$_{13}$/Ta(5)	Sec. 4.3.3
B190208_5	Ta(2)/Pt(5)/[Tb(1.27)/Fe$_{70}$Co$_{30}$(1.23)]$_{8}$/Pt(5)	Sec. 4.3.3

Table A.4: Sample list for Sec. 4.4. A list of all deposited samples used for the presented results in Sec. 4.4 is given. The deposition parameter were selected according to the individual layers in Tab. A.2 and A.3. The samples were prepared on Si(100) substrates with a 100-nm-thick thermally oxidized SiO$_x$ layer.

Name	Composition	Used in
B170518_4	Pt(5)/Tb$_{28}$(Fe$_{70}$Co$_{30}$)$_{72}$(20)/[Co(0.2)/Ni(0.4)/Pt(0.6)]$_{9}$/Ta(5)	Sec. 4.4
B170718_4	Pt(5)/Tb$_{24}$(Fe$_{70}$Co$_{30}$)$_{76}$(20)/[Co(0.2)/Ni(0.4)/Pt(0.6)]$_{9}$/Ta(5)	Sec. 4.4
B170523_5	Pt(5)/Tb$_{32}$(Fe$_{70}$Co$_{30}$)$_{68}$(20)/[Co(0.2)/Ni(0.4)/Pt(0.6)]$_{9}$/Ta(5)	Sec. 4.4
B191216_3	Pt(5)/Tb$_{28}$(Fe$_{70}$Co$_{30}$)$_{72}$(20)/[Co(0.2)/Ni(0.4)/Pt(0.6)]$_{3}$/Ta(5)	Sec. 4.4
B181025_13	Pt(5)/Tb$_{28}$(Fe$_{70}$Co$_{30}$)$_{72}$(20)/[Co(0.2)/Ni(0.4)/Pt(0.6)]$_{5}$/Ta(5)	Sec. 4.4
B191216_4	Pt(5)/Tb$_{28}$(Fe$_{70}$Co$_{30}$)$_{72}$(20)/[Co(0.2)/Ni(0.4)/Pt(0.6)]$_{7}$/Ta(5)	Sec. 4.4
B191216_5	Pt(5)/Tb$_{28}$(Fe$_{70}$Co$_{30}$)$_{72}$(20)/[Co(0.2)/Ni(0.4)/Pt(0.6)]$_{15}$/Ta(5)	Sec. 4.4

Table A.5: Sample list for chapter 5. All deposited samples used for the presented results in this chapter are listed. All thickness are given in nanometer. The thicknesses of the individual Fe, Ir, and Gd layers stayed constant, if nothing else is noted. The deposition angle was fixed at 17.5° for all listed samples. The maximum base pressure was always below 10^{-8} mbar. The working Ar pressure was kept at 3.5×10^{-3} mbar. The sputtering rates of Pt, Gd, Fe, Ir, Cu, Al, and Ta were at 0.05, 0.05, 0.035, 0.03, 0.03, 0.03, and 0.05 nm/s, respectively. The samples were prepared on both Si(100) substrates with a 100-nm-thick thermally oxidized SiO$_x$ layer and 30-nm-thick SiN membranes for LTEM imaging.

Name	Composition	Used in
B180604_1	Pt(5)/[Fe(0.35)/Gd(0.35)]$_{80}$/Pt(5)	Sec. 5.2.2
B180604_2	Pt(5)/[Fe(0.35)/Gd(0.40)]$_{80}$/Pt(5)	Sec. 5.2.2
B180604_3	Pt(5)/[Fe(0.35)/Gd(0.45)]$_{80}$/Pt(5)	Sec. 5.2.2
B180604_4	Pt(5)/[Fe(0.35)/Gd(0.50)]$_{80}$/Pt(5)	Sec. 5.2.2
B180604_5	Pt(5)/[Fe(0.35)/Gd(0.55)]$_{80}$/Pt(5)	Sec. 5.2.2
B200526_1	Pt(5)/[Fe(0.35)/Gd(0.40)]$_{120}$/Pt(5)	Sec. 5.2.4
B190607_4	Pt(5)/[Fe(0.35)/Gd(0.50)]$_{80}$/Pt(5)	Sec. 5.2.4
B191016_3	Pt(5)/[Fe(0.35)/Ir(0.2)/Gd(0.40)]$_{80}$/Pt(5)	Sec. 5.3.3

B191018_2	Pt(5)/[Fe/Ir/Gd]$_{20}$/[Fe/Gd]$_{40}$/[Fe/Ir/Gd]$_{20}$/Pt(5)	Sec. 5.3.3
B191016_5	Pt(5)/[Fe/Ir/Gd]$_{10}$/[Fe/Gd]$_{60}$/[Fe/Ir/Gd]$_{10}$/Pt(5)	Sec. 5.3.3
B191017_2	Pt(5)/[Fe/Ir/Gd]$_{5}$/[Fe/Gd]$_{70}$/[Fe/Ir/Gd]$_{5}$/Pt(5)	Sec. 5.3.3
B191018_1	Pt(5)/[Fe/Ir/Gd]$_{2}$/[Fe/Gd]$_{76}$/[Fe/Ir/Gd]$_{2}$/Pt(5)	Sec. 5.3.3
B191016_4	Pt(5)/[Fe(0.35)/Gd(0.40)]$_{80}$/Pt(5)	Sec. 5.3.3
B191205_5	Pt/[Fe/Gd]$_{2}$/[[Fe/Gd]$_{6}$/Fe/Ir/Gd]$_{10}$/[Fe/Gd]$_{8}$/Pt	Sec. 5.3.9
B191205_4	Pt/[Ir(0.2)/Fe/Gd]$_{5}$/[Fe/Gd]$_{70}$/[Ir(0.2)/Fe/Gd]$_{5}$/Pt	Sec. 5.3.9
B191205_2	Pt/[Fe/Ir(0.6)/Gd]$_{5}$/[Fe/Gd]$_{70}$/[Fe/Ir(0.6)/Gd]$_{5}$/Pt	Sec. 5.3.9
B191205_3	Pt/[Fe/Pt(0.2)/Gd]$_{5}$/[Fe/Gd]$_{70}$/[Fe/Pt(0.2)/Gd]$_{5}$/Pt	Sec. 5.3.9
B200526_6	Pt/[Fe/Cu(0.2)/Gd]$_{5}$/[Fe/Gd]$_{70}$/[Fe/Cu(0.2)/Gd]$_{5}$/Pt	Sec. 5.3.9
B200526_7	Pt/[Fe/Al(0.2)/Gd]$_{5}$/[Fe/Gd]$_{70}$/[Fe/Al(0.2)/Gd]$_{5}$/Pt	Sec. 5.3.9
B210104_1	Pt/[Fe/Ir/Gd(0.40)]$_{5}$/[Fe/Gd]$_{70}$/[Fe/Ir/Gd]$_{5}$/Pt	Sec. 5.5
B210104_2	Pt/[Fe/Ir/Gd(0.45)]$_{5}$/[Fe/Gd]$_{70}$/[Fe/Ir/Gd]$_{5}$/Pt	Sec. 5.5

Appendix B

Bibliography

1. IDC. Worldwide Global StorageSphere Forecast, 2021–2025: To Save or Not to Save Data, That Is the Question. *IDC report* **US47509621** (2020).
2. Lu, R., Zhu, H., Liu, X., Liu, J. K. & Shao, J. Toward efficient and privacy-preserving computing in big data era. *IEEE Netw.* **28,** 46 (2014).
3. Evans, D. & Cisco Internet Business Solutions Group (IBSG). Cisco Annual Internet Report (2018–2023). *White Paper* (2020).
4. Mitchell, T. M. *Machine Learning* (New York: McGraw-Hill, 1997).
5. Moss, S. *Shares in hard drive manufacturers spike due to Chia cryptocurrency* `https://www.datacenterdynamics.com/en/news/shares-in-hard-drive-manufacturers-spike-due-to-chia-cryptocurrency/` (2021).
6. Kwon, Y. & Rhu, M. Beyond the Memory Wall: A Case for Memory-Centric HPC System for Deep Learning. *51st Annual IEEE/ACM Int. Symp. on Microarchitecture,* 148 (2018).
7. Li, S. *et al.* Magnetic skyrmions for unconventional computing. *Mater. Horiz.* **8,** 854 (2020).
8. Marković, D., Mizrahi, A., Querlioz, D. & Grollier, J. Physics for neuromorphic computing. *Nat. Rev. Phys.* **2,** 499 (2020).
9. Moore, G. E. Cramming more components onto integrated circuits. *Electronics* **38,** 114 (1965).
10. Moore, G. E. Progress in digital integrated electronics. *Tech. Dig. Int. Electro. Dev. Meeting,* 11 (1975).
11. Schaller, R. Moore's law: past, present and future. *IEEE Spectrum* **34,** 52 (1997).
12. Fontana, R. E., Biskeborn, R. G., Lantz, M. & Decad, G. M. Tape in the cloud — Technology developments and roadmaps supporting 80 TB cartridge capacities. *AIP Adv.* **9,** 125222 (2019).
13. Kasavajhala, V. Solid State Drive vs. Hard Disk Drive Price and Performance Study. *Dell PowerVault Technical Marketing White Paper* (2011).

14. Fontana, R. E. & Decad, G. M. Moore's law realities for recording systems and memory storage components: HDD, tape, NAND, and optical. *AIP Adv.* **8,** 056506 (2018).
15. Mandelman, J. A. *et al.* Challenges and future directions for the scaling of dynamic random-access memory (DRAM). *IBM J. Res. Dev.* **46,** 187 (2002).
16. Aharoni, A. *Introduction to the Theory of Ferromagnetism* (Clarendon Press, 2001).
17. Morrish, A. H. *The physical principles of magnetism.* (Wiley-VCH, 2001).
18. Jiles, D. *Introduction to magnetism and magnetic materials* (CRC press, 2015).
19. Blundell, S. *Magnetism in Condensed Matter* (Oxford Master Series in Physics, 2001).
20. Stöhr Joachim, S. & Christoph, H. *Magnetism - From Fundamentals to Nanoscale Dynamics* (Springer Series in Solid-State Sciences, 2006).
21. Coronado, E., Tsukerblat, B. S. & Georges, R. *Exchange Interactions I: Mechanisms* (Springer Netherlands, 1996).
22. Ruderman, M. A. & Kittel, C. Indirect Exchange Coupling of Nuclear Magnetic Moments by Conduction Electrons. *Phys. Rev.* **96,** 99 (1954).
23. Kasuya, T. A Theory of Metallic Ferro- and Antiferromagnetism on Zener's Model. *Prog. Theor. Phys.* **16,** 45 (1956).
24. Yosida, K. Magnetic Properties of Cu-Mn Alloys. *Phys. Rev.* **106,** 893 (1957).
25. Van Vleck, J. H. Note on the Interactions between the Spins of Magnetic Ions or Nuclei in Metals. *Rev. Mod. Phys.* **34,** 681 (1962).
26. Parkin, S. S. P. & Mauri, D. Spin engineering: Direct determination of the Ruderman-Kittel-Kasuya-Yosida far-field range function in ruthenium. *Phys. Rev. B* **44,** 7131 (1991).
27. Yafet, Y. Ruderman-Kittel-Kasuya-Yosida range function of a one-dimensional free-electron gas. *Phys. Rev. B* **36,** 3948 (1987).
28. NobelPrize.org. *The Nobel Prize in Physics 2007* `https://www.nobelprize.org/prizes/physics/2007/summary/` (2021).
29. Binasch, G., Grünberg, P., Saurenbach, F. & Zinn, W. Enhanced magnetoresistance in layered magnetic structures with antiferromagnetic interlayer exchange. *Phys. Rev. B* **39,** 4828 (1989).
30. Baibich, M. N. *et al.* Giant Magnetoresistance of (001)Fe/(001)Cr Magnetic Superlattices. *Phys. Rev. Lett.* **61,** 2472 (1988).
31. Moriya, T. Anisotropic Superexchange Interaction and Weak Ferromagnetism. *Phys. Rev.* **120,** 91 (1960).
32. Mühlbauer, S. *et al.* Skyrmion Lattice in a Chiral Magnet. *Science* **323,** 915 (2009).
33. Münzer, W. *et al.* Skyrmion lattice in the doped semiconductor $\mathrm{Fe}_{1-x}\mathrm{Co}_x\mathrm{Si}$. *Phys. Rev. B* **81,** 041203 (2010).

34. Seki, S., Yu, X. Z., Ishiwata, S. & Tokura, Y. Observation of Skyrmions in a Multiferroic Material. *Science* **336,** 198 (2012).
35. Yu, X. Z. *et al.* Near room-temperature formation of a skyrmion crystal in thin-films of the helimagnet FeGe. *Nat. Mater.* **10,** 106 (2011).
36. Jiang, W. *et al.* Blowing magnetic skyrmion bubbles. *Science* **349,** 283 (2015).
37. Srivastava, A. K. *et al.* Observation of Robust Néel Skyrmions in Metallic PtMnGa. *Adv. Mater.* **32,** 1904327 (2020).
38. Hicken, T. J. *et al.* Magnetism and Néel skyrmion dynamics in $GaV_4S_{8-y}Se_y$. *Phys. Rev. Research* **2,** 032001 (2020).
39. Anderson, P. W. Antiferromagnetism. Theory of Superexchange Interaction. *Phys. Rev.* **79,** 350 (1950).
40. Heinze, S. *et al.* Spontaneous atomic-scale magnetic skyrmion lattice in two dimensions. *Nat. Phys.* **7,** 713 (2011).
41. Soumyanarayanan, A. *et al.* Tunable room-temperature magnetic skyrmions in Ir/Fe/Co/Pt multilayers. *Nat. Mater.* **16,** 898 (2017).
42. Jadaun, P., Register, L. F. & Banerjee, S. K. Spontaneous atomic-scale magnetic skyrmion lattice in two dimensions. *Npj Comput. Mater.* **6,** 788 (2020).
43. Duong, N. K. *et al.* Stabilizing zero-field skyrmions in Ir/Fe/Co/Pt thin film multilayers by magnetic history control. *Appl. Phys. Lett.* **114,** 072401 (2019).
44. He, M. *et al.* Realization of zero-field skyrmions with high-density via electromagnetic manipulation in Pt/Co/Ta multilayers. *Appl. Phys. Lett.* **111,** 202403 (2017).
45. He, M. *et al.* Evolution of topological skyrmions across the spin reorientation transition in Pt/Co/Ta multilayers. *Phys. Rev. B* **97,** 174419 (2018).
46. Nayak, A. K. *et al.* Magnetic antiskyrmions above room temperature in tetragonal Heusler materials. *Nature* **548,** 561 (2017).
47. Vir, P. *et al.* Tetragonal Superstructure of the Antiskyrmion Hosting Heusler Compound Mn1.4PtSn. *Chem. Mater.* **31,** 5876 (2019).
48. Ma, T. *et al.* Tunable Magnetic Antiskyrmion Size and Helical Period from Nanometers to Micrometers in a D2d Heusler Compound. *Adv. Mater.* **32,** 2002043 (2020).
49. Yasin, F. S. *et al.* Bloch Lines Constituting Antiskyrmions Captured via Differential Phase Contrast. *Adv. Mater.* **32,** 2004206 (2020).
50. Coey, J. M. D. *Magnetism and Magnetic Materials* (Cambridge University Press, 2010).
51. O'Handley, R. C. *Modern Magnetic Materials* (John Wiley & Sons Inc., 2000).
52. Nakamura, K., Tsunashima, S., Hasegawa, M. & Uchiyama, S. Perpendicular magnetic anisotropy of PdCo alloy in multilayered structure. *J. Magn. Magn. Mater.* **93,** 462 (1991).

53. Leamy, H. J. & Dirks, A. G. Microstructure and magnetism in amorphous rare-earth–transition-metal thin films. I. Microstructure. *J. Appl. Phys.* **49,** 3430 (1978).
54. Itoh, A., Uekusa, H., Tarusawa, Y., Inoue, F. & Kawanishi, K. Magnetostriction and internal stress in GdFe amorphous films with perpendicular anisotropy prepared by RF diode sputtering. *J. Magn. Magn. Mater.* **35,** 241 (1983).
55. Nakajima, N. *et al.* Perpendicular Magnetic Anisotropy Caused by Interfacial Hybridization via Enhanced Orbital Moment in Co/Pt Multilayers: Magnetic Circular X-Ray Dichroism Study. *Phys. Rev. Lett.* **81,** 5229 (1998).
56. Hashimoto, S., Ochiai, Y. & Aso, K. Perpendicular magnetic anisotropy and magnetostriction of sputtered Co/Pd and Co/Pt multilayered films. *J. Appl. Phys.* **66,** 4909 (1989).
57. Rhyne, J. & McGuire, T. Magnetism of rare-earth elements, alloys, and compounds. *IEEE Trans. Magn.* **8,** 105 (1972).
58. Stoner, E. C. Collective electron ferromagnetism. *Proc. R. Soc. Lond.,* 372 (1938).
59. Magnetisation studies in TbFe/Pt single and multilayers. *J. Magn. Magn. Mater.* **153,** 5 (1996).
60. Hansen, P., Clausen, C., Much, G., Rosenkranz, M. & Witter, K. Magnetic and magneto-optical properties of rare-earth transition-metal alloys containing Gd, Tb, Fe, Co. *J. Appl. Phys.* **66,** 756 (1989).
61. Coey, J. M. D. Amorphous magnetic order. *J. Appl. Phys.* **49,** 1646 (1978).
62. Lin, M.-S. *et al.* Effects of perpendicular interlayer coupling strength on canting angles of TbCo-sublattice magnetization. *Phys. Rev. B* **79** (2009).
63. Heiman, N. & Lee, K. Moessbauer effect measurement of the internal fields in amorphous rare earth-iron alloys. *Phys. Lett. A* **55,** 297 (1975).
64. Ruckert, T., Tappert, J., Brand, R. & Keune, W. Moessbauer-effect study of amorphous TbFe films. *J. Magn. Magn. Mater.* **165,** 411 (1997).
65. Urner-Wille, M. & Witter, K. Compensation point switching in homogeneous amorphous GdFe-films. *J. Magn. Magn. Mater.* **13,** 77 (1979).
66. Mimura, Y., Imamura, N. & Kobayashi, T. Magnetic properties and curie point writing in amorphous metallic films. *IEEE Transs. Magn.* **12,** 779 (1976).
67. Ueda, K., Mann, M., de Brouwer, P. W. P., Bono, D. & Beach, G. S. D. Temperature dependence of spin-orbit torques across the magnetic compensation point in a ferrimagnetic TbCo alloy film. *Phys. Rev. B* **96,** 064410 (2017).
68. Li, W. *et al.* Composition and temperature-dependent magnetization dynamics in ferrimagnetic TbFeCo. *Phys. Rev. B* **97,** 184432 (2018).
69. Hebler, B., Hassdenteufel, A., Reinhardt, P., Karl, H. & Albrecht, M. Ferrimagnetic Tb–Fe Alloy Thin Films: Composition and Thickness Dependence of Magnetic Properties and All-Optical Switching. *Front. Mater. Sci.* **3,** 8 (2016).

70. Bhatt, R. C., Ye, L.-X., Luo, Y.-C. & Wu, T.-h. Study of RExFe100-x ferrimagnets for SOT application. *J. Appl. Phys.* **125,** 113902 (2019).
71. Wang, K., Huang, Y., Xu, Z., Dong, S. & Chen, R. Effect of sputtering power on the magnetic properties of amorphous perpendicular TbFeCo films. *J. Magn. Magn. Mater.* **424,** 89 (2017).
72. Gambino, R. J., Chaudhari, P. & Cuomo, J. J. Amorphous Magnetic Materials. *AIP Conf. Proc.* **18,** 578 (1974).
73. Fernandez-Baca, J. A. & Ching, W.-Y. *The Magnetism of Amorphous Metals and Alloys* (World Scientific, 1995).
74. Tewes, M., Zweck, J. & Hoffmann, H. Short range order in amorphous FeTb. *J. Magn. Magn. Mater.* **95,** 43 (1991).
75. Tewes, M., Zweck, J. & Hoffmann, H. Derivation of partial pair distribution functions for amorphous FeTb from electron scattering data based on a new concept. *J. Condens. Matter Phys.* **6,** 835 (1994).
76. Manaila, R., Filoti, G., Florescu, V., Serbanescu, M. & Drinciu, C. Local magnetic interactions and short-range order in amorphous GdxFe1-x films. *J. Magn. Magn. Mater.* **86,** 280 (1990).
77. Mizoguchi, T. & Cargill III, G. S. Magnetic anisotropy from dipolar interactions in amorphous ferrimagnetic alloys. *J. Appl. Phys.* **50,** 3570 (1979).
78. Suzuki, Y., Takayama, S., Kirino, F. & Ohta, N. Single ion model for perpendicular magnetic anisotropy in RE-TM amorphous films. *IEEE Trans. Magn.* **23,** 2275 (1987).
79. Lindbaum, A. & Rotter, M. in *Handbook of Magnetic Materials* (Elsevier, 2002).
80. Heiman, N. & Kazama, N. Magnetization of amorphous RECu alloys (RE=Gd, Tb, Dy, Ho). *J. Appl. Phys.* **49,** 1686 (1978).
81. Stevens, K. W. H. Matrix Elements and Operator Equivalents Connected with the Magnetic Properties of Rare Earth Ions. *Proc. Phys. Soc. A* **65,** 209 (1952).
82. Meiklejohn, W. H. & Bean, C. P. New magnetic anisotropy. *Phys. Rev.* **102,** 1413 (1956).
83. Meiklejohn, W. H. & Bean, C. P. New Magnetic Anisotropy. *Phys. Rev.* **105,** 904 (1957).
84. O'Grady, K., Fernandez-Outon, L. & Vallejo-Fernandez, G. A new paradigm for exchange bias in polycrystalline thin films. *J. Magn. Magn. Mater.* **322,** 883 (2010).
85. Kneller, E. & Hawig, R. The exchange-spring magnet: a new material principle for permanent magnets. *IEEE Trans. Magn.* **27,** 3588 (1991).
86. Skomski, R. & Coey, J. M. D. Giant energy product in nanostructured two-phase magnets. *Phys. Rev. B* **48,** 15812 (1993).
87. Fullerton, E. E., Jiang, J. & Bader, S. Hard/soft magnetic heterostructures: model exchange-spring magnets. *J. Magn. Magn. Mater.* **200,** 392 (1999).

88. Canet, F., Mangin, S., Bellouard, C. & Piecuch, M. Positive exchange bias in ferromagnetic-ferrimagnetic bilayers: FeSn/FeGd. *Europhys. Lett.* **52,** 594 (2007).
89. Balymov, K., Vas'kovskiy, V., Svalov, A., Stepanova, E. & Kulesh, N. Magnetization Reversal of Tb-Co/Fe19Ni81 Films with a Unidirectional Anisotropy. *Phys. Met. Metallogr.* **110,** 526 (2010).
90. Lin, C.-C., Lai, C.-H., Jiang, R.-F. & Shieh, H.-P. D. High interfacial exchange energy in TbFeCo exchange-bias films. *J. Appl. Phys.* **93,** 6832 (2003).
91. Hebler, B., Reinhardt, P., Katona, G. L., Hellwig, O. & Albrecht, M. Double exchange bias in ferrimagnetic heterostructures. *Phys. Rev. B* **95,** 104410 (2017).
92. Yan, S.-s., Barnard, J. A., Xu, F.-t., Weston, J. L. & Zangari, G. Critical dimension of the transition from single switching to an exchange spring process in hard/soft exchange-coupled bilayers. *Phys. Rev. B* **64,** 184403 (2001).
93. Guo, G.-h., Zhang, G.-f. & Wang, X.-g. Crossover from reversible to irreversible magnetic exchange-spring processes in antiferromagnetically exchange-coupled soft/hard bilayer structures. *J. Appl. Phys.* **108,** 043919 (2010).
94. Hauet, T., Borchers, J. A., Mangin, P., Henry, Y. & Mangin, S. Training Effect in an Exchange Bias System: The Role of Interfacial Domain Walls. *Phys. Rev. Lett.* **96,** 067207 (2006).
95. Mangin, S., Hauet, T., Henry, Y., Montaigne, F. & Fullerton, E. E. Influence of lateral domains and interface domain walls on exchange-bias phenomena in GbFeTdFe bilayers. *Phys. Rev. B* **74,** 024414 (2006).
96. Mangin, S. *et al.* Influence of interface exchange coupling in perpendicular anisotropy [Pt/Co]50/TbFe bilayers. *Phys. Rev. B* **78,** 024424 (2008).
97. Schubert, C. *et al.* Interfacial exchange coupling in Fe-Tb/[Co/Pt] heterostructures. *Phys. Rev. B* **87,** 054415 (2013).
98. Guo, G.-h. *et al.* Irreversible magnetic exchange-spring processes in antiferromagnetic exchange-coupled bilayer systems. *Appl. Phys. Lett.* **93,** 102505 (2008).
99. Wang, X.-g., Guo, G.-h. & Zhang, G.-f. Transition from reversible to irreversible magnetic exchange-spring processes in antiferromagnetically exchange-coupled hard/soft/hard trilayer structures. *J. Magn. Magn. Mater.* **323,** 1722 (2011).
100. Heigl, M. *et al.* Microscopic Origin of Magnetization Reversal in Nanoscale Exchange-Coupled Ferri/Ferromagnetic Bilayers: Implications for High Energy Density Permanent Magnets and Spintronic Devices. *ACS Appl. Nano Mater.* **3,** 9218 (2020).
101. Hubert, A. & Schäfer, R. *Magnetic Domains - The Analysis of Magnetic Microstructures* (Springer Berlin Heidelberg, 1998).
102. Lilley, B. Energies and widths of domain boundaries in ferromagnetics. *London Edinburgh Philos. Mag. J. Sci.* **41,** 792 (1950).

103. Kittel, C. Theory of the Structure of Ferromagnetic Domains in Films and Small Particles. *Phys. Rev.* **70,** 965 (1946).
104. Kronmüller, H. *Micromagnetism and the microstructure of ferromagnetic solids* (Cambridge university press, 2003).
105. Middelhoek, S. Domain Walls in Thin Ni–Fe Films. *J. Appl. Phys.* **34,** 1054 (1963).
106. Málek, Z. & Kamberský, V. On the theory of the domain structure of thin films of magnetically uni-axial materials. *Czech. J. Phys.* **8,** 416 (1958).
107. Speckmann, M. *Mikromagnetische Strukturen und magnetischer Reorientierungsubergang in Co/Au(111)* (Ph.D. thesis, Julich, 1996).
108. Kaplan, B. & Gehring, G. A. The domain structure in ultrathin magnetic films. *J. Magn. Magn. Mater.* **128,** 111 (1993).
109. Hehn, M., Padovani, S., Ounadjela, K. & Bucher, J. P. Nanoscale magnetic domain structures in epitaxial cobalt films. *Phys. Rev. B* **54,** 3428 (1996).
110. Saito, N., Fujiwara, H. & Sugita, Y. A New Type of Magnetic Domain Structure in Negative Magnetostriction Ni-Fe Films. *J. Phys. Soc. Japan* **19,** 1116 (1964).
111. Hayashi, M. *et al.* Dependence of Current and Field Driven Depinning of Domain Walls on Their Structure and Chirality in Permalloy Nanowires. *Phys. Rev. Lett.* **97,** 207205 (2006).
112. Chen, G. & Schmid, A. K. Imaging and Tailoring the Chirality of Domain Walls in Magnetic Films. *Adv. Mater.* **27,** 5738 (2015).
113. Gentillon, A. *et al.* Robustness of the remanent magnetic domain pattern formation and associated stripe-bubble transitions in Co/Pt multilayers against field sequencing. *AIP Adv.* **11,** 015339 (2021).
114. Zhang, B. *et al.* Energy-Efficient Domain-Wall Motion Governed by the Interplay of Helicity-Dependent Optical Effect and Spin-Orbit Torque. *Phys. Rev. Appl.* **11,** 034001 (2019).
115. Benitez, M. J. *et al.* Magnetic microscopy and topological stability of homochiral Néel domain walls in a Pt/Co/AlOx trilayer. *Nat. Commun.* **6,** 8957 (2015).
116. Leonov, A. O. & Mostovoy, M. Multiply periodic states and isolated skyrmions in an anisotropic frustrated magnet. *Nat. Commun.* **6,** 8275 (2015).
117. NobelPrize.org. *The Nobel Prize in Physics 2016* `https://www.nobelprize.org/prizes/physics/2016/summary/` (2021).
118. Skyrme, T. A unified field theory of mesons and baryons. *Nucl. Phys.* **31,** 556 (1962).
119. Everschor-Sitte, K., Masell, J., Reeve, R. M. & Kläui, M. Perspective: Magnetic skyrmions-Overview of recent progress in an active research field. *J. Appl. Phys.* **124,** 240901 (2018).
120. Loudon, J. C. *et al.* Do Images of Biskyrmions Show Type-II Bubbles? *Adv. Mater.* **31,** 1806598 (2019).

121. Nagaosa, N. & Tokura, Y. Topological properties and dynamics of magnetic skyrmions. *Nat. Nano.* **8,** 899 (2013).

122. Tretiakov, O. A. & Tchernyshyov, O. Vortices in thin ferromagnetic films and the skyrmion number. *Phys. Rev. B* **75,** 012408 (2007).

123. Heinze, S. *et al.* Spontaneous atomic-scale magnetic skyrmion lattice in two dimensions. *Nat. Phys.* **7,** 1745 (2011).

124. Woo, S. *et al.* Observation of room-temperature magnetic skyrmions and their current-driven dynamics in ultrathin metallic ferromagnets. *Nat. Mater.* **15,** 501 (2016).

125. Jaiswal, S. *et al.* Investigation of the Dzyaloshinskii-Moriya interaction and room temperature skyrmions in W/CoFeB/MgO thin films and microwires. *Appl. Phys. Lett.* **111,** 022409 (2017).

126. Kläui, M. Freezing and melting skyrmions in 2D. *Nat. Nanotechnol.* **15,** 726 (2020).

127. Yu, X. Z. *et al.* Real-space observation of a two-dimensional skyrmion crystal. *Nature* **465,** 901 (2010).

128. Montoya, S. A. *et al.* Tailoring magnetic energies to form dipole skyrmions and skyrmion lattices. *Phys. Rev. B* **95,** 2024415 (2017).

129. Wang, X. S., Yuan, H. Y. & Wang, X. R. A theory on skyrmion size. *Commun. Phys.* **1,** 31 (2018).

130. Güngördü, U., Nepal, R., Tretiakov, O. A., Belashchenko, K. & Kovalev, A. A. Stability of skyrmion lattices and symmetries of quasi-two-dimensional chiral magnets. *Phys. Rev. B* **93,** 064428 (2016).

131. Kovalev, A. A. & Sandhoefner, S. Skyrmions and antiskyrmions in quasi-two-dimensional magnets. *Front. Phys.* **6,** 98 (2018).

132. Zhang, X. *et al.* Skyrmion dynamics in a frustrated ferromagnetic film and current-induced helicity locking-unlocking transition. *Nat. Commun.* **8,** 1717 (2017).

133. Koshibae, W. & Nagaosa, N. Theory of antiskyrmions in magnets. *Nat. Commun.* **7,** 10542 (2016).

134. Zhang, X. *et al.* Skyrmion dynamics in a frustrated ferromagnetic film and current-induced helicity locking-unlocking transition. *Nat. Commun.* **8,** 1717 (2017).

135. Hoffmann, M. *et al.* Antiskyrmions stabilized at interfaces by anisotropic Dzyaloshinskii-Moriya interactions. *Nat. Commun.* **8,** 308 (2017).

136. Camosi, L., Rougemaille, N., Fruchart, O., Vogel, J. & Rohart, S. Micromagnetics of antiskyrmions in ultrathin films. *Phys. Rev. B* **97,** 134404 (2018).

137. Hoffmann, M. *et al.* Thermodynamically stable "vortices" in magnetically ordered crystals. The mixed state of magnets. *Sov. Phys. JETP* **68,** 101 (1989).

138. Bogdanov, A. N., Rößler, U. K., Wolf, M. & Müller, K.-H. Magnetic structures and reorientation transitions in noncentrosymmetric uniaxial antiferromagnets. *Phys. Rev. B* **66,** 214410 (2002).

139. Karube, K. *et al.* Room-temperature antiskyrmions and sawtooth surface textures in a non-centrosymmetric magnet with S4 symmetry. *Nat. Mater.* **20,** 335 (2021).

140. Jena, J. *et al.* Elliptical Bloch skyrmion chiral twins in an antiskyrmion system. *Nat. Commun.* **11,** 1115 (2020).

141. Peng, L. *et al.* Controlled transformation of skyrmions and antiskyrmions in a non-centrosymmetric magnet. *Nat. Nanotechnol.* **15,** 1 (2020).

142. Zhang, S., Petford-Long, A. K. & Phatak, C. Creation of artificial skyrmions and antiskyrmions by anisotropy engineering. *Sci. Rep.* **6,** 31248 (2016).

143. Bobeck, A. H. & Scovil, H. E. D. Magnetic bubbles. *Sci. Am.* **224,** 78 (1971).

144. Lee, J. C. T. *et al.* Synthesizing skyrmion bound pairs in Fe-Gd thin films. *Appl. Phys. Lett.* **109,** 022402 (2016).

145. Finazzi, M. *et al.* Laser-Induced Magnetic Nanostructures with Tunable Topological Properties. *Phys. Rev. Lett.* **110,** 177205 (2013).

146. Yu, X. Z. *et al.* Thermally activated helicity reversals of skyrmions. *Phys. Rev. B* **93,** 134417 (2016).

147. Yu, X. *et al.* Magnetic stripes and skyrmions with helicity reversals. *Proc. Natl. Acad. Sci. U.S.A.* **109,** 8856 (2012).

148. Zhang, J. *et al.* Formation and magnetic-field stability of magnetic dipole skyrmions and bubbles in a ferrimagnet. *Appl. Phys. Lett.* **116,** 142404 (2020).

149. Montoya, S. A. *et al.* Resonant properties of dipole skyrmions in amorphous Fe / Gd multilayers. *Phys. Rev. B* **95,** 224405 (2017).

150. Desautels, R. D. *et al.* Realization of ordered magnetic skyrmions in thin films at ambient conditions. *Phys. Rev. Mater.* **3,** 104406 (2019).

151. Desplat, L., Kim, J.-V. & Stamps, R. L. Paths to annihilation of first- and second-order (anti)skyrmions via (anti)meron nucleation on the frustrated square lattice. *Phys. Rev. B* **99,** 174409 (2019).

152. Xia, J. *et al.* Current-driven skyrmionium in a frustrated magnetic system. *Appl. Phys. Lett.* **117,** 012403 (2020).

153. Kong, L. *et al.* The modes of skyrmionium motion induced by vacancy defects on a racetrack. *J. Magn. Magn. Mater.* **537,** 168173 (2021).

154. Zhang, X. *et al.* Control and manipulation of a magnetic skyrmionium in nanostructures. *Phys. Rev. B* **94,** 094420 (2016).

155. Kent, N. *et al.* Generation and stability of structurally imprinted target skyrmions in magnetic multilayers. *Appl. Phys. Lett.* **115,** 112404 (2019).
156. Kent, N. *et al.* Creation and observation of Hopfions in magnetic multilayer systems. *Nat. Commun.* **12,** 1562 (2021).
157. Okubo, T., Chung, S. & Kawamura, H. Multiple-q States and the Skyrmion Lattice of the Triangular-Lattice Heisenberg Antiferromagnet under Magnetic Fields. *Phys. Rev. Lett.* **108,** 017206 (2012).
158. Garlow, J. A. *et al.* Quantification of Mixed Bloch-Néel Topological Spin Textures Stabilized by the Dzyaloshinskii-Moriya Interaction in Co/Pd Multilayers. *Phys. Rev. Lett.* **122,** 237201 (2019).
159. Weißenhofer, M. & Nowak, U. Orientation-dependent current-induced motion of skyrmions with various topologies. *Phys. Rev. B* **99,** 224430 (2019).
160. Kharkov, Y. A., Sushkov, O. P. & Mostovoy, M. Bound States of Skyrmions and Merons near the Lifshitz Point. *Phys. Rev. Lett.* **119,** 207201 (2017).
161. Göbel, B., Mook, A., Henk, J., Mertig, I. & Tretiakov, O. A. Magnetic bimerons as skyrmion analogues in in-plane magnets. *Phys. Rev. B* **99,** 060407 (2019).
162. Kosevich, A., Ivanov, B. & Kovalev, A. Magnetic Solitons. *Phys. Rep.* **194,** 117 (1990).
163. Yu, X. Z. *et al.* Biskyrmion states and their current-driven motion in a layered manganite. *Nat. Commun.* **5,** 3198 (2014).
164. Zheng, F. *et al.* Experimental observation of chiral magnetic bobbers in B20-type FeGe. *Nat. Nano.* **13,** 451 (2018).
165. Mandru, A.-O. *et al.* Coexistence of distinct skyrmion phases observed in hybrid ferromagnetic/ferrimagnetic multilayers. *Nat. Commun.* **11,** 6365 (2020).
166. Nakatani, Y. & Hayashi, N. Three-dimension calculation of vertical Bloch line and Bloch point. *IEEE Trans. Magn.* **24,** 3039 (1988).
167. Göbel, B., Mertig, I. & Tretiakov, O. A. Beyond skyrmions: Review and perspectives of alternative magnetic quasiparticles. *Phys. Rep.* **895,** 1 (2021).
168. Jonietz, F. *et al.* Spin transfer torques in MnSi at ultralow current densities. *Science* **330,** 1648 (2010).
169. Zang, J., Mostovoy, M., Han, J. H. & Nagaosa, N. Dynamics of Skyrmion Crystals in Metallic Thin Films. *Phys. Rev. Lett.* **107,** 136804 (2011).
170. Jiang, W. *et al.* Direct observation of the skyrmion Hall effect. *Nat. Phys.* **13,** 162 (2017).
171. Jin, C. *et al.* Current-induced motion of twisted skyrmions. *Appl. Phys. Lett.* **114,** 192401 (2019).
172. Huang, S. *et al.* Stabilization and current-induced motion of antiskyrmion in the presence of anisotropic Dzyaloshinskii- Moriya interaction. *Phys. Rev. B* **96,** 144412 (2017).

173. Zhang, X. *et al.* Skyrmion-electronics: writing, deleting, reading and processing magnetic skyrmions toward spintronic applications. *J. Condens. Matter Phys.* **32,** 143001 (2020).
174. Woo, S. *et al.* Deterministic creation and deletion of a single magnetic skyrmion observed by direct time-resolved X-ray microscopy. *Nat. Electron.* **1,** 288 (2018).
175. Barker, J. & Tretiakov, O. A. Static and Dynamical Properties of Antiferromagnetic Skyrmions in the Presence of Applied Current and Temperature. *Phys. Rev. Lett.* **116,** 147203 (2016).
176. Göbel, B., Mook, A., Henk, J. & Mertig, I. Overcoming the speed limit in skyrmion racetrack devices by suppressing the skyrmion Hall effect. *Phys. Rev. B* **99,** 020405 (2019).
177. Zhang, X., Zhou, Y. & Ezawa, M. Magnetic bilayer-skyrmions without skyrmion Hall effect. *Nat. Commun.* **7,** 10293 (2016).
178. Depla, D., Mahieu, S. & Greene, J. *Handbook of Deposition Technologies for Films and Coatings* (William Andrew Publishing, 2010).
179. Kelly, P. & Arnell, R. Magnetron sputtering: a review of recent developments and applications. *Vacuum* **56,** 159 (2000).
180. Gudmundsson, J. T. Physics and technology of magnetron sputtering discharges. *Plasma Sources Sci. Technol.* **29,** 113001 (2020).
181. Hamerich, A., Wunderlich, R. & Müller, J. Modeling of deposition and resputtering rate profiles in planar face to face sputtering systems. *J. Vac. Sci. Technol.* **12,** 2873 (1994).
182. Andrievskii, R. A. Effect of irradiation on the properties of nanomaterials. *Phys. Met. Metallogr.* **110,** 229 (2010).
183. Eaton Corporation. *Model NV-3204 Specification and System Description* (1987).
184. DAVIES, J. *Ion Implantation and Beam Processing* (Academic Press, 1984).
185. Orloff, J., Swanson, L. W. & Utlaut, M. Fundamental limits to imaging resolution for focused ion beams. *J. Vac. Sci. Technol. B* **14,** 3759 (1996).
186. Orloff, J., Swanson, L. & Utlaut, M. *High Resolution Focused Ion Beams: FIB and its Applications: Fib and Its Applications : The Physics of Liquid Metal Ion Sources and Ion Optics and Their Application to Focused Ion Beam Technology* (Springer US, 2003).
187. Hobbs, C., McMillan, J. & Palmer, D. The effects of surface topography in nuclear microprobe Rutherford backscattering analysis. *Nucl. Instrum. Methods Phys. Res. B* **30,** 342 (1988).
188. Van de Graaff, R. J., Compton, K. T. & Van Atta, L. C. The Electrostatic Production of High Voltage for Nuclear Investigations. *Phys. Rev.* **43,** 149 (1933).
189. Mayer, M. *SIMNRA user's guide* (1997).
190. Friedrich, W., Knipping, P. & Laue, M. Interferenzerscheinungen bei Röntgenstrahlen. *Annalen der Physik* **346,** 971 (1913).

191. Bragg, W. H. & Bragg, W. L. The reflection of X-rays by crystals. *Proc. Math. Phys* **88,** 428 (1913).

192. Chateigner, D. Thin film analysis by X-ray scattering. *J. Appl. Crystallogr.* **39,** 925 (2006).

193. Kozawa, Y. & Sato, S. Numerical analysis of resolution enhancement in laser scanning microscopy using a radially polarized beam. *Opt. Express* **23,** 2076 (2015).

194. De Broglie, L. Recherches sur la théorie des Quanta. *Annales de Physique* **10,** 22 (1925).

195. McMullan, D. Scanning electron microscopy 1928–1965. *Scanning* **17,** 175 (1995).

196. Jones, J. E. & Chapman, S. On the determination of molecular fields. From the variation of the viscosity of a gas with temperature. *Proc. Math. Phys* **106,** 441 (1924).

197. Binnig, G., Quate, C. F. & Gerber, C. Atomic Force Microscope. *Phys. Rev. Lett.* **56,** 930 (1986).

198. Zhong, Q., Inniss, D., Kjoller, K. & Elings, V. Fractured polymer/silica fiber surface studied by tapping mode atomic force microscopy. *Surf. Sci. Lett.* **290,** L688 (1993).

199. Giessibl, F. J., Hembacher, S., Bielefeldt, H. & Mannhart, J. Subatomic Features on the Silicon (111)-(7x7) Surface Observed by Atomic Force Microscopy. *Science* **289,** 422 (2000).

200. Van der Pauw, L. J. *A method of measuring specfific resistivity and hall effects of discs of arbitrary shape* 174 (World Scientific, 1991).

201. Drude, P. Zur Elektronentheorie der Metalle. *Annalen der Physik* **306,** 566 (1900).

202. Takayama, S., Niihara, T., Kaneko, K., Sugita, Y. & Ojima, M. Magnetic and magneto-optical properties of Tb-Fe-Co amorphous films. *J. Appl. Phys.* **61,** 2610 (1987).

203. Wang, K., Dong, S., Huang, Y. & Qiu, Y. Magnetic and thermal properties of amorphous TbFeCo alloy films. *J. Magn. Magn. Mater.* **434,** 169 (2017).

204. Blagojevic, V. *et al.* Microstructure and functional properties of FeCuNbSiB amorphous alloy. *Mater. Chem. Phys.* **145,** 12 (2014).

205. Yüzüak, E., Yüzüak, G. & Hütten, A. The effect of heat treatment on the FeCo phase in Tb-Fe-Co thin films. *J. Alloys Compd.* **863,** 158088 (2020).

206. Heigl, M., Mangkornkarn, C., Ullrich, A., Krupinski, M. & Albrecht, M. Enhanced annealing stability of ferrimagnetic Tb/FeCo multilayers. *AIP Adv.* **11,** 085112 (2021).

207. Thompson, C. V. Solid-State Dewetting of Thin Films. *Annu. Rev. Mater. Res.* **42,** 399 (2012).

208. Abbe, E. Beiträge zur Theorie des Mikroskops und der mikroskopischen Wahrnehmung. *Archiv f. mikrosk. Anatomie* **9,** 413 (1873).

209. Haider, M. *et al.* Prerequisites for a Cc/Cs-corrected ultrahigh-resolution TEM. *Ultramicroscopy* **108,** 167 (2008).

210. Williams, D. B. & Carter, C. B. *Transmission Electron Microscopy: A Textbook for Materials Science* (Springer, 2009).

211. Muller, A. & Grazul, J. Optimizing the environment for sub-0.2 nm scanning transmission electron microscopy. *J. Electron Microsc. Tech.* **50,** 219 (2001).

212. Pennycook, S. & Jesson, D. High-resolution Z-contrast imaging of crystals. *Ultramicroscopy* **37,** 14 (1991).

213. M.A., H. M. XCIII. The high-frequency spectra of the elements. *London Edinburgh Philos. Mag. J. Sci.* **26,** 1024 (1913).

214. Fagaly, R. L. Superconducting quantum interference device instruments and applications. *Rev. Sci. Instrum.* **77,** 101101 (2006).

215. Quantum Design. *Magnetic Property Measurement System - MPMS 3 User's Manual* `https://www.mrl.ucsb.edu/sites/default/files/mrl_docs/instruments/%201500-100Rev.F1MPMS3UsersManual.pdf` (2021).

216. Stamenov, P. & Coey, J. M. D. Sample size, position, and structure effects on magnetization measurements using second-order gradiometer pickup coils. *Rev. Sci. Instrum.* **77,** 015106 (2006).

217. Josephson, B. Possible new effects in superconductive tunnelling. *Phys. Lett.* **1,** 251 (1962).

218. Cooper, L. N. Bound Electron Pairs in a Degenerate Fermi Gas. *Phys. Rev.* **104,** 1189 (1956).

219. Malozovsky, Y. & Fan, J. Magnetic flux quantization in superconductors and the Aharonov–Bohm effect. *Phys. Lett. A* **257,** 332 (1999).

220. Buchner, M., Höfler, K., Henne, B., Ney, V. & Ney, A. Tutorial: Basic principles, limits of detection, and pitfalls of highly sensitive SQUID magnetometry for nanomagnetism and spintronics. *J. Appl. Phys.* **124,** 161101 (2018).

221. Sawicki, M., Stefanowicz, W. & Ney, A. Sensitive SQUID magnetometry for studying nanomagnetism. *Semicond. Sci. Technol.* **26,** 064006 (2011).

222. Zieba, A. Image and sample geometry effects in SQUID magnetometers. *Rev. Sci. Instrum.* **64,** 3357 (1993).

223. Mandru, A.-O. *et al.* Pervasive artifacts revealed from magnetometry measurements of rare earth- transition metal thin films. *J. Vac. Sci. Tec.* **A 38,** 023409 (2020).

224. LL.D., J. K. On rotation of the plane of polarization by reflection from the pole of a magnet. *Lond. Edinb. Dubl. Phil. Mag. J. Sci.* **3,** 321 (1877).

225. Caldwell, D., Thorne, J. M. & Eyring, H. Magnetic Circular Dichroism. *Annu. Rev. Phys. Chem.* **22,** 259 (1971).

226. Tomlinson, S., Farley, A., Hoon, S. & Valera, M. Interactions between soft magnetic samples and MFM tips. *J. Magn. Magn. Mater.* **157,** 557 (1996).

227. Zhao, X. *et al.* Magnetic force microscopy with frequency-modulated capacitive tip–sample distance control. *New J.Phys.* **20,** 013018 (2018).

228. Zhao, X. *et al.* Magnetization Reversal of Strongly Exchange-Coupled Double Nanolayers for Spintronic Devices. *ACS Appl. Nano Mater.* **2,** 7478 (2019).

229. Chapman, J. N. The investigation of magnetic domain structures in thin foils by electron microscopy. *J. Phys. D Appl. Phys.* **17,** 623 (1984).

230. Ngo, D.-T. & Kuhn, L. T. In situ transmission electron microscopy for magnetic nanostructures. *Adv. Nat. Sci: Nanosci. Nanotechnol.* **7,** 045001 (2016).

231. Aharonov, Y. & Bohm, D. Significance of Electromagnetic Potentials in the Quantum Theory. *Phys. Rev.* **115,** 485 (1959).

232. Chapman, J. *et al.* Coherent magnetic imaging by TEM. *IEEE Trans. Magn.* **30,** 4479 (1994).

233. McVitie, S. & Cushley, M. Quantitative Fresnel Lorentz microscopy and the transport of intensity equation. *Ultramicroscopy* **106,** 423 (2006).

234. Tanase, M. & Petford-Long, A. K. In situ TEM observation of magnetic materials. *Microsc. Res. Tech.* **72,** 187 (2009).

235. Jiang, W. *et al.* Mobile Néel skyrmions at room temperature: status and future. *AIP Adv.* **6,** 055602 (2016).

236. Teague, M. R. Deterministic phase retrieval: a Green's function solution. *J. Opt. Soc. Am.* **73,** 1434 (1983).

237. Ishizuka, K. & Allman, B. E. Phase Measurement in Electron Microscopy Using the Transport of Intensity Equation. *Micros. Today* **13,** 22 (2005).

238. Chess, J. J. *et al.* Streamlined approach to mapping the magnetic induction of skyrmionic materials. *Ultramicroscopy* **177,** 78 (2017).

239. Podbrdský, J. High resolution in-focus Lorentz electron microscopy. *J. Microsc.* **101,** 231 (1974).

240. Chapman, J., Batson, P., Waddell, E. & Ferrier, R. The direct determination of magnetic domain wall profiles by differential phase contrast electron microscopy. *Ultramicroscopy* **3,** 203 (1978).

241. Müller, K. *et al.* Atomic electric fields revealed by a quantum mechanical approach to electron picodiffraction. *Nat. Commun.* **5,** 5653 (2014).

242. McVitie, S. *et al.* Aberration corrected Lorentz scanning transmission electron microscopy. *Ultramicroscopy* **152,** 57 (2015).

243. Hintermayr, J. *LTEM-contrast* version 1.0. 2020. `https://github.com/Julian-Hi/LTEM-contrast`.

244. Hall, E. H. On a New Action of the Magnet on Electric Currents. *Amer. J. Math.* **2,** 287 (1879).

245. Bakun, A. A., Zakharchenya, B. P., Rogachev, A. A., Tkachuk, M. N. & Fleĭsher, V. G. Observation of a surface photocurrent caused by optical orientation of electrons in a semiconductor. *J. Exp. Theor. Phys.* **40,** 1293 (1984).
246. Sinitsyn, N. A. Semiclassical theories of the anomalous Hall effect. *J. Condens. Matter. Phys.* **20,** 023201 (2007).
247. Bruno, P., Dugaev, V. & Taillefumier, M. Topological Hall effect and Berry phase in magnetic nanostructures. *Phys. Rev. Lett.* **93,** 096806 (2004).
248. Pike, C. R. First-order reversal-curve diagrams and reversible magnetization. *Phys. Rev. B* **68,** 104424 (2003).
249. Farle, M. Ferromagnetic resonance of ultrathin metallic layers. *Rep. Prog. Phys.* **61,** 755 (1998).
250. Cho, J. *et al.* Thickness dependence of the interfacial Dzyaloshinskii-Moriya interaction in inversion symmetry broken systems. *Nat. Commun.* **6,** 1 (2015).
251. Gurevich, A. & G.A., M. in *Magnetization Oscillations and Waves* (CRC Press, 1996).
252. Ummelen, F. C., Lichtenberg, T., Swagten, H. J. M. & Koopmans, B. Controlling skyrmion bubble confinement by dipolar interactions. *Appl. Phys. Lett.* **115,** 102402 (2019).
253. Schubert, C. *et al.* Interfacial exchange coupling in Fe-Tb/[Co/Pt] heterostructures. *Phys. Rev. B* **87,** 054415 (2013).
254. Neubauer, A. *et al.* Topological Hall effect in the A phase of MnSi. *Physs. Rev. Lett.* **102,** 186602 (2009).
255. Tomczak, P. & Puszkarski, H. Ferromagnetic resonance in thin films studied via cross-validation of numerical solutions of the Smit-Beljers equation: Application to (Ga,Mn)As. *Phys. Rev. B* **98,** 144415 (2018).
256. Demokritov, S., Hillebrands, B. & Slavin, A. Brillouin light scattering studies of confined spin waves: linear and nonlinear confinement. *Phys. Rep.* **348,** 441 (2001).
257. Heigl, M., Wendler, R., Haugg, S. D. & Albrecht, M. Magnetic properties of Co/Ni-based multilayers with Pd and Pt insertion layers. *J. Appl. Phys.* **127,** 233902 (2020).
258. Vogler, C. *et al.* Hysteresis-free magnetization reversal of exchange-coupled bilayers with finite magnetic anisotropy. *Phys. Rev. B* **102,** 014429 (2020).
259. Hadri, M. S. E., Hehn, M., Malinowski, G. & Mangin, S. Materials and devices for all-optical helicity-dependent switching. *J. Phys. D: Appl. Phys* **50,** 133002 (2017).
260. Stanciu, C. D. *et al.* All-Optical Magnetic Recording with Circularly Polarized Light. *Phys. Rev. Lett.* **99,** 047601 (2007).
261. Lambert, C.-H. *et al.* All-optical control of ferromagnetic thin films and nano- structures. *Science* **345,** 1337 (2014).

262. Hassdenteufel, A. *et al.* Thermally Assisted All-Optical Helicity Dependent Magnetic Switching in Amorphous Fe100–xTbx Alloy Films. *Adv. Mater.* **25,** 3122 (2013).

263. Ciuciulkaite, A. *et al.* Magnetic and all-optical switching properties of amorphous Tb_xCo_{100-x} alloys. *Phys. Rev. Mater.* **4,** 104418 (2020).

264. Alebrand, S. *et al.* Light-induced magnetization reversal of high-anisotropy TbCo alloy films. *Appl. Phys. Lett.* **101,** 162408 (2012).

265. Lu, X. *et al.* Roles of heating and helicity in ultrafast all-optical magnetization switching in TbFeCo. *Appl. Phys. Lett.* **113,** 032405 (2018).

266. Chang, T.-C., Chang, K.-C., Tsai, T.-M., Chu, T.-J. & Sze, S. M. Resistance random access memory. *Mater. Today* **19,** 254 (2016).

267. Ikegawa, S., Mancoff, F. B., Janesky, J. & Aggarwal, S. Magnetoresistive Random Access Memory: Present and Future. *IEEE Trans. Electron.* **67,** 1407 (2020).

268. Na, T., Kang, S. H. & Jung, S.-O. STT-MRAM Sensing: A Review. *IEEE Trans. Circuits Syst. II: Express Br.* **68,** 12 (2021).

269. Cubukcu, M. *et al.* Ultra-Fast Perpendicular Spin–Orbit Torque MRAM. *IEEE Trans. Magn.* **54,** 1 (2018).

270. Engel, B. *et al.* A 4-Mb toggle MRAM based on a novel bit and switching method. *IEEE Trans. Magn.* **41,** 132 (2005).

271. Bhatti, S. *et al.* Spintronics based random access memory: a review. *Mater. Today* **20,** 530 (2017).

272. Li, M., Lau, D., De Graef, M. & Sokalski, V. Lorentz TEM investigation of chiral spin textures and Néel Skyrmions in asymmetric $[\mathrm{Pt}/(\mathrm{Co}/\mathrm{Ni})_M/\mathrm{Ir}]_N$ multi-layer thin films. *Phys. Rev. Mater.* **3,** 064409 (2019).

273. Zhang, J. *et al.* Formation and magnetic-field stability of magnetic dipole skyrmions and bubbles in a ferrimagnet. *Appl. Phys. Lett.* **116,** 142404 (2020).

274. Brock, J. A., Montoya, S. A., Im, M.-Y. & Fullerton, E. E. Energy-efficient generation of skyrmion phases in Co/Ni/Pt-based multilayers using Joule heating. *Phys. Rev. Mater.* **4,** 104409 (2020).

275. Schneider, R. *et al.* Magnetic-Field-Dependent THz Emission of Spintronic TbFe/Pt Layers. *ACS Photonics* **5,** 3936 (2018).

276. Fix, M. *et al.* Thermomagnetic control of spintronic THz emission enabled by ferrimagnets. *Appl. Phys. Lett.* **116,** 012402 (2020).

277. Goda, K. & Kitsuregawa, M. The History of Storage Systems. *Proc. IEEE* **100,** 1433 (2012).

278. Iwasaki, S. & Nakamura, Y. The magnetic field distribution of a perpendicular recording head. *IEEE Trans. Magn.* **14,** 436 (1978).

279. Piramanayagam, S. N. Perpendicular recording media for hard disk drives. *J. Appl. Phys.* **102,** 011301 (2007).

280. Gibson, G. & Polte, M. Directions for Shingled-Write and Two-Dimensional Magnetic Recording System Architectures: Synergies with Solid-State Disks (2009).

281. Amer, A. *et al.* Data Management and Layout for Shingled Magnetic Recording. *IEEE Trans. Magn.* **47,** 3691 (2011).

282. Re, M. Tech Talk on HDD Areal Density. *Seagate - Tech Talk* (2018).

283. Wood, R. The feasibility of magnetic recording at 1 Terabit per square inch. *IEEE Trans. Magn.* **36,** 36 (2000).

284. Charap, S., Lu, P.-L. & He, Y. Thermal stability of recorded information at high densities. *IEEE Trans. Magn.* **33,** 978 (1997).

285. Mallinson, J. A new theory of recording media noise. *IEEE Trans. on Magn.* **27,** 3519 (1991).

286. Néel, L. Théorie du traînage magnétique des ferromagnétiques en grains fins avec application aux terres cuites. *Annales de géophysique* **5,** 99 (1949).

287. Dickson, D. *et al.* Determination of f0 for fine magnetic particles. *J. Magn. Magn. Mater.* **125,** 345 (1993).

288. Wang, F. *et al.* Excellent soft magnetic Fe-Co-B-based amorphous alloys with extremely high saturation magnetization above 1.85 T and low coercivity below 3 A/m. *J. Alloys Compd.* **711,** 132 (2017).

289. Takano, K. *et al.* Micromagnetic simulation of various pole-tip design perpendicular magnetic recording heads. *J. Appl. Phys.* **105,** 07B711 (2009).

290. Shiroishi, Y. *et al.* Future Options for HDD Storage. *IEEE Trans. Magn.* **45,** 3816 (2009).

291. Richter, H. *et al.* Recording on Bit-Patterned Media at Densities of 1 Tb/in^{2}and Beyond. *IEEE Trans. Magn.* **42,** 2255 (2006).

292. Grobis, M. K., Hellwig, O., Hauet, T., Dobisz, E. & Albrecht, T. R. High-Density Bit Patterned Media: Magnetic Design and Recording Performance. *IEEE Trans. Magn.* **47,** 6 (2011).

293. Wang, J.-P., Shen, W. & Bai, J. Exchange coupled composite media for perpendicular magnetic recording. *IEEE Trans. Magn.* **41,** 3181 (2005).

294. Victora, R. H. & Shen, X. Exchange Coupled Composite Media. *Proc. IEEE* **96,** 1799 (2008).

295. Suess, D., Lee, J., Fidler, J. & Schrefl, T. Exchange-coupled perpendicular media. *J. Magn. Magn. Mater.* **321,** 545 (2009).

296. Makarov, D. *et al.* Perpendicular FePt-based exchange-coupled composite media. *Appl. Phys. Lett.* **96,** 062501 (2010).

297. Zhu, J.-G., Zhu, X. & Tang, Y. Microwave Assisted Magnetic Recording. *IEEE Trans. Magn.* **44,** 125 (2008).

298. Fukuda, H. & Shiroishi, Y. Performance Limitation of Microwave Assisted Magnetic Recording Combined With Exchange Coupled Composite Media Explored by Genetic Algorithm. *IEEE Trans. Magn.* **49,** 3640 (2013).

299. Challener, W. A. *et al.* Heat-assisted magnetic recording by a near-field transducer with efficient optical energy transfer. *Nat. Photonics* **3,** 220 (2009).

300. Piramanayagam, S. N. & Chong, T. C. *Developments in data storage : materials perspective* (Hoboken, NJ : Wiley, 2012).

301. Evans, R. F. L., Chantrell, R. W., Nowak, U., Lyberatos, A. & Richter, H.-J. Thermally induced error: Density limit for magnetic data storage. *Appl. Phys. Lett.* **100,** 102402 (2012).

302. Richter, H. J., Lyberatos, A., Nowak, U., Evans, R. F. L. & Chantrell, R. W. The thermodynamic limits of magnetic recording. *J. Appl. Phys.* **111,** 033909 (2012).

303. Seagate. *Seagate's 2021 Virtual Analyst Event* 2021. `https://investors.seagate.com/events/event-details/2021/Seagates-2021-Virtual-Analyst-Event/default.aspx`.

304. WesternDigital. Hard Drive Roadmap. *5th Annual Virtual Wells Fargo TMT Summit Conference* (2021).

305. Granz, S. *et al.* Areal Density Comparison Between Conventional, Shingled, and Interlaced Heat-Assisted Magnetic Recording With Multiple Sensor Magnetic Recording. *IEEE Trans. Magn.* **55,** 1 (2019).

306. Weller, D. *et al.* A HAMR Media Technology Roadmap to an Areal Density of 4 $\mathrm{Tb/in^2}$. *IEEE Trans. Magn.* **50,** 1 (2014).

307. Vogler, C., Abert, C., Bruckner, F., Suess, D. & Praetorius, D. Areal density optimizations for heat-assisted magnetic recording of high-density media. *J. Appl. Phys.* **119,** 223903 (2016).

308. Ju, G. *et al. Heat Assisted Magnetic Recording – Next Generation Mass Storage Technology.* in *2018 IEEE Int. Magnetics Conference (INTERMAG)* (2018).

309. Dwivedi, N. *et al.* Graphene overcoats for ultra-high storage density magnetic media. *Nat. Commun.* **12,** 2854 (2021).

310. Suess, D. & Schrefl, T. Breaking the thermally induced write error in heat assisted recording by using low and high Tc materials. *Appl. Phys. Lett.* **102,** 162405 (2013).

311. Hernandez, S. *et al.* Geometrical Scaling Limits of Heat-Assisted Magnetic Recording. *IEEE Trans. Magn.* **57,** 1 (2021).

312. Wu, A. Q. *et al.* HAMR Areal Density Demonstration of 1+ Tbpsi on Spinstand. *IEEE Trans. Magn.* **49,** 779 (2013).

313. Ju, G. *et al.* High Density Heat-Assisted Magnetic Recording Media and Advanced Characterization—Progress and Challenges. *IEEE Trans. Magn.* **51,** 1 (2015).

314. Lisfi, A. *et al.* Static magnetism and thermal switching in randomly oriented L10 FePt thin films. *AIP Adv.* **8,** 056438 (2018).

315. Zhu, J.-G. & Yan, Y. Incoherent Magnetic Switching of L10 FePt Grains. *IEEE Trans. Magn.* **57,** 1 (2021).

316. Weller, D. *et al.* High K/sub u/ materials approach to 100 Gbits/in/sup 2/. *IEEE Trans. Magn.* **36,** 10 (2000).

317. Wang, K., Xu, Z. & Dong, S. A simple method for tuning perpendicular magnetic properties of ultra-thin TbFeCo films. *Mater. Lett.* **236,** 89 (2019).

318. Hovorka, O. *et al.* The Curie temperature distribution of FePt granular magnetic recording media. *Appl. Phys. Lett.* **101,** 052406 (2012).

319. Ren, Y. *et al.* Correlation Between Ultrafast Demagnetization Process and Gilbert Damping in Amorphous TbFeCo Films. *IEEE Trans. Magn.* **49,** 3159 (2013).

320. Chen, Z. *et al.* Spin waves and small intrinsic damping in an in-plane magnetized FePt film. *Appl. Phys. Lett.* **101,** 222402 (2012).

321. Natekar, N. A., Hsu, W.-H. & Victora, R. H. Calculated dependence of FePt damping on external field magnitude and direction. *AIP Adv.* **7,** 056004 (2017).

322. Girod, S. *et al.* Strong perpendicular magnetic anisotropy in Ni/Co(111) single crystal superlattices. *Appl. Phys. Lett.* **94,** 262504 (2009).

323. Gottwald, M. *et al.* Co/Ni(111) superlattices studied by microscopy, x-ray absorption, and ab initio calculations. *Phys. Rev. B* **86,** 014425 (2012).

324. Beaujour, J. M. *et al.* Ferromagnetic resonance study of sputtered Co|Ni multilayers. *Euro. Phys. J. B* **59,** 475 (2007).

325. Den Broeder, F. J. A., Hoving, W. & Bloemen, P. J. H. Magnetic anisotropy of multilayers. *J. Magn. Magn. Mater.* **93,** 562 (1991).

326. Daalderop, G. H. O., Kelly, P. J. & den Broeder, F. J. A. Prediction and Confirmation of Perpendicular Magnetic Anisotropy in Co/Ni Multilayers. *Phys. Rev. Lett.* **68,** 5 (1992).

327. Arora, M., Hübner, R., Suess, D., Heinrich, B. & Girt, E. Origin of perpendicular magnetic anisotropy in Co/Ni multilayers. *Phys. Rev. B* **96,** 024401 (2017).

328. Kirby, B. J. *et al.* Vertically graded anisotropy in Co/Pd multilayers. *Phys. Rev. B* **81,** 100405R (2010).

329. Etz C. and Zabloudil J. and Weinberger P. & Y., V. E. Magnetic properties of single atoms of Fe and Co on Ir(111) and Pt(111). *Phys. Rev. B* **77,** 184425 (2008).

330. Childress, J. R. & Fontana, R. E. Magnetic recording read head sensor technology. *Comptes Rendus Physique* **6,** 997 (2005).

331. Mao, S. *et al.* Commercial TMR heads for hard disk drives: characterization and extendibility at 300 gbit2. *IEEE Trans. Magn.* **42,** 97 (2006).

332. Hashimoto, S. & Ochiai, Y. Co/Pt and Co/Pd multilayers as magneto-optical recoding materials. *J. Magn. Magn. Mater.* **88,** 211 (1990).

333. Fullerton, E. E. *et al.* All-optical control of ferromagnetic thin films and nanostructures. *Science* **345,** 1337 (2014).

334. Zhang, P., Xie, K., Lin, W., Wu, D. & Sang, H. Anomalous Hall effect in Co/Ni multilayers with perpendicular magnetic anisotropy. *Appl. Phys. Lett.* **104,** 082404 (2014).

335. Katine, J. A. & Fullerton, E. E. Device implications of spin-transfer torques. *J. Magn. Magn. Mater.* **320,** 1217 (2008).

336. Meena, J. S., Sze, S. M., Chand, U. & Tseng, T. Y. Overview of emerging nonvolatile memory technologies. *Nanoscale Res. Lett.* **9,** 526 (2014).

337. L. You and R. C. Sousa and S. Bandiera and B. Rodmacq & Dieny, B. Co/Ni multilayers with perpendicular anisotropy for spintronic device applications. *Appl. Phys. Lett.* **100,** 172411 (2012).

338. Sankey, J. C. *et al.* Measurement of the spin-transfer-torque vector in magnetic tunnel junctions. *Nature Phys.* **4,** 67 (2008).

339. Yang, S. H., Ryu, K. S. & Parkin, S. Domain-wall velocities of up to 750 m s -1 driven by exchange-coupling torque in synthetic antiferromagnets. *Nature Nanotechn.* **10,** 221 (2015).

340. Le Gall, S. *et al.* Thermally activated domain wall motion in [Co/Ni](111) superlattices with perpendicular magnetic anisotropy. *Appl. Phys. Lett.* **106,** 062406 (2015).

341. Albrecht, T. *et al.* Bit Patterned Magnetic Recording: Theory, Media Fabrication, and Recording Performance. *IEEE Trans. Magn.* **51,** 0800342 (2015).

342. Albrecht, T. R. *et al.* Bit Patterned Media at 1 Tdot/in2 and Beyond. *IEEE Trans. Magn.* **49,** 773 (2013).

343. Albrecht, M. *et al.* Magnetic multilayers on nanospheres. *Nat. Mater.* **4,** 203 (2005).

344. Hellwig, O. *et al.* Coercivity tuning in Co/Pd multilayer based bit patterned media. *Appl. Phys. Lett.* **95,** 232505 (2009).

345. Bauer, U. *et al.* Magneto-ionic control of interfacial magnetism. *Nat. Mater.* **14,** 174 (2015).

346. Gilbert, D. A. *et al.* Realization of ground-state artificial skyrmion lattices at room temperature. *Nat. Commun.* **6,** 8462 (2015).

347. Moreau-Luchaire, C. *et al.* Additive interfacial chiral interaction in multilayers for stabilization of small individual skyrmions at room temperature. *Nat. Nano.* **11,** 444 (2016).

348. Varvaro, G. *et al.* Co/Pd-Based synthetic antiferromagnetic thin films on Au/resist underlayers: Towards biomedical applications. *Nanoscale* **11,** 21891 (2019).

349. Eichler-Volf, A. *et al.* Sensitivity of PS/CoPd Janus particles to an external magnetic field. *RSC Adv.* **11,** 17051 (2021).

350. Yara, A. *et al.* Control over self-assembled Janus clusters by the strength of magnetic field in H2O2. *Eur. Phys. J. E* **44,** 23 (2021).

351. Gimbert, F., Calmels, L. & Andrieu, S. Localized electron states and spin polarization in Co/Ni(111) overlayers. *Phys. Rev. B* **84,** 094432 (2011).

352. Andrieu, S. *et al.* Co/Ni multilayers for spintronics: High spin polarization and tunable magnetic anisotropy. *Phys. Rev. Mater.* **2,** 064410 (2018).

353. Song, H. S. *et al.* Observation of the intrinsic Gilbert damping constant in Co/Ni multilayers independent of the stack number with perpendicular anisotropy. *Appl. Phys. Lett.* **102,** 102401 (2013).

354. Chen, W., Beaujour, J. M. L., De Loubens, G., Kent, A. D. & Sun, J. Z. Spin-torque driven ferromagnetic resonance of CoNi synthetic layers in spin valves. *Appl. Phys. Lett.* **92,** 012507 (2008).

355. Ertl, L., Endl, G. & Hoffmann, H. Structure and magnetic properties of sputtered Tb/Co multilayers. *J. Magn. Magn. Mater.* **113,** 227 (1992).

356. Seki, T. *et al.* Magnetic anisotropy and damping for monolayer-controlled Co | Ni epitaxial multilayer. *J. Phys. Soc. Japan* **86,** 074710 (2017).

357. Johnson, M. T., Bloemen, P. J. H., den Broeder, F. J. A. & de Vries, J. J. Magnetic anisotropy in metallic multilayers. *Rep. Prog. Phys.* **59,** 1409 (1996).

358. Sander, D. The magnetic anisotropy and spin reorientation of nanostructures and nanoscale films. *J. Phys. Condens. Mater.* **16,** R603 (2004).

359. Sakamaki, M. *et al.* Perpendicular magnetic anisotropy in a Pt/Co/Pt ultrathin film arising from a lattice distortion induced by ion irradiation. *Phys. Rev. B* **86,** 024418 (2012).

360. Chang, C. R. Magnetostrictive surface anisotropy of epitaxial multilayers. *Phys. Rev. B* **48,** 15817 (1993).

361. G. H. O. Daalderop and P. J. Kelly & Schuurmans, M. F. H. First-principles calculation of the magnetic anisotropy energy of (Co),l(X) multilayers. *Phys. Rev. B* **42,** 7270 (1990).

362. Den Broeder, F., Janssen, E., Hoving, W. & Zeper, W. Perpendicular Magnetic Anisotropy and Coercivity of Co/Ni Multilayers. *IEEE Trans. Magn.* **28** (1992).

363. Bloemen, P. J. H., De Jonge, W. J. M. & Den Broeder, F. J. A. Magnetic anisotropies in Co/Ni(111) multilayers. *J. Appl. Phys.* **72,** 4840 (1992).

364. Carcia, P. F. Perpendicular magnetic anisotropy in Pd/Co and Pt/Co thin-film layered structures. *J. Appl. Phys.* **63,** 5066 (1988).

365. Knepper, J. W. & Yang, F. Y. Oscillatory interlayer coupling in Co Pt multilayers with perpendicular anisotropy. *Phys. Rev. B* **71,** 209 (2005).

366. Li, Z., Zhang, Z., Zhao, H., Ma, B. & Jin, Q. Y. High giant magnetoresistance and thermal annealing effects in perpendicular magnetic [Co/Ni]N-based spin valves. *J. Appl. Phys.* **106,** 013907 (2009).

367. Akbulut, S., Akbulut, A., Özdemir, M. & Yildiz, F. Effect of deposition technique of Ni on the perpendicular magnetic anisotropy in Co/Ni multilayers. *J. Magn. Magn. Mater.* **390,** 137 (2015).
368. Posth, O. *et al.* Influence of growth parameters on the perpendicular magnetic anisotropy of [Co/Ni] multilayers and its temperature dependence. *J. Appl. Phys.* **106,** 023919 (2009).
369. Liu, E. *et al.* Seed layer impact on structural and magnetic properties of [Co/Ni] multilayers with perpendicular magnetic anisotropy. *J. Appl. Phys.* **121** (2017).
370. Zhang, Y. B. & Woollam, J. a. Annealing Effects of Co/Ni Multilayers. *IEEE Trans. Magn.* **31,** 3262 (1995).
371. Kurt, H., Venkatesan, M. & Coey, J. M. Enhanced perpendicular magnetic anisotropy in Co/Ni multilayers with a thin seed layer. *J. Appl. Phys.* **108,** 073916 (2010).
372. Stanescu, D. *et al.* Tailoring magnetism in CoNi films with perpendicular anisotropy by ion irradiation. *J. Appl. Phys.* **103,** 07B529 (2008).
373. Schuppler, C. *et al.* Control of magnetic anisotropy and magnetic patterning of perpendicular Co/Pt multilayers by laser irradiation. *Appl. Phys. Lett.* **88,** 012506 (2006).
374. Ulbrich, T. C., Assmann, D. & Albrecht, M. Magnetic properties of Co/Pt multilayers on self-assembled particle arrays. *J. Appl. Phys* **104,** 084311 (2008).
375. Nakajima, N. *et al.* Perpendicular Magnetic Anisotropy Caused by Interfacial Hybridization via Enhanced Orbital Moment in Co/Pt Multilayers: Magnetic Circular X-Ray Dichroism Study. *Phys. Rev. Lett.* **81,** 5229 (1998).
376. Zeper, W. B., Greidanus, F. J. A. M., Carcia, P. F. & Fincher, C. R. Perpendicular magnetic anisotropy and magneto-optical Kerr effect of vapor-deposited Co/Pt layered structures. *J. Appl. Phys.* **65,** 4971 (1989).
377. Chen, X., Li, M., Yang, K., Jiang, S. & Han, G. Large enhancement of perpendicular magnetic anisotropy and high annealing stability by Pt insertion layer in (Co/Ni)-based multilayers. *AIP Adv.* **5,** 097121 (2015).
378. D. Weller, Y. Wu, J. Stohr and M. G. Samant and B. D. Hermsmeier & Chappert, C. Orbital magnetic moments of Co in multilayers with perpendicular magnetic anisotropy. *Phys. Rev. B* **49,** 888 (1994).
379. Chafai, K. *et al.* Magnetic studies in evaporated Ni/Pd multilayers. *J. Magn. Magn. Mater.* **323,** 596 (2011).
380. Benkirane, K. *et al.* Magnetic properties of Ni/Pt multilayers. *Mater. Sci. Eng. B* **116,** 25 (2005).
381. Chafai, K. *et al.* Magnetic studies in evaporated Ni/Pd multilayers. *J. Magn. Magn. Mater.* **323,** 596 (2011).
382. Asymmetric interfacial perpendicular magnetic anisotropy in Pt/Co/Pt trilayers. *IEEE Magn. Lett.* **2,** 3000504 (2011).

383. Tang, X. T., Wang, G. C. & Shima, M. Superparamagnetic behavior in ultrathin CoNi layers of electrodeposited CoNi/Cu multilayer nanowires. *J. Appl. Phys.* **99,** 15 (2006).

384. Macià, F. *et al.* Perpendicular magnetic anisotropy in ultrathin Co | Ni multilayer films studied with ferromagnetic resonance and magnetic x-ray microspectroscopy. *J. Magn. Magn. Mater.* **324,** 3629 (2012).

385. Al Risi, S., Bhatti, S., Al Subhi, A., Piramanayagam, S. N. & Sbiaa, R. Magnetic domain structure and magnetization reversal in (Co/Ni) and (Co/Pd) multilayers. *J. Magn. Magn. Mater.* **503,** 166579 (2020).

386. Wang, X. *et al.* Effect of the repeat number and Co layer thickness on the magnetization reversal process in [Pt/Co(x)]N multilayers. *J. Phys. D: Appl. Phys.* **53,** 215001 (2020).

387. F. J. A. den Broeder and H. W. van Kesteren and W. Hoving & Zeper, W. B. Co / Ni multilayers with perpendicular magnetic anisotropy : Kerr effect and thermomagnetic writing. *Appl. Phys. Lett.* **61,** 1468 (1992).

388. Carcia, P., Zeper, W., van Kesteren, H., Jacobs, B. & Spruit, J. Materials' Challenges for Metal Multilayers As a Magneto-Optical Recording Medium. *J. Magn. Soc. Japan* **15,** 151 (1991).

389. Hansen, M., Anderko, K. & Salzberg, H. W. *Constitution of Binary Alloys* (New York, McGraw-Hill, 1958).

390. Robinson, C., Samant, M. & Marinero. EXAFS study of the atomic structure of amorphous Tb20Fe80. *Appl. Phys. A* **49,** 619 (1989).

391. Tewes, M., Zweck, J. & Hoffmann, H. Short range order in amorphous FeTb. *J. Magn. Magn. Mater.* **95,** 43 (1991).

392. Harris, V. G., Aylesworth, K. D., Das, B. N., Elam, W. T. & Koon, N. C. Structural origins of magnetic anisotropy in sputtered amorphous Tb-Fe films. *Phys. Rev. Lett.* **69,** 1939 (1992).

393. Yoshino, S., Takagi, H., Tsunashima, S., Masuda, M. & Uchiyama, S. Perpendicular Magnetic Anisotropy of TbCo Films. *Jpn. J. Appl. Phys.* **23,** 188 (1984).

394. Ota, S. *et al.* Strain-induced modulation of temperature characteristics in ferrimagnetic Tb–Fe films. *Sci. Rep.* **11,** 6237 (2021).

395. Krupinski, M., Hintermayr, J., Sobieszczyk, P. & Albrecht, M. Control of magnetic properties in ferrimagnetic GdFe and TbFe thin films by He^+ and Ne^+ irradiation. *Phys. Rev. Mater.* **5,** 024405 (2021).

396. Cheng, S.-C. N. & Kryder, M. H. Separation of perpendicular anisotropy components in dc-magnetron sputtered TbFe amorphous films. *J. Appl. Phys.* **69,** 7202 (1991).

397. Sato, N. Magnetic properties of amorphous Tb-Fe thin films with an artificially layered structure. *J. Appl. Phys.* **59,** 2514 (1986).

398. Kneller, E. F. & Hawig, R. The exchange-spring magnet: a new material principle for permanent magnets. *IEEE Trans. Magn.* **27,** 3588 (1991).

399. Ungureanu, M. *et al.* Using a zero-magnetization ferromagnet as the pinning layer in exchange-bias systems. *Phys. Rev. B* **82,** 174421 (2010).

400. S. Romer and M. A. Marioni and K. Thorwarth and N. R. Joshi and C. E. Corticelli and H. J. Hug and S. Oezer and M. Parlinska- Wojtan & Rohrmann, H. Temperature dependence of large exchange- bias in TbFe-Co/Pt. *Appl. Phys. Lett.* **101,** 222404 (2017).

401. Hauet, T., Montaigne, F., Hehn, M., Henry, Y. & Mangin, S. Magnetoresistance in an amorphous exchange-coupled bilayer. *Phys. Rev. B* **79,** 224435 (2009).

402. Watson, S. M., Hauet, T., Borchers, J. A., Mangin, S. & Fullerton, E. E. Interfacial magnetic domain wall formation in perpendicular-anisotropy, exchange-spring films. *Appl. Phys. Lett.* **92,** 202507 (2008).

403. Mangin, S. *et al.* Influence of interface exchange coupling in perpendicular anisotropy [Pt/Co] 50/TbFe bilayers. *Phys. Rev. B* **78,** 024424 (2008).

404. Zhao, X. *et al.* Magnetization Reversal of Strongly Exchange-Coupled Double Nanolayers for Spintronic Devices. *ACS Appl. Nano Mater.* **2,** 7478 (2019).

405. Dieny, B. *et al.* Giant magnetoresistive in soft ferromagnetic multilayers. *Phys. Rev. B* **43,** 1297 (1991).

406. Radu, F., Abrudan, R., Radu, I., Schmitz, D. & Zabel, H. Perpendicular exchange bias in ferrimagnetic spin valves. *Nat. Commun.* **3,** 715 (2012).

407. Redon, O. & Freitas, P. P. Mechanism of exchange anisotropy and thermal stability of spin valves biased with ultrathin TbCo layers. *J. Appl. Phys.* **83,** 2851 (1998).

408. Lai, C.-H., Wu, Z.-H., Lin, C.-C. & Huang, P. H. Thermally assisted-writing giant magnetoresistance with perpendicular magnetization. *J. Appl. Phys.* **97,** 10C511 (2005).

409. Liao, J., He, H., Zhang, Z., Ma, B. & Jin, Q. Y. Enhanced difference in switching fields for perpendicular magnetic spin valves with a composite [Co/Ni]N/TbCo reference layer. *J. Appl. Phys.* **109,** 023907 (2011).

410. Lin, M.-S. *et al.* Perpendicular giant magnetoresistance composed of [Co/Pt] multilayer and CoFe/TbCo. *J. Appl. Phys.* **99,** 08T106 (2006).

411. Moodera, J. S., Kinder, L. R., Wong, T. M. & Meservey, R. Large magnetoresistance at room temperature in ferromagnetic thin film tunnel junctions. *Phys. Rev. Lett.* **74,** 3273 (1995).

412. Hassdenteufel, A. *et al.* Low-remanence criterion for helicity-dependent all-optical magnetic switching in ferrimagnets. *Phys. Rev. B* **91,** 104431 (2015).

413. Liu, T.-M. *et al.* Nanoscale Confinement of All-Optical Magnetic Switching in TbFeCo - Competition with Nanoscale Heterogeneity. *Nano Lett.* **15,** 6862 (2015).

414. Huisman, T. J. *et al.* Spin-photo-currents generated by femtosecond laser pulses in a ferrimagnetic GdFeCo/Pt bilayer. *Appl. Phys. Lett.* **110,** 072402 (2017).

415. Schneider, R. *et al.* Spintronic GdFe/Pt THz emitters. *Appl. Phys. Lett.* **115,** 152401 (2019).

416. Fix, M., Schneider, R., Michaelis de Vasconcellos, S., Bratschitsch, R. & Albrecht, M. Spin valves as magnetically switchable spintronic THz emitters. *Appl. Phys. Lett.* **117,** 132407 (2020).

417. Richomme, F., Teillet, J., Fnidiki, A., Auric, P. & Houdy, P. Experimental study of the structural and magnetic properties of Fe/Tb multilayers. *Phys. Rev. B* **54,** 416 (1996).

418. Yamauchi, K., Habu, K. & Sato, N. Magnetic structure of Tb-Fe films with an artificially layered structure. *J. Appl. Phys.* **64,** 5748 (1988).

419. Cherifi, K., Donovan, P., Dufour, C., Mangin, P. & Marchal, G. Microstructural Observations of Rare-Earth/Iron Multilayers. *Phys. Status Solidi A* **122,** 311 (1990).

420. Nawate, M., Doi, K. & Honda, S. Structure and perpendicular anisotropy in Gd/Fe multilayers sputter-deposited with substrate bias. *J. Magn. Magn. Mater.* **126,** 279 (1993).

421. Tappert, J. *et al.* The magnetic texture of Tb/Fe multilayers. *J. Magn. Magn. Mater.* **157,** 317 (1996).

422. Honda, S., Nawate, M. & Sakamoto, I. Magnetic structure and perpendicular magnetic anisotropy of rare-earth (Nd,Pr,Gd)/Fe multilayers. *J. Appl. Phys.* **79,** 365 (1996).

423. Richomme, F. *et al.* Study of Tb/Fe multilayers by temperature-dependent CEMS. *Hyperfine Interact.* **92,** 1243 (1994).

424. Avilés-Félix, L. *et al.* Single-shot all-optical switching of magnetization in Tb/Co multilayer-based electrodes. *Sci. Rep.* **10,** 5211 (2020).

425. Avilés-Félix, L. *et al.* All-optical spin switching probability in [Tb/Co] multilayers. *Sci. Rep.* **11,** 6576 (2021).

426. Heigl, M. *et al.* Dipolar-stabilized first and second-order antiskyrmions in ferrimagnetic multilayers. *Nat. Commun.* **12,** 2611 (2021).

427. Ranchal, R., Lopez, E., Prieto, J. & Aroca, C. Enhancement of the crystallization of TbFe thin films upon the formation of Tb phase. *Acta Mater.* **59,** 2865 (2011).

428. Ranchal, R., Prieto, J. L., Sánchez, P. & Aroca, C. Influence of the substrate stiffness on the crystallization process of sputtered TbFe2 thin films. *J. Appl. Phys.* **107,** 113918 (2010).

429. Ye, L.-X., Bhatt, R. C., Lee, C.-M., Chang, S.-M. & Wu, T.-h. The effects of annealing temperature and heating rate on Ta/TbFeCo bilayers. *AIP Adv.* **9,** 125316 (2019).

430. Bhatt, R. C., Ye, L.-X. & Wu, T.-h. MgO-TbFeCo interface enhancement of TbFeCo-based perpendicular magnetic tunnel junctions. *J. Magne. Magn. Mater.* **498,** 166159 (2020).

431. Yin, S. Q., Li, X. Q., Xu, X. G., Miao, J. & Jiang, Y. Effect of Ta Underlayer on Perpendicular Anisotropy of TbFeCo Films. *IEEE Trans. Magn.* **47,** 3129 (2011).

432. Cheng, W., Miao, X., Yan, J. & Lin, G. The influence of underlayers on the magnetic properties of TbFeCo films for hybrid recording. *Eighth Int. Symp. on Optical Storage and 2008 Int. Workshop on Information Data Storage* **7125,** 183 (2009).

433. Shin, S.-C. Dependence of microstructure and magneto-optical properties on deposition angle in evaporated TbFe and TbFeCo films. *J. Appl. Phys.* **61,** 3340 (1987).

434. Frąckowiak, Ł. *et al.* Magnetic properties of Co-Tb alloy films and Tb/Co multilayers as a function of concentration and thickness. *J. Magn. Magn. Mater.* **544,** 168682 (2022).

435. Ishibashi, M. *et al.* Ferrimagnetic compensation and its thickness dependence in TbFeCo alloy thin films. *Appl. Phys. Lett.* **120,** 022405 (2022).

436. Hebler, B. *et al.* Influence of the Fe-Co ratio on the exchange coupling in TbFeCo/[Co/Pt] heterostructures. *Phys. Rev. B* **93,** 184423 (2016).

437. Victora, R. H. & Falicov, L. M. Calculated magnetization of iron-cobalt disordered alloys. *Phys. Rev. B* **30,** 259 (1984).

438. Merchant, A. & Kryder, M. Investigation of coercive squareness in TbFeCo films. *IEEE Trans. Magn.* **27,** 3690 (1991).

439. Gimenez, C., Urban, A. & Vitton, J. A study of the stability of Co-rich TbFeCo thin films. *IEEE Trans. Magn.* **24,** 1738 (1988).

440. Dirks, A., Biesterbos, J. & Buschow, K. Magnetic compensation temperatures of amorphous rare earth-cobalt alloys. *Physica B+C* **86,** 761 (1977).

441. Fujiwara, Y. *et al.* Structural anisotropy of Tb/Fe multilayers. *J. Appl. Phys.* **79,** 6270 (1996).

442. Kim, W.-S., Andrä, W. & Kleemann, W. Influence of interfaces on the perpendicular magnetic anisotropy in Tb/Fe multilayers. *Phys. Rev. B* **58,** 6346 (1998).

443. Mangin, S., Montaigne, F. & Schuhl, A. Interface domain wall and exchange bias phenomena in ferrimagnetic/ferrimagnetic bilayers. *Phys. Rev. B* **68,** 140404 (2003).

444. Pommier, J. *et al.* Magnetic and magneto-optical properties of Tb/Fe multilayers. *J. Magn. Magn. Mater.* **136,** 251 (1994).

445. Grundy, P., Lacey, E. & Wright, C. Microstructural and magnetic properties of amorphous TbFe films. *J. Magn. Magn. Mater.* **54,** 227 (1986).

446. Schwertmann, U. & Cornell, R. M. *The Iron Oxides* 9 (John Wiley & Sons, Ltd, 2003).

447. Schwertmann, U. & Cornell, R. M., 111 (John Wiley & Sons, Ltd, 2003).

448. Umadevi, K. *et al.* Effect of Wheel Speed on the Structure, Microstructure, Magnetic, and Electrical Properties of Tb-Fe-Co Ribbons. *J. Supercond. Nov. Magn.* **29** (2016).

449. Fischbacher, J. *et al.* On the limits of coercivity in permanent magnets. *Appl. Phys. Lett.* **111,** 072404 (2017).

450. Zeng, H. X. *et al.* Clarifying the effects of La and Ce in the grain boundary diffusion sources on sintered NdFeB magnets. *Mater. Res. Express* **6,** 106105 (2019).

451. Kim, T.-H. *et al.* Microstructure and coercivity of grain boundary diffusion processed Dy-free and Dy-containing NdFeB sintered magnets. *Acta Mater.* **172,** 139 (2019).

452. Hauet, T., Mangin, S., Montaigne, F., Borchers, J. A. & Henry, Y. Tuning exchange-bias properties by thermal effects in a hard/soft bilayer. *Appl. Phys. Lett.* **91,** 022505 (2007).

453. Patra, M., Thakur, M., Majumdar, S. & Giri, S. The exchange bias effect in phase separated Nd1-xSr xCoO3 at the spontaneous ferromagnetic/ferrimagnetic interface. *J. Phys. Condens. Matter.* **21,** 236004 (2009).

454. Tokunaga, T., Taguchi, M., Fukami, T., Nakaki, Y. & Tsutsumi, K. Study of interface wall energy in exchange-coupled double-layer film. *J. Appl. Phys.* **67,** 4417 (1990).

455. Mangin, S., Montaigne, F. & Schuhl, A. Interface domain wall and exchange bias phenomena in ferrimagnetic/ferrimagnetic bilayers. *Phys. Rev. B* **68,** 140404(R) (2003).

456. Influence of lateral domains and interface domain walls on exchange-bias phenomena in GbFe TdFe bilayers. *Phys. Rev. B* **74,** 024414 (2006).

457. Lin, C.-C., Lai, C.-H., Jiang, R.-F. & Shieh, H.-P. D. High interfacial exchange energy in TbFeCo exchange-bias films. *J. Appl. Phys.* **93,** 6832 (2003).

458. Canet, F., Mangin, S., Bellouard, C. & Piecuch, M. Positive exchange bias in ferromagnetic-ferrimagnetic bilayers: FeSn/FeGd. *Europhys. Lett.* **52,** 594 (2000).

459. Romer, S. *et al.* Temperature dependence of large exchange-bias in TbFe-Co/Pt. *Appl. Phys. Lett.* **101,** 222404 (2012).

460. Hebler, B., Reinhardt, P., Katona, G. L., Hellwig, O. & Albrecht, M. Double exchange bias in ferrimagnetic heterostructures. *Phys. Rev. B* **95,** 104410 (2017).

461. Vaskovskiy, V. O., Svalov, A. V., Balymov, K. G. & Kulesh, N. A. Effect of annealing on the magnetic anisotropy and hysteretic properties of film structures containing Tb-Co amorphous layers. *Phys. Met. Metallogr.* **113,** 862 (2012).

462. Bai, Y. *et al.* Multi-interface spin exchange regulated biased magnetoelectric coupling in Cluster-assembled multiferroic heterostructural fims. *Acta Mater.* **155,** 166 (2018).

463. Hug, H. J. *et al.* A low temperature ultrahigh vaccum scanning force microscope. *Rev. Sci. Instruments* **70,** 3625 (1999).

464. Radu, F. & Zabel, H. in *Magnetic Heterostructures: Advances and Perspectives in Spinstructures and Spintransport* 97 (Springer Berlin Heidelberg, 2008).

465. Graves, C. *et al.* Nanoscale spin reversal by non-local angular momentum transfer following ultrafast laser excitation in ferrimagnetic GdFeCo. *Nat. Mater.* **12,** 293 (2013).

466. Suess, D. *et al.* Exchange spring media for perpendicular recording. *Appl. Phys. Lett.* **87,** 012504 (2005).

467. Kang, W., Huang, Y., Zhang, X., Zhou, Y. & Zhao, W. Skyrmion-Electronics: An Overview and Outlook. *Proc. IEEE* **104,** 2040 (2016).

468. Marrows, C. H. & Zeissler, K. Perspective on skyrmion spintronics. *Appl. Phys. Lett.* **119,** 250502 (2021).

469. Finocchio, G., Büttner, F., Tomasello, R., Carpentieri, M. & Kläui, M. Magnetic skyrmions: from fundamental to applications. *J. Phys. D: Appl. Phys* **49,** 423001 (2016).

470. Parkin, S. S. P., Hayashi, M. & Thomas, L. Magnetic Domain-Wall Racetrack Memory. *Science* **320,** 190 (2008).

471. Bogart, L. K., Atkinson, D., O'Shea, K., McGrouther, D. & McVitie, S. Dependence of domain wall pinning potential landscapes on domain wall chirality and pinning site geometry in planar nanowires. *Phys. Rev. B* **79,** 054414 (2009).

472. Ryu, K.-S., Thomas, L., Yang, S.-H. & Parkin, S. Chiral spin torque at magnetic domain walls. *Nat. Nanotech.* **8,** 527 (2013).

473. Emori, S., Bauer, U., Ahn, S.-M., Martinez, E. & Beach, G. S. D. Current-driven dynamics of chiral ferromagnetic domain walls. *Nat. Mater.* **12,** 611 (2013).

474. Parkin, S. & Yang, S.-H. Memory on the racetrack. *Nat. Nanotech.* **10,** 195 (2015).

475. Fert, A., Cros, V. & Sampaio, J. Skyrmions on the track. *Nat. Nanotechnol.* **8,** 152 (2013).

476. Tomasello, R. *et al.* A strategy for the design of skyrmion racetrack memories. *Sci. Rep.* **4,** 6784 (2014).

477. Juge, R. *et al.* Current-Driven Skyrmion Dynamics and Drive-Dependent Skyrmion Hall Effect in an Ultrathin Film. *Phys. Rev. Appl.* **12,** 044007 (2019).

478. Heigl, M. *Entdeckung: neuartige magnetische Wirbel für die Datenspeicherung* `https://www.uni-augsburg.de/de/campusleben/neuigkeiten/2021/05/11/4326/` (2021).

479. Yu, X. Z. *et al.* Real-space observation of a two-dimensional skyrmion crystal. *Nature* **465,** 901 (2010).

480. Ganguly, A. *et al.* Competition between Chiral Energy and Chiral Damping in the Asymmetric Expansion of Magnetic Bubbles. *ACS Appl. Electron. Mater.* **3,** 4734 (2021).

481. Yu, X. Z. *et al.* Near room-temperature formation of a skyrmion crystal in thin-films of the helimagnet FeGe. *Nat. Mater.* **10,** 106 (2011).

482. Romming, N. *et al.* Writing and Deleting Single Magnetic Skyrmions. *Science* **341,** 636 (2013).

483. Li, W. *et al.* Voltage-controlled skyrmion deletion device based on magnetic defects. *J. Phys. D: Appl. Phys.* **54,** 445001 (2021).

484. Yang, S. *et al.* Electrical Generation and Deletion of Magnetic Skyrmion-Bubbles via Vertical Current Injection. *Adv. Mater.* **33,** 2104406 (2021).

485. Srivastava, T. *et al.* Large-Voltage Tuning of Dzyaloshinskii–Moriya Interactions: A Route toward Dynamic Control of Skyrmion Chirality. *Nano Lett.* **18,** 4871 (2018).

486. Shen, X. *et al.* Breaking the topological protection of target skyrmions by the excitation of spin wave modes under microwave magnetic field. *J. Magn. Magn. Mater.* **541,** 168521 (2022).

487. Yokouchi, T. *et al.* Creation of magnetic skyrmions by surface acoustic waves. *Nat. Nanotechnol.* **15,** 361 (2020).

488. Ge, H. *et al.* Observation of Acoustic Skyrmions. *Phys. Rev. Lett.* **127,** 144502 (2021).

489. Ezawa, M. Giant Skyrmions Stabilized by Dipole-Dipole Interactions in Thin Ferromagnetic Films. *Phys. Rev. Lett.* **105,** 197202 (2010).

490. Hamamoto, K., Ezawa, M. & Nagaosa, N. Purely electrical detection of a skyrmion in constricted geometry. *Appl. Phys. Lett.* **108,** 112401 (2016).

491. Kasai, S., Sugimoto, S., Nakatani, Y., Ishikawa, R. & Takahashi, Y. K. Voltage-controlled magnetic skyrmions in magnetic tunnel junctions. *Appl. Phys. Express* **12,** 083001 (2019).

492. Chen, H., Bouckaert, W. & Majetich, S. A. Tunnel magnetoresistance detection of skyrmions. *J. Magn. Magn. Mater.* **541,** 168552 (2022).

493. Tolley, R., Montoya, S. A. & Fullerton, E. E. Room-temperature observation and current control of skyrmions in Pt/Co/Os/Pt thin films. *Phys. Rev. Materials* **2,** 044404 (2018).

494. Caretta, L. *et al.* Fast current-driven domain walls and small skyrmions in a compensated ferrimagnet. *Nat. Nanotech.* **13,** 1154 (2018).

495. Suess, D. *et al.* Spin Torque Efficiency and Analytic Error Rate Estimates of Skyrmion Racetrack Memory. *Sci. Rep.* **9,** 4827 (2019).

496. Hoffmann, M. *et al.* Antiskyrmions stabilized at interfaces by anisotropic Dzyaloshinskii-Moriya interactions. *Nat. Commun.* **8,** 308 (2017).

497. Müller, J. Magnetic skyrmions on a two-lane racetrack. *New J. Phys.* **19,** 025002 (2017).

498. Suess, D., Vogler, C., Bruckner, F., Heistracher, P. & Abert, C. A repulsive skyrmion chain as a guiding track for a racetrack memory. *AIP Adv.* **8,** 115301 (2018).

499. Hopfield, J. J. Neural networks and physical systems with emergent collective computational abilities. *Proc. Natl. Acad. Sci. USA* **79,** 2554 (1982).

500. Shin, D. & Yoo, H.-J. The Heterogeneous Deep Neural Network Processor With a Non-von Neumann Architecture. *Proc. IEEE* **108,** 1245 (2020).

501. Li, S. *et al.* Magnetic skyrmion-based artificial neuron device. *Nanotechnology* **28,** 31LT01 (2017).

502. Huang, Y., Kang, W., Zhang, X., Zhou, Y. & Zhao, W. Magnetic skyrmion-based synaptic devices. *Nanotechnology* **28,** 08LT02 (2017).

503. Yu, Z. *et al.* Voltage-controlled skyrmion-based nanodevices for neuromorphic computing using a synthetic antiferromagnet. *Nanoscale Adv.* **2,** 1309 (2020).

504. Song, K. M. *et al.* Skyrmion-based artificial synapses for neuromorphic computing. *Nat. Electron.* **3,** 148 (2020).

505. Grollier, J. *et al.* Neuromorphic spintronics. *Nat. Electron.* **3,** 360 (2020).

506. Chen, C. *et al.* Surface acoustic wave controlled skyrmion-based synapse devices. *Nanotechnology* **33,** 115205 (2021).

507. Akinaga, H. & Shima, H. Resistive Random Access Memory (ReRAM) Based on Metal Oxides. *Proc. IEEE* **98,** 2237 (2010).

508. RM, B. & GN, B. Information coding on the basis of synchronization of neuronal activity. *Biosystems.* **40,** 3 (1997).

509. Chen, X. *et al.* A compact skyrmionic leaky–integrate–fire spiking neuron device. *Nanoscale* **10,** 6139 (2018).

510. Chen, M.-C., Sengupta, A. & Roy, K. Magnetic Skyrmion as a Spintronic Deep Learning Spiking Neuron Processor. *IEEE Trans. Magn.* **54,** 1 (2018).

511. Zhang, X., Ezawa, M. & Zhou, Y. Magnetic skyrmion logic gates: conversion, duplication and merging of skyrmions. *Sci. Rep.* **5,** 9400 (2015).

512. Luo, S. *et al.* Reconfigurable Skyrmion Logic Gates. *Nano Lett.* **18,** 1180 (2018).

513. Zhang, X., Zhou, Y., Ezawa, M., Zhao, G. P. & Zhao, W. Magnetic skyrmion transistor: skyrmion motion in a voltage-gated nanotrack. *Sci. Rep.* **5,** 11369 (2015).

514. Tanaka, G. *et al.* Recent advances in physical reservoir computing: A review. *Neural Networks* **115,** 100 (2019).

515. Prychynenko, D. *et al.* Magnetic Skyrmion as a Nonlinear Resistive Element: A Potential Building Block for Reservoir Computing. *Phys. Rev. Appl.* **9,** 014034 (2018).

516. Papp, A., Csaba, G. & Porod, W. Characterization of nonlinear spin-wave interference by reservoir-computing metrics. *Appl. Phys. Lett.* **119,** 112403 (2021).

517. Poppelbaum, W. J., Afuso, C. & Esch, J. W. Stochastic Computing Elements and Systems. *Proceedings of Fall Joint Computer Conference. AFIPS '67 (Fall)* 635 (1967).

518. Pinna, D. *et al.* Skyrmion Gas Manipulation for Probabilistic Computing. *Phys. Rev. Appl.* **9,** 064018 (2018).

519. Miltat, J., Rohart, S. & Thiaville, A. Brownian motion of magnetic domain walls and skyrmions, and their diffusion constants. *Phys. Rev. B* **97,** 214426 (2018).

520. Rapley, A. Iterative decoding using stochastic computation. *Electron. Lett.* **39,** 299(2) (2003).

521. Suggs, D., Subramony, M. & Bouvier, D. The AMD "Zen 2" Processor. *IEEE Micro* **40,** 45 (2020).

522. LeCun, Y., Bengio, Y. & Hinton, G. Deep learning. *IEEE Trans. Magn.* **521,** 436 (2015).

523. Chen, R., Li, Y., Pavlidis, V. F. & Moutafis, C. Skyrmionic interconnect device. *Phys. Rev. Research* **2,** 043312 (2020).

524. Jalali, B. & Fathpour, S. Silicon Photonics. *J. Light. Technol.* **24,** 4600 (2006).

525. Wong, D., De Micheli, G., Flynn, M. & Huston, R. A bipolar population counter using wave pipelining to achieve 2.5* normal clock frequency. *IEEE J. Solid-State Circuits* **27,** 745 (1992).

526. Infineon Technologies AG. TLE5046iC. *Data Sheet,* 1 (2020).

527. Tumanski, S. Modern magnetic field sensors–a review. *Organ* **10,** 1 (2013).

528. Silva, Ana V. *et al.* Linearization strategies for high sensitivity magnetoresistive sensors. *Eur. Phys. J. Appl. Phys.* **72,** 10601 (2015).

529. Suess, D. *et al.* Topologically protected vortex structures for low-noise magnetic sensors with high linear range. *Nat. Electron.* **1,** 362 (2018).

530. Néel, L. Anisotropie magnétique superficielle et surstructures d'orientation. *J. Phys. Radium* **15,** 225 (1954).

531. Wisniowski, P., Wrona, J., Stobiecki, T., Cardoso, S. & Freitas, P. Magnetic Tunnel Junctions Based on Out-of-Plane Anisotropy Free and In-Plane Pinned Layer Structures for Magnetic Field Sensors. *IEEE Trans. Magn.* **48,** 3840 (2012).

532. Muehlenhoff, C., Vogler, C., Raberg, W., Suess, D. & Albrecht, M. Spin-Canting Effects in GMR Sensors With Wide Dynamic Field Range. *IEEE Sens. J.* **21,** 13176 (2021).

533. Bernand-Mantel, A., Muratov, C. B. & Simon, T. M. Unraveling the role of dipolar versus Dzyaloshinskii-Moriya interactions in stabilizing compact magnetic skyrmions. *Phys. Rev. B* **101,** 045416 (2020).

534. Azim, Z. A., Chen, M.-C. & Roy, K. Skyrmion Sensor-Based Low-Power Global Interconnects. *IEEE Trans. Magn.* **53,** 1 (2017).

535. Malozemoff, A. & Slonczewski, J. in *Magnetic Domain Walls in Bubble Materials* 217 (Academic Press, 1979).

536. Hintermayr, J., Ullrich, A. & Albrecht, M. Structure and magnetic properties of ferrimagnetic [Gd/Fe]n multilayer and Gdx Fe100-x thin films. *AIP Adv.* **11,** 095214 (2021).

537. Garlow, J. A., Beleggia, M., Pollard, S. D., Yang, H. & Zhu, Y. Unconventional domain-wall pairs and interacting Bloch lines in a Dzyaloshinskii-Moriya multilayer thin film. *Phys. Rev. B* **102,** 214429 (2020).

538. Stavrou, E. & Röll, K. Magnetic anisotropy in Gd/(FeCo) and Gd/Fe multilayers for high density magneto-optical recording. *J. Appl. Phys.* **85,** 5971 (1999).

539. Stavrou, E., Sbiaa, R., Suzuki, T., Knappmann, S. & Röll, K. Magnetic anisotropy and spin reorientation effects in Gd/Fe and Gd/(FeCo) multilayers for high density magneto-optical recording. *J. Appl. Phys.* **87,** 6899 (2000).

540. Seaberg, M. H. *et al.* Spontaneous fluctuations in a magnetic Fe/Gd skyrmion lattice. *Phys. Rev. Research* **3,** 033249 (2021).

541. Heistracher, P., Bruckner, F., Abert, C., Vogler, C. & Suess, D. Hybrid FFT algorithm for fast demagnetization field calculations on non-equidistant magnetic layers. *J. Magn. Magn. Mater.* **503,** 166592 (2020).

542. Abert, C., Exl, L., Bruckner, F., Drews, A. & Suess, D. magnum.fe: A micromagnetic finite-element simulation code based on FEniCS. *J. Magn. Magn. Mater.* **345,** 29 (2013).

543. Landau, L. & Lifshitz, E. in *Perspectives in Theoretical Physics* 51 (Pergamon, 1992).

544. Gilbert, T. A phenomenological theory of damping in ferromagnetic materials. *IEEE Trans. Magn.* **40,** 3443 (2004).

545. Abert, C. Micromagnetics and spintronics: models and numerical methods. *Eur. Phys. J. B* **92,** 120 (2019).

546. Tian, Z., Sander, D. & Kirschner, J. Nonlinear magnetoelastic coupling of epitaxial layers of Fe, Co, and Ni on Ir(100). *Phys. Rev. B* **79,** 024432 (2009).

547. Dinia, A., Stoeffel, M., Rahmouni, K., Stoeffler, D. & van den Berg, H. A. M. Exchange coupling and magnetoresistance in Co/Ir multilayers prepared by ion beam sputtering. **42,** 331 (1998).

548. Talik, E. & Ślebarski, A. Properties of Gd3T compounds (T = Rh, Ir, Pd). *J. Alloys Compd.* **223,** 87 (1995).

549. E, W., Ren, W. & Vanden-Eijnden, E. Simplified and improved string method for computing the minimum energy paths in barrier-crossing events. *Int. J. Chem. Phys.* **126,** 164103 (2007).

550. Koraltan, S. *et al.* Dependence of energy barrier reduction on collective excitations in square artificial spin ice: A comprehensive comparison of simulation techniques. *Phys. Rev. B* **102,** 064410 (2020).

551. Kim, D.-H. *et al.* Bulk Dzyaloshinskii–Moriya interaction in amorphous ferrimagnetic alloys. *Nat. Mater.* **11,** 1115 (2020).

552. Moreau-Luchaire, C. *et al.* Additive interfacial chiral interaction in multilayers for stabilization of small individual skyrmions at room temperature. *Nat. Nanotechnol.* **11,** 444 (2016).

553. Craik, D. & Cooper, P. Criteria for uniaxial magnetostatic behaviour in thin platelets. *Phys. Lett. A* **41,** 255 (1972).

554. Cuadrado, R. *et al.* A multiscale model of the effect of Ir thickness on the static and dynamic properties of Fe/Ir/Fe films. *Sci. Rep.* **8,** 3879 (2018).

555. Louzazna, K. & Haroun, A. Magnetism of strained bcc Fe/Ir(001). *Solid State Commun.* **112,** 649 (1999).

556. Samant, M. *et al.* Induced spin polarization in Cu spacer layers in Co/Cu multilayers. *Phys. Rev. Lett.* **72,** 1112 (1994).

557. White, R. & Friedman, D. Theory of the magnetic proximity effect. *J. Magn. Magn. Mater.* **49,** 117 (1985).

558. Meng, K.-Y. *et al.* Observation of Nanoscale Skyrmions in SrIrO3/SrRuO3 Bilayers. *Nano Lett,* **19,** 3169 (2019).

559. McGrouther, D. *et al.* Internal structure of hexagonal skyrmion lattices in cubic helimagnets. *New J. Phys.* **18,** 095004 (2016).

560. Je, S.-G. *et al.* Direct Demonstration of Topological Stability of Magnetic Skyrmions via Topology Manipulation. *ACS Nano* **14,** 3251 (2020).

561. Fin, S. *et al.* In-plane rotation of magnetic stripe domains in $\mathrm{Fe}_{1-x}\mathrm{Ga}_x$ thin films. *Phys. Rev. B* **92,** 224411 (2015).

562. Kerber, N. *et al.* Anisotropic Skyrmion Diffusion Controlled by Magnetic-Field-Induced Symmetry Breaking. *Phys. Rev. Appl.* **15,** 044029 (2021).

563. Zhang, S. *et al.* Deformation of Néel-type skyrmions revealed by Lorentz transmission electron microscopy. *Appl. Phys. Lett.* **116,** 142402 (2020).

564. Shibata, K. *et al.* Large anisotropic deformation of skyrmions in strained crystal. *Nat. Nano.* **10,** 589 (2015).

565. Masell, J., Rodrigues, D. R., McKeever, B. F. & Everschor-Sitte, K. Spin-transfer torque driven motion, deformation, and instabilities of magnetic skyrmions at high currents. *Phys. Rev. B* **101,** 214428 (2020).

566. Salimath, A., Zhuo, F., Tomasello, R., Finocchio, G. & Manchon, A. Controlling the deformation of antiferromagnetic skyrmions in the high-velocity regime. *Phys. Rev. B* **101,** 024429 (2020).

567. Litzius, K. *et al.* The role of temperature and drive current in skyrmion dynamics. *Nat. Electron.* **3,** 30 (2020).

568. Krupinski, M. *et al.* Ion induced ferromagnetism combined with self-assembly for large area magnetic modulation of thin films. *Nanoscale* **11,** 8930 (2019).

569. Rettner, C. T., Anders, S., Baglin, J. E. E., Thomson, T. & Terris, B. D. Characterization of the magnetic modification of Co/Pt multilayer films by He+, Ar+, and Ga+ ion irradiation. *Appl. Phys. Lett.* **80,** 279 (2002).

570. Jeong, J.-R. *et al.* Fabrication of Hexagonal Lattice Co/Pd Multilayer Nanodot Arrays Using Colloidal Lithography. *Small* **3,** 1529 (2007).

571. Krupinski, M., Perzanowski, M., Zarzycki, A., Zabila, Y. & Marszałek, M. Ordered FePdCu nanoisland arrays made by templated solid-state dewetting. *Nanotechnology* **26,** 425301 (2015).

572. Krupinski, M. *et al.* Magnetic transition from dot to antidot regime in large area Co/Pd nanopatterned arrays with perpendicular magnetization. *Nanotechnology* **28,** 085302 (2017).

573. Sapozhnikov, M. V. *et al.* Artificial dense lattice of magnetic bubbles. *Appl. Phys. Lett.* **109,** 042406 (2016).
574. Akinoglu, E. M., Morfa, A. J. & Giersig, M. Understanding Anisotropic Plasma Etching of Two-Dimensional Polystyrene Opals for Advanced Materials Fabrication. *Langmuir* **30,** 12354 (2014).
575. Brombacher, C. *et al.* Tailoring particle arrays by isotropic plasma etching: an approach towards percolated perpendicular media. *Nanotechnology* **20,** 105304 (2009).
576. Urbánek, M. *et al.* Research Update: Focused ion beam direct writing of magnetic patterns with controlled structural and magnetic properties. *APL Mater.* **6,** 060701 (2018).
577. Makarov, D. *et al.* Magnetic strip patterns induced by focused ion beam irradiation. *J. Appl. Phys.* **103,** 063915 (2008).
578. Ahrens, V. *et al.* Focused ion beam irradiation for generation of skyrmionic bubble like structures. *J. Magn. Magn. Mater.* **523,** 167591 (2021).
579. Montoya, S. A. *et al.* Spin-orbit torque induced dipole skyrmion motion at room temperature. *Phys. Rev. B* **98,** 104432 (2018).
580. Abert, C., Exl, L., Bruckner, F., Drews, A. & Suess, D. magnum.fe: A micromagnetic finite-element simulation code based on FEniCS. *J. Magn. Magn. Mater.* **345,** 29 (2013).

Appendix C

Abbreviations and Symbols

C.1 Abbreviations

ADF	**A**nnular **D**ark-**F**ield	(Sec. 3.2.7)
AF	**A**nti**F**erromagnet	(Sec. 2.2.0)
AFM	**A**tomic **F**orce **M**icroscopy	(Sec. 3.2.5)
AHE	**A**nomalous **H**all **E**ffect	(Sec. 3.3.4)
Al	**Al**uminum	(Sec. 5.3.9)
AMR	**A**nisotropic **M**agneto**R**esistance	(Sec. 5.1.3)
ANN	**A**rtifical **N**eural **N**etwork	(Sec. 5.1.2)
AOS	**A**ll-**O**ptical **S**witching	(Sec. 4.1.0)
Ar	**Ar**gon	(Sec. 3.1.1)
BF	**B**right **F**ield	(Sec. 3.2.7)
BLS	**B**rilloin **L**ight **S**cattering	(Sec. 3.3.4)
BPM	**B**it **P**atterned **M**edia	(Sec. 4.1.1)
CCD	**C**harge-**C**oupled **D**evice	(Sec. 3.2.7)
ccw	**c**ounter**c**lock**w**ise	(Sec. 2.4.2)
CEITEC	**C**entral **E**uropean **I**nstitute of **TEC**hnology	(Sec. 3.2.7)
Co	**Co**balt	(Sec. 2.1.4)
Cu	**C**opper	(Sec. 3.2.2)
cw	**c**lock**w**ise	(Sec. 2.4.2)
DC	**D**irect **C**urrent	(Sec. 3.1.1)
DF	**D**ark-**F**ield	(Sec. 3.2.7)
DFG	**D**eutsche **F**orschungs**G**emeinschaft (German Research Foundation)	(Sec. 4.4.0)
DMI	**D**zyaloshinskii–**M**oriya **I**nteraction	(Sec. 2.1.1)
DPC	**D**ifferential **P**hase **C**ontrast	(Sec. 3.3.3)
DRAM	**D**ynamic **R**andom-**A**ccess **M**emory	(Sec. 4.1.0)
DW	**D**omain **W**all	(Sec. 2.4.1)
EB	**E**xchange **B**ias	(Sec. 2.0.0)

ECC	**E**xchange-**C**oupled **C**omposite	(Sec. 4.1.1)
EDS/EDX	**E**nergy-**D**ispersive **X**-ray **S**pectroscopy	(Sec. 3.2.7)
EMPA	**E**idgenössische **M**aterial**P**rüfungs- und Forschungs-**A**nstalt (Swiss Federal Laboratories for Materials Science and Technology)	(Sec. 3.3.2)
EPFL	**É**cole **P**olytechnique **F**édérale de **L**ausanne (Swiss Federal Institutes of Technology in Lausanne)	(Sec. 3.3.4)
Eq.	**Eq**uation	(Sec. 2.1.3)
Fe	iron	(Sec. 2.2.0)
FI	**F**erri**M**agnet	(Sec. 2.2.0)
FIB	**F**ocused **I**on **B**eam	(Sec. 3.1.2)
Fig.	**Fig**ure	(Sec. 2.1.1)
FL	**F**ree **L**ayer	(Sec. 4.1.0)
FM	**F**erro**M**agnet	(Sec. 2.1.3)
FMR	**F**erro**M**agnetic **R**esonance	(Sec. 3.3.4)
FORC	**F**irst-**O**rder-**R**eversal-**C**urve	(Sec. 3.3.4)
Gd	**G**a**d**olinium	(Sec. 2.2.0)
GMR	**G**iant **M**agneto**R**esistive	(Sec. 2.1.1)
HAADF	**H**igh **A**ngle **A**nnular **D**ark-**F**ield	(Sec. 3.2.7)
HAMR	**H**eat-**A**ssisted **M**agnetic **R**ecording	(Sec. 1.0.0)
HDD	**H**ard **D**isk **D**rive	(Sec. 1.0.0)
HSV	**H**ue **S**aturation **V**alue	(Sec. 3.3.3)
IDW	**I**nterface **D**omain **W**all	(Sec. 2.3.0)
ip	**i**n-**p**lane	(Sec. 2.1.3)
Ir	**Ir**idium	(Sec. 5.2.0)
LLG	**L**andau-**L**ifshitz-**G**ilbert	(Sec. 5.3.1)
LSM	**L**aser **S**canning **M**icroscopy	(Sec. 3.2.3)
LTEM	**L**orentz **T**ransmission **E**lectron **M**icroscopy	(Sec. 3.3.3)
LTO	**L**inear **T**ape-**O**pen	(Sec. 1.0.0)
MAMR	**M**icrowave-**A**ssisted **M**agnetic **R**ecording	(Sec. 4.1.0)
MFM	**M**agnetic **F**orce **M**icroscopy	(Sec. 3.3.2)
ML	**M**ulti**L**ayer	(Sec. 1.0.0)
MnSi	**M**a**n**ganese **Si**licide	(Sec. 2.1.1)
MOKE	**M**agneto-**O**ptic **K**err **E**ffect	(Sec. 3.3.4)
MPMS	**M**agnetic **P**roperty **M**easurement **S**ystem	(Sec. 3.3.1)
MRAM	**M**agnetoresistive **R**andom **A**ccess **M**emory	(Sec. 4.1.0)
MTJ	**M**agnetic **T**unnel **J**unction	(Sec. 4.1.0)
NFT	**N**ear-**F**ield **T**ransducer	(Sec. 4.1.1)
Ni	**Ni**ckel	(Sec. 2.2.0)
NV	**N**on-**V**olatile	(Sec. 1.0.0)
oop	**o**ut-**o**f-**p**lane	(Sec. 2.1.3)

Pd	Palladium	(Sec. 2.1.4)
PMA	Perpendicular Magnetic Anisotropy	(Sec. 2.1.4)
PMR	Perpendicular Magnetic Recording	(Sec. 4.1.0)
Pt	Platin	(Sec. 2.1.4)
RAM	Random-Access Memory	(Sec. 1.0.0)
RBS	Rutherford Backscattering Spectrometry	(Sec. 3.2.1)
RE	Rare Earth	(Sec. 2.2.0)
Ref.	Reference	(Sec. 2.1)
RF	Radio Frequency	(Sec. 5.6.1)
RKKY	Ruderman–Kittel-Kasuya-Yosida	(Sec. 2.1.1)
RRAM	Resistive Random-Access Memory	(Sec. 5.1.2)
RT	Room Temperature	(Sec. 2.2.0)
SAF	Synthetic AntiFerromagnet	(Sec. 2.4.3)
SAW	Surface Acoustic Waves	(Sec. 5.1.1)
Sec.	Section	(Sec. 1.0.0)
SEM	Scanning Electron Microscopy	(Sec. 3.2.4)
SHE	Spin Hall Effect	(Sec. 3.3.4)
Si	Silicon	(Sec. 4.2.1)
SiO	Silicon Oxide	(Sec. 4.2.1)
SkHE	Skyrmion Hall Effect	(Sec. 2.4.2)
SMR	Shingled Magnetic Recording	(Sec. 4.1.1)
SNR	Signal-to-Noise Ratio	(Sec. 4.1.1)
SOC	Spin-Orbit Coupling	(Sec. 2.1.1)
SOT	Spin Orbit Torque	(Sec. 2.4.2)
SRAM	Static Random-Access Memory	(Sec. 4.1.0)
SRO	Short Range Order	(Sec. 2.2.0)
SSD	Solid-State Drive	(Sec. 1.0.0)
STEM	Scanning Transmission Electron Microscopy	(Sec. 3.2.7)
STT	Spin Transfer Torque	(Sec. 2.4.2)
SQUID	Superconducting QUantum Interference Device	(Sec. 3.3.1)
Ta	Tantalum	(Sec. 4.3.1)
Tb	Terbium	(Sec. 2.2.0)
TB	TeraByte	(Sec. 1.0.0)
TEM	Transmission Electron Microscopy	(Sec. 3.2.7)
THE	Topological Hall Effect	(Sec. 3.3.4)
TIE	Transport of Intensity Equation	(Sec. 3.3.3)
TM	Transition Metal	(Sec. 2.2.0)
TMR	Tunneling MagnetoResistance	(Sec. 4.1.0)
TRR	TransRegional Collaborative Research Center	(Sec. 5.0.0)
UHV	Ultra-High Vacuum	(Sec. 3.1.1)
VSM	Vibrating Sample Magnetometry	(Sec. 3.3.1)

X	Insertion layer (Pd, Pt, no insertion layer)	(Sec. 4.2.1)
XMCD	**X**-ray **M**agnetic **C**ircular **D**ichroism	(Sec. 2.2.0)
XMR	**M**agneto**R**esistance	(Sec. 5.1.3)
XRD	**X**-**R**ay **D**iffraction	(Sec. 3.2.2)

C.2 Latin Symbols

a_{hkl}	distance of the lattice planes	(Sec. 3.2.2)
A	magnetic exchange stiffness constant	(Sec. 2.1.1)
$\boldsymbol{B}$	magnetic field	(Sec. 3.1.1)
B_{ip}	ip component of the magnetic induction	(Sec. 3.3.3)
c	speed of light	(Sec. 3.2.4)
d	resolution limit	(Sec. 3.2.7)
D	magnetic domain size	(Sec. 2.4.1)
$\boldsymbol{D}$	DMI vector	(Sec. 2.1.1)
e	electron charge	(Sec. 3.2.6)
e_{d}	dipolar energy per area	(Sec. 2.4.1)
e_{dw}	domain wall energy per area	(Sec. 2.4.1)
$\boldsymbol{e}_{\mathrm{oop}}$	unit vector oop	(Sec. 5.3.1)
$\boldsymbol{E}$	electric field	(Sec. 3.1.1)
$E_{0,\mathrm{ion}}$	incident ion energy	(Sec. 3.2.1)
E_{ani}	anisotropy energy	(Sec. 2.1.4)
E_{d}	magnetic dipolar energy	(Sec. 2.1.3)
E_{DMI}	DMI contribution energy	(Sec. 2.1.1)
E_{ex}	magnetic exchange energy	(Sec. 2.1.1)
E_{fermi}	Fermi energy	(Sec. 2.2.0)
E_{ion}	back-scattered ion energy	(Sec. 3.2.1)
E_{kin}	kinetic energy	(Sec. 3.2.4)
E_{zee}	Zeeman energy	(Sec. 2.1.2)
ΔE_0	energy barrier	(Sec. 4.1.1)
$\boldsymbol{F}_{\mathrm{l}}$	Lorentz force	(Sec. 3.3.3)
Δf	defocus	(Sec. 3.3.3)
h	Planck's constant	(Sec. 3.2.4)
H	magnetic field	(Sec. 2.1.2)
H_{a}	anisotropy field	(Sec. 2.1.4)
H_{appl}	applied magnetic field	(Sec. 3.3.3)
H_{c}	coercive field	(Sec. 2.1.4)
$\boldsymbol{H}_{\mathrm{d}}$	demagnetization field	(Sec. 2.1.3)

$\boldsymbol{H}_{\mathbf{eff}}$	effective magnetic field	(Sec. 5.3.1)
H_{ext}	external magnetic field	(Sec. 2.1.2)
H_{ip}	ip magnetic field component	(Sec. 3.3.3)
H_{n}	nucleation magnetic field	(Sec. 2.3)
H_{oop}	oop magnetic field component	(Sec. 3.3.3)
I_{b}	bias current	(Sec. 3.3.1)
I_{c}	critical current	(Sec. 3.3.1)
δI	induced current	(Sec. 3.3.1)
J	quantum mechanical exchange integral	(Sec. 2.1.1)
k	incident wave vector	(Sec. 3.2.2)
k'	scatter wave vector	(Sec. 3.2.2)
k_{B}	Boltzmann constant	(Sec. 4.1.1)
K_{eff}	effective magnetic anisotropy	(Sec. 2.1.4)
K_{shape}	shape magnetic anisotropy	(Sec. 2.1.3)
K_{strain}	magnetoelastic anisotropy	(Sec. 2.1.4)
K_{u}	uniaxial magnetic anisotropy	(Sec. 2.1.4)
l	length	(Sec. 5.3.1)
l_{ex}	exchange length	(Sec. 5.3.1)
$\boldsymbol{m}$	magnetization density	(Sec. 2.4.2)
$\boldsymbol{M}$	local magnetization	(Sec. 2.1.1)
M_{r}	remanent magnetization	(Sec. 2.1.4)
M_{s}	saturation magnetization	(Sec. 2.1.3)
$M_{\mathrm{s,Co}}$	M_{s} of the Co layer	(Sec. 4.2.2)
$M_{\mathrm{s,Co+X}}$	$M_{\mathrm{s,Co}}$ and partially M of the insertion layer	(Sec. 4.2.2)
$M_{\mathrm{s,hard}}$	M_{s} of the magnetically harder layer	(Sec. 2.3)
$M_{\mathrm{s,Ni}}$	M_{s} of the Ni layer	(Sec. 4.2.2)
$M_{\mathrm{s,Ni+X}}$	$M_{\mathrm{s,Ni}}$ and partially M of the insertion layer	(Sec. 4.2.2)
$M_{\mathrm{s,soft}}$	M_{s} of the magnetically softer layer	(Sec. 2.3)
$\boldsymbol{m}_{\mathrm{sk}}$	magnetization density of a skyrmion	(Sec. 2.4.2)
m'	mass	(Sec. 3.1.1)
m_e^*	effective electron mass	(Sec. 3.2.6)
m'_{e}	electron rest mass	(Sec. 3.2.4)
m'_{ion}	ion mass	(Sec. 3.2.1)
m'_{nucleus}	nuclei mass	(Sec. 3.2.1)
n	density of electrons	(Sec. 3.2.6)
n'	refractive index	(Sec. 3.2.7)
N	multilayer repetition number	(Sec. 2.1.4)
N_{grains}	number of grains	(Sec. 4.1.1)
N_{sk}	topological charge	(Sec. 2.4.2)
NA	numerical aperture	(Sec. 3.2.7)
p	polarity	(Sec. 2.4.2)

Q	quantity of spin objects	(Sec. 5.5.1)
R	deposition rate	(Sec. 3.1.1)
$\boldsymbol{R}$	reciprocal lattice vector	(Sec. 3.2.2)
$\boldsymbol{S}$	electron spin direction	(Sec. 2.1.1)
Δs	path difference	(Sec. 3.2.2)
t	film thickness	(Sec. 2.4.1)
t_{Co}	cobalt layer thickness	(Sec. 4.2.1)
t_{Gd}	gadolinium layer thickness	(Sec. 5.2.1)
t_{Ni}	nickel layer thickness	(Sec. 4.2.1)
$t_{\mathrm{Pd/Pt}}$	palladium/platinum layer thickness	(Sec. 4.2.1)
t'	time	(Sec. 5.3.1)
T	temperature	(Sec. 4.1.1)
T_{anneal}	annealing temperature	(Sec. 4.3.3)
T_{c}	curie temperature	(Sec. 4.1.1)
T_{comp}	compensation temperature	(Sec. 2.2)
u	atomic mass	(Sec. 3.1.1)
δU	induced voltage change	(Sec. 3.3.1)
v	vorticity	(Sec. 2.4.2)
$\boldsymbol{v}$	velocity	(Sec. 3.3.3)
V	volume	(Sec. 2.1.1)
w	width	(Sec. 5.3.1)
X, Y	element place holder	(Sec. 3.1.1)

C.3 Greek Symbols

α	opening angle of the objective	(Sec. 3.2.7)
α_{damp}	Gilbert damping constant	(Sec. 5.3.1)
β	TEM tilt angle	(Sec. 3.3.3)
β_{l}	angle of Lorentz deflection	(Sec. 3.3.3)
γ	helicity	(Sec. 2.4.2)
γ_{dw}	energy of a domain wall per area	(Sec. 2.4.1)
γ_{gyro}	reduced gyromagnetic ratio	(Sec. 5.3.1)
δ_{dw}	domain wall width	(Sec. 2.4.1)
θ	azimuthal/glancing angle	(Sec. 2.4.2)
ϑ	RBS angle	(Sec. 3.2.1)
κ	angle between the magnetization and the easy-axis	(Sec. 2.1.4)
λ	wavelength	(Sec. 3.2.2)
λ_{e}	electron wavelength	(Sec. 3.2.4)
λ_{s}	saturation magnetostriction constant	(Sec. 2.1.4)

μ_0	magnetic vacuum permeability	(Sec. 2.1.3)
ρ	density	(Sec. 3.1.1)
σ	sheet resistance	(Sec. 3.2.6)
σ'	mechanical strain	(Sec. 2.1.4)
ς	resistivity	(Sec. 3.2.6)
τ	average free time between scattering events	(Sec. 3.2.6)
τ_0	attempt period	(Sec. 4.1.1)
τ_N	Néel relaxation time	(Sec. 4.1.1)
ϕ	polar angle	(Sec. 2.4.2)
$\boldsymbol{\phi}$	out-of-plane magnetization density	(Sec. 2.4.2)
Φ_0	quantized magnetic flux	(Sec. 3.3.1)
Φ_ext	external magnetic flux	(Sec. 3.3.1)
Ω_m	a magnetic region	(Sec. A.3)

Appendix D

Publications, Contributions, and Participations

D.1 Publications

- Heigl, M., Koraltan, S., Seidler M., Lienhart, M., Boltje, R. A., Ullrich, A., Lienhart, R., Abert, C., Suess, D. & Albrecht, M., The influence of an in-plane magnetic field on dipolar-stabilized antiskyrmions and other magnetic textures evaluated by a convolutional neural network, *in-progress* (2023).
- Hassan, M., Koraltan, S., Ullrich, A., Bruckner, F., Serha, R., Levchenko, K., Varvaro, G., Kiselev, N. S., Heigl, M., Abert, C., Suess, D. & Albrecht, M., High-order skyrmions and antiskyrmions at room temperature, *in-review Nature Physics* (2023).
- Koraltan, S., Abert, C., Bruckner, F., Heigl, M., Albrecht, M. & Suess, D., Generation and annihilation of skyrmions and antiskyrmions in magnetic heterostructures, *arXiv* 2207.12260 (2022).
- Zayko, S., Kfir, O., Heigl, M., Lohmann, M., Sivis, M., Albrecht, M. & Ropers, C., Ultrafast high-harmonic nanoscopy of magnetization dynamics, *Nature Communications* **12**, 6337 (2021).
- Kreuzpaintner, W., Schmehl, A., Book, A., Mairoser, T., Ye, J., Wiedemann, B., Mayr, S., Moulin, J.-F., Stahn, J., Gilbert, D., Heigl, M., Gabold, H., Masalovich, S., Georgii, R., Albecht, M., Mannhart J. & Böni, P., Reflectometry with Polarized Neutrons on In situ Grown Thin Films, *Physica Status Solidi B* 2100153 (2021).
- Heigl, M., Mangkornkarn, C., Ullrich, A., Krupinski, M. & Albrecht, M., Enhanced annealing stability of ferrimagnetic Tb/FeCo multilayers, *AIP Advances* **11**, 085112 (2021).
- Heigl, M., Koraltan, S., Vanatka, M., Kraft, R., Abert, C., Vogler, C., Semisalova, A., Che, P., Ullrich, A., Schmidt, T., Hintermayr, J., Grundler, D., Farle, M., Urbanek, M., Suess, D. & Albrecht, M., Dipolar-stabilized first and second-order antiskyrmions in ferrimagnetic multilayers, *Nature Communications* **12**, 2611 (2021).

- Volf, A., Alsaadawi, Y., Luna, F. V., Khan, Q. A. , Stierle, S., Xu, C., Heigl, M., Fekri, Z., Zhou, S., Zahn, P., Albrecht, M., Steinhart, M. & Erbe, A., Sensitivity of CoPd/PS Janus particles to an externally applied magnetic field, *RCS Advances* **11**, 17051 (2021).
- Küß, M., Heigl, M., Flacke, L., Hörner, A., Weiler, M., Albrecht, M. & Wixforth, A., Nonreciprocal magnetoacoustic waves in dipolar-coupled ferromagnetic bilayers, *Physical Review Applied* **15**, 034060 (2021).
- Küß, M., Heigl, M., Flacke, L., Hefele, A., Hörner, A., Weiler, M., Albrecht, M. & Wixforth, A., Symmetry of the magnetoelastic interaction of Rayleigh- and shear horizontal-magnetoacoustic waves in nickel thin films on LiTaO$_3$, *Physical Review Letters* **15**, 034046 (2021).
- Alsaadawi, Y., Volf, A., Heigl, M., Zahn, P., Albrecht, M. & Erbe, A., Control over self-assembled Janus clusters by the strength of magnetic field in H2O2, *The European Physical Journal E* **44**, 23 (2021).
- Zayko, S., Kfir, O., Heigl, M., Lohmann, M., Sivis, M., Albrecht, M. & Ropers, C., Femtosecond nanoscopy with high harmonics, *The 22nd International Conference on Ultrafast Phenomena, OSA Technical Digest*, paper W2B.2 (2020).
- Küß, M., Heigl, M., Flacke, L., Hörner, A., Weiler, M., Albrecht, M. & Wixforth, A., Nonreciprocal Dzyaloshinskii–Moriya Magnetoacoustic Waves, *Physical Review Letters* **125**, 217203 (2020).
- Heigl, M., Vogler, C., Mandru, A. O., Zhao, X., Hug, H. J., Suess, D. & Albrecht, M., Microscopic Origin of Magnetization Reversal in Nanoscale Exchange-Coupled Ferri/Ferromagnetic Bilayers: Implications for High Energy Density Permanent Magnets and Spintronic Devices, *ACS Applied Nano Materials* **3**, 9218 (2020).
- Vogler, C., Heigl, M., Mandru, A. O., Hebler, B., Marioni, M. A., Hug, H. J., Albrecht, M. & Suess, D., Hysteresis-free magnetization reversal of exchange-coupled bilayers with finite magnetic anisotropy, *Physical Review B* **108**, 014429 (2020).
- Heigl, M., Wendler, R., Haugg, S. D. & Albrecht, M., Magnetic properties of Co/Ni-based multilayers with Pd and Pt insertion layers, *Journal of Applied Physics* **127**, 233902 (2020).
- Mandru, A. O., Yıldırım, O., Marioni, M. A., Rohrmann, H., Heigl, M., Ciubotariu, O. T., Penedo, M., Zhao, X., Albrecht, M. & Hug, H. J., Pervasive artifacts revealed from magnetometry measurements of rare earth-transition metal thin films, *Journal of Vacuum Science & Technology A* **38**, 023409 (2020).
- Zayko, S., Kfir, O., Heigl, M., Lohmann, M., Sivis, M., Albrecht, M. & Ropers, C., Ultrafast Spin Dynamics Resolved with High-Harmonic Generation Microscopy, *2019 Conference on Lasers and Electro-Optics Europe and European Quantum Electronics Conference, OSA Technical Digest*, paper cg93 (2019).

- Zayko, S., Kfir, O., Heigl, M., Lohmann, M., Sivis, M., Albrecht, M. & Ropers, C., Ultrafast Magnetic Microscopy using High-Harmonic Radiation, *Conference on Lasers and Electro-Optics, OSA Technical Digest*, paper FW4M.4 (2019).
- Aravind, P. B., Heigl, M., Fix, M., Groß, F., Gräfe, J., Mary, A., Rajgowrav, C. R., Krupiński, M., Marszałek, M., Thomas, S., Anantharaman, M. R. & Albrecht, M., Bistability of magnetic states in Fe-Pd nanocap arrays, *Nanotechnology* **30**, 405705 (2019).
- Zayko, S., Kfir, O., Heigl, M., Sivis, M., Albrecht, M. & Ropers, C., Magnetic sub-Wavelength Imaging using High-Harmonic Radiation, *CLEO Pacific Rim Conference 2018, OSA Technical Digest*, paper Th1B.4 (2018).
- Zayko, S., Kfir, O., Heigl, M., Sivis, M., Albrecht, M. & Ropers, C., Nanoscale Magnetic Imaging using High-Harmonic Radiation, *Conference on Lasers and Electro-Optics, OSA Technical Digest*, paper FM4F.3. (2018).

D.2 Conference and Seminar Contributions

- Dipolar-stabilized antiskyrmions in post-deposition anisotropy engineered ferrimagnetic multilayers, oral presentation, *16th International Conference on Nanostructured Materials Sevilla 2022*.
- Dipolar-stabilized first and second-order antiskyrmions in ferrimagnetic multilayers, oral presentation, *Joint MMM-Intermag Conference New Orleans 2022*.
- Dipolar-stabilized first and second-order antiskyrmions in ferrimagnetic multilayers, invited lecture within the "Young and Brilliant" session, *The European Conference Physics of Magnetism 2021*.
- Dipolar-stabilized first and second-order antiskyrmions in ferrimagnetic multilayers, oral presentation, *Sol-Skymag: International Conference on Magnetism and Spintronics 2021*.
- Spin textures in ferrimagnetic multilayers, oral presentation, *TRR80 Online Retreat Meeting 2021*.
- Dipolar-stabilized first and second-order antiskyrmions in ferrimagnetic multilayers, contributed talk, *736. WE-Heraeus-Seminar: Magnetism at the Nanoscale 2021*.
- Microscopic origin of magnetization reversal in exchange-coupled ferro-/ferri- magnetic bilayers, oral presentation, *MMM Virtual Conference 2020*.
- Zoo of spin textures in Fe/Gd-based multilayers, oral presentation, *TRR80 Retreat Meeting 2020*.
- Dipole stabilized bubbles and skyrmions in Fe/Gd multilayers, poster presentation, *MMM Conference Las Vegas 2019*.

- Dipole stabilized bubble-like skyrmions in Fe/Gd multilayers, poster presentation, *JEMS Conference Uppsala 2019*.
- Magnetic skyrmions in Fe/Gd multilayer thin films, oral presentation, *TRR80 Retreat Meeting 2019*.
- Dipole stabilized bubble-like skyrmions in Fe/Gd multilayers, poster presentation, *DPG-Frühjahrstagung Regensburg 2019*.
- TbCoFe/$[\mathrm{Co/Ni/Pt}]_N$ exchange-coupled heterostructure, oral presentation, *JEMS Conference Mainz 2018*.
- TbCoFe/$[\mathrm{Co/Ni/Pt}]_N$ exchange coupled heterostructure as a heat-assisted magnetic recording media, oral presentation, *DPG-Frühjahrstagung Berlin 2018*.

D.3 School and Workshop Participations

- DPG - Leading for Tomorrow 2021, Bad Honnef and Berlin, Germany (seven days).
- European School on Magnetism 2018, Kraków, Poland (two weeks).
- TRR80 IGS Workshop 2018 on Project Management, Riva del garda, Italy (four days).
- IFF Spring School 2017 on Toplological Matter, Jülich, Germany (two weeks).

.

Appendix E

Acknowledgements

All the successful work would have never been possible without many people's great help and support. I appreciated the exciting time within the chair of Experimental Physics IV (EPIV) and the amazing experiences I had at all the conferences, project meetings, workshops, and schools. The great atmosphere present in the group, with collaborators, and colleagues, always motivated me for my scientific work, and I am really thankful for that. My gratitude appertains in particular to:

- **Prof. Dr. Manfred Albrecht**. I would like to thank him first for giving me the opportunity to work on these fascinating research topics and exciting projects. I am very grateful for his continuous support, the broad knowledge he shared, and the freedom of choice I had in my work.
- **Prof. Dr. Dieter Suess** and **Prof. Dr. Hans Josef Hug** for being my second and third examiner as well as great collaboration partners. Their expertise was of utmost importance for this work.
- My amazing office mates: **Mario Fix**, who has always been there for so many helpful discussions, even about the tiniest details of our work. **Oana Ciubotariu**, who always found my mistakes and has never been shy pointing them out, which sounds annoying but has been so helpful for me to improve. **Johannes Seyd**, who has never hesitated a second to help and always impressed me with his kindness and knowledge about grammar, science, and the most random things. **Christian Holzmann**, who taught me a lot about garnets and hopefully will discover skyrmions in them sooner rather than later. Thanks to them, it has been a pleasure to come to the office. This, I learned to appreciate even more during COVID times.
- The great magnetism and thermoelectrics group of EPIV, which I had the honor to be a part of: **Matthias Küß**, **Mariam Hassan**, **Aladin Ullrich**, **Florian Jung**, **Clemens Mühlenhoff**, **Michał Krupiński**, **Felix Timmermann**, **Julian Hintermayr**, **Nataliia Schmidt**, **Marc Lindorf**, **Dmitriy Mitinh**, **Birgit Hebler**, and **Dennis Nissen**.

- The best Bachelor and Master students I could have wished for: **Ralph Wendler**, **Simon Haugg**, **Timo Schmidt**, **Chayangkoon Mangkornkarn**, **Maximilian Seidler**, and **Raluca Boltje**.
- The other chair members of EPIV and in particular the technical staff: **Olga Lik**, **Wolfgang Reiber**, **Birgit Knoblich**, **Wolfgang Brückner**, and our always friendly and patient secretaries: **Claudia Löflath** and **Bettina Schestak**.
- Our collaborators from the University of Vienna: **Sabri Koraltan**, **Christoph Vogler**, **Claas Abert**, **Olivia Muthsam**, and **Prof. Dr. Dieter Süss**.
- Our collaborators from the EMPA: **Andrada-Oana Mandru** and **Prof. Dr. Hans Josef Hug**.
- Our collaborators from the CEITEC: **Marek Vanatka**, **Igor Turčan**, **Lukáš Flajšman**, and **Michal Urbánek**.
- Our collaborators from the Georg-August-University of Göttingen: **Sergey Zayko**, **John Gaida**, **Ofer Kfir**, and **Prof. Dr. Claus Ropers**.
- Our collaborators from the Technical University of Munich **Zahra Inanloo-Maranloo**, **Henrik Gabold**, **Wolfgang Kreuzpaintner**, and **Prof. Dr. Peter Böni**.
- The many other collaborators with whom I had the pleasure to work with, including but not limited to: **Che Ping** and **Prof. Dr. Dirk Grundler** (EPFL), **Anna Volf** (HZDR), and **Aravind Pthriath Balan** (The University of Manchester).
- The great and inspiring people that I had the pleasure to meet and listen to at conferences, lectures, workshops, and schools, who are to many to be named here.
- My physics teacher **Herr Gräupner**, without whom I maybe would have never studied physics and who ignited my passion for it.
- Meinen Eltern **Bernd** und **Gisela Heigl**, die mich durch mein gesamtes Studium und die Promotion unterstützt haben. Ich hoffe meinem Vater ist klar, dass ich mit dem Abschluss dieser Arbeit immer noch nicht alle seine Fragen über Astrophysik beantworten kann.
- Meinem Großvater **Theodor Müller**, der immer an meiner Forschung interessiert war. Leider war es mir nicht möglich diese Arbeit rechtzeitig für ihn fertig zu stellen, was ich zutiefst bedauere.
- All my friends and colleagues, who I had the pleasure to meet throughout my university life. In particular, my close friends and gym buddies **Tobias Petzak**, **Manuel Milling**, and **Patrick Kudella**, who always paid attention that my physical activity is in balance with my mental work.
- Finally, I thank **Michelle Lienhart**. For everything. She always motivated me and helped me to relax at the right moments. This work would not be the same without her, and it would definitely have been a lot less fun. I love you.